Converting wave energy from fluid-elasticity interactions

Clotilde Nové-Josserand

THÈSE DE DOCTORAT
DE L'UNIVERSITÉ SORBONNE PARIS CITÉ
PRÉPARÉE À L'UNIVERSITÉ PARIS DIDEROT

École Doctorale : Physique en Île-de-France (ED 564)

Spécialité : Mécanique des Fluides

Converting wave energy from fluid-elasticity interactions*

*Convertir l'énergie des vagues à partir d'interactions fluide-élasticité

Présentée par Clotilde NOVÉ-JOSSERAND

Dirigée par Benjamin THIRIA et Ramiro GODOY-DIANA

Soutenue à Paris le 1er octobre 2018 devant le jury composé de

M^{me} Sandra Lerouge, Professeur, Université Paris-Diderot	Présidente du jury
M. Médéric Argentina, Professeur, Université Nice Sophia Antipolis	Rapporteur
M. Olivier Doaré, Professeur, ENSTA-ParisTech	Rapporteur
M. William Megill, Professeur, Hochschule Rhein-Waal	Examinateur
M. Aurélien Babarit, Ingénieur de Recherche, École Centrale Nantes	Examinateur
M^{me} Delphine Doppler, Maître de Conférences, Université Lyon 1	Examinatrice
M^{me} Gaële Perret, Maître de Conférences, Université du Havre	Examinatrice
M. Ramiro Godoy-Diana, Chargé de Recherche, Sorbonne Université	Directeur de thèse
M. Benjamin Thiria, Maître de Conférences, Sorbonne Université	Directeur de thèse

Abstract

Understanding the mechanisms involved in wave-structure interactions is of high interest for the development of efficient wave energy harvesters as well as for coastal management. In this thesis, we study the interactions of surface waves with a model array of slender flexible structures, in view of developing an efficient system for both attenuating and harvesting wave energy. The presented results are based around experimental investigations, by means of small scale facilities, in which the spatial arrangement of the flexible objects is the key parameter of study. The model array is first characterised by evaluating the role played by various parameters (configuration, flexibility, wave frequency) on the energy distribution in our system. Following these first observations, an interference model is then developed in order to describe the observed global effects of the array on both the wave field and the blade dynamics, based on known local parameters of a unit item of the array. This model then serves as a tool for exploring many possible array configurations, in order to determine the optimal choice regarding both the attenuation and the absorption of the imposed waves. A final experimental study is presented, in which the key results from the interference model are evaluated and the underlying principles of array optimisation are identified.

Keywords: fluid-structure interaction, wave damping, elasticity, wave energy, interference.

Résumé

Le développement des systèmes houlomoteurs ainsi que la gestion du littoral reposent sur une bonne compréhension des mécanismes liés aux interactions houle-structure. Dans cette thèse, nous nous intéressons à l'étude d'un champ de structures flexibles soumises à des ondes de surface, en vue de développer un système qui puisse à la fois atténuer les vagues et absorber l'énergie qui leur est associée de manière efficace. Les résultats présentés se basent autour d'expériences réalisées dans des installations de petite échelle, dans lesquelles la disposition spatiale des objets flexibles est le principal paramètre étudié. Dans un premier temps, nous caractérisons notre champ modèle afin d'évaluer l'influence de divers paramètres (configuration, flexibilité, fréquences des vagues) sur la distribution de l'énergie dans le système. Sur la base de ces résultats, nous développons ensuite un modèle d'interférences permettant de décrire les observations globales du système à partir de paramètres locaux connus, associés à une portion unitaire du champ. Ce modèle nous sert ensuite d'outil pour l'exploration d'une multitude de configurations spatiales, afin de déterminer le choix optimal vis-à-vis de l'atténuation et de l'absorption des vagues incidentes. Enfin, une campagne de mesures supplémentaire est utilisée afin d'expliquer les résultats obtenus avec le modèle et d'identifier les principes sous-jacents à cette optimisation.

Mots-clés: interaction fluide-structure, atténuation des vagues, élasticité, énergie des vagues, interférence.

Acknowledgements

First of all, I would like to thank my two PhD supervisors Benjamin Thiria and Ramiro Godoy-Diana for offering me this wonderful opportunity. Although I had left academia for a few years, you trusted me (more than myself!) and you gave me the chance to take on this fascinating thesis. Thank you also for your guidance and support throughout these three years, you knew when to push me, when to reassure me, making sure I didn't give up. I am extremely grateful.

Secondly, I want to thank my dear professor William Megill who has followed me for a while now (since Bath!) and who has always encouraged in me. Thank you for your investment and for always finding solutions. I doubt this thesis would have happened if you hadn't offered me a position in Cleves. Along with William, I would like to thank the entire bionics team at the Hoschschule, especially Claudio and Gaga, for the very warm welcome and for all your help with my arrival. It was far from easy!

I also wish to thank the PMMH lab in general, where the atmosphere was extremely pleasant. Thank you Eduardo, Alex, Thomas and more globally the "Ondes de surface" team for your precious help with my experiments. I knew nothing when I arrived and I learned so much with you. Thank you also Florian, Anaëlle, Luce-Marie, Sarah, for your dedication during your internships. I was very happy to work with you and wish you all the best in the future. Of course, I also want to thank Vincent and Eliott for the wonderful moments shared together in our office, and our many discussions. Thanks to you both, I now have a new view on the world... Fred, Claudette, thank you for dealing with my administrative issues so wonderfully. Thank you also Gaële and Sixtine. I very much enjoyed our work at the LOMC.

Finally, I want to thank my friends and family for their unconditional support, even if they might still not quite understand what I did or why I did it. It's a real privilege! Last but far from least, I wish to thank my dear husband Sam for his patience, his support, his generosity. You made this PhD possible and wonderful.

Contents

List of Symbols

a	amplitude of wave	m
P	power	W (J s^{-1})
$\mathcal{N}$	number of blades	
$\mathcal{R}$	number of rows	
K_r	global reflection coefficient	
K_t	global transmission coefficient	
K_a	internally damped energy coefficient	
K_d	externally dissipated energy coefficient	
r	local reflection coefficient (single row)	
t	local transmission coefficient (single row)	
k_a	local damped energy coefficient	
v_1	first modal shape of beam	
X	blade tip displacement amplitude	m
T	wave period	s
u	water particle horizontal velocity	m s^{-1}
h	water depth	m
h_s	beam length	m
k	wave number	rad s^{-1}
f	frequency	Hz
m	mass	kg
m_a	added mass	kg
v_ϕ	phase velocity	m s^{-1}
v_g	group velocity	m s^{-1}
ρ	density of solid	kg m^{-3}
ρ_w	density of fluid	kg m^{-3}
d	lateral spacing between objects	m
l	longitudinal spacing between objects	m
D	object width or diameter	m
b	object thickness	m
E	Young's modulus	Pa
I	Second moment area	m^4
C_D	drag coefficient	
ω	angular frequency	rad
λ	wave length	m
Φ	wave potential	
φ	phase shift	rad
η	surface wave deformation	m
Γ	linear damping coefficient	s^{-1}
β	natural dissipation coefficient	
μ	linear mass	kg m^{-1}
ν	kinematic viscosity	m^2/s

Chapter 1

Introduction

Covering 71% of Earth, the ocean is essential to human life. It provides us with oxygen, water, and food, as well as managing our climate by means of thermal and gas exchanges. At a time when conventional fuels are becoming limited, the ocean is also an enormous potential renewable energy source, which has thus far gone largely unexploited. Our blue planet is, however, vulnerable to human activity and struggles to regulate CO_2 emissions, thereby reinforcing global warming. This instability is reflected in the many natural disasters observed around the world and represents a real threat to our society. Humans are therefore searching for alternative solutions to provide protection from the consequences of climate change as well as new means of producing sustainable energy. These challenges are the foundation of this thesis, which aims to further our scientific understanding of wave-structure interactions in view of developing a novel system able to both benefit from the ocean as well as protect coastlines from its associated hazards.

1.1 Wave attenuation through fluid-plant interactions

The energy in ocean waves is considerable and is especially evident when the water gets shallow near the shore. Coastal erosion is a major concern in many cases, and flooding prevention is a high priority for land use planners in vulnerable coastal regions. Around 10% of the world population ($\sim$ 634 million people) live in coastal regions less than 10m above sea level, and the density of these regions is increasing. Some of the most populated cities are located in these areas, such as Bombay, Shanghai, Jakarta in Asia, or even London and New York in western countries. In addition to the local populations, marine traffic and tourism also rely on these vulnerable regions. Coastal erosion is facilitated by rising sea levels, which are also thought to cause greater and more frequent natural hazards, such as tsunamis, storms, and extreme tides (FitzGerald et al., 2008). In this sense, waves can be a threat to both human population and marine ecosystems.
Protective solutions are therefore sought to slow down and reduce the phenomenon, and rely thus far mostly on the installation of obstacles in order to stop incoming waves before they reach the shore. These solutions are referred to as 'hard' solutions and typically include rock or pile barriers. However, they tend to shift the problem rather than to solve it fully, which can sometimes lead to increased damage in neighbouring areas (Rangel-Buitrago, Williams, and Anfuso, 2017). Alternatives are therefore required.

Many engineering solutions already exist in nature and the study of biological systems as a source of inspiration is known as "biomimetics" (the imitation of biological systems). In the context of coastal erosion, natural wave-attenuating systems include coral reefs, mangroves, sea grass and kelp (Figure 1.1).

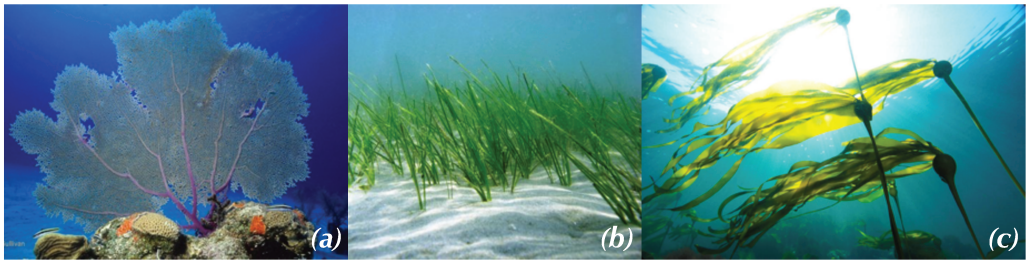

FIGURE 1.1: Examples of wave-attenuating aquatic plants. Gorgonians (a), sea grass (b) and bull kelp (c).

In fact, Smith and Bayliss-Smith (1998) studied the effect of kelp plucking on coastal erosion and demonstrated that waves are rapidly attenuated when propagating through kelp beds. Additionally, Løvås and Tørum (2001) performed an experimental study on wave attenuation and dune erosion due to the presence of kelp plants that also demonstrated a clear reduction of both wave height and wave breaking.

More generally, studies of aquatic vegetation have shown that the flexible nature of these natural structures plays an essential role in the observed attenuation. These plants can passively alter their shape in order to become more streamlined and reduce any drag forces imposed by the incoming flow, which suggests that the flexibility of the plant material plays a key role in their survivorship. This mechanism is known as 'reconfiguration' and was introduced by Vogel in the 1990s (Vogel, 1989; Vogel, 1984). In fact, while many aquatic organisms develop into small and tough objects, and tend to live in relative shelter on the sea floor, marine macroalgae (such as kelp) extend their long, flexible stipes to the surface of the water, where the wave energy is the highest and the hydrodynamic forces are the largest. Their ability to live in these rough conditions is in part thanks to their capacity to reconfigure . A similar mechanism is evident in terrestrial vegetation subject to wind (see De Langre, 2008a, for a review).

The mechanisms involved in the reconfiguration of vegetation subject to fluid flow have been the focus of a number of recent studies (see e.g. Luhar and Nepf, 2016; Barsu et al., 2016; Leclercq and De Langre, 2016; Leclercq and Langre, 2018). This is especially interesting when looking at sediment transport (Järvelä et al., 2006) and coastal erosion (Feagin et al., 2009; Manca et al., 2012). It has been observed that when flow passes through a vegetation field —which we refer to as canopy (Nepf, 2012)—, the kinetic energy of the fluid is transferred to the plant through mechanical bending, which results in a damping of the flow.

Along with being an obstacle, this mechanical feature therefore allows the plants to withstand and dissipate the energy carried ashore by ocean waves (Dubi and Torum, 1994; Koehl and Wainwright, 1977; Koehl, 1984; Denny and Gaylord, 2002; Buck and Buchholz, 2005). Denny and Gaylord (2002) reviewed the mechanics of wave-swept marine algae in order to understand how these plants can survive such forces, by looking at their size, shape and their interaction with the surrounding flow.

Experimental studies have investigated the interaction of flow over a bed of vegetation (Dubi and Torum, 1996; Løvås and Tørum, 2001; Anderson and Smith, 2014; Möller et al., 2014). In particular, Augustin, Irish, and Lynett (2009) compared wave

dissipation through emergent and near-emergent vegetation fields, and found the former to be more effective by 50%-200% per wavelength, due to the larger wave energy at the surface of the water. Nonetheless, both experimental data and field data provide varied results (Anderson, Smith, and McKay, 2011), and the role played by each parameter in these systems with strong fluid-structure interaction couplings is yet to be studied in more detail.

Several models have been developed for vegetation motion under wave-forcing in order to predict hydrodynamic forces and quantify wave energy dissipation (Dubi and Torum, 1994; Massel, Furukawa, and Brinkman, 1999; Asano, Deguchi, and Kobayashi, 1992; Henry, Myrhaug, and Aberle, 2015; Luhar and Nepf, 2016), but these are limited as there is not yet a universally-accepted model for describing plant movement. Therefore, most studies base their results on fitted bulk drag coefficients (Luhar and Nepf, 2016). The most recent and complete model developed by Zeller

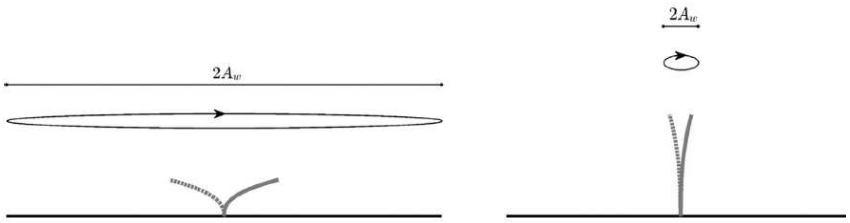

FIGURE 1.2: Difference in blade behaviour at the limit of large (left) and small (right) wave excursions. For a small ratio (left), the bending of the blade is maximal (Luhar and Nepf, 2016)

et al. (2014) is capable of simulating finite-amplitude deflections while accounting for drag and added mass. This model demonstrated that the drag generated by the vegetation motion depends strongly on the ratio of blade tip excursion to wave orbital excursion. More recently, Luhar and Nepf (2016) presented a simple, predictive framework to account for blade motion in wave energy dissipation models, based on experimental and numerical work. The results showed that for certain values of Cauchy number, which represents the ratio of the hydrodynamic forcing to the restoring force due to blade stiffness, the flexible blades exerted larger hydrodynamic forces than their rigid equivalent, possibly due to a vortex shedding that is currently missing in the simple model. Figure 1.2 illustrates the two limiting cases of blade behaviours depending on the ratio L of blade length to wave excursion. This observation was confirmed by the recent works of (Leclercq and Langre, 2018), in which flexibility was seen to provoke a magnification of internal stresses, when external forcing was inertia-dominated. Concerning hydrodynamic forces, the role of the canopy density is also seen to be crucial because of the sheltering effect, as demonstrated recently in the experimental work of Barsu et al. (2016).

Along with the study of fluid-plant mechanics, wave attenuation has also been studied though the problem of wave diffraction. A number of works have addressed the problem of water wave diffraction by arrays of vertical structures (see e.g. Kagemoto and Yue, 1986; Linton and Evans, 1990), leading to the evaluation of forces related to trapped modes within the rigid array (Kakuno and Liu, 1993; Duclos and Clément, 2004; Kamath et al., 2015). Wave diffraction has also been considered as a result of a localised area of wave energy dissipation, a global perspective where the attenuation is a result of local energy losses due to a cluster of cylinders (Dalrymple, Kirby, and Hwang, 1984). Mei et al. (2011) and Mei, Chan, and Liu (2014) developed a semi-analytic theory for predicting wave propagation through patches

of rigid emergent cylinders, which was later adapted to periodic arrays and circular forests (Guo, Wang, and Mei, 2014; Liu et al., 2015) and extended to heterogenous forests (Chang et al., 2017b; Chang et al., 2017a). The theory models turbulence with a constant eddy viscosity that is based on measured values of drag forces. These models, therefore, depend on experimental data and fitted factors.

The literature on wave attenuation through wave-structure interactions is extensive but remains complex due, in part, to the large number of parameters involved. The spacing between elements in a model canopy will be the experimental parameter under scrutiny in this thesis.

1.2 Wave energy harvesting

Most studies focusing on wave energy dissipation by aquatic vegetation consider the context of protecting shorelines or understanding the hydrodynamics of the nearshore currents. Yet, the recent developments in piezoelectric materials such as electro-active polymers bring forth a new perspective to the application of flexible wave dampers. The energy stored in the mechanical deformation of these structures could also be harvested and transformed into useful electricity (Xie, Wang, and Wu, 2014; Jbaily and Yeung, 2015). This is of particular interest given the potential of

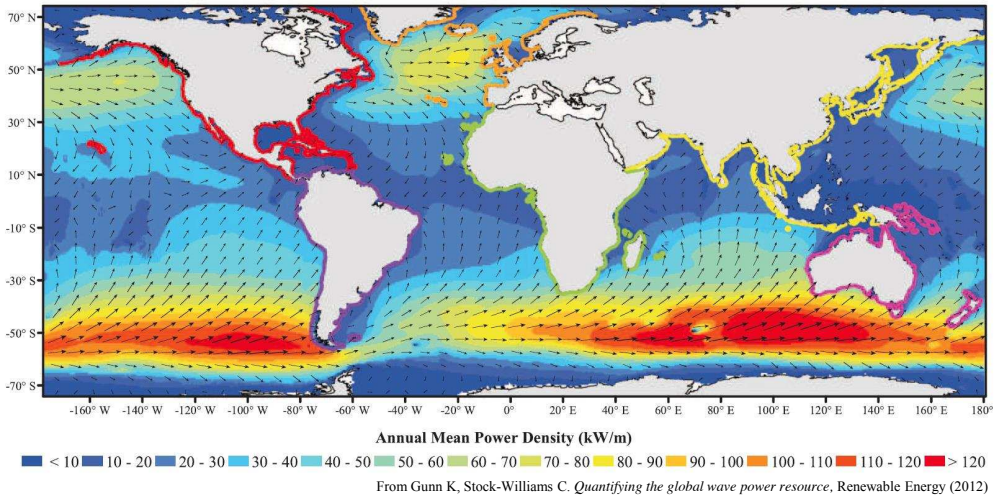

FIGURE 1.3: Cartography of available global wave power resources (Gunn and Stock-Williams, 2012).

ocean waves as a source of renewable energy could reach up to 2TW (Drew, Plummer, and Sahinkaya, 2009), with an annual mean power density estimated around 90-100kW/m of wave front along the European coast (see the cartography provided in Figure 1.3). A large effort has been made in the last two decades regarding the development of wave energy converters (WEC), with many proposed designs (see (Falnes, 2007; Antonio, 2010; De Chowdhury et al., 2015; Day et al., 2015) for reviews). Yet, only a small portion is harvested to date and mostly through early-stage prototypes Clément et al., 2002. The working principles of oscillating body harvesters are illustrated in Figure 1.4 below.

While a few have been demonstrated at full scale in the sea for several years, the high cost of wave energy in comparison with other renewable energy sources makes it hard to achieve economically-competitive energy wave power, and at present, there are still no commercial wave farms in operation (Day et al., 2015). In fact,

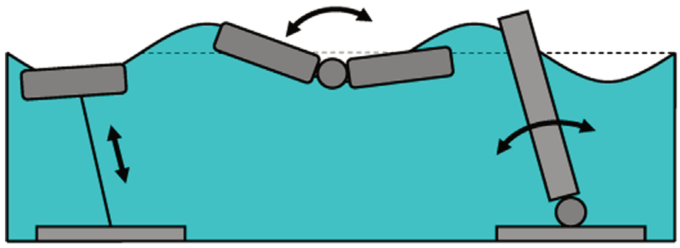

FIGURE 1.4: Principles of oscillating body energy converts. From left to right: point absorber, floater, flap-type. (see Day et al., 2015)

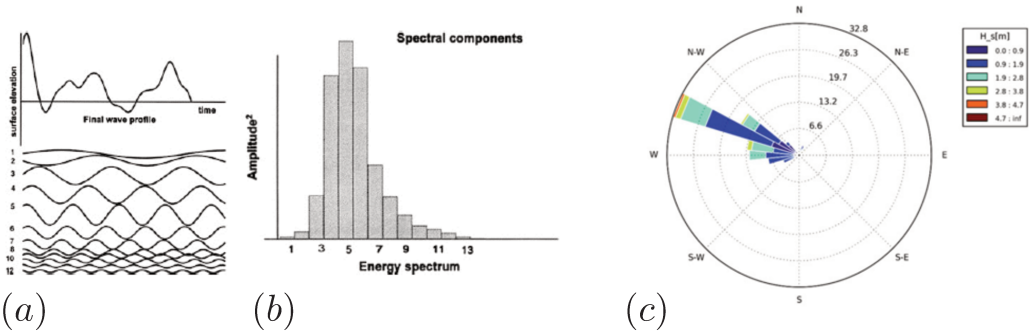

FIGURE 1.5: Frequency decomposition of a typical polychromatic surface wave (a) and the corresponding energy spectrum (b). Example of a wave rose diagram providing values of the significant wave height H_s associated with waves of various orientations (c) (Pecher and Kofoed, 2017)

ocean waves provide a highly variable source of energy, since these are polychromatic and multi-directional by nature, as shown in Figure 1.5. For this reason, the Power Take-Off (PTO) or conversion system of a WEC device is tuned in order to match its resonant bandwidth with the frequency spectrum of a specific site. This will dictate the efficiency of the device. However, wave variability combined with the harsh environment that is the ocean leads to costly designs, often relying on complex control systems (Pecher and Kofoed, 2017). Using piezoelectric materials as a means of converting the captured mechanical energy could therefore help alleviate some of those difficulties and reduce these costs by allowing for simplified and lighter designs (Moretti, Fontana, and Vertechy, 2015; Elvin and Erturk, 2013).

Given the limited power output and efficiency of WEC devices, deployments in large arrays will nonetheless be necessary. Each device can then be impacted by the presence of neighbours, due to wave interferences. Many studies have explored the influence of array configurations on WEC performance and have highlighted the possible strong interferences between waves within the array (Dias et al., 2017; Babarit, 2013; Borgarino, Babarit, and Ferrant, 2012; Sarkar, Renzi, and Dias, 2014; Sarkar, Doherty, and Dias, 2016; Wei et al., 2016). In fact, one interesting phenomenon is observed when the devices are placed in regular patterns, separated by a distance equal to half the wavelength of the incoming wave. In this case, strong reflection is observed, similar to the Bragg resonance seen in wave scattering through crystal lattices (Arnaud et al., 2017). This strong effect has been the source of extensive research in areas of solid-state physics and acoustics, with specific interest for the development of metamaterials that could absorb waves efficiently (Kaina, Fink, and Lerosey, 2013). This research can in theory also be extended to water

waves (Hu and Chan, 2005) and could apply to WEC farm design. Indeed, these arrays could also serve to attenuate waves and reduce coastal erosion since their aim is to extract the energy of waves over large surface areas (Abanades, Greaves, and Iglesias, 2015; Guazzelli, Rey, and Belzons, 1992; Couston, Jalali, and Alam, 2016). In this sense, Bragg resonance could be very useful. While the associated array configuration could benefit wave attenuation, it is also found to reduce the device oscillations, thereby limiting power extraction. This was predicted numerically by Garnaud and Mei (2009). The latter developed an analytical model describing the interaction of waves and an array of small wave energy converting buoys. Using a Froude-Krylov approximation to model the force on a WEC element, as well as multiple scale analysis, the results demonstrated a clear reduction of the array's efficiency in case of Bragg resonance. Similarly, Sarkar, Renzi, and Dias (2014) studied the effect of lateral spacing of flap-type converters (Aquamarine's Oyster©) on the resulting capture factors. Results showed very clear peaks in performances. The principal observations conclude that as devices are placed further away from each other, these tend to behave as single units and therefore oscillate more, which benefits the amount of energy harvested. On the other hand, placing devices back to back was found to create destructive interferences causing each device to oscillate much less, leading to lower efficiency in the system. These observations highlight the difficulty in designing optimal wave farms, which will have to result from a trade-off between wave damping and energy harvesting.

The study of array optimisation has been undertaken by a number of numerical studies, based on various applied mathematical tools. A recent semi-analytical model has for example been developed by Göteman et al. (2015) in order to test configurations that minimise power fluctuations. However, most optimisation studies thus far have been limited to small arrays or to specific conditions, due to the costly and heavy numerical calculations required. It is therefore difficult to obtain general conclusions. The influence of array configurations on wave attenuation and absorption will be the core investigation of this thesis.

1.3 Towards a bio-inspired wave energy absorber

The literature therefore suggests that aquatic plants are good examples of natural systems able to attenuate waves thanks to a transfer of the fluid's energy into the deformation of the flexible structure. However, the biological function of this mechanical feature is neither to reduce fluid flow nor to harvest its associated energy, but instead to alleviate external loads sensed by the plant in order to improve its survivability. While several technologies have already been developed in order to harvest flow energy through bio-inspired designs, these are not designed to attenuate flow. Examples include BioStream© based on the movement of tuna fish tails behind a Karman Vortex Street flow, EelEnergy© that imitates the undulatory swimming motion of eels and BioWave© inspired from kelp oscillations in waves (c.f. Figure 1.6).
This thesis investigates the mechanisms involved between wave-driven fluid motion and an array of flexible vegetation-inspired structures. The influence of key parameters on the energy distribution of the system is studied experimentally, in order to examine how an optimal dual application could be reached.

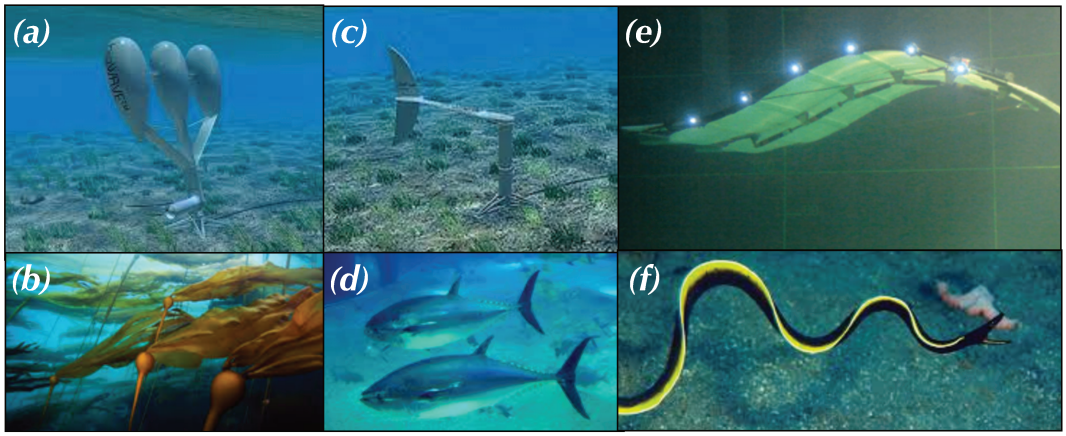

FIGURE 1.6: Examples of bio-inspired energy harvesters. BioWave© (a) inspired from bull kelp oscillations (b), BioStream© (c) inspired from the motions in a Karman Vortex Street (d) and Eel Energy© (e) inspired from the undulations of eels in water currents (f).

1.4 Thesis plan

In this thesis, we focus on the study of wave energy distribution within arrays of emergent flexible blades. The goal is to better understand the mechanisms involved in the interactions between surface waves and the deformable structures, in the hope to evaluate how specific arrangements can improve wave attenuation and energy absorption. Following a review of the key principles of linear wave and beam theories in Chapter 2, the experimental methods used throughout the thesis are presented in Chapter 3. The experimental results obtained from parametric studies of our model system are then discussed in Chapter 4, which will provide some insight regarding the wave-array interactions and highlight some characteristic phenomena, ruling the energy distribution of our system. These experimental observations then serve as the basis for Chapter 5, in which an interference model is developed and explored. Finally, a possible optimisation of our model system is then further investigated in Chapter 6 by means of both experimental analysis and the interference developed model.

Chapter 2

Theoretical Background

Our system is studied as a fluid-structure problem, with an interaction between surface gravity waves and flexible cantilevered beams. The relevant notions of both fluid and solid mechanics are therefore recalled in this chapter, with the description of linear potential wave theory and the linear theory of elasticity . The basic principles are then combined in order to provide the key tools for the analysis of this fluid-structure interaction problem.

2.1 Surface gravity waves

Wave theory Ocean waves are surface gravity waves, which correspond to unsteady free surface flow subjected to gravitational forces. These can be caused by different sources (wind, earthquakes, swimming objects or organisms) and exist in many different forms for which no general mathematical solution exists. Many theories have been developed using different approximations, which Le Méhauté (1969) has classified according to a leading parameter taken as the ratio between wave height (here H) and water depth (here d). For small ratios, linear wave theory applies, which is shaded in yellow in Figure 2.1 below.

Linear Potential Flow Let us consider an irrotational fluid for which the particle velocity vector $\underline{u}$ can be expressed as a potential derivative:

$$\underline{u} = \left\{ \begin{array}{c} u \\ v \\ w \end{array} \right\} = \nabla\Phi \tag{2.1}$$

Assuming the fluid is incompressible, the continuity equation must be satisfied, which can be written as:

$$\nabla \cdot \underline{u} = \frac{\partial u}{\partial x} + \frac{\partial v}{\partial y} + \frac{\partial w}{\partial z} = 0 \tag{2.2}$$

This leads to the Laplace equation:

$$\nabla^2\Phi = \frac{\partial^2\Phi}{\partial x^2} + \frac{\partial^2\Phi}{\partial y^2} + \frac{\partial^2\Phi}{\partial z^2} = 0 \tag{2.3}$$

Therefore the momentum balance for irrotational flow becomes (Bernoulli equation):

$$gz + \frac{p}{\rho} + \frac{1}{2}(u^2 + v^2 + w^2) + \frac{\partial\Phi}{\partial t} = C \tag{2.4}$$

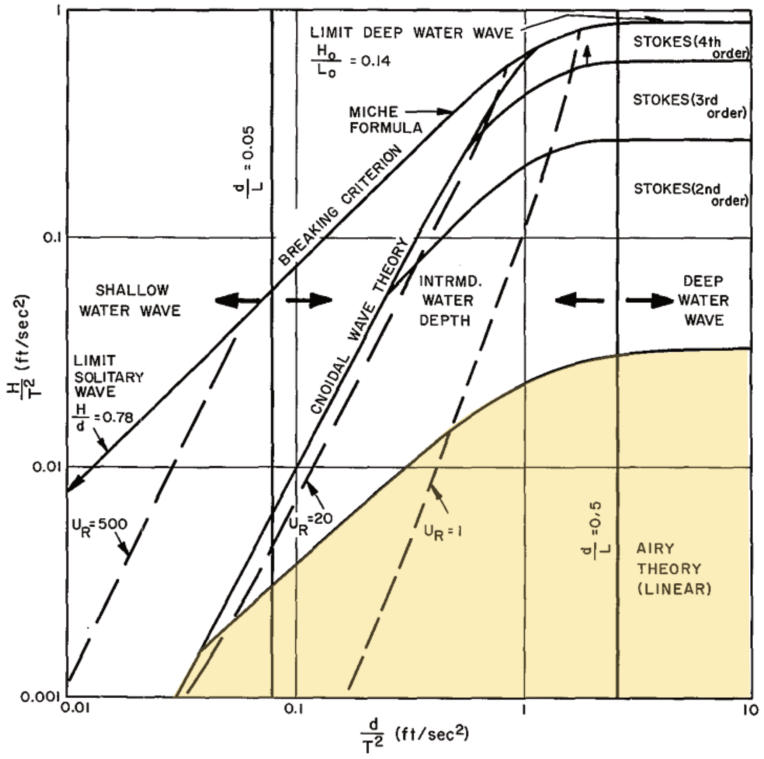

FIGURE 2.1: Validity of wave theories, depending on wave height ratio H/d, where H is the wave height and d is the water depth. (see Le Méhauté, 1969)

where C is a constant, p and ρ are , respectively, the pressure and density of the fluid, g is the gravitational constant. The solution to these equations must satisfy the following boundary conditions.

1. Sea bed boundary condition. This condition states the no-slip condition of the wave particles at the sea bed interface. We therefore have:

$$\frac{\partial \Phi_{z=-h}}{\partial z} = 0 \tag{2.5}$$

where h is the water depth.

2. Free surface kinematic boundary condition. The vertical velocity of a water particle located at the free surface must equal that of the free surface itself (no leakage). This gives:

$$\frac{\partial \Phi_{z=0}}{\partial z} = \frac{\partial \eta}{\partial t} + \frac{\partial \Phi}{\partial x}\frac{\partial \eta}{\partial x} + \frac{\partial \Phi}{\partial y}\frac{\partial \eta}{\partial y} \tag{2.6}$$

where $\eta(x, y, t)$ describes free surface elevation (at $z = 0$).

3. Free surface dynamic boundary condition. The pressure of the fluid at the free surface must equal the pressure of the atmosphere p_0, leading to the following free surface dynamic boundary condition using Eq. 2.4 (surface tension is ignored):

$$\frac{\partial \Phi_{z=0}}{\partial t} + g\eta = 0 \tag{2.7}$$

In order to linearize these equations, the Stokes expansion approximates the expressions of η and Φ as a series, depending on parameter ϵ:

$$\eta = \epsilon\eta_1 + \epsilon^2\eta_2 + \epsilon^3\eta_3... \tag{2.8}$$
$$\Phi = \epsilon\Phi_1 + \epsilon^2\Phi_2 + \epsilon^3\Phi_3... \tag{2.9}$$

where ϵ is taken as the wave steepness parameter $\frac{H}{\lambda}$. The general solution to the first order equations is of the form:

$$\eta_1(x,t) = a\cos(kx - \omega t) \tag{2.10}$$

where $a = H/2$ is the amplitude of the wave, k is the wave number, and ω is the wave frequency. Illustrations of the traveling wave in space and time are provided in Figures 2.2b and 2.2a, respectively (c.f. Journée and Massie, 2001). The expression for the wave potential can then be obtained from boundary conditions, to give:

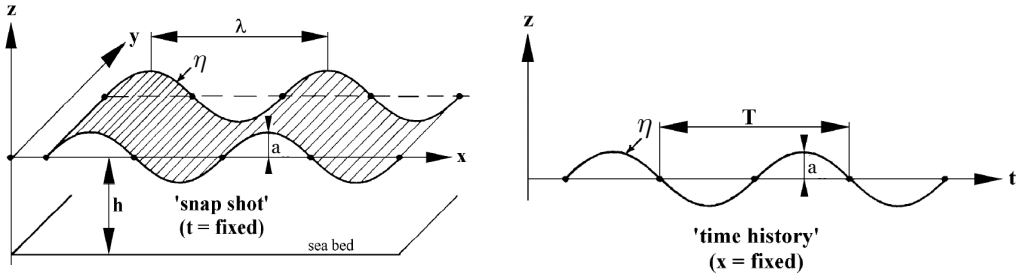

(A) Regular wave in space (B) Regular wave in time

FIGURE 2.2: Illustrations of a typical regular wave traveling in space at a specific time (A) and a fixed spatial point in varying time (B)

$$\Phi(x,z,t) = \frac{ag}{\omega}\cdot\frac{\cosh k(h+z)}{\cosh kh}\cdot\sin(kx - \omega t) \tag{2.11}$$

Finally, the relationship between the wave length k and the wave period T or frequency ω is given by the dispersion relation:

$$\omega^2 = kg\tanh kh \tag{2.12}$$

Wave conditions In other words, the dispersion relation describes how the waves propagate depending on the water depth h. Note that phase velocity can now be defined as: $v_\phi = \frac{\lambda}{T} = \sqrt{\frac{g}{k}\tanh kh}$. Regular waves can be grouped according to ratio h/λ, which leads to further simplifications:

- deep water waves: when the water depth is much greater than half the wavelength $h >> \lambda/2$, the dispersion relation simplifies to $\omega_{dw} = \sqrt{gk}$. Deep water waves are not affected by the seafloor topography. Moreover, the wave group velocity is half the phase velocity: $v_g = 1/2v_\phi$.
- capillary-gravity waves: $\lambda/20 < h < \lambda/2$. In this case, the dispersion relation is $\omega_{cg} = \sqrt{gk\tanh kh(1 + \frac{\gamma k^2}{\rho g})}$.

- shallow water waves: the water is considered to be shallow if the water depth is less than 1/20 of the wavelength $h < \lambda/20$. The dispersion relation writes $\omega_{gc} = k\sqrt{gh}$. The sea floor has a very large influence on the characteristics of shallow-water waves. The group velocity is identical to the phase velocity.

Wave kinematics The wave particle kinematics can be deduced from the potential given by Eq. 2.11. With $\omega^2 = kg \tanh kh$ from the dispersion relation (Eq. 2.12), the horizontal velocity u and acceleration $\dot{u}$ of water particles can be written as:

$$u = \frac{\partial \Phi}{\partial x} = \frac{dx}{dt} = a\omega \cdot \frac{\cosh k(h+z)}{\sinh kh} \cdot \cos(kx - \omega t) = u_a \cos(kx - \omega t) \tag{2.13}$$

$$\dot{u} = \frac{d^2x}{dt^2} = \frac{du}{dt} = a\omega^2 \cdot \frac{\cosh k(h+z)}{\sinh kh} \cdot \sin(kx - \omega t) = \dot{u}_a \sin(kx - \omega t) \tag{2.14}$$

where $u_a = a\omega \cdot \frac{\cosh k(h+z)}{\sinh kh}$ represents the velocity amplitude, as a function of z, and similarly $\dot{u}_a = a\omega^2 \cdot \frac{\cosh k(h+z)}{\sinh kh} = \omega u_a$ represents the acceleration amplitude, as a function of z.

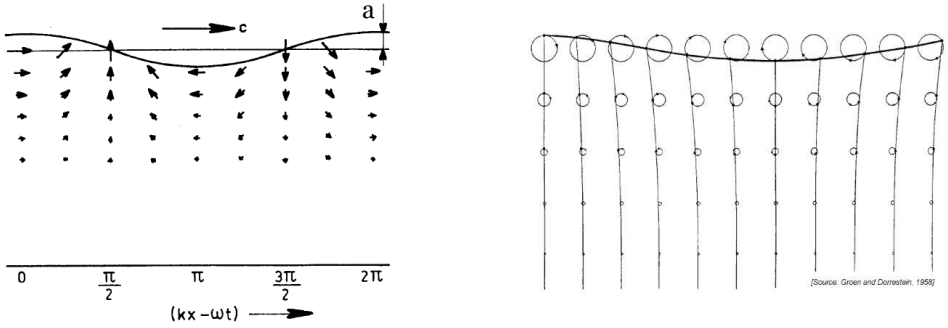

(A) Water particle orbital velocities (B) Water particle trajectories

FIGURE 2.3: Illustrations of a water particle velocities (A) and trajectories (B) along the water column over one period

Illustrations of velocity and trajectory variations over one period are provided in Figure 2.3 above. For a wave traveling to the right, the water particles will move in clockwise circles while for a wave traveling to the left, the water particles will move in anticlockwise circles.

Wave energy In our system, we study the distribution of wave energy, which is the sum of the potential energy, resulting from the displacement of the free surface and the kinetic energy, due to the fact that water particles are moving in elliptic forms (Journée and Massie, 2001).
The kinetic energy is calculated for the volume of displaced fluid over one wave length (see Figure 2.4 (a)):

$$E_c = \int_{volume} \frac{1}{2}(u^2 + w^2) \cdot dm \; = \; \frac{1}{2}\,\rho \int_0^{\lambda} \int_0^{a} (u^2 + w^2) \cdot dz \cdot dx \tag{2.15}$$

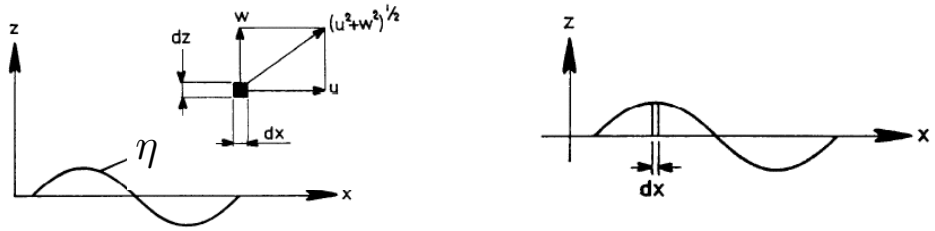

(A) Kinetic energy (B) Potential energy

FIGURE 2.4: Wave energy definition

By substituting the expressions for longitudinal velocity $u = a \cdot \omega \cdot \frac{\cosh\ k(h+z)}{\sinh\ kh} \cdot \cos(kx - \omega t)$ and lateral velocity $w = a \cdot \omega \cdot \frac{\sinh\ k(h+z)}{\sinh\ kh} \cdot \sin(kx - \omega t)$ in Eq. 2.15, we obtain:

$$E_c = \frac{1}{4}\rho g a^2 \quad \text{per unit horizontal sea surface area} \tag{2.16}$$

The potential energy is calculated as follows (see Figure 2.4 (b)):

$$E_p = \frac{1}{2}\int_0^{\lambda} \rho g \eta^2 \cdot dx \ = \ \frac{1}{2}\,\rho g a^2 \int_0^{\lambda} \cos^2(kx - \omega t) \cdot dx \tag{2.17}$$

and its final expression is:

$$E_p = \frac{1}{4}\rho g a^2 \quad \text{per unit horizontal sea surface area} \tag{2.18}$$

From equations 2.16 and 2.17, the total wave energy becomes $E_w = E_c + E_p$:

$$E_w = \frac{1}{2}\rho g a^2 \tag{2.19}$$

The speed at which the wave energy is transfered is given by the group velocity, which represents the velocity of the wave envelope. It is related to the phase velocity by the following expression:

$$v_g = \frac{v_\phi}{2} \cdot (1 + \frac{2kh}{\sinh 2kh}) \tag{2.20}$$

The power or energy flux per unit width can then be defined as:

$$P_w = \frac{1}{2}\rho g a^2 \cdot v_g \tag{2.21}$$

And, in the case of deep water conditions for which $v_g = \frac{1}{2}v_\phi$, this becomes:

$$P_w = \frac{1}{4}\rho g a^2 \cdot \frac{\lambda}{T} \tag{2.22}$$

Spectral analysis The most common ocean waves can be studied using linear theory. Although they are in reality irregular, the superposition principle enables these complex waves to be decomposed into the sum of multiple regular waves. This assumption, combined with the spectral analysis of the irregular wave for a specific site, can be used in order to extract more realistic quantities of estimations of the

wave power, based on two characteristic quantities: the significant wave height H_s and the period associated to the spectrum peak T_s. Taking these into account has shown a reduction in power of around 60% compared to a regular wave (Babarit et al., 2009).

2.2 Elasticity

We now turn the mechanics of our structures. These are modeled as partially submerged cantilevered beams, fixed at their root (sea bed) and free at the end. Subject to water flow and wave oscillations, these structures will deform.

Deflection statics Consider a beam of length h_s, width D, thickness b, fixed at one end (c.f. Figure 2.5 (a)). For small $b, D \ll h_s$, we can assume that the beam bends in the preferred x-direction. Additionally, we assume small deformations meaning that any elementary section of the beam remains perpendicular to the neutral axis, represented by the red line in Figure 2.5 (b). With such assumptions, the equations of Euler-Bernoulli can apply.

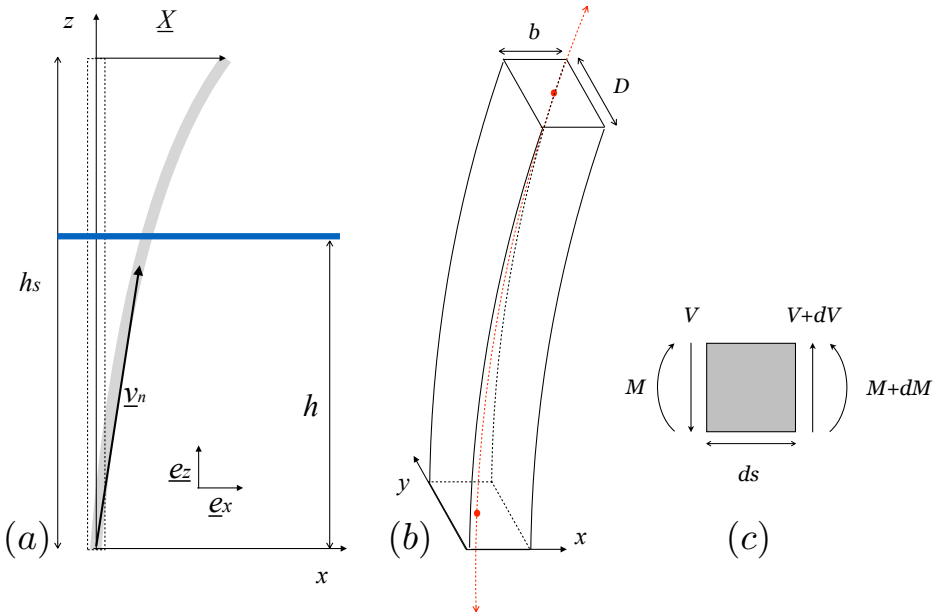

FIGURE 2.5: Sketch of a cantilevered beam, with length h_s, thickness b, width D, submerged in depth h. Side view of the beam deflection with deformation vector $\underline{v}_n$ (a) and neutral central line in red (b). Static equilibrium of moment and shear forces for elementary section of length ds (c)

Using Hooke's law and the assumption of small deformations, the bending moment $\mathcal{M}$ can be approximated as:

$$EI\frac{d^2v}{ds^2} = \mathcal{M}(s) \tag{2.23}$$

where E is the Young's modulus of the beam material, I is the second moment of inertia of the beam, $v(s)$ is the local deflection of the beam along the curvilinear coordinate s. For a rectangular beam, $I = Db^3/12$, with b the thickness of the beam. Taking a local section of the beam shown in Figure 2.5 (c), with length ds subject to

local elastic load qds, we can write the local equilibrium of internal shear forces V and bending moment $\mathcal{M}$, as follows:

$$-V - qds + V + dV = 0 \rightarrow q(s) = \frac{\partial V}{\partial s} \tag{2.24}$$

$$-\mathcal{M} - V\frac{ds}{2} + (V + dV)\frac{ds}{2} + (\mathcal{M} + d\mathcal{M}) = 0 \rightarrow V = -\frac{\partial \mathcal{M}}{\partial s} \tag{2.25}$$

Differentiating twice the bending moment from Eq. 2.23 then gives:

$$q(s) = -EI\frac{\partial^4 v}{\partial s^4} \tag{2.26}$$

where $q(s)$ is the elastic restoring force of the beam.

Deflection dynamics We now look at the dynamics of the deflected cantilevered beam, meaning its response in time caused by the competition between its mass and inertia and its elastic returning force. From the dynamic Euler-Bernoulli equations, we have:

$$\mu\frac{\partial^2 \underline{v}}{\partial t^2} + \frac{\partial \underline{F}}{\partial s} = 0 \tag{2.27}$$

where μ is the linear mass of the beam along its curvilinear axis, $\underline{v}(s,t)$ is the local position vector of the deformed beam, and $\underline{F}$ is the local internal loading of the blade. No external loading is considered here (vacuum). Internal loadings are shared between the local shear forces $\underline{V}$ described previously and the axial tension $\underline{T}$ of the blade, which prevents the beam from changing length during its deformation (inextensibility condition). In the case of small deformations, the curvilinear coordinate s can be approximated as z with $s(x,z) \sim (z)$ and the dynamic deflection of the beam can then be reduced to its linear form, as follows (Landau, 1970):

$$EI\frac{\partial^4 v(z,t)}{\partial z^4} + \mu\frac{\partial^2 v(z,t)}{\partial t^2} = 0 \tag{2.28}$$

with linear mass $\mu = \rho S$ of the beam where $S = Db$ and ρ are respectively its cross-section and density.

In order to solve this equation, we separate the temporal and spatial parts of the function and search for a complex solution of the form $w(z,t) = v(z)e^{i\omega t}$. Eq. 2.28 now becomes:

$$\frac{\partial^4 v(z)}{\partial z^4} + k^4 v(z) = 0 \tag{2.29}$$

where k^4 is defined as $\omega^2 \frac{\mu}{EI}$.

The general solution to this fourth order differential equation takes the form

$$v(z) = a\cos(kz) + b\sin(kz) + c\cosh(kz) + d\sinh(kz) \tag{2.30}$$

and the constants a, b, c and d are to be found thanks to the cantilever boundary conditions, which are:

- $v(0) = 0$: no displacement at the beam base
- $\frac{dv}{dz}(0) = 0$: no rotation at the beam base
- $\frac{d^2v}{dz^2}(h_s) = 0$: no bending moment at the free end
- $\frac{d^3v}{dz^3}(h_s) = 0$: no shear forces at the free end

The first two conditions imply that $b = -d$ and $a = -c$ while the last two conditions lead to the following system of equations:

$$\begin{bmatrix} \cos(kh_s) + \cosh(kh_s) & \sin(kh_s) + \sinh(kh_s) \\ \sin(kh_s) - \sinh(kh_s) & -[\cos(kh_s) + \cosh(kh_s)] \end{bmatrix} \begin{bmatrix} a \\ b \end{bmatrix} = \begin{bmatrix} 0 \\ 0 \end{bmatrix} \tag{2.31}$$

Solutions to this system require the determinant to be equal to zero, which leads to the condition:

$$\cosh(kh_s)\cos(kh_s) = -1 \tag{2.32}$$

A set of roots k_n can be found numerically or graphically, each of which are associated to a resonant frequency given by :

$$\omega_n = k_n^2 \sqrt{\frac{EI}{\mu}} \tag{2.33}$$

The modal deformations can then be deduced by rearranging equations 2.31 and substituting in Eq. 2.30 for which the first four modes are represented in Figure 2.6a below:

$$v_n(z) = a\big[\cos(k_n z) - \cosh(k_n z) + \frac{\sin(k_n h_s) + \sinh(k_n h_s)}{\cos(k_n h_s) - \cosh(k_n h_s)}[\sin(k_n z) - \sinh(k_n z)]\big] \tag{2.34}$$

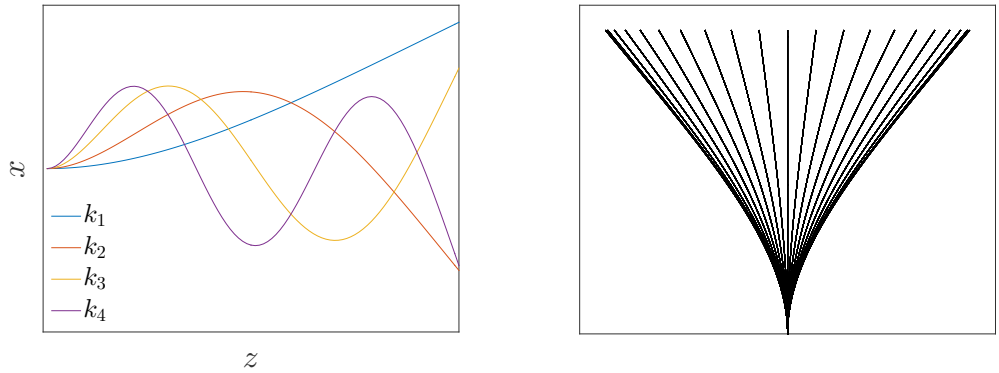

(A) First four modal deformations for a simple cantilever beam

(B) Illustration of 1st mode deflection for an undamped oscillating cantilever beam

FIGURE 2.6: Illustrations of cantilevered beam modal deformations

The coefficient a is determined from boundary conditions. In our case, we require $v_n(L, 0) = X(0)$, which leads to a coefficient $a = 1/2$. Furthermore, we will assume that the blades oscillate only in their first modal deformation which we will refer to in the following chapters as $v_1(z)$ (blue curve of Figure 2.6a), for which the associated root $k_1 h_s = 1.87$. We are now able to determine the local position $\underline{x}(z, t)$ as the product of local curvature $v_1(z)$ and blade tip position $\underline{X}(t)$:

$$\underline{x}(z, t) = v_1(z)\underline{X}(t) \tag{2.35}$$

An illustration of typical deflections for a cantilever beam oscillating as $X(t) = X\cos(\omega t)$, with X the amplitude of oscillation, ω the resonant frequency of the blade is given in Figure 2.6b.

2.3 Wave-structure interactions

So far, we have looked at the separate mechanics of the fluid and of the solid and we now turn to the description of the interaction between the two, i.e. the wave-structure interactions. In any fluid-structure interaction problem, the fluid conditions cause the structure to move or deform, which in turn affects the surrounding fluid, which again influences the movement of the structure, and so on. The circular principle is summarised in Figure 2.7 below:

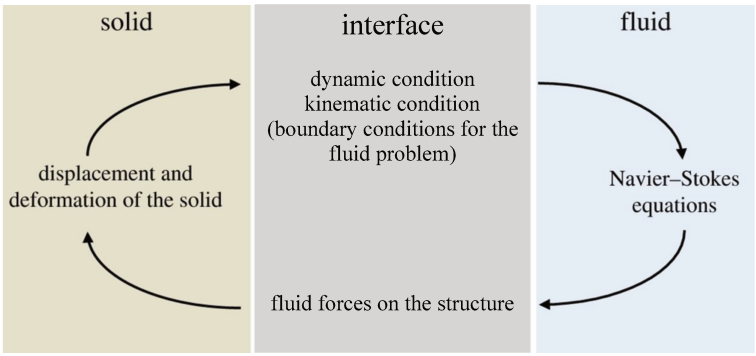

FIGURE 2.7: The principles of fluid-structure interactions, as summarised by Godoy-Diana and Thiria, 2018.

The dynamic equation 2.29 can be re-written to include external forces F:

$$\mu\ddot{x} + Bx'''' = F \tag{2.36}$$

For ease of reading, time- derivatives are denoted $\dot{()}$ while space- derivatives (with respect to z in this case) are denoted $()'$.
These external loads include hydrostatic and hydrodynamic loads. However, the blades used in our system are neutrally-buoyant structures, i.e. the densities of the fluid (ρ_w) and of the solid (ρ) are equal, so that gravity and buoyancy forces cancel each other and only hydrodynamic forces remain.

Hydrodynamic forces are caused by the motions of both the oscillating structure and the traveling wave:

- the wave imposes an external force onto the object, referred to as the Froude-Krylov force
- the presence of the object alters the wave field by means of forces associated with diffraction and radiation effects
- the relative motion of the fluid against the oscillating object can cause flow separation leading to drag forces

The wave potential resulting from these interactions can then be expressed as follows:

$$\Phi_{tot} = \Re\{(\phi_I(x,z) + \phi_D(x,y,z) + \phi_R(x,y,z))e^{i\omega t}\} \tag{2.37}$$

where $\phi_I(x,z)$ is the incident wave potential (assumed regular, monochromatic), $\phi_D(x,y,z)$ is the diffracted wave potential due to the presence of the static object,

and $\phi_R(x, y, z)$ is the radiated potential caused by the motion of the object in the fluid. An illustration of the interacting waves leading to the disturbed wave field is provided in Figure 2.8 below.

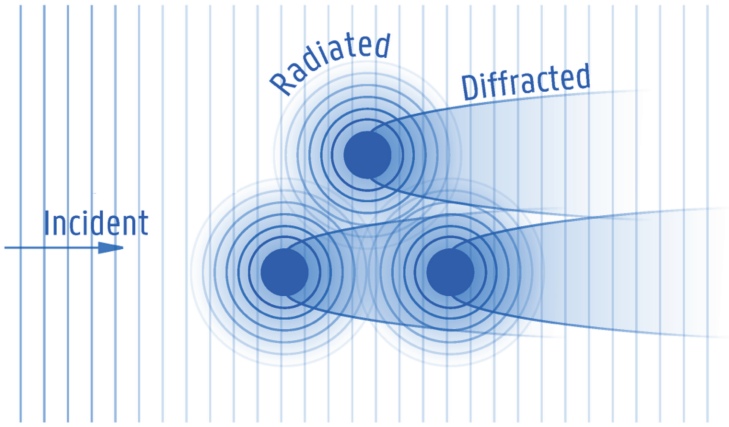

FIGURE 2.8: Illustration of the mechanisms involved in the wave field modification due to the objects' presence (illustration from Verbrugghe et al., 2017).

The associated forces are described below.

Static beam in waves - rigid case The unsteady pressure associated with the incident regular wave propagating at the free surface leads to the Froude-Krylov force. Its expression is derived from the incident wave potential to give:

$$F_{FK}(t) = \mu_d \dot{u}(t) \tag{2.38}$$

where $u(t)$ refers to the velocity (horizontal) of the fluid particles, and μ_d is the linear mass of the displaced fluid equal to $\rho_w S$. This term can sometimes be referred to as the virtual buoyancy force (Leclercq and Langre, 2018). It corresponds to the incoming waves, without any obstacles.
An additional force term must be added to account for the disturbance of the flow due to the beam's presence. For small bodies ($D << \lambda$), this force can be expressed as a reactive force term, which is analog to the force associated with the added mass, as given by the Morison equation (Morison, Johnson, Schaaf, et al., 1950):

$$F_D(t) = \mu_a \dot{u}(t) \tag{2.39}$$

where μ_a corresponds to the added mass of the dragged fluid. For a flat plate or blade, this can be taken as $\mu_a = \rho_w \pi D^2/4$. In the case of a large body compared with the wave length, however, this approximation is no longer valid and the diffraction problem should instead be considered. The wave diffraction potential generated by this interaction is complex, and depends essentially on the width D of the object with respect to the wave number k of the incoming waves. These parameters will dictate how much of the incoming waves are either reflected or transmitted. The diffracted

wave field can be modeled using for example the multiple scattering theory developed by Martin (2006). Renzi and Dias (2012) also developed a semi-analytical expression for both the diffraction and radiated potentials (which we describe below) resulting from the Oyster© device.

The forces associated with Froude-Krylov and diffraction effects form together the external excitation force imposed by the waves that will initiate the motion of the beam:

$$F_{ext} = F_{FK} + F_D = (\mu_d + \mu_a)\dot{u}(t) \tag{2.40}$$

The final force that we consider is the resistive force caused by flow detachment and friction losses as the fluid travels around the beam. This force depends on the drag coefficient C_D which varies depending on the shape and surface roughness of the structure, and is usually determined empirically.

$$F_{drag}(t) = \frac{1}{2}\rho_w C_D D|u_r|u_r \tag{2.41}$$

where C_D is the drag coefficient of the object, ρ_w is the density of the fluid, D is the width of the blade, which for a blade shape corresponds to the local wetted surface area, and $u_r = u - \dot{x}$ is the relative velocity between the the fluid and the moving object (in this rigid case, $u_r = u$).

Oscillating beam in waves - flexible case In our system, the objects are flexible and able to oscillate in response to the incoming waves. In this case, the oscillating structure radiates waves associated with additional inertial forces. Using the radiation potential ϕ_R, this can be expressed in the time domain by means of a convolution product, as follows (Cummins, 1962):

$$F_R(t) = -\mu_{a_\infty}\ddot{x}(t) - h(t) * \dot{x}(t) \tag{2.42}$$

where $\mu_{a_\infty} = \lim_{\omega\to\infty} \mu_a(\omega)$ is the added mass at infinite frequency and $h(t)$ is a radiation impulse response function. The latter is related to the frequency-dependent radiation damping coefficient $\gamma_{rad}(\omega)$ by $h(t) = \frac{2}{\pi}\int_0^\infty \gamma_{rad}(\omega)\cos(\omega t)d\omega$.
This force is therefore composed of two terms: the first term is proportional to the acceleration of the object and represents the additional inertial force required for the object to move against the fluid; the second term represents the damping part of the force, i.e. the energy that is sent in the far field. The latter relies on the knowledge of the body motion expressed through the impulse or memory function $h(t)$.

Finally, the internal shear stresses of the beam material also create a damping force, which we express as a function of the velocity of oscillation:

$$F_{damp} = -\gamma_s\dot{x}(t) \tag{2.43}$$

where γ_s corresponds to the linear internal damping coefficient of the beam.

The total sum of external forces applied onto the structure can then be summarised in Eq. 2.44 below:

$$\sum F = F_{ext} + F_R + F_{drag} + F_{damp} \tag{2.44}$$

to give our local equation of motion (Eq. 2.45):

$$(\mu + \mu_a)\ddot{x} + (\gamma_s \dot{x} + h * \dot{x}) + Bx'''' = (\mu_d + \mu_a)\dot{u} + \frac{1}{2}\rho_w C_D D \left|u_r\right| u_r \tag{2.45}$$

Note that the terms grouped on the left-hand side of Eq. 2.45 take the classical form of a damped harmonic oscillator.

Dimensionless numbers The interaction between an oscillating structure and surface waves can be described through various dimensionless parameters, which include:

- Froude number $F_r = \frac{u_a}{\sqrt{gD}}$, where u_a is the velocity amplitude of the fluid particles, D is the width of the beam, and g is the gravitational constant. This dimensionless number compares the pressure forces to gravity forces. It is often used for scaling purposes of model systems.
- Reynolds number $R_n = \frac{u_a D}{\nu}$, where ν is the fluid kinematic viscosity. This number compares inertial fluid forces to drag or viscous forces. For high values of R_n, the system becomes inertia-dominated, and viscous forces can be neglected. In our small-scale experiments, the Reynolds numbers are sufficiently large so that friction forces can be neglected.
- Keulegan-Carpenter number $KC = \frac{u_a T}{D}$, where T is the wave period. This number compares drag to inertial forces for oscillating objects or flow. It is therefore well suited to our system and will be the governing parameter throughout the study. In our case, $KC < 1$, which corresponds to inertia-dominating regimes.
- Diffraction number $\mathcal{D} = \frac{D}{\lambda}$. As the name suggests, this number compares the size of the object to that of the wave length and so evaluates the diffracting effect that the interaction will cause to the wave field. We will see in the next chapters that while the size of our individual objects may not be negligible in front of the wave length λ.
- Finally, the Cauchy number C_y which characterizes the shape changes of an elastic solid under the effect of flow. It is defined as the ratio between the dynamic pressure of the fluid and the elastic modulus of the solid ((De Langre, 2008b)). In the case of a oscillatory flow , the Cauchy number can be written as $C_Y = \rho C_D D h_s^3 u_a^2 / EI$, where D is the blade width, and h_s is the blade length, u_a is the maximal orbital velocity of the wave particles (Leclercq and De Langre, 2016).

The effect of the different force terms can therefore be characterised according to those parameters. A summary of the various regimes is provided in Figure 2.9 below (c.f. (Yue, 2005)). As we will see the next chapters, the problem studied in this thesis is usually positioned in regions I and II of the summary graph 2.9, diffraction and drag effects cannot be neglected.
It should also be noted that the drag coefficient was shown to depend on dimensionless numbers R_n and KC by Sarpkaya (1976). The dependence on KC is plotted in Figure 2.10 below.

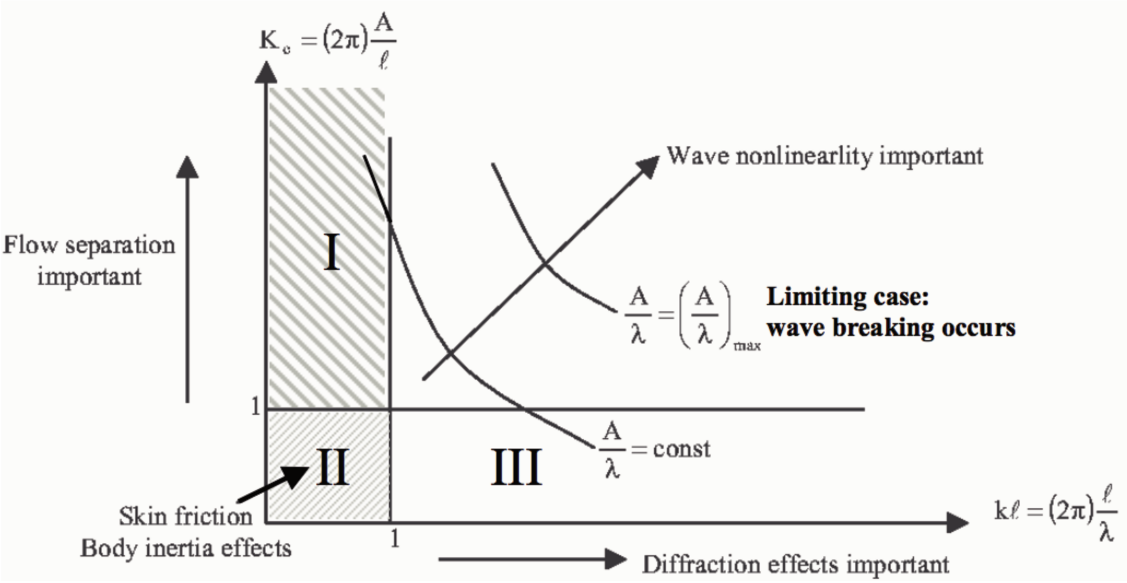

FIGURE 2.9: Summary of dominating forces depending to dimensionless parameters. (image source: Yue (2005))

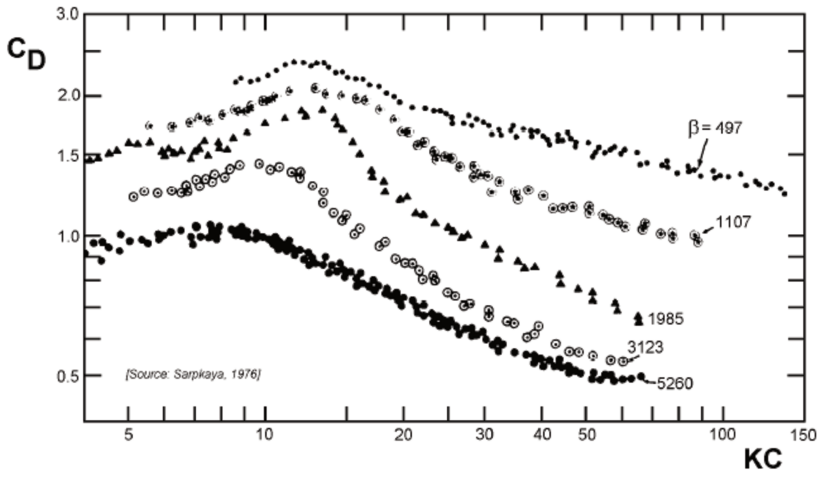

FIGURE 2.10: Variation of measured drag C_D coefficients depending on KC number for a cylinder subject to an oscillating flow (illustration from (Journée and Massie, 2001)).

2.4 Energy balance

This study aims to analyse the energy distribution of the surface waves within an artificial canopy, in order to develop a system able to both dissipate and extract this available energy efficiently. In a non-dissipative system, all the energy associated with the incoming waves is either reflected or transmitted, so that $E_r + E_t = 1$, with E_r the reflected energy, E_t the transmitted energy. In our system, part of the energy is neither reflected nor transmitted and is dissipated through various mechanisms, which are either lost in the fluid or absorbed through the mechanical bending of the elastic structures (internal dissipation). The latter is of particular interest given that it is that which could potentially be harvested and converted into electricity. This corresponds to the power extracted through "Power Take-Off" (PTO) systems in existing wave energy converters.

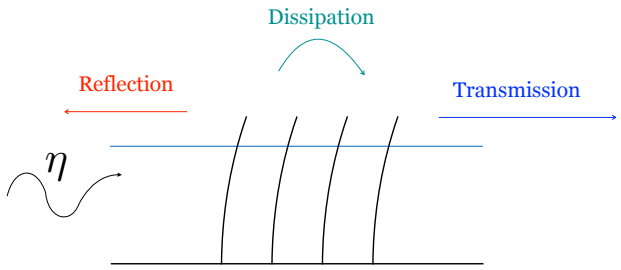

FIGURE 2.11: Illustration of the global energy distribution in the system of study.

The energy balance of our system can be presented as:

$$E_{tot} = E_w + E_{diss} \tag{2.46}$$

with the energy of the wave field E_w shared between a reflected part E_r (includes both diffracted and radiated waves) and a transmitted part E_t, and the dissipated energy E_{diss} shared between an internal damping of the material E_a, an external dissipation of the fluid E_{drag}.

Now that the main theoretical tools have been recalled, we turn to the description of the experiments undertaken to evaluate the influence of geometrical and mechanical parameters on the energy distribution of E_{tot}.

Chapter 3

Experimental methods

This chapter presents the methods and facilities used for the different experiments undertaken during the thesis. The general aim of the project is to acquire a better understanding of the mechanisms involved in wave-structure interactions between ocean waves and flexible oscillators (plant or energy converter) from an energy point of view.

3.1 Facilities and equipment

3.1.1 Wave tanks

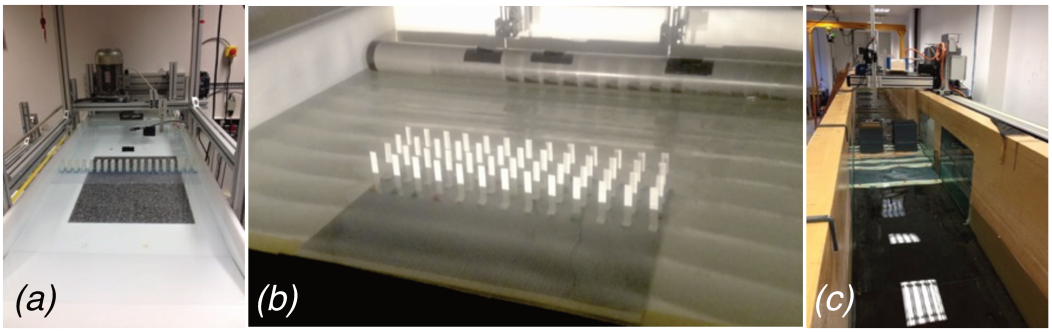

FIGURE 3.1: Photos of the various wave tanks used, which include the small tank at the PMMH in which the array spans the canal width (a), the intermediate tank at the PMMH in which the array covers around 1/3 of the canal width (b) and the large scale tank at the LOMC in which a reduced portion of the array is used (c).

Three different experimental wave tanks were used throughout the project, depending on the desired scale, and the required measurements. At the PMMH laboratory, two small-scale (1/1000) wave canals were used, both of which were associated with two-dimensional surface wave measurement techniques. The first small-scale tank was 0.6 m wide and 1.8 m long and will be referred to as the "small tank" (see Figure 3.1 (a)). The small size of the tank restricted the experiments to be run based on short waves. A second larger and longer wave canal sized 1.5 m wide and 4.3 m long was therefore used to work at various frequencies by avoiding strong lateral, beach and motor reflections. This wave canal will be referred to as the "intermediate tank" (Figure 3.1 (b)).
Both set-ups enabled to measure surface waves in two dimensions ("map"), but each technique has its own specificities, which will be further discussed in the following paragraphs. The third set-up was based at the "Laboratoire d'Ondes et Milieux Complexes" (LOMC) laboratory in Le Havre, and allowed for intermediate-scale (1/100)

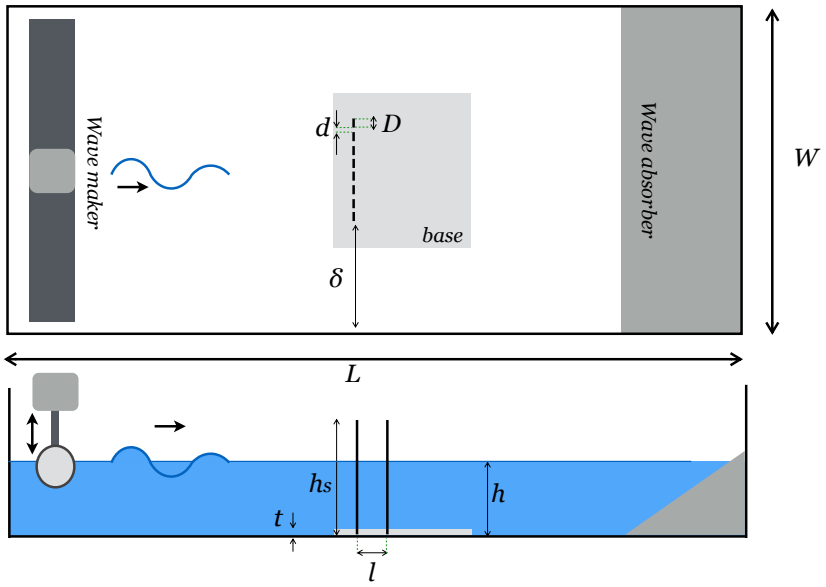

FIGURE 3.2: Sketch of experimental set-up (intermediate tank).

experiments by means of a long 34mx0.9mx1.2m wave canal. In this set-up, however, measurements of surface waves were only one-dimensional. This canal will be referred to as the "large tank" (Figure 3.1 (c)). In the rest of this chapter, we will

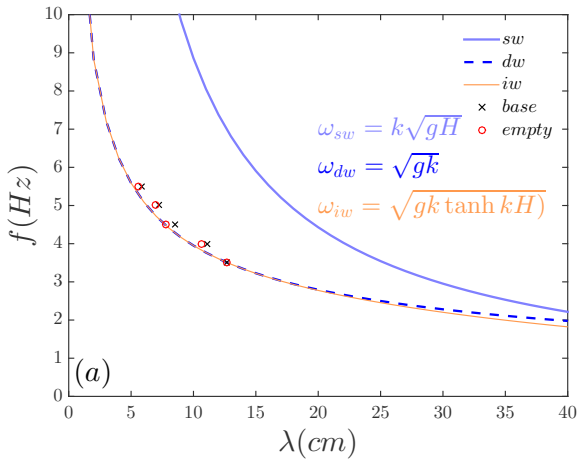

FIGURE 3.3: Measured dispersion relation for our experimental set-up. The water depth is 8 cm. Red dots correspond to data values measured without any obstacle in the tank, the black crosses are those measured with the lego base placed at the bottom of the tank, and the full-blue, dashed blue and orange lines correspond to the theoretical values for shallow, deep, and intermediate water conditions, respectively, as defined by the dispersion relation (Eq. 2.12).

discuss the methods used to perform experimental measurements in the two small-scale set-ups, for which these are similar. The details for those performed at the larger scale in the LOMC laboratory will be discussed in the dedicated description provided in Appendix D.

The experiments were performed with a constant water depth of h=8 cm in all small-scale experiments. This was chosen in order to match deep water conditions

and avoid strong effects due the bottom topography. A verification of these characteristics was performed as shown in Figure 3.3, where theoretical dispersion relations were compared to measured data points. Theoretical expressions are represented in light blue (shallow water), dark blue (deep water) and orange (intermediate water), based on the dispersion relation (Eq. 2.12), while measured data with and without the base boards are represented by black crosses and red circles, respectively. In the small tank, both linear and flap-type motors were used, while in the intermediate tank, a linear wave maker moving vertically was used to create controlled monochromatic waves. Finally, an angled polymer (PVC) sheet was placed at the end of the canal to act as a beach and minimise wall reflections, for all small-scale experiments (slope of 10-15 degrees) (Figure 3.2).

3.1.2 Flexible objects

The system studied here is inspired from kelp vegetation (*Laminaria hyperborea*). These macroalgae are formed of a strong holdfast rooting system, a long flexible stem called "stipe" and a collection of flat blades forming the floating "frond" (c.f. Figure 3.5).

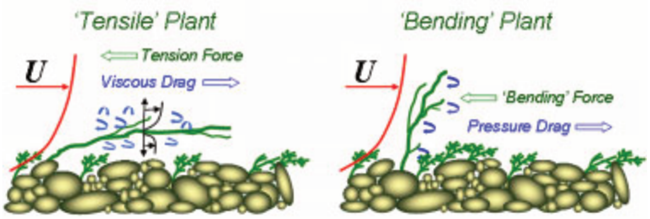

FIGURE 3.4: Typical bending regimes found in plant-flow interactions (Nikora, 2010)

Our study focuses on the stipe's interaction with the waves, which behaves as a 'bending' plant, following the classification presented by Nikora (2010). According to Smith and Bayliss-Smith (1998), kelp plants can be separated into two categories, exhibiting different mechanical properties: sub-tidal usually found in the deep water regions and intertidal growing closer to the coast. Sub-tidal kelp includes the giant bull kelp plant (*Nereocystis*) which is a long (up to 40m), large, very flexible (low tensile strength) and extensible. It is this last mechanical feature that is thought to be responsible for the great capacity of the plant to absorb energy (Koehl and Wainwright, 1977). More specifically, this is believed to stem from the material composition, which involves a crossed helical array of cellulose fibrils combined with a visco-elastic gel. However, inter-tidal kelp are in contrast much smaller and stiffer plants, with high tensile strength (Smith and Bayliss-Smith, 1998) and they must also survive the highly turbulent and energetic environment. These two types of biomechanical beams were studied and modeled by Denny and Gaylord (2002) as shown in Figure 3.5.

In order to simplify the problem, a blade structure was used to represent the stipe section. Due to the beam geometry, bending is therefore limited to a single direction. The blades were made from Mylar® material (*polyethelene terephthalate*) of thickness 350 μm, density 1380 kg.m^{-3} and Young's Modulus (E) 5 GPa. In order to explore spatial configuration, individual Mylar® blades were fixed to Lego® blocks, which were arranged on a Lego® base board. Each block-blade element could then be easily fixed and removed from the common base to create the desired blade arrangements, varying l and d as shown in Figure 3.2. The natural resonant

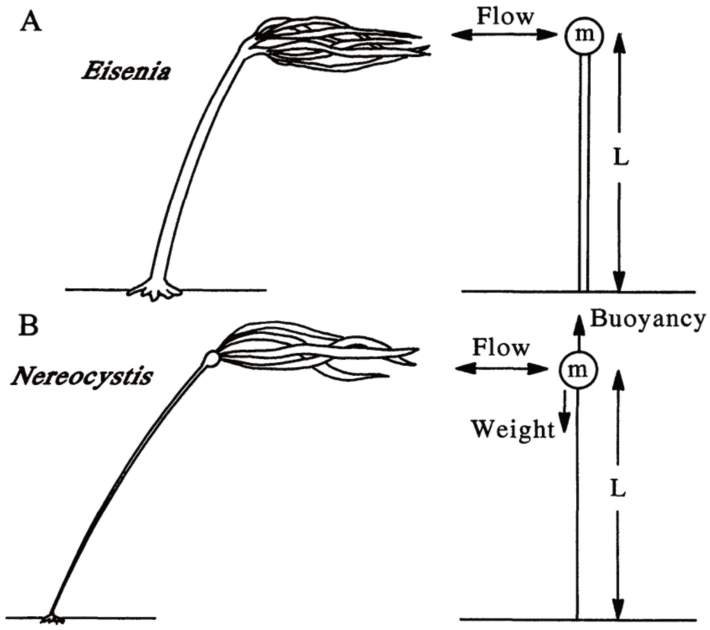

FIGURE 3.5: Kelp model studied by Denny and Gaylord (2002)

frequencies of the blades were measured both in air and in water matching experimental conditions. Results using these structures are presented in Chapters 4 and 5. A scaled-up version of these blades was used in the experiments undertaken in the LOMC, for which details are provided in appendix D.
A second more representative model of stipes was sought, based on cylindrical shapes. In this case, a silicon material was used (Elite© Double). This product used in dentistry is specifically designed for a fast dry and can be easily removable from a given mold. Several flexibilities exist and that selected for our experiments had a Young's Modulus was $E = 650kPa$. Preliminary results using these objects are provided in appendix C.

Model vs. real object All characteristic dimensions of our experimental set-ups are summarised in table 3.1 below, for both the model objects and the tested waves. Principal governing dimensionless parameters are deduced from these values, including the diffraction parameter $\mathcal{D}$, the Keulegan-Carpenter number KC and, for flexible objects, the Cauchy number C_y. For comparison, the same values are summarised for typical kelp plants (data from (Denny and Gaylord, 2002)) and a the Oyster© device, taken as a reference for flap-type wave energy converters (data from (Renzi et al., 2014)).
From the collected data, it is clear that the mechanical characteristics associated with macroalagae differ greatly from those of typical energy converting systems. Our model array places itself in between the two, as a means of studying its effects on wave damping and wave energy absorption, depending on flexibility and spatial configuration.

Wave damping occurs through two mechanisms in our system: either the energy of the flow is dissipated through friction and drag effects, or it is transferred to the object in the form of internal damping. We wish to maximise the damping through bending rather than drag, as the associated energy could be potentially extracted. Therefore, we choose to work in the inertial regime, with small KC numbers ($\sim$0.314

	Plant	**WEC**	**Model**		
Dimensions	Kelp	Oyster©	Blade	Cylinder	Plate
Object					
D [m]	4×10^{-2}	26	14×10^{-3}	14×10^{-3}	$[10.5\text{-}30]\times10^{-2}$
b [m]	-	-	350×10^{-6}	-	$[2\text{-}17]\times10^{-3}$
h_s [m]	[3-40]	13	$[9\text{-}12]\times10^{-2}$	12×10^{-2}	67.5×10^{-2}
$\rho[kg.m^{-3}]$	1050	-	1380	1140	1430
E [Pa]	$[10\text{-}200]\times10^{6}$	-	5×10^{9}	650×10^{3}	2.5×10^{9}
f_0 [Hz]	-	0.05	0.9-5	4.2	[0.2;0.8;1.07]
Waves					
a [m]	[0.2-1]	[0.2-1]	$[1\text{-}3]\times10^{-3}$	3×10^{-3}	$[1.5\text{-}3]\times10^{-2}$
$\lambda[m]$	10	10	$[5\text{-}12]\times10^{-2}$	10×10^{-2}	[0.47-2]
f [Hz]	0.14	0.14	[2.5-5.5]	4.2	[0.86-1.82]
h [m]	[3-20]	13	8×10^{-2}	8×10^{-2}	$[45;60]\times10^{-2}$
Dimensionless numbers					
a/D	10^{2}	10^{-2}	$[10^{-1}\ 10^{-2}]$	10^{-1}	$[10^{-1}\ 10^{-2}]$
$\mathcal{D}$	10^{-4}	10^{1}	10^{-1}	10^{-1}	$[10^{-1}\ 10^{-2}]$
KC	10^{3}	10^{-2}	10^{-1}	10^{-1}	10^{-1}
C_y	10^{5}	-	$[10^{-1}\ 10^{1}]$	10^{-1}	$[10^{-1}\ 10^{1}]$
F_r	-	10^{-2}	10^{-1}	10^{-1}	10^{-1}

TABLE 3.1: Summary of characteristic dimensions of real and model objects, waves, and associated dimensionless numbers. Real object data is taken from Denny and Gaylord (2002) and Renzi et al. (2014) for Kelp and Oyster©, respectively. Preliminary results using cylinder and plate models are provided in appendices C and D, respectively.

for all experiments). The diffraction number is also important when studying wave-structure interactions, as it evaluates how the object alters the wave field. For large objects, i.e. $\mathcal{D} = D/\lambda > 1$, the waves will be deviated due to the presence of the obstacle; diffraction cannot be neglected. On the other hand, when this number is much less then 1, i.e. when $\mathcal{D} << 1$ then the presence of the object has no effect on the wave field. Here again, the choice of the diffraction number illustrates the interaction between the obstacle and the waves. We wish to have large interactions in order to maximise the driving torque of our bending blades. Therefore, we choose to work in a regime where the collective presence of the structures have an effect on the wave field, with $\mathcal{D} \sim 0.2$.

3.2 Measurement techniques

As mentioned previously, this project studies the energy balance between incoming waves and an artificial canopy. The total energy injected into our system is associated with the incident waves and is shared between a reflected part, a transmitted part and a dissipated part within the model array. In order to evaluate this distribution, we rely on the measurement of two quantities: the surface wave amplitude a from which wave energy can be estimated (c.f. Eq. 2.19), and the blade tip displacement X from which the dissipated energy can be calculated (as we will discuss later in the chapter).

Experimental measurements were therefore performed in two parts:

1. surfaces waves were analysed before and after the array in order to obtain information on reflection and transmission;

2. blade oscillations were studied in order to quantify the energy dissipated through the dynamic response of the array.

Measurement and analysis techniques are discussed in this section for the small-scale experiments performed at the PMMH.

3.2.1 Surface wave measurements

Two different techniques were used to measure the 2-D surface wave elevations. Fourier Transform Profilometry (FTP) was initially used, a technique which had been developed at the PMMH, and which allows for high precision measurements of the surface waves. This technique was set-up and associated with the small tank. However, an intermediate tank was later used, for which FTP was no longer compatible; it relies on the use TiO_2 particles mixed in with demineralised water, and can therefore become quickly expensive and impractical for large bodies of water. For this reason, surface wave maps were in that case measured using the second method of Synthetic Schlieren. While this technique is a little less precise than FTP, it was also adopted for subsequent experiments undertaken in the small tank, as it offers the advantage of requiring a single video recording for both wave and blade oscillation measurements, as will be described below.

Fourier Transform Profilometry Fourier Transform Profilometry (FTP) is a high-resolution mapping technique, first introduced by (Takeda, Ina, and Kobayashi, 1982), that allows for the measurement of surface deformation (Cobelli et al., 2009). The system consists of a video-projector and a digital camera. The technique relies on a fringe pattern of controlled characteristics projected on the free surface and registered by the camera (Figure 3.6). The deformed fringe pattern arising from the surface waves is compared to the reference fringe pattern, projected onto the surface of still water, to reconstruct surface height maps.
In order to visualise the fringe pattern at the water surface, the liquid's light diffusivity is enhanced by the addition of white particles (titanium-dioxide based), which does not affect water's hydrodynamical properties. A Photron fast-speed camera SA4 is used with an acquisition frequency of 60 fps. Each experiment is run using 300 reference images and 500 images of the deformed surface, which corresponds to 35 wave periods.

The principle is based on measuring the phase difference between the deformed and reference patterns, i.e. $\Delta\phi \equiv \phi(Y) - \phi_0(Y)$, leading to a phase map from which

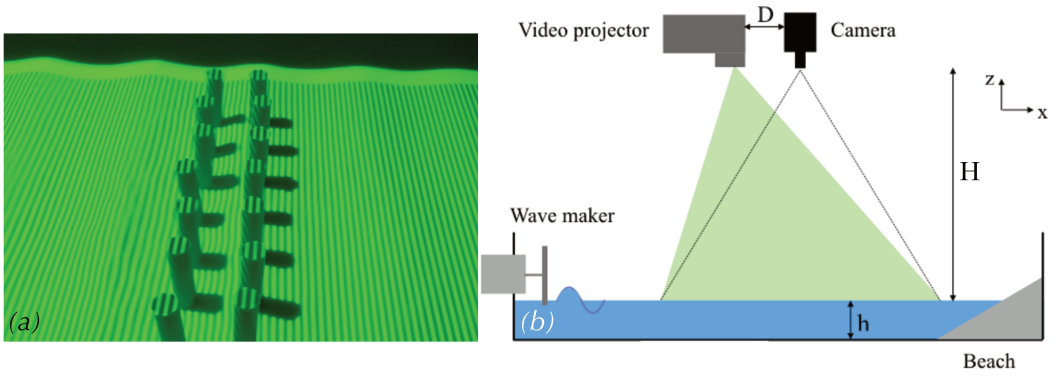

FIGURE 3.6: Experimental set-up for using FTP. A green sinusoidal pattern is projected onto the water surface pigmented with TiO_2 particles (a). The technique measures the phase difference between the deformed fringe pattern and the reference pattern (still water) and reconstructs the surface elevation. Sketch of the FTP set-up (b).

the free surface can be reconstructed. The surface elevation in each pixel of the image is deduced from the phase shift based on the optical relation in Eq. 3.1 (Cobelli et al., 2009).

$$h(x+\delta x, y+\delta y) = \frac{\Delta\phi H}{\Delta\phi - 2\pi/pD} \tag{3.1}$$

$$\delta y = \frac{D-y}{H}h \tag{3.2}$$

$$\delta x = \frac{x}{H}h \tag{3.3}$$

where h is the water height at the point $(x+\delta x, y+\delta y)$ of the deformed surface. D is the distance between the camera and projector and H, the height of their aperture over the reference plane (Oxy), which corresponds to the undeformed water surface (Figure 3.6). The underlying principle of the FTP is that the projection and observation directions are different so that the registered fringe pattern is distorted according to the surface's topography.

According to this principle, the surface wave height maps are calculated using the FTP algorithm running on MATLAB®. A laser wave gage was placed downstream from the wave maker to directly measure the wave height and serve as a verification point for the treated surface maps. Examples of treated images are presented Figure 3.7: surface wave maps for a control configuration without any blades (top left) and a configuration composed of 6 rows (bottom left). The additional wave damping due to the array of blades can be noticed, compared to the natural wave attenuation.

Synthetic Schlieren The 2-D surface wave maps can also be calculated using a synthetic Schlieren method developed by Moisy, Rabaud, and Salsac (2009). This optical method relies on the analysis of the refracted images of a random dot pattern placed at the bottom of the tank. The apparent deformed images are then visualised and recorded through the transparent fluid using a fast camera placed above the water surface, and are compared to the reference image taken with a flat water surface. Figure 3.8 (a) shows a portion of the reference dot pattern, while Figure 3.8 (b) the deformed pattern due to surface waves. A wave crest can be noticed near the left edge of the image, as it acts as a magnifying (convex) lens and wave troughs as reducing

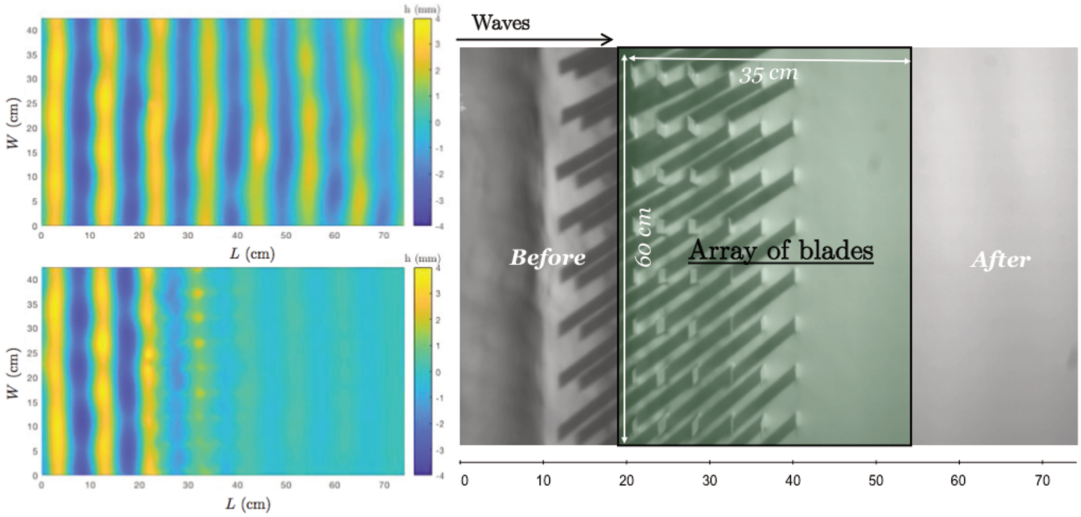

FIGURE 3.7: Surface wave maps obtained with FTP method for a configuration without (top left) and with blades (bottom left), where W and L denote respectively the width and length of the tank. Zones of analysis for reflection ('Before') and transmission ('After') coefficients (right).

(concave) lens. Each recorded image of size 1935x1216 pixels is then analysed using the PIVlab algorithm running on MATLAB®. It is based on standard Direct Image Correlation algorithms (DIC): displacement vectors are detected within "overpixels" by statistically analysing correlations with the reference images in order to define the deformation of the image due to surface waves (see Figure 3.8 (c)).

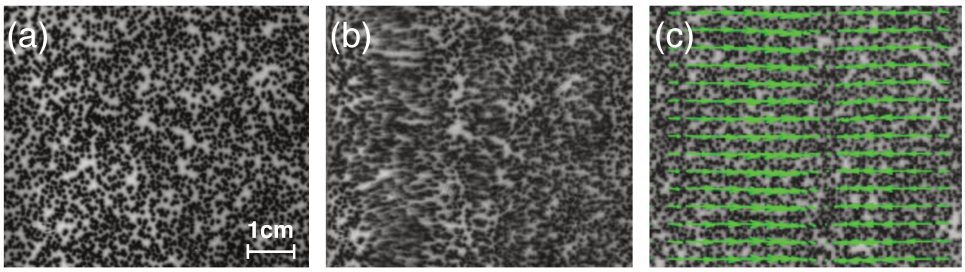

FIGURE 3.8: Illustration of the correlation technique used for the synthetic Schlieren analysis of the surface wave maps. The random dotted pattern taken from a reference image without waves (a) is compared to its deformed equivalent (b) through the DIC algorithm provided by the PIVlab Matlab toolbox, in order to provide the displacement vector fields detected in (c).

With optical calculations, these deformations are converted into a surface gradient field (Moisy, Rabaud, and Salsac, 2009). The surface elevation is then reconstructed by numerically integrating the surface gradient. Due to the correlation windows of analysis, the final treated images of the surface waves provide an image precision of 1.58 mm/px.

Although the Moisy correlation technique is designed to work with a background pattern of random dots, we also use this technique on the dotted lego base to extend the zone of analysis and have access to the wave maps directly behind the array of blades. The surface waves maps are therefore calculated before the array using

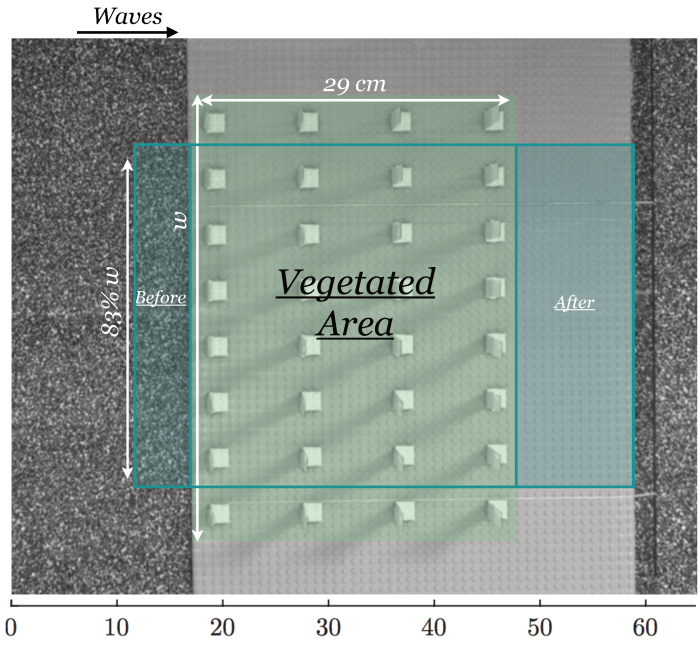

FIGURE 3.9: View of the area on which the synthetic Schlieren method is applied to obtain treated surface wave maps.

the random pattern and after the array using the base (area represented in green in Figure 3.9).

Base effects Despite deep water conditions, it is important to check and evaluate the influence of the Lego© base on the wave field. This verification was performed in the small tank, using the synthetic Schlieren method described above and is provided in Appendix A. Wave transients were recorded over 1500 images with a camera frequency of 200fps, from the moment wave motion was noticed within the camera's field of view, and are plotted for a single point in Figure A.1 (a), with associated Fourier Transform decomposition in Figure A.1 (b). Lateral averages were taken over a central zone of the wave canal as shown in plot (c) of Fig. A.1.

Recording time-frame Although preliminary work was undertaken in steady-state wave conditions, it was found that canal modes and multiple reflections with the motor and the beach could alter the results. In order to avoid including these unrealistic measurements, the data was can be recorded for the first traveling waves only. In other words, knowing the group velocity of each tested wave frequency and the distances between the area of study and the reflecting surfaces of the canal, a "valid frame of analysis" can be determined, within which noisy reflections are limited. An example of the method is presented for the intermediate tank case. As shown in figure 3.10, the array is subject to both wave-maker and beach reflections, which both can distort the resulting behaviour of our system. Therefore, we chose to work in a restrictive time frame for which no reflections have yet reached the recording area of the camera. For each frequency tested, camera recordings were launched as the motor was started and these were taken over 500 images.

For each test, a spatio-temporal plot was drawn using the software package ImageJ®, making it possible to determine the specific frame at which the first full

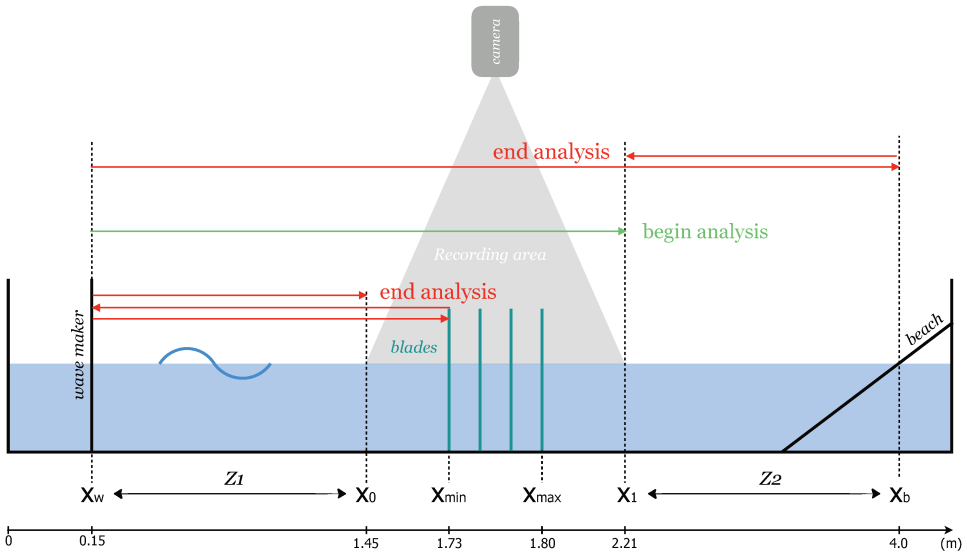

FIGURE 3.10: Sketch of analysis restrictions for experiments run in the intermediate scale. Z1 corresponds to the area between the wave-maker and the beginning of the recording area, while Z2 represents the area separating the end of the recording area and the beach. Recordings are launched when the first waves reach position x_1 (green arrow) and stopped before wave-maker and beach reflections have reached the camera area (red arrows).

wave has traveled through the array and reached the end of the recording area (x_1) (see Figure 3.11). From the known wave characteristics and canal dimensions, one could then calculate the total number of frames over which the analysis could be done while remaining free of reflections.

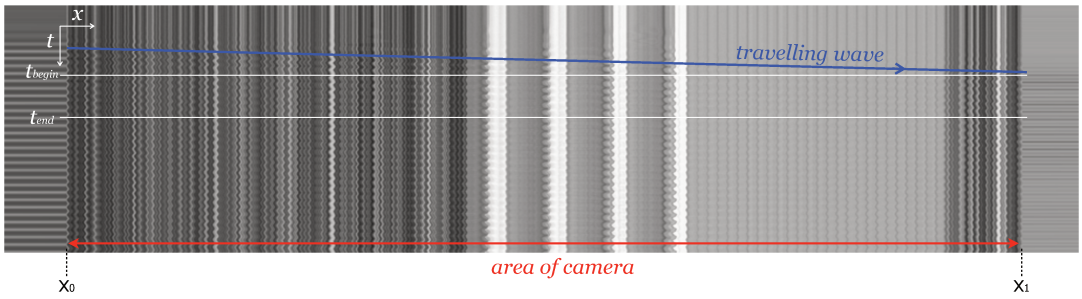

FIGURE 3.11: Spatio-temporal plot from which an acceptable time frame can be determined for the analysis of the surface wave maps. The propagation of the first wave is tracked (blue arrow) within the camera's recording area (red arrow) to measure starting (t_{begin}) and ending (t_{end}) frames.

With a starting distance d_{start} of 1.91m and an ending distance d_{end} of 4.46m, and with a fast camera acquisition frequency of 30 fps, it was calculated that the lowest frequency of 2Hz allowed for a working window of 217 frames following the calculated t_{begin}. The analysis was performed over 100 images and began at the measured t_{begin}. These restrictions correspond to 7 - 16 wave periods and allowed for large error margins (see Table A.1 of appendix A for details). A similar method was adapted to the small tank, for the single frequency tested.

3.2.2 Wave analysis - Reflection and Transmission

To compare configurations in terms of wave damping, we choose to evaluate the reflection and transmission coefficients of each configuration tested. The output of the 2-D surface wave map treatments is a matrix H of water height for each point (x, y) of the tank, and for each recorded frame (three-dimensional matrix: length L$\times$width W$\times$time). Reflected and transmitted energies are quantified as follows. Three zones are defined as presented in Figure 3.12: the zone upstream of the blades between x_0 and x_R (left), the zone corresponding to the array of blades (middle) and the downstream zone between x_T and x_{max} (right). For comparison, all configurations are analysed with the same defined zones: reflection is evaluated in the upstream zone and transmission in the downstream zone. Several methods for calculating these coefficients have been tested and will now be described.

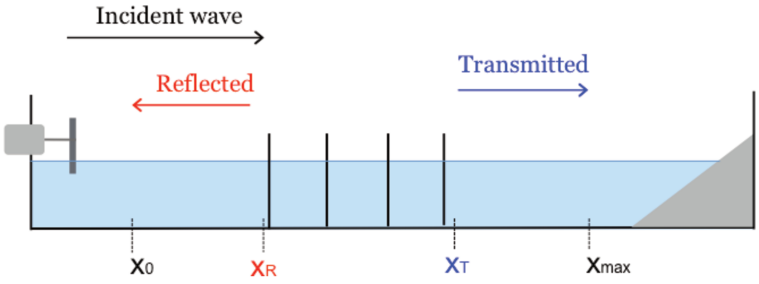

FIGURE 3.12: Sketch of reflected and transmitted waves. Consider x_R the coordinates of the beginning of the blade array zone, and x_T the end of that zone (for largest longitudinal spacing l).

Amplitude ratios - real analysis Small tank experiments were originally run using steady-state conditions of the imposed waves. The surface elevation maps are averaged in phase to provide the information of the 35 periods over a single average wave period. The acquisition frequency of the camera is 60 fps and the wave period is $1/f = 0.235$, so waves are recorded with 14 images per period (so 14 phases for each wave period). For phase 1 for example, we average the first image of each of the 35 periods. We repeat this operation for the second images of each period in order to compute phase 2, and in general, we average the i-th images of each period in order to obtain phase i and a final wave period is reconstructed from the 14 averaged images. Figure 3.13 plots on the same graph the wave profiles of each phase.

Transmission and reflection coefficients are then computed for each tested configuration, based on these phase-averaged height maps. The reflection and transmission coefficients (respectively K_r and K_t) are defined as:

$$K_r = \frac{H_R}{H_{R_0}} - 1 \text{ and } K_t = \frac{H_T}{H_{T_0}} \tag{3.4}$$

where H_R and H_T are the average surface wave heights (peaks) in the zones $[x_0; x_R]$ and $[x_T; x_{max}]$, respectively, as illustrated in Figure 3.13. The reflection and transmission coefficients are normalised with respect to base amplitudes H_{R_0} and H_{T_0} of the control configuration in absence of any flexible blades, in order to remove the intrinsic attenuation of the waves. The attenuation is caused by the experimental conditions of reference, which include viscosity, wall and base friction, as well as reflections.

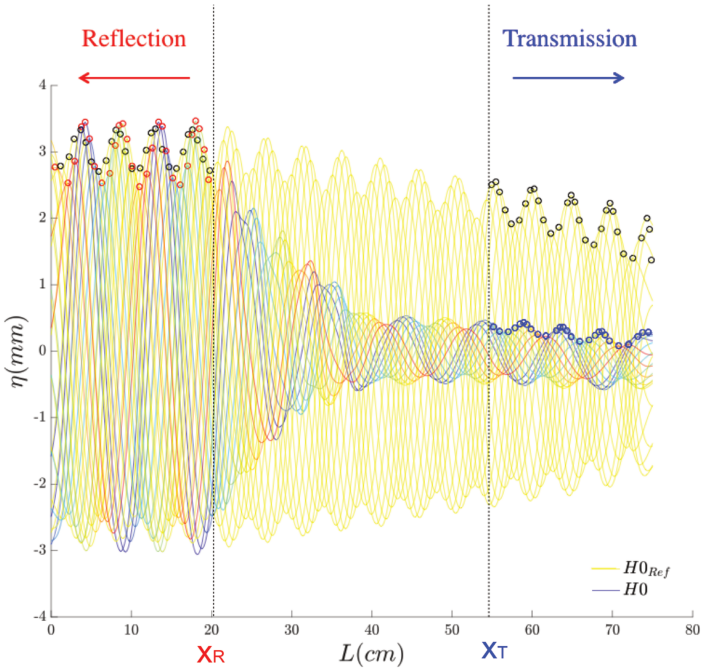

FIGURE 3.13: Peaks used to compute reflection coefficient (in red in $[0; x_R]$) and transmission coefficients (in blue in $[x_T; x_{max}]$)

Curve fitting - complex analysis The previous method described for the evaluation of reflected and transmitted parts relies on accurate measurements of associated reference configurations, that is, without any blades. This therefore presents limitations: firstly because it requires additional measurements following each case and secondly, because the results become very sensitive to natural wave dissipation. While this method is a good first step for qualitative evaluations, it can quickly become impractical and inaccurate. For this reason, a second method was used, relying on the analysis of waves in their complex form.

In this new method, the control case is used to estimate the natural wave attenuation and serves only as a corrective factor of the coefficients. A discrete Fourier Transform Analysis is applied to obtain the complex form of the wave fields. We assume in our study that the imposed waves are linear, thereby allowing us to work with the 1^{st} (fundamental) mode of the wave, averaged over time:

$$\eta(x,y) = \frac{2}{T}\int_0^T \eta(x,y,t).e^{i\omega t}dt \tag{3.5}$$

Considering that the waves are sufficiently homogeneous along the y-direction and can thus be averaged, the problem of determining the transmission and reflection coefficients based on the wave field is then simplified to a one-dimensional problem. From Figure 3.12, we define the upstream zone before the blades as $[x_0; x_R]$, and the downstream zone as $[x_T; x_{end}]$. At either side of the array, the reflected and transmitted waves take the form:

$$\eta(x) = \begin{cases} ae^{-ikx} + K_r ae^{ikx} & \text{in } [x_0; x_R] \\ K_t ae^{-ikx} & \text{in } [x_T; x_{end}] \end{cases} \tag{3.6}$$

where a, the amplitude of the incident wave is known, k, the known wave number,

and K_r and K_t the reflection and transmission coefficients that are to be found. Taking x_a and $x_b \in [x_0; x_R]$, and $x_c \in [x_T; x_{end}]$ with transfer functions $H_{x_b x_a} = \frac{\eta(x_b)}{\eta(x_a)}$ and $H_{x_c x_a} = \frac{\eta(x_a)}{\eta(x_c)}$, it can be shown that:

$$K_r = \frac{e^{-ikx_b} - H_{x_b x_a} e^{-ikx_a}}{H_{x_b x_a} e^{ikx_a} - e^{ikx_b}}$$
$$K_t = \frac{e^{-ikx_a} + Re^{ikx_a}}{H_{x_c x_a} e^{-ikx_c}}$$

The choice of positions x_a, x_b, and x_c is crucial in the determination of these coefficients. This is seen with a simple sensitivity test for the choice of x_a as presented in Figure 3.14 below, with fixed values of x_b and x_c (dash-dotted lines). x_a is varied within the shaded area of the plot, for which the corresponding K_r and K_t coefficients are shown in red and blue lines, respectively. The averaged surface wave η is represented by the black curve.

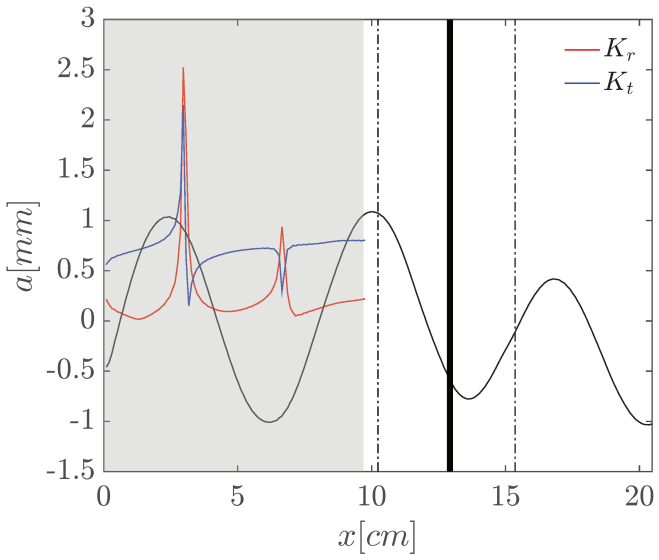

FIGURE 3.14: Calculated K_r and K_t versus chosen x_a position. The example is shown for a single row of rigid blades with $d = \lambda/2$. Variations of x_a are taken within the grey area, x_b and x_c are fixed (dash-dotted lines). The full black line shows the row of blades.

Following a convergence test (see Appendix A), we choose to calculate the coefficients over 200 iterations of randomly chosen points x_a, x_b, and x_c, in order to smooth these errors and obtain reliable K_r and K_t coefficients.
Finally, coefficients are corrected from natural dissipation, evaluated on the control cases to give $\tilde{K}_t = K_t/K_{t0}$, where K_{t0} is the coefficient calculated on the *Control* case (without blades). This attenuation is found to be similar for all control cases. This method therefore gives more reliable results, especially for reflection as it is based only on the wave profiles for the configuration tested. This method was used for the experiments undertaken in the intermediate tank presented in Chapter 4.

Curve fitting of the wave signal can also be used, thereby using the information provided by all points of the curve. This method can prove to be more precise in

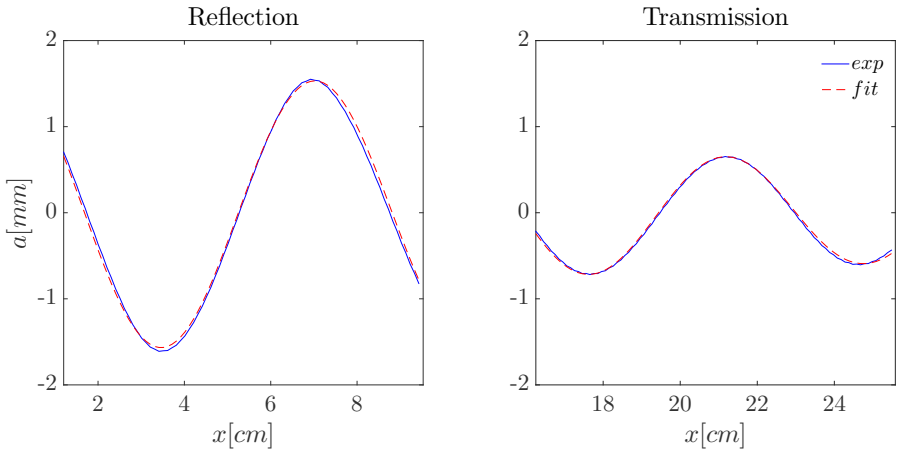

FIGURE 3.15: Example of fitted curves for waves before (left) and after (right) the array for the measurement of reflection and transmission coefficients, using Eq. 3.7. The example is shown for a single row of blades with $d = \lambda/2$.

some cases, especially regarding reflection coefficients, given that it avoids the sharp peaks altogether. It can however be more sensitive. This method was chosen for the results presented in Chapter 6, for experiments run in the small tank.
Waves are here assumed to take the following form in both areas of study (Eq. 3.7):

$$\eta(x) = C_1 e^{-iC_3 x} + C_2 e^{iC_3 x} \tag{3.7}$$

where C_1, C_2 and C_3 are all complex fitting parameters to be found. Reflection and transmission coefficients can then be determined as $K_r = |C_2/C_1|_{before}$ and $K_t = \left|(C_1)_{after}/(C_1)_{before}\right|$. The reflection from the beach can then also be evaluated, along with the dissipation rate β from the complex wave number $C_3 = k + i\beta$. An example of the fit is shown in Figure 3.15.

3.2.3 Blade dynamics - Tracking method

Recalling the general equation of motion (Eq. 2.45) provided in Chapter 2, it is clear that the energy dissipation within the artificial canopy relies on the knowledge of the blades' velocity of oscillation $\dot{x}(t)$. This is done by following the movement of each blade tip, which we will refer to as "tracking". The principle relies on a sufficient contrast between the blade tips and the background so that spatio-temporal plots can be easily extracted using the "reslice" module provided in the software package ImageJ©: a line going through all the rows of the array is extracted from each image of the recorded video, and these are then stacked together onto a single plot as shown in Figure 3.16 below. x is the spatial axis in the direction of propagation of incoming waves, and t is the time axis, for which each pixel represents a single frame of the complete video. Knowing the camera calibration and frame rate, amplitudes X, periods T and phase shifts $\Delta\phi$ can therefore be measured. Though the principle is the same for all experiments, the measurement methods sometimes had to be adapted depending on the experimental set-up used for the surface wave maps. These are briefly detailed in the following paragraphs.

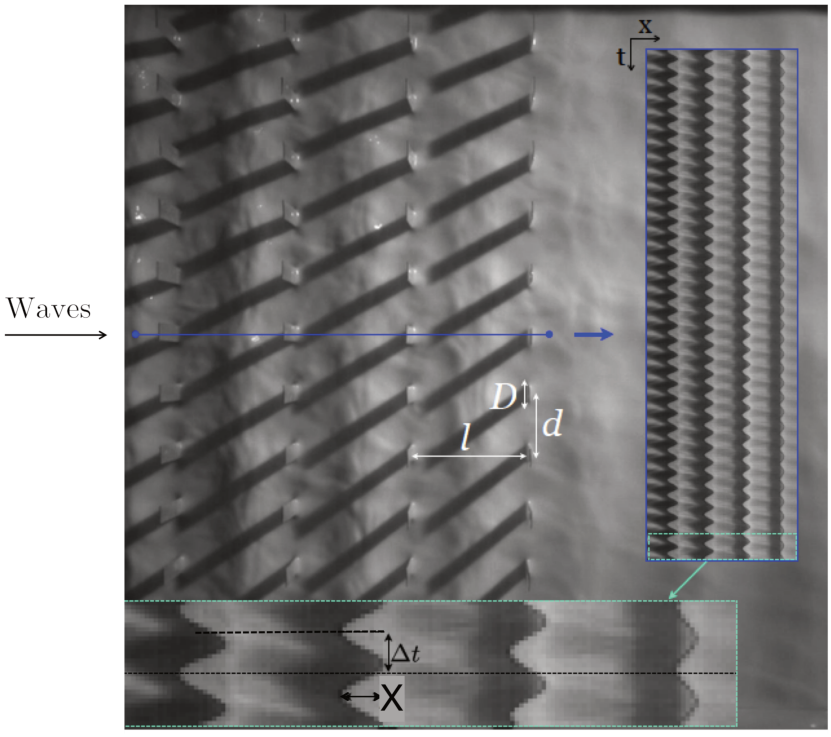

FIGURE 3.16: Principle of the tracking measurement technique.

Tracking of blades combined with FTP technique This surface elevation measurement technique uses TiO_2 particles in order to dye the water surface white, thereby allowing for the projection of a fringed pattern (c.f. previous section 3.2.1). For the purpose of blade tracking, the blade tips were therefore painted black and a dimmed light setting was used in order to enhance the contrast between the blade tips and the background. This is shown in Figure 3.16. For each experiment, 500 images were recorded at a frame rate of 60 fps. While the results are clear, the blade shadows added noise to the images and so an automatic tracking of the oscillations was made very difficult. Manual measurements were preferred, in spite of the increase in possible errors. Additionally, FTP measurements must be performed in the

dark for the visualisation of the projected fringe. Tracking measurements thus had to be done on separate video recordings and so surface wave maps and corresponding tracking data could not stem from a single recording.

Tracking of blades combined with Synthetic Schlieren technique The tracking method used combined with Schlieren measurements depended on the choice of Lego© base board. Experiments run in the intermediate scale tank used white blocks and so the associated tracking technique was almost identical to that described in the previous paragraph. In this case, however, the same video recording could be used for both Schlieren processing and tracking analysis.
The Schlieren method for measuring surface deformations was also used for several small-scale experiments for which transparent Lego© parts were used, in order to benefit from these measurements also within the array. With a dark background, blade tips were made white in this case. Furthermore, without blade shadows and with identical contrast all around the blade tips, it was then possible to measure oscillations automatically through a simple Matlab script. An example is shown in Figure 3.17 (a) below.

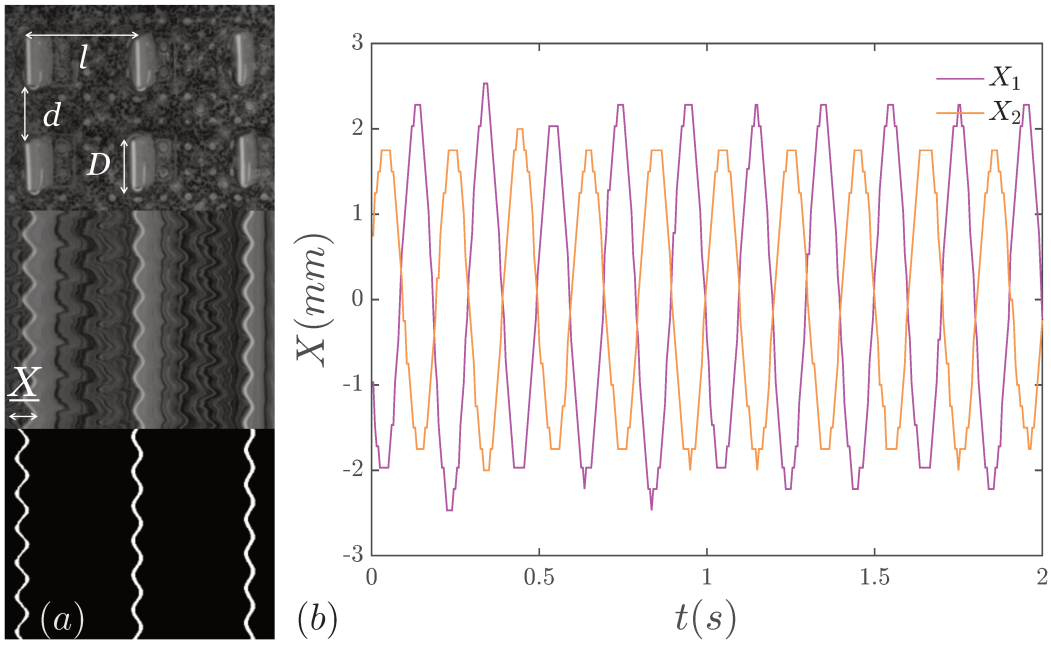

FIGURE 3.17: Typical tracking process for experiments relying on Synthetic Schlieren measurement techniques, with transparent Lego parts (a). Example of oscillations $X(t)$ measured for two blades oscillating out of phase (b).

Typical results of the treated signal are provided in Figure 3.17 (b), for a case of two blades oscillating out of phase. The amplitudes could then be measured from the extracted peaks which averaged around 1.7mm, with a standard deviation of approximately 0.105mm.

3.2.4 Array analysis - Absorbed and dissipated energy

The amount of energy that is dissipated through beam bending can be evaluated from the known blade tip displacements, as follows.

When the beam is placed out of balance, its elastic returning force will tend to restore equilibrium. With no external force applied, the beam will oscillate freely with its total mechanical energy being shared between its potential elastic energy E_{el} and its kinetic energy E_{kin}. Recalling Eq. 2.45 and integrating over the total blade length h_s of the beam gives:

$$E_{el} = \frac{1}{2}\frac{\mathcal{M}^2}{EI} = \frac{EI}{2}\int_{z=0}^{h_s}\left(\frac{d^2\underline{x}(z,t)}{dz^2}\right)^2 dz \tag{3.8}$$

$$E_{kin} = \frac{1}{2}m\left|\underline{V}^2\right| = \frac{1}{2}\int_{z=0}^{h_s}\mu\left(\frac{d\underline{x}(z,t)}{dt}\right)^2 dz \tag{3.9}$$

where $\mathcal{M}$ and $\underline{V}$ are respectively the bending moment and the velocity vector of the beam, and m is its mass. In the case where no damping takes place, energy is conserved and the beam oscillates indefinitely. In reality, however, part of the energy is dissipated in the material due to internal friction. The equation of motion of this simple damped oscillator can be expressed as:

$$m\ddot{x}(z,t) + kx(z,t) = -\gamma\dot{x}(z,t) \tag{3.10}$$

where γ is the linear damping coefficient of the material and k is the stiffness coefficient of the beam equal to $k = EI\int_{s=0}^{h_s}\frac{d^2v_1(s)}{ds^2}^2 ds$ from Eq. 3.8. A linear damping term is chosen here given that our system is limited to small deformations. Substituting equation 2.35 the equation becomes:

$$mv_1(z)\ddot{\underline{X}}(t) + kv_1(z)\underline{X}(t) = -\gamma_s v_1(z)\dot{\underline{X}}(t) \tag{3.11}$$

The general solution to this equation takes the form:

$$X(t) = Xe^{-\Gamma t} \tag{3.12}$$

with $\Gamma = \gamma/(2m)$ and the mechanical power associated with this internal dissipation is therefore given by:

$$\mathcal{P} = \gamma\dot{x}^2(z,t) = 2m\Gamma\dot{x}^2(z,t) \tag{3.13}$$

It is clear that the ability for the beam to dissipate its motion and therefore absorb part of the system's energy is determined by the value of this damping coefficient Γ, which depends on the material's flexural rigidity $B = EI$, and its mass m. It should be emphasized that this quantity corresponds to the amount of power that could be potentially extracted, if a conversion technology were included, e.g. piezoelectric energy extractor. This was measured experimentally by means of a free oscillation test (the beam is placed out of balance and left to oscillate freely). The recorded signal (blue curve) and linear fitting (red curve) are shown in Figure 3.18 below for the case of the 12 cm long Mylar© blades. A damping coefficient $\Gamma_{int} = 0.7s^{-1}$ was therefore extracted. As we will see in the later chapters, the oscillations of our blades do not exceed 5mm in amplitude so a linear fit is assumed sufficient.

When the same blade oscillates in water, however, an additional damping term must be considered, that is caused by the presence of the fluid. Given the range of Reynolds number associated with our system, this term should be taken as non-linear, using the drag expression $\frac{1}{2}\rho_w C_D D\left|u_r\right|u_r$. An attempt to measure the drag

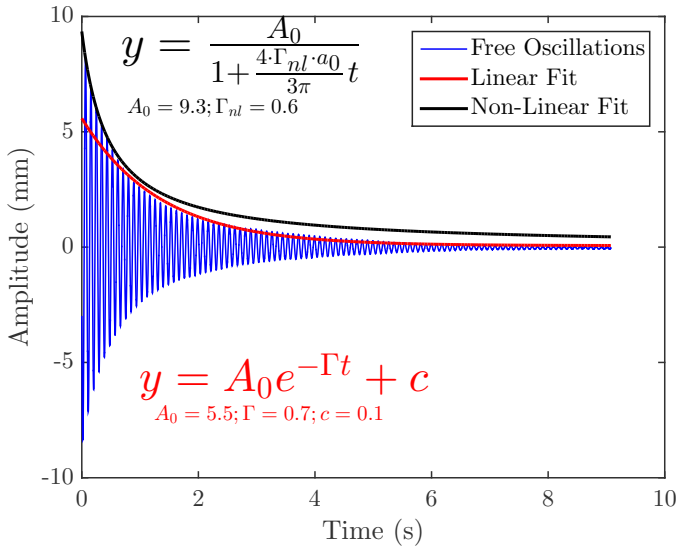

FIGURE 3.18: Free oscillation test in air

FIGURE 3.19: Free oscillation test (blue curves) in air for the measurements of internal Γ_{int} damping coefficients, by means of a linear curve fitting (red curve).

coefficient experimentally was performed by means of a free oscillation test in water. However, the total measured damping term then also includes the internal damping term described above, as well as radiative damping term, which in our balance of energy, is already measured through the reflection coefficients. This, together with the limited set of points available from the free oscillation signal in water makes it difficult to extract the external dissipation coefficient directly from our experimental data. Instead, this quantity will be calculated using the drag force equation introduced in Chapter 2, based on an empirical drag coefficient C_D (typically equal to 2 for the case of a thin plate (Leclercq and Langre, 2018)).

The total dissipated power then be expressed as the sum of the internally absorbed power due to the work of the blade ($\mathcal{P}_a$), and the externally dissipated power due to the relative motion of the blade in water ($\mathcal{P}_d$). Substituting Eq. 2.35 and integrating over the beam length leads to the expressions provided in Eq. 3.14 and 3.16 below:

$$\mathcal{P}_a = 2\Gamma_{int}\left(\int_0^{h_s} \mu_s \left(\frac{d[v_1(z)X(t)]}{dt} \right)^2 dz + \int_0^{h} \mu_l \left(\frac{d[v_1(z)X(t)]}{dt} \right)^2 dz) \right) \tag{3.14}$$

$$\mathcal{P}_{drag} = \frac{1}{2} C_D \rho_w D \left(\int_0^{h} \left(u_a(z) - \frac{d[v_1(z)X(t)]}{dt} \right)^3 dz \right) \tag{3.15}$$

$$\tag{3.16}$$

3.2.5 Force measurements

Force measurements were also carried out on the blades. In fact, the experimental analysis presented in the previous paragraphs relies on indirect measurements of the forces applied to our oscillating objects. In order to validate the hypothesis of linearity, which links forces to blade tip oscillations, the former were directly measured experimentally by means of a FUTEK submersible force sensor, placed at the base of one blade, as presented in Figure 3.20(a) below. The sensor was carefully integrated to the system so that the edge attached to the blade was able to move freely with respect to the opposite fixed end. Voltage differences between both ends could therefore provide accurate measurements of the blade forces.

The set-up consisted of a signal conditioner, linked to an analog to digital converter, itself connected to a computer, where force signals were measured and recorded via a LabView program. A calibration linking voltages to forces was first performed using small weights. Results are presented in Figure 3.20(b) below.

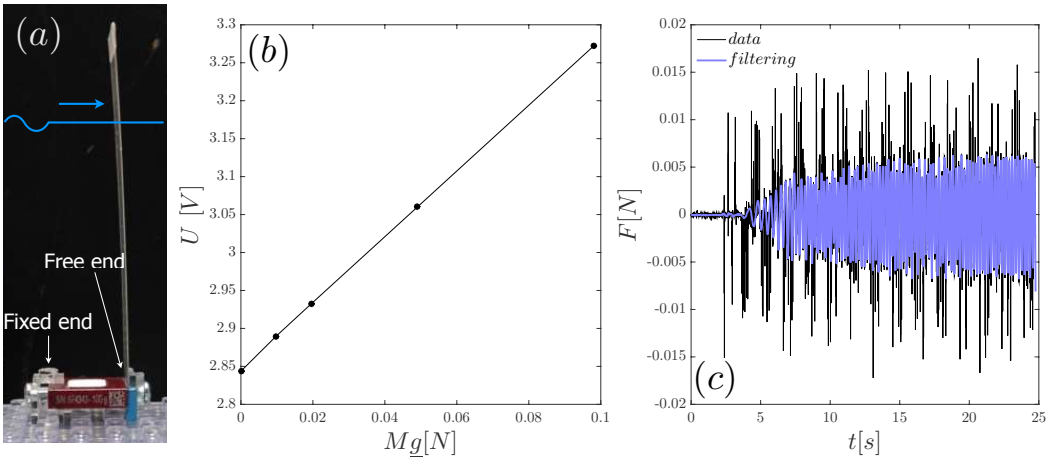

FIGURE 3.20: Force sensor measurement treatment. Image of the force sensor attachment system (a). Results from the calibration test (b). Typical raw signal (black) vs. smoothed data (blue) for the force measured on a single blade subject to waves at $f_0 = 5Hz$.

Although force measurements and camera recordings were not synchronised, force measurements are recorded before the wave maker is started until after the final camera image is saved. The first traveling waves could then be easily identified from the full force signal, along with matching camera frames. While the measurements did not match perfectly, the same stabilised wave condition was analysed.

The sensor was placed on its most sensitive setting, in order to ensure measurement of all (even small) forces. However, this led to relatively noisy signals. Smoothing of the raw data was performed using a low span of 0.005 in the Matlab function. An example of raw (black) and smoothed (blue) signals is shown in Figure 3.20(c) below. Note that the camera recordings correspond to the time frame $t \in [8 - 10]s$ of the signal, when the first full wave has traveled through the array, and before wave tank modes have been created.

For each recorded force measurement, a reference recording is taken before and after the waves have been launched, in order to centre the values around zero, and avoid voltage drift errors.

Chapter 4

Parametric study of wave-structure interactions

The goal of this thesis is to study the mechanisms involved in the interaction of wave-driven fluid motion and an array of flexible vegetation-inspired structures, with a focus on how the wave energy is distributed in such a system. This is first investigated by means of an experimental study, which is presented and discussed in this chapter, based on the small-scale facilities presented in Chapter 3. As mentioned before, we chose to model the vegetation-like objects as slender blades, thereby limiting their bending motion to a single degree of freedom. These individual objects can then be placed behind or next to each other in order to form various array patterns for which the collective behaviour may demonstrate different responses when subject to the incoming waves.
Following the works of (Sarkar, Renzi, and Dias, 2014) regarding the effects of spatial arrangements on wave energy absorption efficiency for flap-type converters, the study presented here aims to improve our understanding of the role played by these spatial parameters regarding wave attenuation and energy absorption. Particular interest is given to the estimation of energy harvesting potential of the bending of our structures and their consequent de-energising effect on the wave-driven flow. The analysis is therefore performed in two parts: tested arrays are first evaluated regarding their impact on the wave field, i.e. which arrays convey the least amount of energy downstream (low transmission), and in the second part, focus is directed at the energy absorption due to the blades' elastic restoring force, i.e. which arrays present the best energy harvesting potential.

The array response is however studied in stages. In the first section, we present the results obtained from preliminary tests run in the small-tank, at the single resonant frequency of the blades. We first focus on individual elements and gradually build a full array in order to characterise the influence of neighbouring blades on each other, regarding imposed forces and resulting oscillations. The results are dominated by the spacing along the $x-$axis, i.e. in the direction of propagation of the waves regarding neighbouring effects. This is tested further on full arrays by comparing blade mechanics in aligned and staggered patterns as well as the effects on the wave field, by means of reflection and transmission coefficients. These additional results confirm that it is the longitudinal spacing separating back-to-back rows which dominates the array response, thereby demonstrating the 1-directional nature of our system.
These first experiments were then completed with a larger study undertaken in the intermediate tank. This wider facility made it possible to perform experiments over a range of frequencies, while avoiding strong reflections, and to evaluate each parameter separately. Focus in this case was directed at evaluating the effect of both spatial configuration and flexibility on the global wave energy distribution.

4.1 Preliminary study

Before analysing our system in its full array form, it is essential to first understand how single objects interact with the wave field and with each other. This is done by characterising single units and gradually increasing the size of the system. The results presented in this section are based on the 1D blade objects made from Mylar© sheets of thickness 350μm, width D 14mm and length h_s 9cm. The study focuses on the blade oscillations and is based on the measurements of both forces and tip tracking, with the methods described in the previous Chapter 3.

4.1.1 Response of a single blade

We first look at the response of a single blade subject to monochromatic waves, as sketched in the Figure 4.1 (c). The experiment is performed at the resonant frequency of the blades, previously measured as 5Hz from a free oscillation test. Using the same blade shape, we test an equivalent "rigid" blade made from 2mm thick plexiglas. Converted filtered signals are presented in Figure 4.1 (a). Note that the signal recording being triggered before the launch of waves, a force transient is seen around $t = 1000s$ before reaching a steady-state.

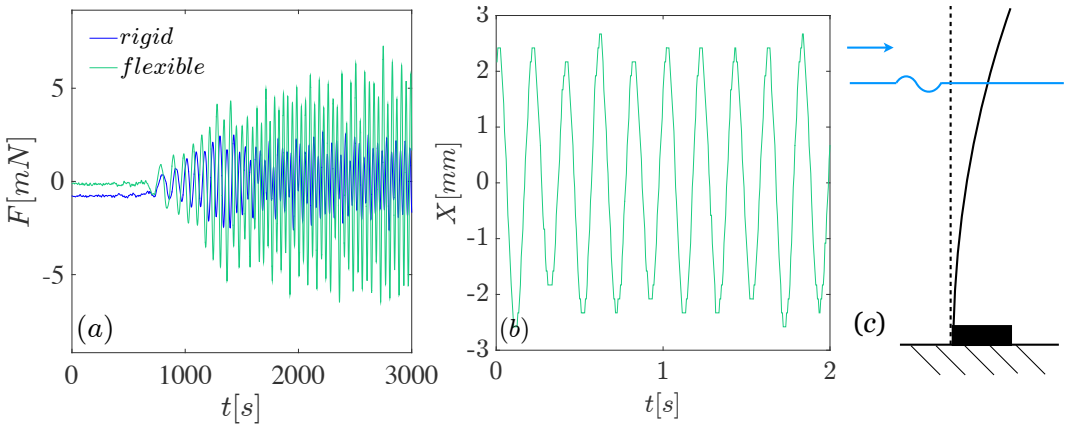

FIGURE 4.1: Comparison of recorded forces for a single rigid (blue curve) and flexible (green curve) blade subject to monochromatic waves at f=5Hz (a). Typical blade tip tracking signal for a single flexible blade (b) and illustrative sketch of the set-up (c).

The results show a clear difference in the loading sensed by the blades, depending on their mechanical characteristics. While the magnitude of the force remains constricted to values of 1-2mN for both rigid and flexible cases, these exceed 5mN, over double, for the flexible case. This is due, in part, to the internal stresses caused by the resonance of the blade dynamics. The imposed frequency matches the resonant frequency measured for the flexible blades in water. Therefore, at that same frequency, the forces and oscillation amplitudes are amplified. In fact, part of the difference in force measured between the semi-flexible and rigid blades is associated with the energy transfered from the imposed waves into elastic energy of the bending blade. This is why the maximum transfer would occur at the condition of maximum deformation, i.e. at resonance, and why real scale converters are tuned as best as possible to the specific sea state they will be subject to.
This observation is coherent with recent studies by Luhar and Nepf, 2016 and Leclercq and Langre, 2018. Until these, flexibility was believed to always be beneficial with

respect to load reductions. However, this is seen to be true only in drag-dominating regimes and for very flexible objects. In the case of inertial-dominating oscillatory flows ($KC < 1$) and for low Cauchy numbers $C_y \sim \mathcal{O}(1)$ as it is here (c.f. Chapters 2 and 3), then flexibility can in fact enhance forces, due to an increase in the relative motion between the blade and the fluid particles (Luhar and Nepf, 2016). If we assume that the blade excursion is of the same order as that of the water fluid particles, we can show that the relative velocity magnitude is equal to $\sqrt{2}u$ (see Appendix B for the experimental details). Therefore, the increased force sensed by the flexible blade is triggered by both inertial and viscous hydrodynamic loadings, that are amplified by the dynamic response of the elastic structure.
This bending deformation is studied through the blade tip motions, as described in Chapter 3. A typical recorded tracking signal of the single semi-flexible blade is plotted in Figure 4.1 (b), extracted over 2 seconds beyond reaching a steady-state regime. Oscillations of the blade tip are measured at around 2mm in amplitude, or 4mm peak to peak. In the following discussions, measured force and tip oscillations will always be studied through normalised quantities $\tilde{F}$ and $\tilde{X}$, which correspond to the measured maximum amplitudes divided by those measured for the single isolated blade, as shown in Figure 4.1.

Let us now look at the effect of the blade on the wave field. The surface wave maps were measured by means of the Synthetic Schlieren method presented in Chapter 3.

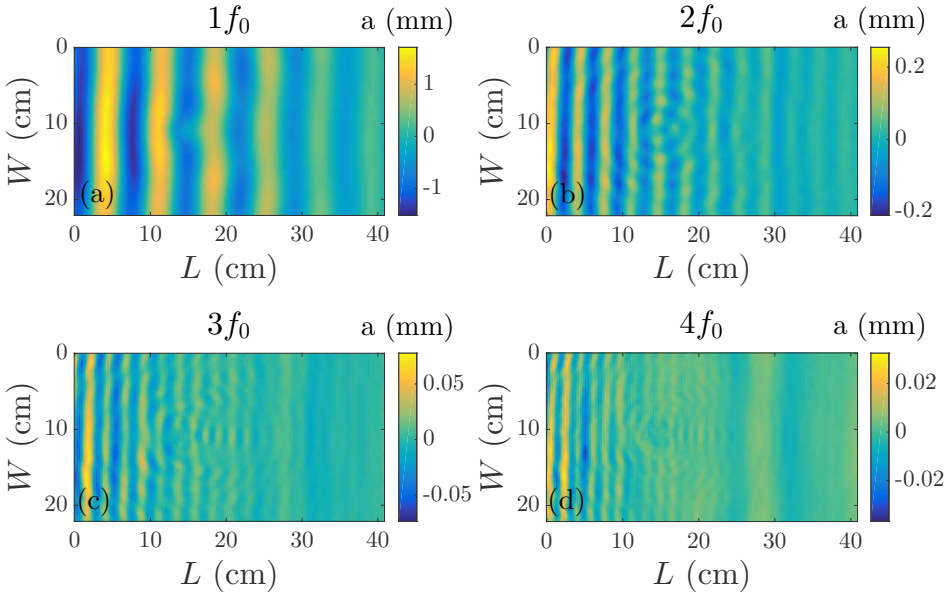

FIGURE 4.2: Modal decomposition of the wave field for a single oscillating blade. The first four modes are presented, for a fundamental frequency f_0 of imposed waves equal to 5Hz.

Figure 4.2 shows the modal decomposition of the wave field for a single flexible blade. The first four frequencies extracted from a Fast Fourier Transform of the wave field are presented, with f_0 corresponding to the excitation frequency of the incoming waves of 5Hz. The same decomposition is plotted for the rigid blade in Figure 4.3 below. The multi-directional scattered wave field is clearly visible on the second mode for both cases, which corresponds to a subfrequency of $f_1 = 2f_0$. It is also noticeable in the third and fourth modes but the corresponding amplitudes at these subfrequencies are very small ($\mathcal{O}(10^{-2})$mm) in front of those measured for

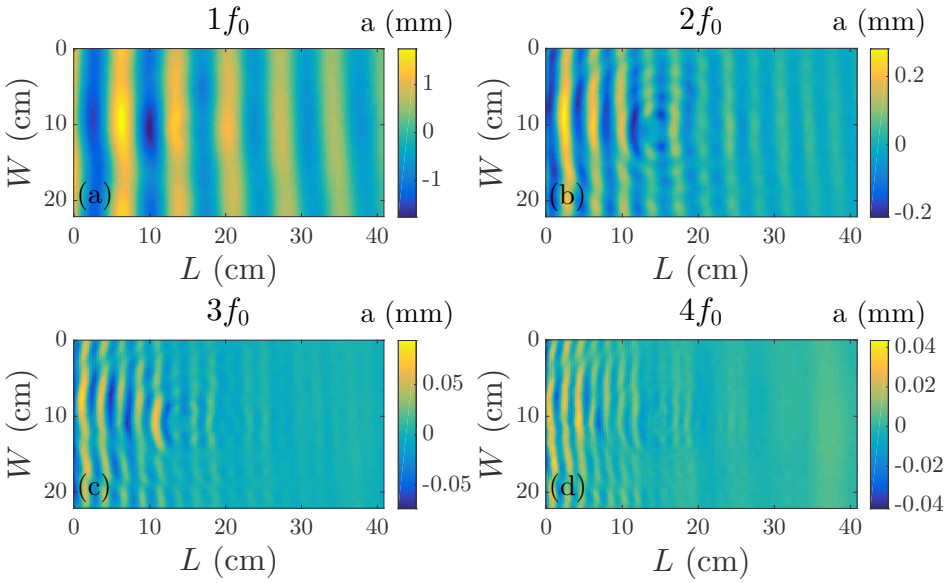

FIGURE 4.3: Modal decomposition of the wave field for a single rigid blade. The first four modes are presented, for a fundamental frequency f_0 of imposed waves equal to 5Hz.

the fundamental frequency f_0, and are thus negligible. When looking at the first two modes, the scattering is shown to be stronger in the $x-$direction than in the lateral $y-$direction, since this corresponds to the direction of travel of the incoming waves. The resulting wave in the $y-$direction will be the sum of the incoming and reflected waves.

4.1.2 Effect of neighbouring blades

The influence of the spacing parameters l/λ and d/λ is now evaluated on the forcing and oscillations of our blades. This was tested using 2 blades placed one behind each other for the first case, and 3 blades placed next to each other for the second case. A representative sketch of the layout is shown in Figure 4.4 below.

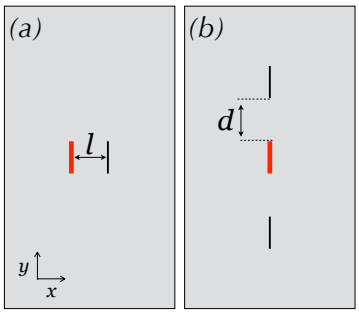

FIGURE 4.4: Sketch of 2 blade (a) and 3 blade (b) experiments. Incoming waves travel from left to right and force sensor is attached to front and central blade, represented in red here.

Longitudinal l and lateral d spacings were increased to vary within the range $[\lambda/4 - \lambda]$. For each configuration, forces were measured on the front, central blade

(represented in red in Figure 4.4) and the same blade's tip oscillations were tracked using the method described previously in Chapter 3. Average values were then extracted and normalised by the case of a single isolated blade. These are denoted $\tilde{F}$ and $\tilde{X}$, respectively. For comparison, the same experiments were repeated using rigid blades made from 2mm thick plexiglas sheets.

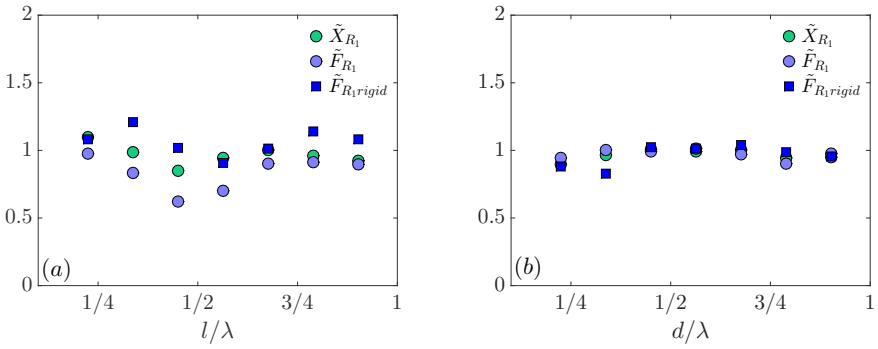

FIGURE 4.5: Variations of force and oscillations depending on separating distance l/λ for 2 blades (a) and d/λ for 3 blades (b). Comparison of average normalised oscillations of the front flexible blade (green), normalised flexible force recorded for the flexible blade located at the front (light blue) and that recorded for the front rigid blade (dark blue)

Results for spacing l are presented in Figure 4.5 (a). These demonstrate an oscillatory variation as the parameter l/λ is increased, with a minimum at $l/\lambda = 1/2$. This observation is seen for both measured forces (blue dots) and blade oscillations (green dots). The rigid case follows a similar variation and demonstrates that the dip in blade oscillations is due to a dip in wave forcing on the blades, thereby confirming a linear relationship between blade oscillations and the applied wave force on the structure.

The same results are plotted for the case of varying spacing d/λ in Figure 4.5 (b). Unlike longitudinal spacing l, d shows very little impact on blade oscillations and wave forcing. In fact, wave forces and oscillations fall on the same curve, and results obtained with rigid blades match those of flexible blades as well. This could be caused by the fact that the blades are very thin with $b << D$ so their width is negligible in front of the wave length. Transverse waves caused by scattering would therefore be negligible compared to those propagating in the direction of incoming waves, as seen previously in the modal decomposition of the surface wave maps. Given the single direction of propagation of the incoming waves, the scattered waves will be predominantly influential in that same direction. In fact, the amplitude of the scattered wave is of the same order as $2f_0$, so the associated force applied onto neighbouring blades is negligible compared to that imposed by the incoming waves.

4.1.3 Behaviour of a full row/line

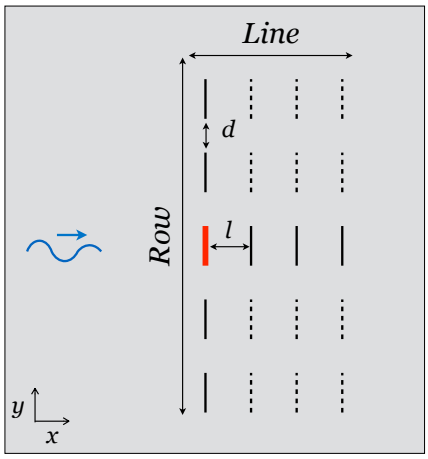

FIGURE 4.6: Sketch of a full array.

We now gradually build our array in directions x and y separately to study the response of a line as well as a complete row of blades, i.e. when it fills the entire canal width. A representative sketch of these is provided in Figure 4.6. The results of normalised forces (blue) and oscillations (green) measured on the same frontal blade (represented by a red line in the sketches), are shown in Figure 4.7 for increasing number of blades B in the line (a) or in the row (b). Here, both spacings l and d are fixed, and approximately equal to $\lambda/4$. Note that the distance d is measured edge to edge which, unlike longitudinal spacing l does not match the centre of the blade and, thus, the centre of the scattered wave.

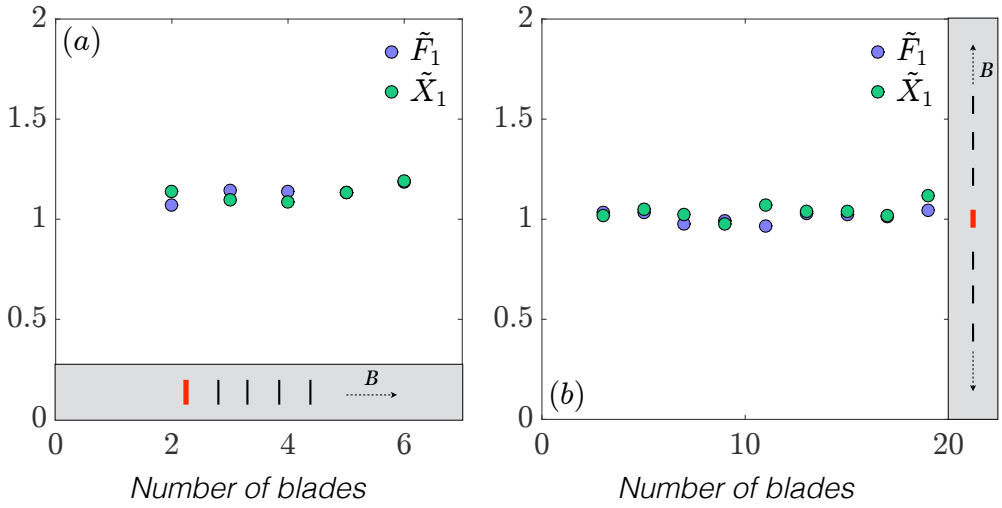

FIGURE 4.7: Building a full line (a) and a full row (b). Measured normalised forces (blue markers) and oscillations (green markers) of front blade (red blade) for increasing number of blades B in a single line (a) and a single row (b). Longitudinal l and lateral d spacings are fixed at 16 mm $\sim \lambda/4$.

The results for both force and oscillations fall again on the same curve, thereby confirming the linear relationship between excitation force and blade tip displacement. Furthermore, these also demonstrate no clear variations due to the number B of blades. The scattered waves from added blades in a same line or row do not impact the front blade, possibly due to the sheltering of its immediate neighbours. This would suggest that it is the separating distance with immediate neighbours rather than the total number B of blades that dictates resulting forces.

4.1.4 Array response - aligned vs. staggered

With some elements of understanding acquired regarding the local behaviour of individual elements, we now explore the response of a full array of blades and investigate the influence of spatial configuration. In this section, we compare aligned and staggered patterns for various spatial parameters, and for different array sizes, thereby combining the previously tested parameters. Sketches of these patterns are provided in Figure 4.8 below. The staggered pattern is created by shifting every other row laterally, so that the blades of two neighbouring rows are no longer positioned directly back-to-back. In doing so, the sheltering effect of blades belonging to a same line would then be reduced.
These are tested regarding blade oscillations and forces, as before, along with the effects on the wave field by means of measured reflection and transmission coefficients.

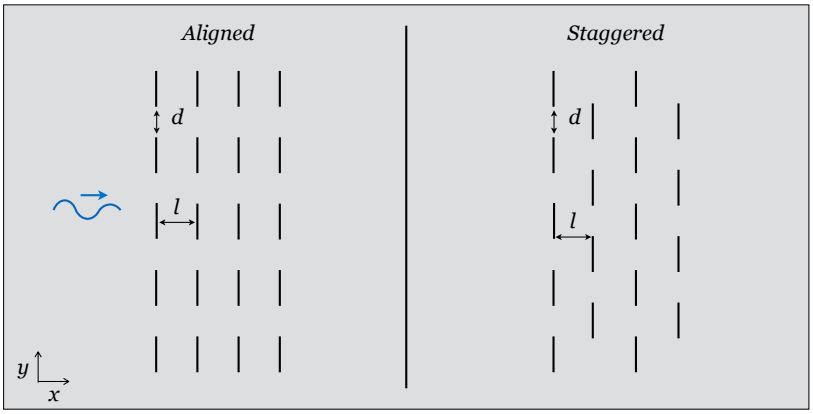

FIGURE 4.8: Sketch of aligned (left) and staggered (right) patterns for an array composed of 4 rows.

This second set of preliminary tests was run in the small tank associated with the FTP measurement technique for the surface wave maps (see Chapter 3). The blades in this case had $h_s = 12$ cm and a corresponding resonant frequency measured as 4.2Hz. Water depth was 8 cm and the imposed waves had λ=9.8 cm. Waves were imposed at the single resonant frequency of the blades and we vary the total number of blades B along with the lateral (d) and longitudinal (l) spacings between neighbours (c.f. Figure 4.4). A summary of the tested configurations is listed in Table 4.1 below.

Typical images of staggered arrangements are presented in Figure 4.9 for increasing number of rows $\mathcal{R}$, Figure 4.10 for configurations of varying d and Figure 4.11 for configurations of varying l.

Configuration	$d[cm]$	d/λ	$l[cm]$	l/λ	N
Increasing l					
l	3.4	0.35	3.2	0.33	[1-6]
	3.4	0.35	4.8	0.49	[1-6]
	3.4	0.35	8	0.81	[1-5]
Increasing d					
d	1.8	0.2	4.8	0.49	[1-5]
	3.4	0.35	4.8	0.49	[1-6]
	6.6	0.67	4.8	0.49	[1-6]

TABLE 4.1: Set of Spacing parameters tested

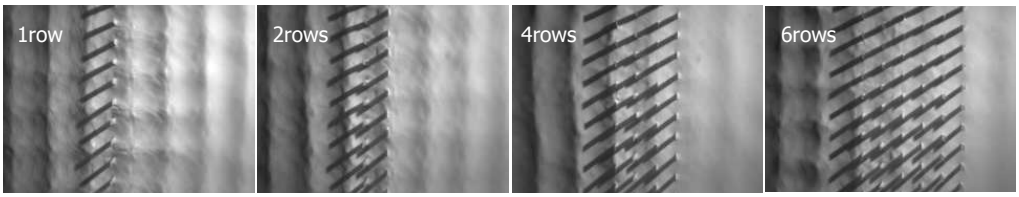

FIGURE 4.9: Typical images for increasing number of rows $\mathcal{R}$ of a staggered pattern (here, $\mathcal{R}_1$, $\mathcal{R}_2$, $\mathcal{R}_4$, and $\mathcal{R}_6$). The presented configurations have fixed $l = 4.8$cm and $d = 3.4$cm.

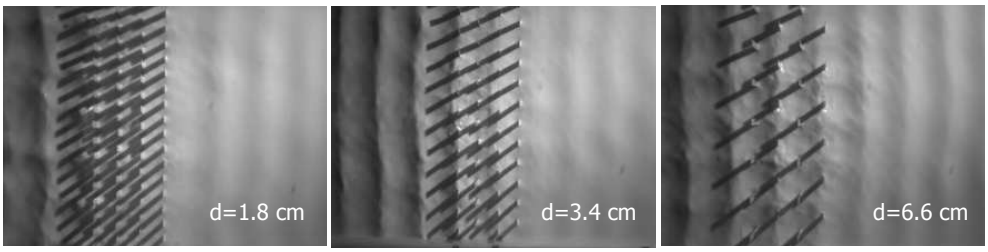

FIGURE 4.10: Typical images of configuration d, for a staggered pattern, with fixed $l = 4.8$ cm.

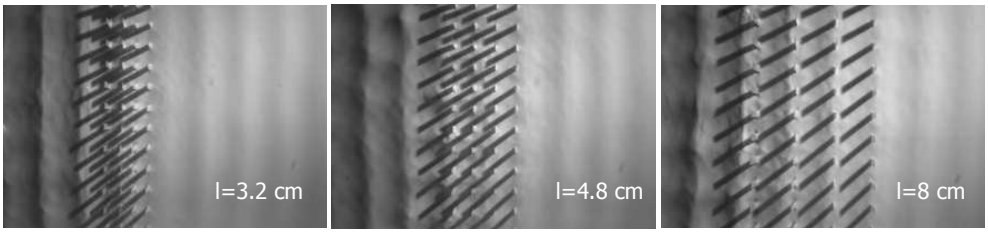

FIGURE 4.11: Typical images of configuration l for an aligned pattern, with fixed $d = 3.4$ cm.

Reflection K_r and transmission K_t coefficients were measured using the method described in Chapter 3. The results for configuration l are presented for both aligned (square markers) and staggered (circular markers) patterns, in Figure 4.12 below, as

a function of the total number of blades $\mathcal{N}$ in the array. Each test was repeated in order to average results over two sets of data. It is clear from the transmission coefficients plotted in (a) that wave damping decreases proportionally to array size, i.e. blade density. Furthermore, values for identical configurations of both aligned and staggered patterns fall on very nearly identical curves, thereby suggesting that the staggered arrangement is not itself responsible for the reduced transmission. A separation in results can however be noticed regarding the chosen distance l. The smallest (light green) and largest (dark green) separations l are more effective than the intermediate case, with a clearer difference as the array size becomes larger. This is thought to arise from wave interferences rather than confinement effects, given that the larger transmission is found for $l \sim \lambda/2$, which corresponds to the middle case of our tested range. This effect will be further investigated in the following chapters. Reflection, on the other hand, does not seem to follow as clear trends (b). In fact, the results do not mirror those of transmission, as one would expect from classical optics and acoustics theories. Given that our objects move and dissipate energy within the material's shear forces, the statement $K_t^2 = 1 - K_r^2$ is not valid here. The variations in reflection coefficients are however not clear and require further investigation that will be discussed in the following chapters. Nonetheless, differences between aligned and staggered patterns seem here again nonexistent.

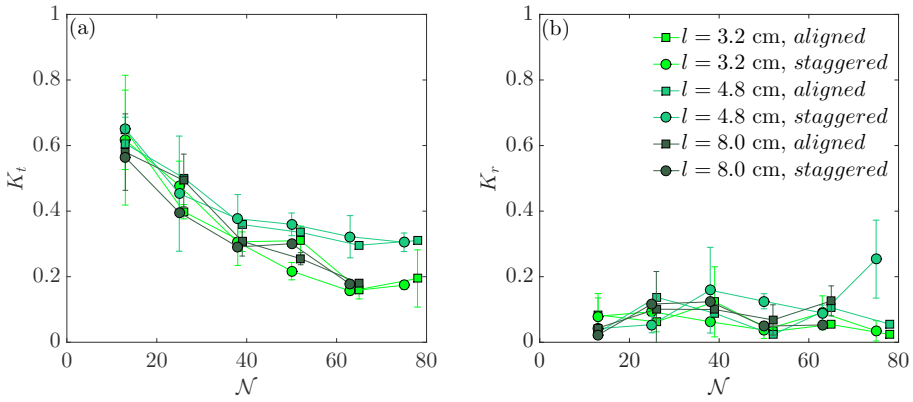

FIGURE 4.12: Transmission (a) and reflection (b) coefficients for various separating distances l between rows, as a function of the total number of blades $\mathcal{N}$. Square and circular markers refer to aligned and staggered patterns respectively, with averages taken over two sets of data, when possible. Distance $d = 3.4$ cm is constant and the chosen colour gradient increases with distance l.

Following this observation, results of reflection and transmission coefficients for varying distance d are averaged for both aligned and staggered pattern and presented in Figure 4.13. As previously seen for l, spacing d does not appear to be the leading parameter influencing transmission coefficient K_t but rather blade density (Figure 4.13 (a)). In this case, all configurations follow a similar trend but the curves are shifted downwards as d reduces. This is consistent with the previous discussion on the role of d regarding the transmission of a singled row: transmission increases as the confinement ratio decreases. The influence of d on reflection is plotted in Figure 4.13 (b). As seen for spacing l tendencies are not obvious and require further investigation here again.

Finally, we complete the study by comparing blade oscillations for staggered and aligned patterns, as shown in Figure 4.14 below. Average oscillations $\bar{X}$ are plotted for each row R of the array, for increasing sizes from 1 to 6 rows. Results are

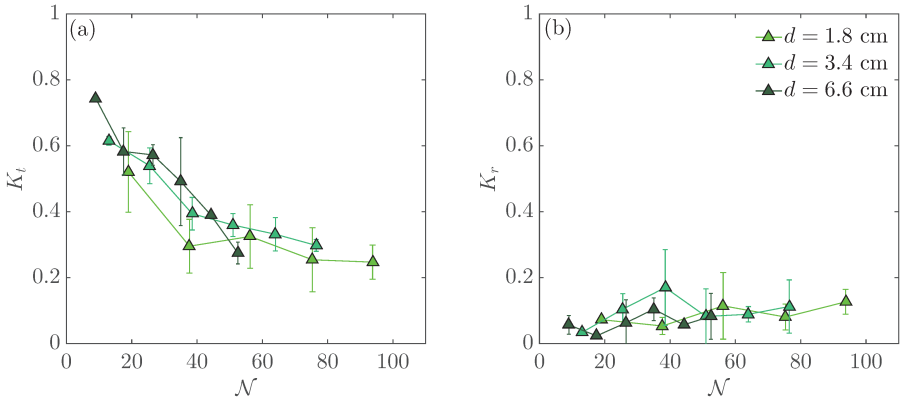

FIGURE 4.13: Transmission (a) and reflection (b) coefficients for various separating distances d between rows, as a function of the total number of blades $\mathcal{N}$. Results are represented using triangular markers, as these are averaged over both aligned and staggered patterns. Distance $l = 4.8$ cm is constant and the chosen colour gradient increases with distance d.

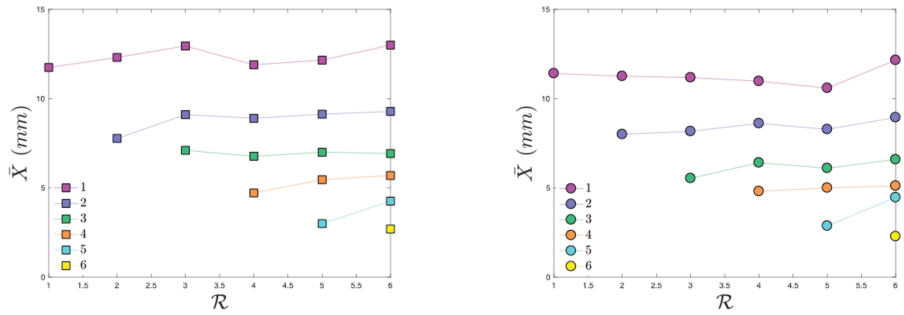

(A) Aligned arrangement (B) Staggered arrangement

FIGURE 4.14: Average oscillation amplitudes $\overline{X}$ for each row of the array, identified with specific colours, as a function of the total number of rows $\mathcal{R}$. Results are shown for fixed $l = 3.2$ cm and $d = 3.4$ cm for aligned (a) and staggered (b) patterns.

provided for the aligned pattern in (a) and the same staggered pattern in (b). The results clearly demonstrate that the row offsets do not influence blade oscillations. In other words, each row must be considered as a full object, rather than individual blades and it is therefore the distance between these full rows that dominates the response, i.e. spacing l.

4.2 Parametric study

The previous results enabled us to draw preliminary conclusions on the influence of spatial parameters on blade responses to monochromatic waves. It was demonstrated that a stronger influence of neighbouring blades occurs when these are placed behind each other in the longitudinal direction ($x-$direction). This axis corresponds to the direction of propagation of the incoming waves as well as the preferred bending direction of the slender blades. Therefore, the nature of the interaction is kept 1-dimensional. These observations were confirmed when comparing aligned to staggered arrays, from which the oscillations were seen to vary identically between both patterns, given that spacing l was kept the same. However, the variations in reflection and transmission of the full array are still unclear and require further investigation. In order to perform a full parametric study of our system in terms of wave energy distribution, we chose to work with the intermediate tank size. Lateral and multiple tank reflections could then be avoided over an entire span of wave frequencies. Additionally, spacing parameter d and blade number N could be tested separately: with a very large tank compared to the array width, the number of blades per row could be maintained constant, whilst avoiding strong diffraction. The system response was tested depending on both spatial configurations and flexibility, and for various frequencies. Surface wave maps were measured using the Synthetic Schlieren method described in Chapter 3, along with the associated tracking method for the measurement of blade oscillations.

4.2.1 Conditions and configurations

Wave conditions Given the natural resonant frequency of blades of ~ 4.5 Hz, the imposed frequencies of the wave maker are chosen to range from 2 Hz to 5 Hz. For frequencies above 5 Hz, transverse modes occur, i.e. periodic waves along the width of the canal, and limit data analysis. A time Fast Fourier Transform (FFT) of the surface wave maps was performed, for a single central line as presented in Figure 4.15 below.

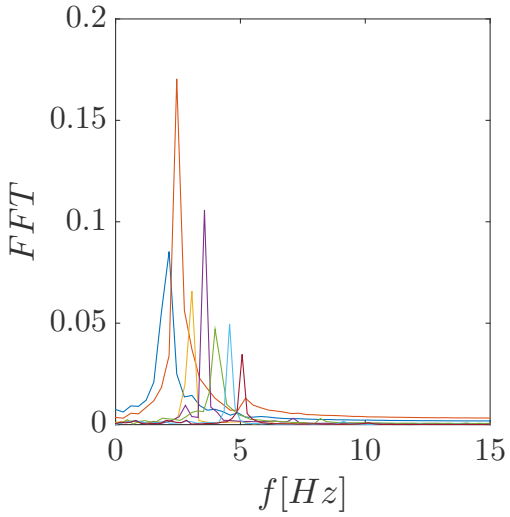

FIGURE 4.15: FFT decomposition for the central line of the treated surface wave maps over the range of tested frequencies. The results correspond to a reference case without any object in the canal (empty tank).

This decomposition shows the clean signals of the imposed waves, with very little subfrequencies in the spectrum. Therefore, a regular monochromatic analysis is valid. It should be noted however, that the amplitudes of the waves vary non-linearly with frequency, and so the measurement of the amplitudes, with the most energetic waves at $f = 2.5Hz$. This will be taken into account in the analysis. Additionally, the natural dissipation and beach reflections were also measured and were also found to vary strongly with frequency. These are summarised in Table 4.2 below. The measurements are taken on the transverse average of each surface wave map, for the first mode of the decomposition at ($f0$=frequency imposed). A complex fitting of the curve is applied to the averaged wave, according to Eq. 3.7. The coefficient β represents the natural dissipation of the wave, and depends on the surface conditions of the water, along with the wave characteristics. It is measured from the imaginary part of the fitting complex wave number k_z, with $k_z = k + i\beta$.

$f[Hz]$	β	K_r
2	-0.1701	0.070
2.5	-0.1879	0.040
3	-0.8004	0.009
3.5	-1.6209	0.0015
4	-1.9878	0.0035
4.5	-1.9878	0.0014
5	-2.1326	0.0006

TABLE 4.2: Wave frequency f, dissipation ratio β, reflection coefficient K_r of imposed waves.

The natural dissipation of the waves is clearly stronger as f increases, with an inversely proportional decrease of the reflection coefficient of the empty canal. As described in the previous Chapter 3, in the chosen frequency range and for a water depth of 8 cm, imposed waves match both capillary-gravity and deep water conditions. Therefore, group velocity can be assumed to equal half the phase velocity (Eq. 2.20). The imposed wave conditions are presented in Table 4.3. It should however be noted that the longest waves (2Hz) may tend towards shallow water as well.

Tested configurations Blades were 14 mm wide and 12 cm long. Aspect ratio, defined as width over length, was $D/h_s = 0.12$. To study the influence of blade

$f[Hz]$	$a[mm]$	$\lambda[cm]$	$v_\phi[m/s]$	$v_g[m/s]$	KC
2	1.8	35.24	0.70	0.35	0.80
2.5	3.5	25.4	0.63	0.32	1.57
3	1.9	18.56	0.55	0.28	0.9
3.5	2.3	13.96	0.48	0.24	1.03
4	1.2	10.8	0.43	0.21	0.45
4.5	1	8.72	0.39	0.20	0.43
5	0.7	7.16	0.35	0.18	0.29

TABLE 4.3: Experimental conditions: Frequency f, amplitude a, wave lengths λ, with phase v_ϕ and group v_g velocities of imposed waves.

spatial arrangement on the wave energy distribution, three types of experiments were run:

- varying the number $\mathcal{R}$ of rows, for fixed l and d,
- varying the distance l, for fixed d and $\mathcal{R}$,
- varying the distance d, for fixed l and $\mathcal{R}$.

Values of l and d were varied between $0.06 - 1.11\lambda$ and $0.03 - 0.92\lambda$, respectively. For each frequency, a reference case without blades (*Control*) was also run. A summary of the configurations is listed in Table 4.4. To investigate the role of flexibility on wave energy damping, additional experiments were conducted using rigid blades of the same dimensions, cut from 2 mm thick plexiglas sheets. All configurations presented in Table 4.4 were repeated with the rigid blades, along with an equivalent flexible staggered configuration for which the space l was kept identical. An example of all three cases for configuration R_4 is presented in Figure 4.16 (b). All experiments were run using the same base board, 65.5cm wide by 35cm long. For both l and d configurations, the total number of blades was fixed to 32 (8 blades per row) in order to separate the influence of these two space parameters independently from the number of blades.

A partially submerged configuration was chosen in order to allow for maximal interaction between the incoming waves and the blades. With a water depth of 8 cm, the submergence ratio was $h_s/h = 1.38$. The average incident wave amplitude η varied between 0.7 and 3.5 mm, depending on the frequency of the wave-maker. Finally, the distance δ separating the edge of the array from the edge of the wave tank was chosen to be sufficiently large compared to the water wave lengths, in order to avoid strong lateral reflections and any subsequent diffraction within the array (c.f. Table 4.4).

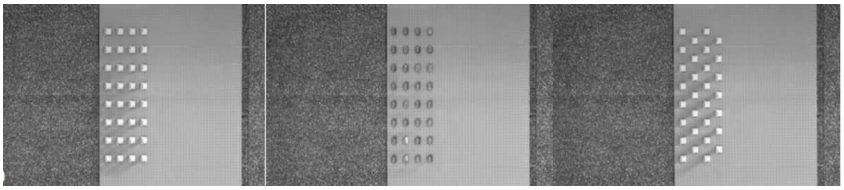

FIGURE 4.16: Examples of the experimental set-up used for flexible aligned (left), rigid (center) and flexible staggered cases (right).

Given the dimensions of our blades and the amplitudes of our waves, the values of KC produced in the laboratory range between [0.3-1.57] (c.f. Table 4.3). In real seas, wave amplitudes range between [1-5m], which would impose a width of $\mathcal{O}$(10-20)m for real scale blades, in order to maintain similar values of KC. Such sizes are coherent with the dimensions of existing WECs, such as Aquamarine's Oyster device which is 18 m wide (Sarkar, Renzi, and Dias, 2014). Additionally, from Table 4.3, the Reynolds numbers R_n range from $R_n = [286 - 770]$.

Name	$\mathcal{R}$	$l[cm]$	$d[cm]$	l/λ	d/λ	δ/λ
1. Increasing number of rows						
R_1	1	3.2	3.4	[0.09 - 0.44]	[0.09 - 0.47]	[1.57 - 7.74]
R_2	2					
R_3	3					
R_4	4					
2. Increasing distance l						
l_1	4	2.4	3.4	[0.06 - 0.33]	[0.09 - 0.47]	[1.57 - 7.74]
l_2		3.2		[0.09 - 0.44]		
l_3		4.0		[0.11 - 0.55]		
l_4		4.8		[0.13 - 0.67]		
l_5		5.6		[0.15 - 0.78]		
l_6		6.4		[0.18 - 0.89]		
l_7		7.2		[0.20 - 1.00]		
l_8		8.0		[0.22 - 1.11]		
3. Increasing distance d						
d_1	4	2.4	1.0	[0.06 - 0.33]	[0.03 - 0.14]	[1.87 - 9.20]
d_2			1.8		[0.05 - 0.25]	[1.77 - 8.72]
d_3			2.6		[0.07 - 0.36]	[1.67 - 8.23]
d_4			3.4		[0.09 - 0.47]	[1.57 - 7.74]
d_5			4.2		[0.11 - 0.58]	[1.47 - 7.25]
d_6			5.0		[0.14 - 0.69]	[1.37 - 6.76]
d_7			5.8		[0.16 - 0.81]	[1.17 - 6.27]
d_8			6.6		[0.18 - 0.92]	[1.17 - 5.78]

TABLE 4.4: Configurations tested for varying number of rows, distance l in between rows, and distance d within rows.

4.2.2 Results - Wave map analysis

Reflection and transmission coefficients were calculated from the treated surface wave maps, as described in Chapter 3, by means of a complex curve fitting of the transverse average of the wave. In this experimental set-up, however, the canal width exceeds that of the array by a distance δ (c.f. Table 4.4). It is therefore worth noting that given the range of frequencies tested and the variable array widths, diffraction will be visible for cases where the total width of the array is of the order $\mathcal{O}(\lambda)$. It is the case, for example, for configuration d_1 at the resonant frequency 4.5Hz. Nonetheless, these effects are limited, with a resulting error on the transmission coefficients of approximately 3%.

Reflection and transmission coefficients are plotted in Figure 4.17 over the entire range of tested frequencies for configuration l_2 (aligned, flexible case). The results show a decrease in transmission with a minimal value at 4.5Hz, which corresponds to the natural resonant frequency of the blades measured in water. Therefore, the results for all configurations were chosen to be analysed at two bounding frequencies: 2.5Hz (Figure 4.18) and 4.5Hz (Figure 4.19). All configurations presented in Table 4.4 are shown, and results are plotted as a function of the varied parameter: increasing number of blades $\mathcal{N}$, and increasing spacings d and l, both scaled to λ.

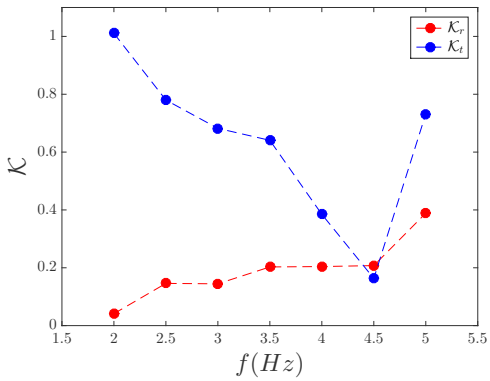

FIGURE 4.17: Measured reflection and transmission coefficients for configuration l_2 as a function of frequency.

Results show that all configurations follow similar trends with a constant offset in the transmission coefficients between rigid (dashed lines) and flexible cases (solid lines). The value of this offset is measured around 0.2 for frequency 2.5Hz and increases to reach values of up to 0.6 for frequency 4.5Hz, thus showing that the flexible arrays can reduce wave damping by an average of around 40% compared to rigid ones (c.f. Figure 4.19). This global observation highlights the role played by flexibility regarding wave energy transmission. It is found that as the imposed wave frequency tends towards the natural resonant frequency of the blades, they transmit less then their rigid equivalent, regardless of the spatial arrangement. This is expected since the oscillations of the blades are largest at their resonant frequency. Details on the mechanics of these oscillations will be presented in the dedicated section below. However, it is noticed that this distinction is not true regarding reflection. In fact, the curves for all three cases (rigid (dashed line), flexible aligned (squares, solid line) and flexible staggered (circles, solid line)) remain very close together, for both imposed frequencies (see Figures 4.18 and 4.19), which suggests that flexibility has little influence on the reflection of waves. This first observation is consistent with the variations of K_r and K_t for a single row previously discussed, as shown in

Figure 4.7. There again, no difference was noticed between rigid and flexible blades for the reflection, and the difference in transmission is seen to increase linearly with the total number of blades (each additional row adding to the total viscous damping of the array). Furthermore, as previously observed, it is seen that the results of transmission and reflection coefficients are very similar between aligned and staggered configurations. In fact, most curves match exactly. This is unexpected given that in a staggered configuration, a larger number of blades are directly facing the incident wave front. Yet, this result shows that the parameter l dominates the interference between rows, rather than the lateral offset of the neighbouring rows. The results

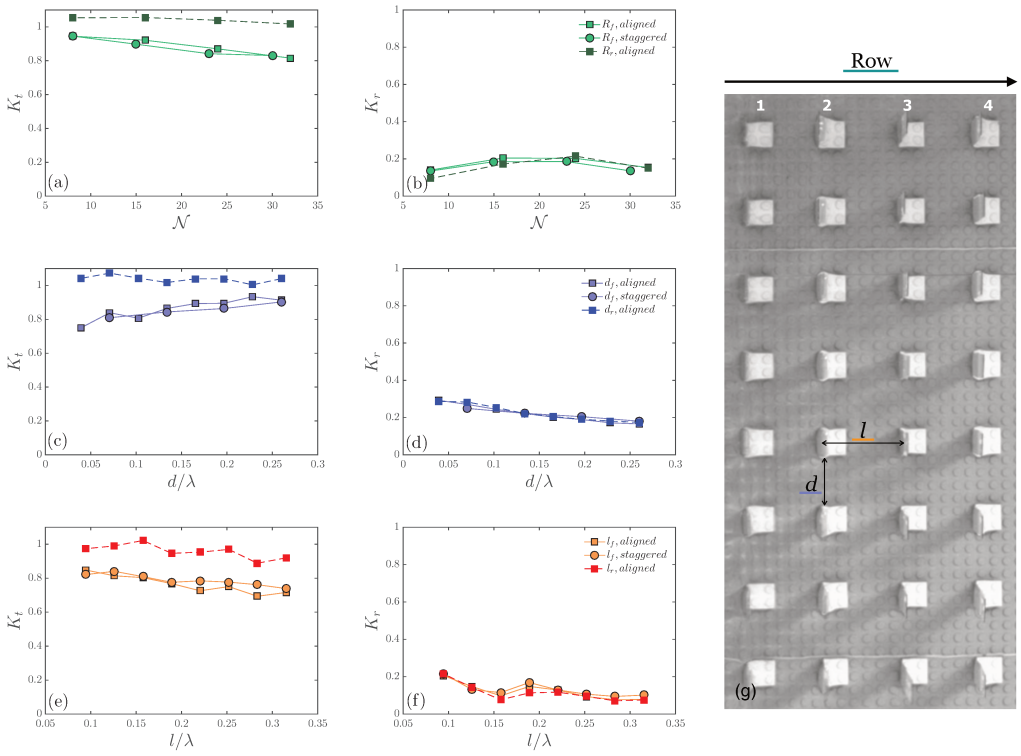

FIGURE 4.18: Measured reflection and transmission coefficients for all configurations, far from resonant frequency of blades ($f = 2.5Hz$).

for frequency 2.5Hz (c.f. Figure 4.18) show varying tendencies for each configuration. The transmission coefficient is seen to decrease as $\mathcal{N}$ increases (Figure 4.18 (a)), stabilising towards a minimal value of 0.8 beyond $\mathcal{N}$=24 (configuration R_3). In parallel, a decrease in reflection is noticed at R_3 (Figure 4.18 (b)). This suggests that maximal efficiency regarding wave attenuation is reached with an array composed of 3 rows. In contrast, the transmission coefficient K_t for the flexible cases increases linearly with the spacing d (Figure 4.18 (c)), while the reflection coefficient K_r decreases (Figure 4.18 (d)). Both observations imply that as the array spreads out, i.e. d becomes larger, the waves interact less with the array leading to lower damping and reflection. Finally, transmission seems to remain more or less stable, regardless of the size of l (figure 4.18 (e)), with values that fluctuate around 0.8 for the flexible cases. Similarly, reflection coefficients oscillate around 0.1 for all cases (figure 4.18 (f)). Parameter d is therefore more influential than l at that frequency.

Figure 4.19 presents the same results for a wave frequency matching the natural frequency of the blades (4.5Hz). As seen previously, increasing the number of rows

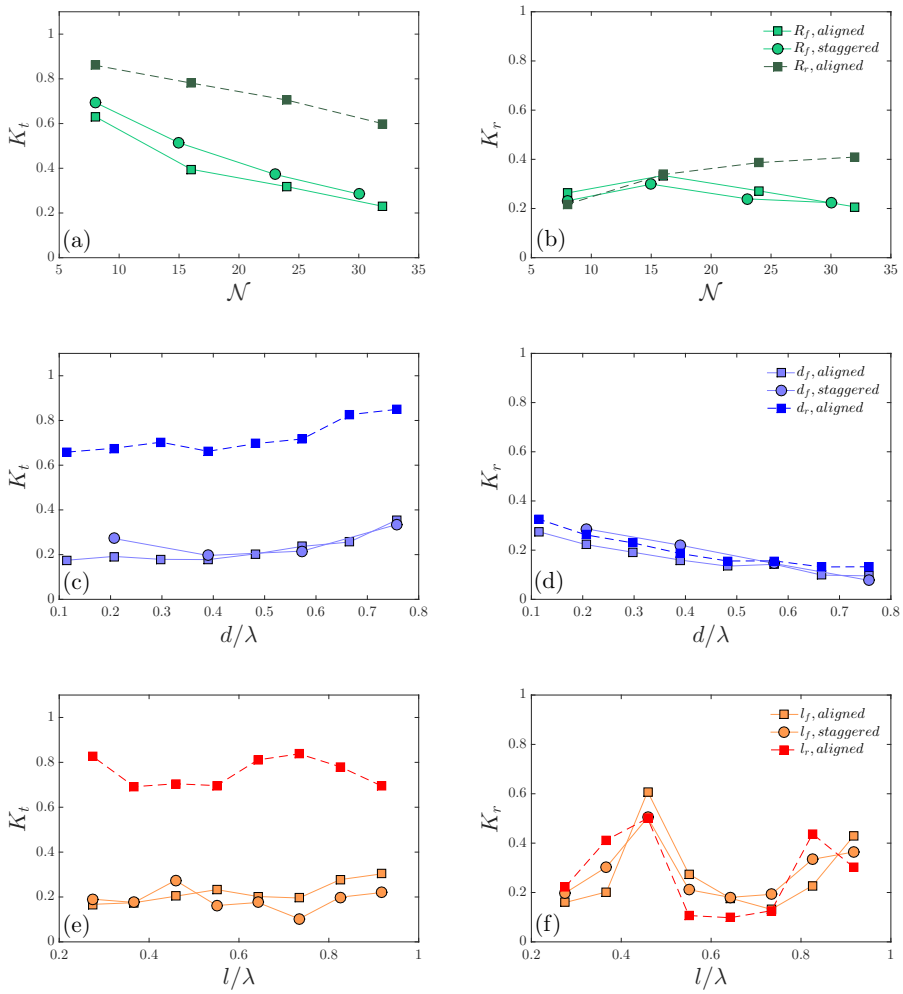

FIGURE 4.19: Measured reflection and transmission coefficients for all configurations, at resonant frequency of blades ($f = 4.5Hz$).

leads to a decrease in transmission (Figure 4.19 (a)), reducing it by 10% for the rigid case and by 20% for the flexible cases. The collective behaviour of the flexible array would therefore benefit wave damping. An inflexion point at R_2 is noticed here again for K_r values of both flexible cases (Figure 4.19 (b)), also pointing towards an effect due to the interactions between blades. The mechanical behaviour of the array will be further discussed in the following section.

As before, increasing d increases transmission coefficients while the reflection coefficients decrease (Figure 4.19 (c) and (d)). It should be noted, however, that the increase in K_t is not quite linear and appears to sharpen starting from d/λ=0.5 for both flexible cases. In contrast, the reflection decreases sharply for lower values of d. This implies that this specific spacing serves as a point of inflexion regarding the dominance of transmission versus reflection. In the case of a flexible aligned configuration, transmission overtakes reflection beyond a spacing of $d < \lambda/2$.

Finally, increasing the size of l shows oscillatory variations in both transmission and reflection (Figure 4.19 (e) and (f)), with higher points near $l/\lambda = \{0.5; 1\}$ and

lower K_t points near $l/\lambda = \{0.25; 0.75\}$, for flexible cases. The oscillations in K_t are mirrored in the case of rigid blades. This is due to the interference between incident and reflected waves within the array. Indeed, when a regular arrangement of obstacles such as ours in subject to incoming waves, crystallographic behaviours can be considered. Bragg's law states the condition for constructive or destructive interferences of incident waves as $2l \sin\theta = n\lambda$, with l being the spacing between two lattices and θ the incident angle of waves. When n is an integer, then the reflected waves are perfectly in phase with the incident wave, thereby building large amplitudes in the resulting waves. In our case, $\theta = \pi/2$, which simplifies the condition as $n = 2l/\lambda$. We therefore have $n = 1$ for l/λ=0.5 and, similarly, $n = 2$ for l/λ=1. This explains the large reflection coefficients obtained for these two points. In the case of rigid blades, these oscillations are mirrored in the transmission coefficient, due to the fact that this large reflected energy is not transmitted. While the same observations can be made for the flexible cases regarding reflection, this does not hold for transmission. In this case, although the resulting amplitudes are larger, the wave forcing is in fact lower leading to reduced blade oscillations (see Figure 4.22). The reduction due to increased reflection is limited by the reduced blade oscillations, i.e. reduced energy absorption. The analysis of the blade oscillations will be further discussed in the next section.

We now look at the variations of K_r and K_t over all tested frequencies. Figures 4.20 (a-c) plots reflection (red dots) and transmission (blue dots) coefficients for flexible aligned (a), rigid (b), and flexible staggered (c) configurations, for all frequencies, as a function of parameter l/λ. Bragg peaks are very clearly apparent for all cases of K_r (identified by means of black arrows), while mirrored troughs appear clearly for transmission coefficients in the case of rigid arrays only. The peaks are much less clear for flexible configurations. Plot (d) presents the reflection coefficients of all three array types, as a function of l/λ, which all fall on the same curve. Reflection peaks are therefore found to depend on array geometry, rather than on blade flexibility, unlike transmission. Plots (e) and (f) focus on the transmission coefficients, plotted for flexible aligned (light blue dots), rigid (dark blue dots) and flexible staggered (green dots) cases, as a function of array spacing l/λ (e) and imposed wave frequency f (f). The wide scatter of the collected data in (e) demonstrate there is no clear dependency on the geometrical pattern chosen for the array configuration. However, the dependence on frequency is evident in plot (f). The clear separation between rigid values and flexible values is found to increase as the frequency tends towards the system resonance. Notice the global decrease in transmission coefficients, also in the rigid cases. This is due to varying diffraction effects: as frequency increases and wave length decreases, the diffraction number $\mathcal{D}$ increases as well, since our object size is kept constant. Also, wave energy power decreases with wave frequency (c.f. Eq. 2.22 in Chapter 2), leading to more effective arrays. Smith and Bayliss-Smith (1998) found wave damping through kelp forests to be more effective at higher frequencies.

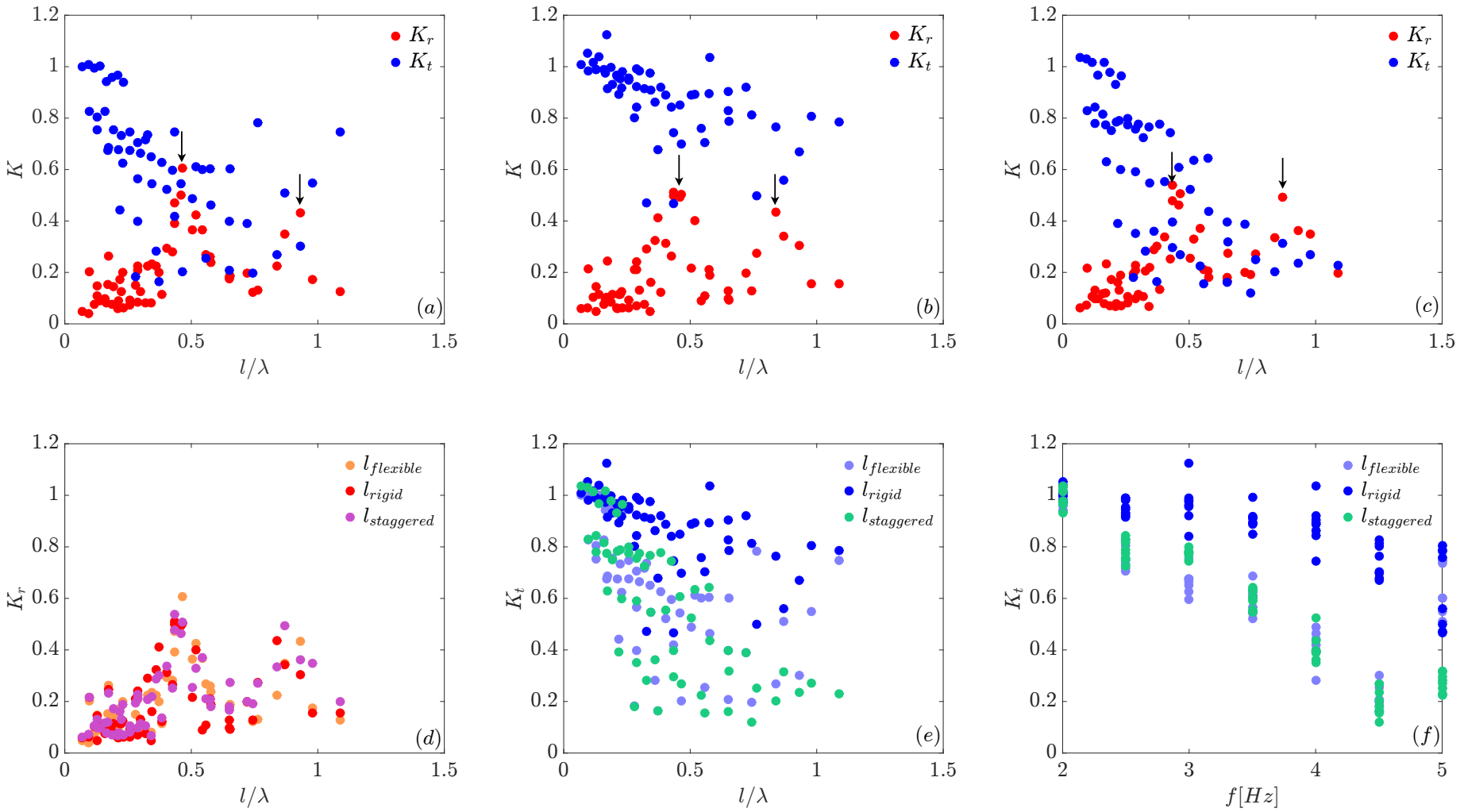

FIGURE 4.20: Measured reflection and transmission coefficients for all configurations, over all frequencies, as a function of l/λ. Flexible aligned (a), rigid aligned (b) and flexible staggered (c) configurations are compared, and K_r (d), K_t (e) are plotted against l/λ and frequency (f).

4.2.3 Results - Array damping analysis

The second part of the experiment involved tracking the movement of the blades. Both the amplitude and the phase of each blade oscillation was determined from the spatio-temporal tracking method described in Chapter 3. The time shifts Δt of the blade oscillation peaks were directly measured and converted into phase shifts, with $\phi_{shift} = (\Delta t/T)2\pi$, where T is the oscillation period in seconds (see Figure 4.21 (a)). These oscillation time delays Δt were compared to the time taken for the wave to travel between blades $t = l/v_\phi$, where v_ϕ is the phase velocity of the wave, equal to $f\lambda$. Figure 4.21 (b) shows this relationship is linear, which suggests that the phase shifts observed between rows depend directly on the time needed for the waves to travel between them.

The oscillation amplitudes X were also directly measured for each blade and the average $\bar{X}$ of each row is presented in Figure 4.22, for all tests. In general, results show that for all cases, amplitudes $\bar{X}$ are largest in the first row, and decrease as we travel further into the array, due to both natural dissipation and to the wave interaction with each row.

Figures 4.22 (a) and (b) show the variation of these amplitudes as a function of the number of rows for configurations $R_{aligned}$ and $R_{staggered}$, respectively. In the case of an aligned configuration, the average amplitude of each row decreases while it remains constant for the staggered configuration, regardless of the number of rows present. This highlights the influence of the reflected waves within the array, depending on their longitudinal alignment. Indeed, it is suggested by Sarkar, Renzi, and Dias, 2014 that for inline configurations, the presence of neighbouring oscillating structures in the x-direction (longitudinal direction) provides strong destructive interference, leading to limited oscillating amplitudes. This is coherent with our observation.

The following two Figures 4.22 (c) and (d) plot the mean variations of amplitudes for each row belonging to configurations $d_{aligned}$ and $d_{staggered}$, respectively. Both arrangements provide similar results, demonstrating that amplitudes increase with spacing d. Once again, Sarkar, Renzi, and Dias, 2014 predict that as oscillating structures are spread out, these tend to behave like individual systems with larger movements. Yet, it should be noted that this increase is slowed down as d becomes larger, especially in the case of a staggered arrangement (Figure 4.22 (d)). This lower slope mirrors the steeper slope previously observed in the transmission coefficients (c.f. Figure 4.19 (c)), found to occur for $d > \lambda/2$.

Finally, the amplitude variations for configurations $l_{aligned}$ and $l_{staggered}$ are presented in Figures 4.22 (e) and (f), respectively. One can notice very similar behaviour between the two arrangements, with a narrow point of oscillation at $l = \lambda/2$. This confirms the observations made for both transmission and reflection coefficients in Figures 4.19 (e) and (f). As mentioned before, the corresponding spatial arrangement of the blades cause wave interferences within the array to be detrimental towards blade oscillations.

Absorbed power From these oscillations, we are now able to evaluate the amount of energy dissipated internally and externally due to blade oscillations. Let us first evaluate the internal damping, which corresponds to the amount of energy that is stored through the mechanical bending of the blades and that could potentially be harvested. As explained in Chapter 3, the internal dissipated power $\mathcal{P}_a$ can be calculated from Eq. 3.14, based on the measured damping coefficient Γ_{int} (recall Figure 3.18) and on the blade tip velocity $\dot{X}$. The latter can be easily deduced from the

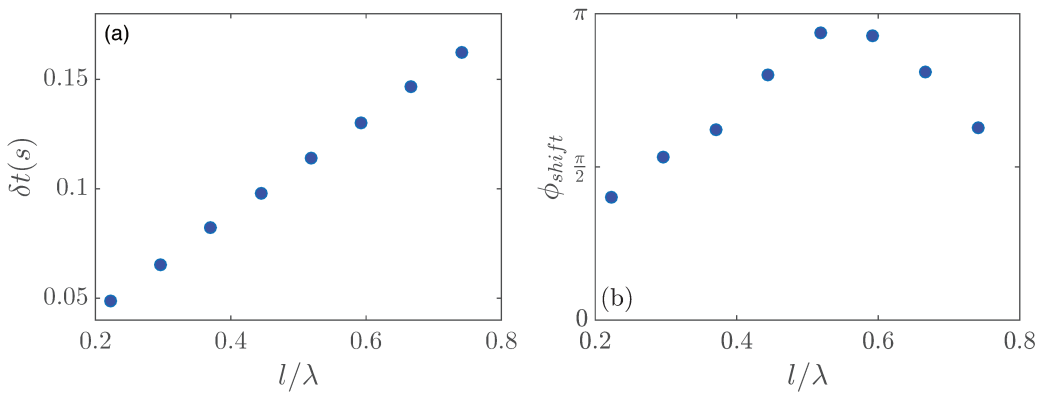

FIGURE 4.21: Time delay (a) and phase shift (b) between rows of the array.

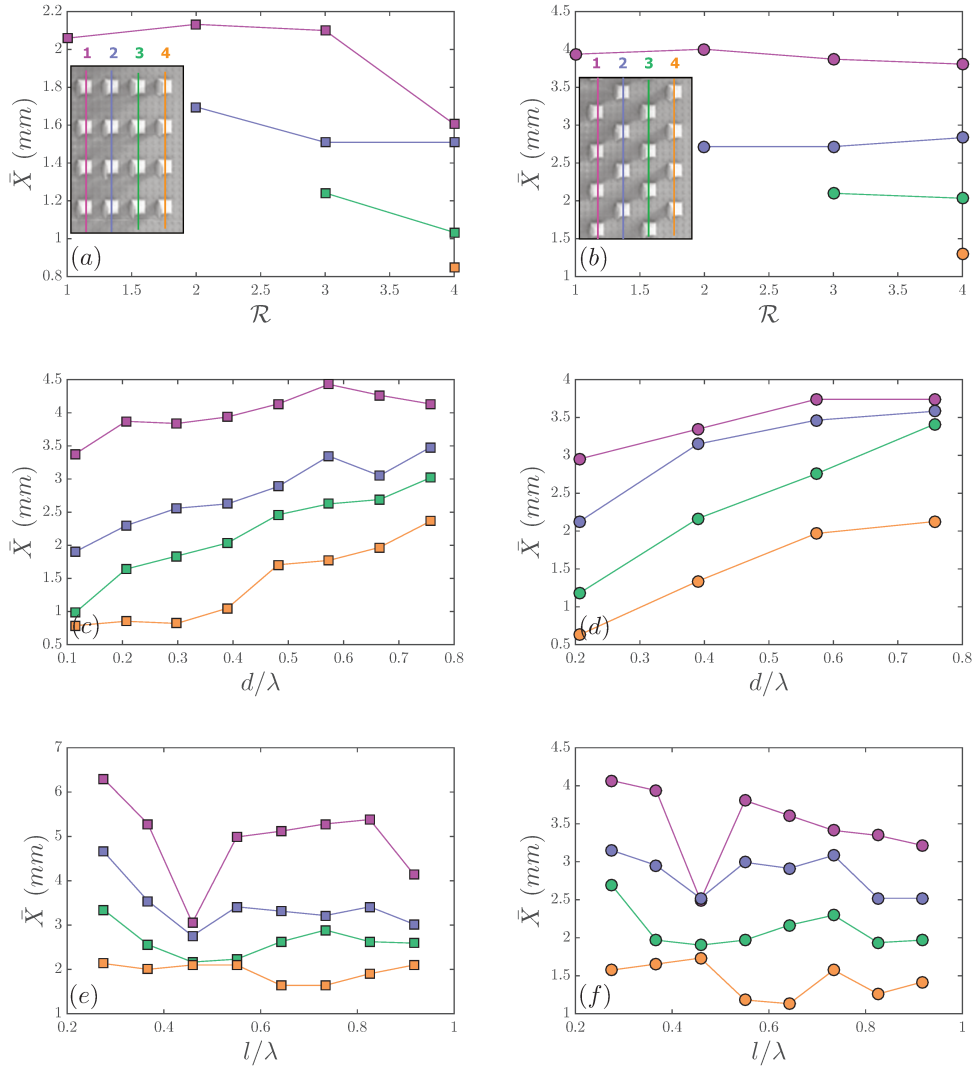

FIGURE 4.22: Average row oscillations for all configurations tested.

spatio-temporal plots of tip oscillations. The total internal power damped through the entire array $\mathcal{P}_a$ can then be calculated by summing that of the individual structures, such that:

$$\mathcal{P}_a = \sum_{i=1}^{\mathcal{N}} (\mathcal{P}_a)_i \tag{4.1}$$

where $\mathcal{N}$ is the total number of blades.

This quantity can then be compared to the incoming wave power. Equation 2.22 provides the expression of wave energy flux per unit width over one period. Therefore, the total power seen by the blades will be:

$$\mathcal{P}_{tot} = P_w \cdot W \tag{4.2}$$

where W is the total width occupied by one row of blades. It is then possible to estimate the proportion of the incoming power that was absorbed by the array using a coefficient $K_a = \mathcal{P}_a / \mathcal{P}_{tot}$. The results of these calculations are presented in Figure

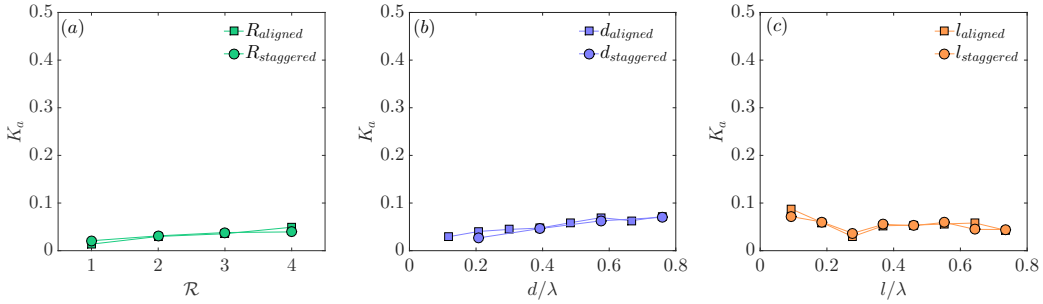

FIGURE 4.23: Calculated energy absorption K_a coefficients for configurations R (a), d (b), and l (c). Results of aligned and staggered patterns are represented by square and circle markers, respectively.

4.23 for all configurations at the excitation frequency of 4.5Hz. The total amount of absorbed power depends, of course, on the total number of blades present in the array and the results for configuration R in Figures 4.23 (a) show a maximal value of around 10% of absorbed power. Similarly, increasing d also shows an increase in absorbed and dissipated power within the array, due to the increase in oscillation amplitudes seen in Figure 4.22 (b) and (c). It is also noted that unlike wave attenuation, increasing d favours energy absorption. Finally, recalling Figure 4.19 (e) and (f), the transmission coefficients curves for configurations l and $l_{staggered}$ mirror the tendencies seen here for K_a (Figure 4.23 (e)). Once again, the troughs found at l/λ=0.5 are caused by the lower amplitudes of oscillation of the blades due to wave interferences within the array. This lower amount of energy dissipation is therefore seen as a higher amount of transmission in Figure 4.19.

External damping Internal absorption is seen to reach maximal values of around 10% of the total incoming energy of waves. Yet, these flexible arrays are found to attenuate waves by much more than that, due to an additional external damping, which represents the energy lost to the fluid through heat and vortices.
In order to evaluate this quantity, we model the drag using the following expression (c.f. Chapters 2 and 3):

$$\mathcal{P}_d = \frac{1}{2} \rho_w C_D A \cdot u_r^3 \tag{4.3}$$

where $A = D \cdot h$ corresponds to the projected area facing the incoming flow, C_D is the drag coefficient of the obstacle, and u_r is the relative velocity between the fluid particles and the blades. We choose to use a drag coefficient equal to 2, typically used for oscillating plates. We estimate the relative velocity to be $u_r \approx \sqrt{2}u$ due to the phase shift between the two compared velocities (see Appendix B). This assumes that the blades oscillate with an amplitude of the same order as that of the wave particle velocities. Note that the same calculation can be performed for the rigid case, with $u_r = u$ instead. The corresponding energy coefficient can then be defined as $\mathcal{E}_{drag} = K_d = \mathcal{P}_d/\mathcal{P}_{tot}$.

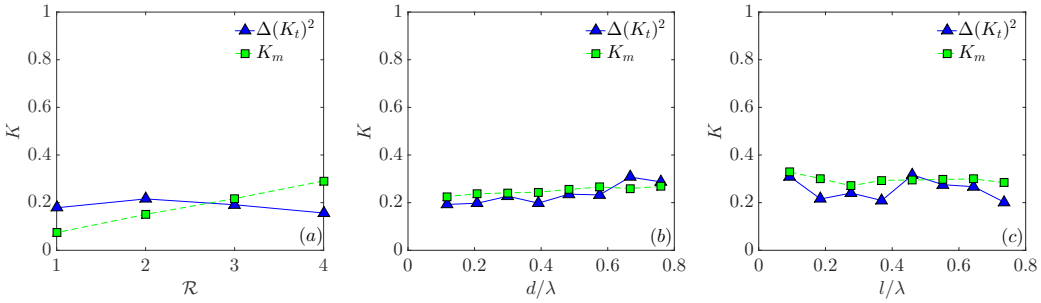

FIGURE 4.24: Comparison of the additional wave attenuation and the total mechanical damping due to blade oscillations. The difference in transmitted energy $\Delta(K_t^2)$ between the rigid and the flexible arrays are compared to the total additional damping energy of the oscillating motion of the blades, for increasing number of rows (a), increasing spacing d (b) and increasing spacing l (c).

We can now evaluate the effect of flexibility on the distribution of energy. Compared to the rigid case, the flexible blade further reduces the transmitted energy through its oscillating motion by absorbing part of it through internal damping and increasing the drag losses. The latter is quantified by $K_d - K_{d_{rigid}}$, where $K_{d_{rigid}}$ corresponds to the drag losses for the rigid case, i.e. for which $u_r = u$. The the sum of these two quantities therefore represents the total added dissipation K_m caused by the motion of the blades. Given that reflection was seen to be almost identical between rigid and flexible cases, we therefore expect the reduced transmission to match to additional dissipation. This is verified as plotted in Figure 4.24, where we compare the difference in transmitted energies $\Delta(K_t^2) = K_{t_{rigid}}^2 - K_{t_{flexible}}^2$ to the total additional dissipation K_m of the waves from internal damping and external drag, calculated as $K_m = K_a + K_d - K_{d_{rigid}}$.

We can see that the mechanical energy dissipation matches the difference in transmitted energies, with very similar variations, as described by our model. It should be reminded that both quantities rely on two separate measurement methods and, therefore, are bound to demonstrate variations due to experimental errors, as seen here. Nonetheless, the results suggest that our model provides a good description of the system.

Energy balance We can now combine all measured quantities in order to evaluate the total energy distribution in our system. Recalling Eq. 2.46 from Chapter 2, we can now write the normalised energy balance of our system as:

$$\mathcal{E}_{tot} = \mathcal{E}_r + \mathcal{E}_t + \mathcal{E}_{damping} + \mathcal{E}_{drag} \tag{4.4}$$

$$\mathcal{E}_{tot} = \tilde{K}_r^2 + \tilde{K}_t^2 + \tilde{K}_a + \tilde{K}_d \tag{4.5}$$

where $\mathcal{E}_r$ is the reflected energy, $\mathcal{E}_t$ is the transmitted energy, $\mathcal{E}_{damping}$ is the damped energy through blade oscillations, $\mathcal{E}_{drag}$ is the energy lost through flow detachment behind our objects. All energy quantities have been normalised by the transmitted energy term K_{t0}^2 without obstacles, in order to exclude the natural dissipation of waves from the energy balance. The sum of all energies is plotted in Figure 4.25 below by means of stack diagram. The rigid cases are presented on the left-hand side while those on corresponding to the flexible arrays are shown in the right-hand-side plots. $\mathcal{E}_r$, $\mathcal{E}_t$, $\mathcal{E}_{damping}$ and $\mathcal{E}_{drag}$ are shown in red, blue, green and orange colours, respectively.

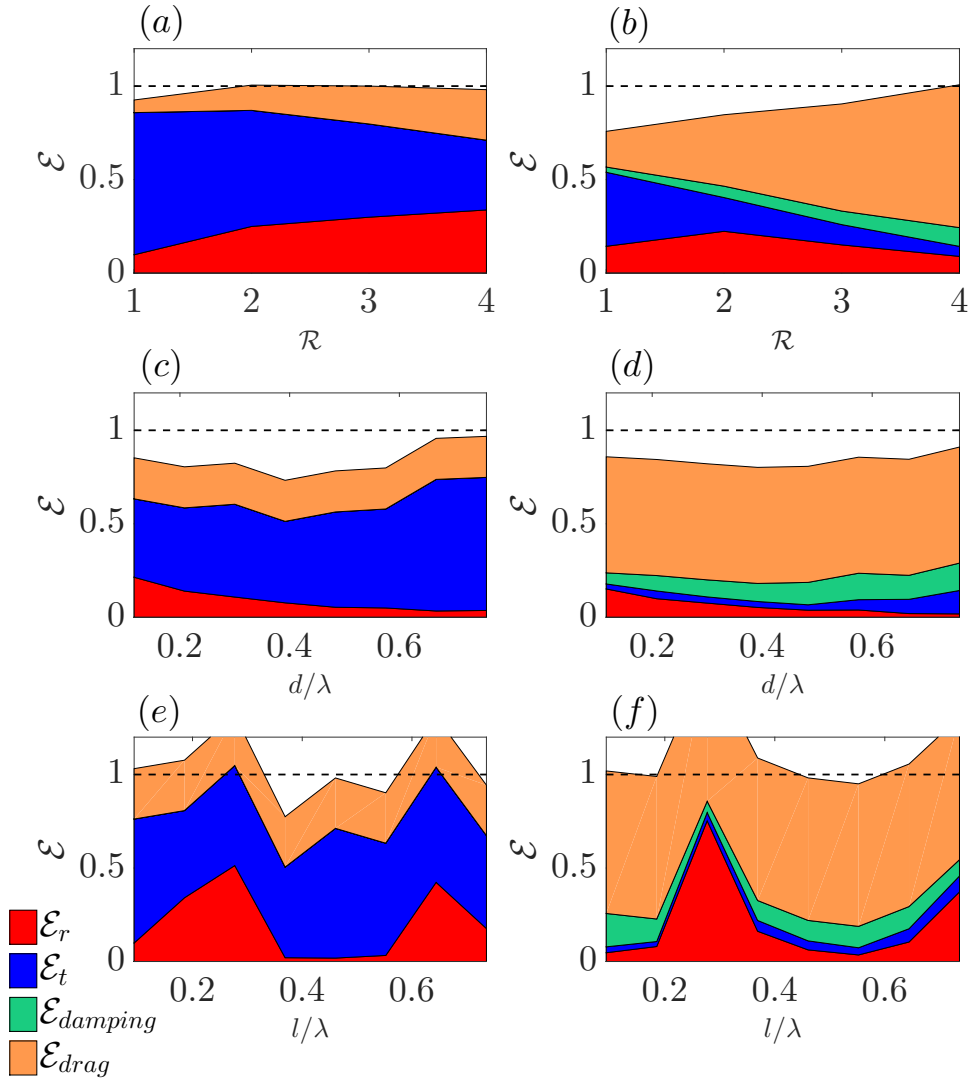

FIGURE 4.25: Energy balance for rigid (left) and flexible aligned (right) configurations of increasing rows (a) and (b), increasing spacing d (c) and (d), and increasing spacing l (e) and (f). The normalised reflection $\mathcal{E}_r$, transmitted $\mathcal{E}_t$, absorbed $\mathcal{E}_{damping}$ and dissipated $\mathcal{E}_{drag}$ energy shared are represented in red, blue, green and orange stacks, respectively. An empirical model was used for the estimation of $\mathcal{E}_{drag}$, based on Eq. 4.3

The results show satisfactory estimations of the energy distribution in our arrays,

with values close to 1 for most cases. Deviations are however noticeable especially where the reflection Bragg peaks occur, with values largely exceeding 1. This is thought to be caused by an over-estimation of the relative velocities in those cases. It is noted that the orbital velocity amplitudes u_a used to calculate the velocity u in the drag models are based on the known amplitudes of incoming waves, with an added dissipation coefficient to correct for the natural wave decay as it travels through the array. Yet, the simple presence of the array modifies the wave field, thereby causing many interferences through the multiple scattered waves, as presented in Chapter 2. Therefore, the water particle velocities can no longer be considered from the unique incoming wave, but should be deduced from all scattered waves. Our estimations of u would therefore be insufficient.

4.3 Conclusion

In this chapter, we have explored by means of experiments the influence of spatial parameters and configuration patterns on the energy distribution of monochromatic surface waves in an array of flexible blades. We first studied the influence of the array on the wave field (4.2.2), from which the results showed a clear dependence of reflection on array spacing, with Bragg peaks appearing for patterns where $l/\lambda = n\frac{1}{2}$, n being an integer. The peak was found for all tested frequencies, with decreasing intensity as the imposed frequencies were moved further away from the system's resonant frequency. While these peaks were mirrored in transmission for the rigid cases, this was found to be much less evident for flexible arrays. Finally, little difference was found between aligned and staggered patterns, which is thought to be due to the unidirectional bending of the blades. The analysis was completed by studying the blade mechanics (4.2.3). The oscillations of the blades were found to vary strongly depending on array configurations, with increasing values for each row found for increasing d, and variations mirroring the Bragg peaks in reflection when l is increased. These variations were sometimes found to contradict variations in transmission, with, for example, both oscillations and transmission increasing together. The associated mechanical damping was found to match the difference in wave attenuation between rigid and flexible cases, thereby suggesting that our model provides a satisfying description of our system. It is thus understood that the added damping due to the elastic nature of the blades stems from a dual phenomenon, with deflection causing a transfer between the inertial hydrodynamic forces and the blade's elastic restoring force, while also causing an increase in viscous hydrodynamic forces due to the larger relative velocity between the blade and the surrounding fluid. Both effects are maximised at resonance, therfore leading to maximal wave attenuation. Finally, while the total energy balance approached a total of 1 for most results, large deviations were noticed specifically around the Bragg peaks of reflection., possibly due to incorrect evaluations of the relative velocities. These are in fact dependent on the complex structure of wave field interferences. In the following chapter, we look to better understand the interactions involved in our system and the variations observed in our experiments by means of a 1D wave interference model.

Chapter 5

Modelling

In the previous experimental study, it was seen that the interaction between the flexible array and surface water waves causes complex mechanisms, arising from both array geometry and blade oscillations, making it difficult to conclude on an ideal array configuration when looking to increase both damping and absorption through mechanical bending. Indeed, dense and compact arrays (small d) tend to reduce transmission but also reduce blade oscillations and, therefore, energy absorption. On the other hand, reflection was seen to be highest for specific longitudinal spacing l, compared to λ. In those cases, the transmission is yet not equally diminished, since the blades are found to oscillate at a strongly reduced amplitude X. The role played by array geometry therefore seems to cause opposing effects regarding transmission and power absorption, which we do not yet understand. These observations raise two questions: why do reflection and dissipation follow opposing trends? Is there an optimal configuration that leads to both minimal transmission and maximal absorption? In this chapter, we aim to answer these questions by building a simplified interference model of transmitted and reflected waves, and their influence on array oscillations. Starting with local interactions of minimal arrays, we develop the model for a full-sized array of variable internal spacings, so that both regular and irregular arrays can be studied.

5.1 1-D interference model

Let η_i be the incident wave with amplitude a, wave number k and angular frequency ω. As this wave travels through the array, it will interact with each row n of blades, which behave as obstacles transmitting part of the wave with a local coefficient t and reflecting another part with a local coefficient r. This is represented with the schematic below.

5.1.1 Local analysis

Forces Let us look further at the wave forces acting on a single row, starting with the front row. The Froude-Krylov force introduced in Chapter 2 describes the inertial force of the wave and is proportional to the acceleration of the wave particles. This is the driving force imposed by the incoming waves on our structures, and is expressed as (see Figure 5.2 (c) for illustration):

$$\underline{F}^{FK}(t) = m_d \cdot \underline{\ddot{u}}(t) \tag{5.1}$$

where m_d is the mass of the displaced fluid.

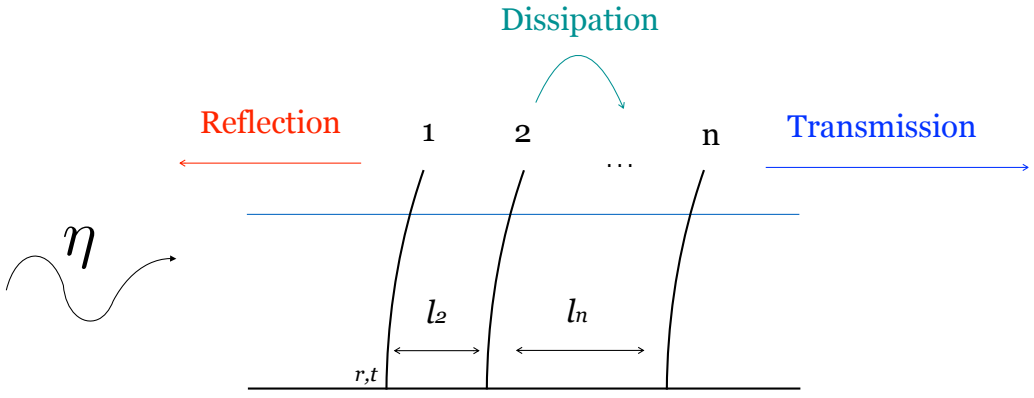

FIGURE 5.1: Sketch of the 1D interference model.

Recalling Eq. 2.14 from Chapter 2, this can be re-written as:

$$\underline{F}^{FK}(t) = m_d\omega \cdot [u_a \cdot \sin(kx - \omega t)] \cdot \underline{e}_x \tag{5.2}$$

where the horizontal particle velocity amplitude $u_a = a\omega \cdot \frac{\cosh k(h+z)}{\sinh kh}$. Therefore, for a constant depth h and at elevation $z = 0$ (point of interaction between the blade and the fluid), the force F^{FK} becomes directly proportional to $\eta = \Re\{\eta_z\}$, with a constant of proportionality $\mathcal{C}^{FK} = m_d\omega^2 \cdot \frac{\cosh k(h+z)}{\sinh kh}$. The magnitude of the force can therefore be written as follows:

$$F^{FK}(t) = \left|\mathcal{C}^{FK} \cdot \eta_z\right| \tag{5.3}$$

where subscript $_z$ denotes the complex form of the wave, so that $\eta_z = e^{i(kx-\omega t)}$ represents the complex form of the travelling sinusoidal wave. The front row of the array is then subject to the sum of Froude-Krylov forces associated with all the waves that interact with it. In our 1D-case, we therefore only consider two directions of waves: incident and transmitted (η_i) waves traveling in the positive x-direction and reflected waves (η_r) traveling in the negative x-direction. The associated horizontal wave particle motions are illustrated in the Figure 5.2 (a-b) below (blue and red ellipses):

As explained in Chapter 2, two waves traveling in opposite directions force water particles to move in opposite circular trajectories. Taking incident wave $\eta_i = \Re\{ae^{i(kx-\omega t)}\}$ and reflected wave $\eta_r = \Re\{rae^{i(kx+\omega t)}\}$, the corresponding Froude-Krylov forces can be written as:

$$\underline{F}_i^{FK} = m_d\underline{\dot{u}}_i = \mathcal{C}^{FK} \cdot \eta_{i_z} \cdot \underline{e}_x \tag{5.4}$$

$$\underline{F}_r^{FK} = m_d\underline{\dot{u}}_r = \mathcal{C}^{FK} \cdot \eta_{r_z} \cdot -\underline{e}_x \tag{5.5}$$

where $\underline{e}_x$ is taken to be the unit vector in the positive x-direction. The direction of the force applied by η is thus determined by both its phase and its direction of propagation. Note that the Froude-Krylov force will simply be shifted by $\pm\pi/2$ from η. At any point in time, we take incident wave $\eta_i = \Re\{ae^{i(kx)}\}$ and reflected wave $\eta_r = \Re\{rae^{i(kx+\varphi)}\}$, where $\varphi = x\frac{2\pi}{\lambda}$ represents the phase shift between the two waves due to the distance x traveled by the reflected part of the incident wave. Substituting these expressions into equations 5.4 and 5.5, the total force $\underline{F}_{tot}^{FK}$ acting

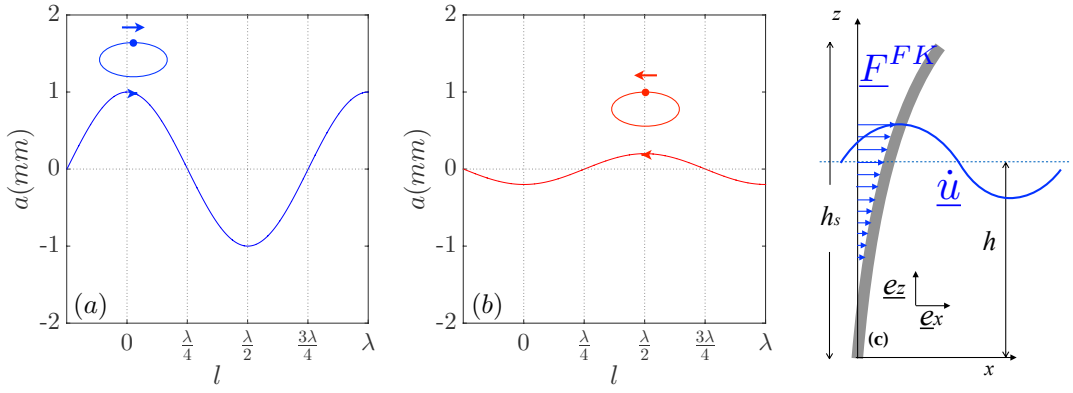

FIGURE 5.2: Illustration of incident (a) and reflected (b) waves with associated horizontal wave particle motion x. Sketch of the distributed Froude-Krylov wave force $\underline{F}^{FK}$ on a partially submerged flexible blade, which is proportional to the water particle accelerations $\underline{\dot{u}}$ (c).

on the front row becomes:

$$\underline{F}_{tot}^{FK} = \sum \underline{F}^{FK} = \underline{F}_{i}^{FK} + \underline{F}_{r}^{FK} = \mathcal{C}^{FK}(\eta_i - \eta_r) \cdot \underline{e}_x \tag{5.6}$$

$$\underline{F}_{tot}^{FK} = \mathcal{C}^{FK}\Re\{a(1 - re^{i\varphi})e^{i(kx)}\} \cdot \underline{e}_x \tag{5.7}$$

The resulting force magnitude is then written:

$$F_{tot}^{FK} = \left|\mathcal{C}^{FK} \cdot a(1 - re^{i\varphi}) \cdot e^{i(kx)}\right| = \mathcal{C}^{FK} \cdot \left|(1 - re^{i\varphi})\right| \cdot \eta_i \tag{5.8}$$

We can now understand how a spacing l between two back-to-back rows can influence each other's oscillations. An illustration of incident η_i and reflected η_r waves traveling through a 2-row array, is presented in Figure 5.3 below, along with resulting blade bending. The position x_i of the water particles based on the incident wave is also shown (orbital position on the blue circle). For a distance $l = \lambda/4$, the reflected wave will interfere with the incident wave at the location of the first row with a phase shift of $\varphi = 2l * 2\pi/\lambda = \pi$. Therefore $\eta_r = r\eta_i + \pi = -r\eta_i$. Since both waves travel in opposing directions, we have $F_1^{FK} = \mathcal{C}^{FK} \cdot (\eta_i - (-r\eta_i)) = \mathcal{C}^{FK} \cdot (1 + r)\eta_i$. The same result is found using equation 5.8: $F_{tot}^{FK} = \mathcal{C}^{FK} \cdot \left|(1 - re^{i\pi})\right| \cdot \eta_i = \mathcal{C}^{FK} \cdot (1 + r) \cdot |\eta_i|$.

The force associated with the reflected wave will act in the same direction as that of the incident wave so that their magnitudes add up leading to an increased resulting wave force onto the blade. Notice this principle follows that of Bragg's law regarding wave reflections with constructive force interferences occurring at $\varphi = n\pi + \frac{\pi}{2}$, where n a positive integer. The periodicity is shifted by $\pi/2$ compared with Bragg scattering, due to the fact that the opposite direction of propagation of the interfering waves. The added phase shift between the two is π, thereby causing constructive and destructive interferences with a shift of $\pi/2$. An example of this force interference is illustrated in Figure 5.4 below for an array of two rows, with represented water particle accelerations of incident (purple dotted lines) and reflected (orange dotted lines) waves, for each quarter of a period of the wave cycle, with associated force directions (arrows of the same colours).

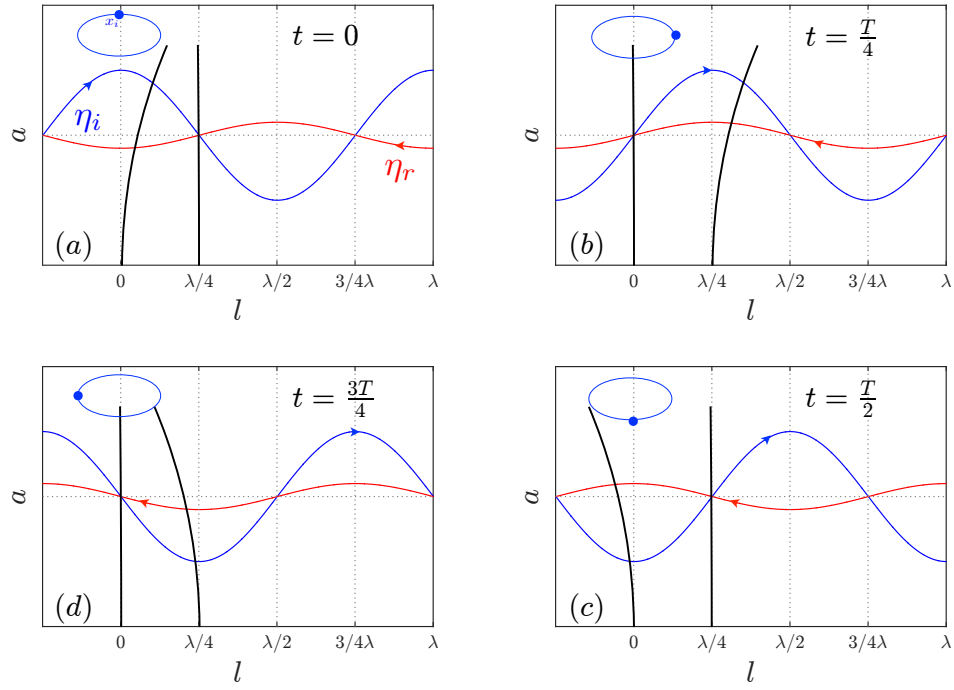

FIGURE 5.3: Illustration of incident η_i and reflected η_r traveling waves with associated horizontal water particle motion x_i of the incident wave (orbital position on the blue circle), for a 2-row array, separated by distance $l = \lambda/4$.). The resulting blade bending is also illustrated (vertical black lines).

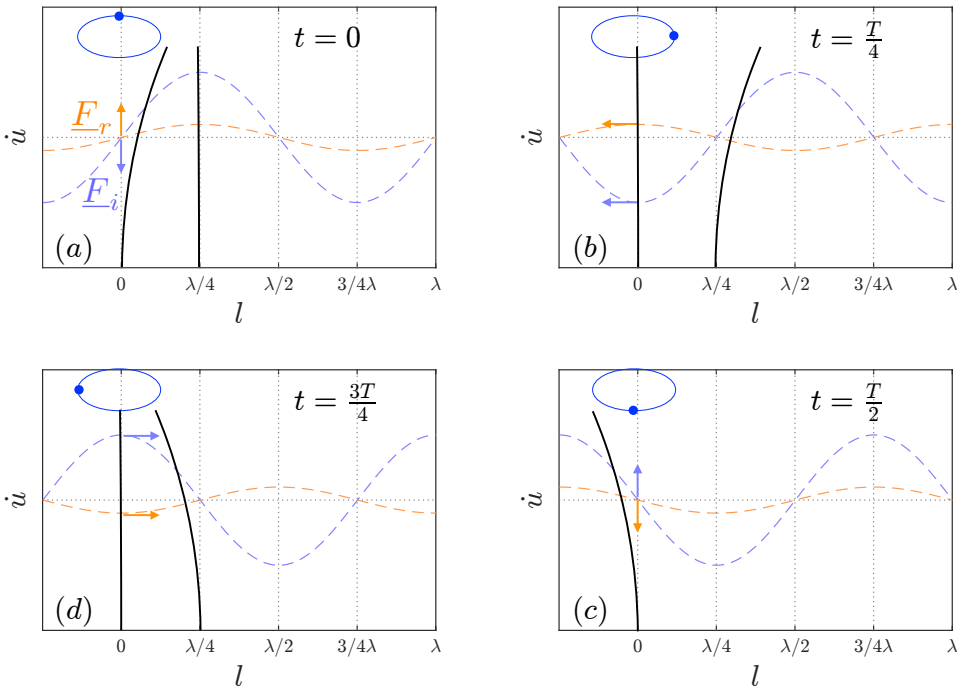

FIGURE 5.4: Illustration of incident (purple dotted lines) and reflected (orange dotted lines) wave accelerations, and associated wave force directions (arrows) acting on the front row of a 2-row array, separated by distance $l = \lambda/4$.

In the more general case, a row n of the array will be subject to the total wave force F_n^{FK} resulting from all interfering transmitted (or incident) and reflected waves acting on it. This is expressed as:

$$F_n^{FK} = \mathcal{C}^{FK}\mathcal{A}_n\eta_i \tag{5.9}$$
$$\mathcal{A}_n = |T_n - R_n| \tag{5.10}$$

where $\mathcal{A}_n$ represents the amplification factor due to wave interferences, with R_n the global reflection coefficient of all reflected waves acting on row n, and T_n the global transmission coefficient of all the transmitted (or incident) waves acting on it. Note that in the previous example the amplitude coefficient $\mathcal{A}_1 = \left|1 - re^{i\varphi}\right|$ (c.f. equation 5.8).

With ω and m_d assumed constant, the total force acting on any row is therefore directly proportional to the amplification coefficient. The analysis of array excitation forces can therefore be reduced to the analysis of all $\mathcal{A}_n$ coefficients of the individual rows.

Building interferences - 2rows We now test this theory for two small arrays composed of 2 and 3 rows only. Taking the case of an array composed of two rows only, we have:

$$\mathcal{A}_1 = |T_1 - R_1| = |1 - R_1| \tag{5.11}$$
$$\mathcal{A}_2 = |T_2 - R_2| = |T_2| \tag{5.12}$$

Developing R_1 with multiple reflections gives:

$$R_1 = rte^{i(2\varphi)} + r^3te^{i(4\varphi)} + ... + r^nte^{i((n+1)\varphi)} = t \cdot re^{i2\varphi}\sum_{k=0}^{N} r^{2n}e^{i2n\varphi} \tag{5.13}$$

$$R_1 = t \cdot re^{i2\varphi}\frac{1 - (r^2e^{i2\varphi})^n}{1 - r^2e^{i2\varphi}} = \frac{tre^{i2\varphi}}{1 - r^2e^{i2\varphi}} \tag{5.14}$$

Developing T_2 with multiple reflections gives:

$$T_2 = te^{i(\varphi)} + r^2te^{i(3\varphi)} + ... + r^nte^{i((n+1)\varphi)} = t \cdot e^{i\varphi}\sum_{n=0}^{N} r^{2n}e^{i2n\varphi} \tag{5.15}$$

$$T_2 = t \cdot e^{i\varphi}\frac{1 - (r^2e^{i2\varphi})^n}{1 - r^2e^{i2\varphi}} = \frac{te^{i\varphi}}{1 - r^2e^{i2\varphi}} \tag{5.16}$$

Substituting into equations 5.11 and 5.12, we now have:

$$\mathcal{A}_1 = \left|1 - \frac{tre^{i2\varphi}}{1 - r^2e^{i2\varphi}}\right| \tag{5.17}$$

$$\mathcal{A}_2 = \left|\frac{te^{i\varphi}}{1 - r^2e^{i2\varphi}}\right| \tag{5.18}$$

Building interferences - 3 rows We follow the same method for the case of a 3 row array. Amplification factors for each row are expressed as:

$$\mathcal{A}_1 = |1 - (R_{12} + R_{13})| \tag{5.19}$$
$$\mathcal{A}_2 = |T_{21} - R_{23}| \tag{5.20}$$
$$\mathcal{A}_3 = |T_{32}| \tag{5.21}$$

where the first indexes of the reflection and transmission coefficients R and T represent the row on which the waves are acting, and the second indexes represent the row from which the wave is reflected intermediately. Recalling Figure 5.1, let phase shift φ_n between two rows equal $l_n \frac{2\pi}{\lambda}$, where l_n is the distance separating rows n and $n-1$. Developing multiple reflections gives:

- Row 1:

$$R_{12} = \frac{tre^{i2\varphi_2}}{1 - r^2 e^{i2\varphi_2}} \tag{5.22}$$
$$R_{13} = \frac{rt^3 e^{i2(\varphi_2+\varphi_3)}}{1 - r^2 t^2 e^{i2(\varphi_2+\varphi_3)}} \tag{5.23}$$

- Row 2:

$$T_{21} = \frac{te^{i\varphi_2}}{1 - r^2 e^{i2\varphi_2}} \tag{5.24}$$
$$R_{23} = \frac{rt^2 e^{i(\varphi_2+2\varphi_3)}}{1 - r^2 e^{i2\varphi_3}} \tag{5.25}$$

- Row 3:

$$T_{32} = \frac{t^2 e^{i(\varphi_2+\varphi_3)}}{1 - r^2 e^{i2\varphi_3}} \tag{5.26}$$

Substituting into equations 5.19, 5.20 and 5.21, we now have:

$$\mathcal{A}_1 = \left| 1 - [\frac{tre^{i2\varphi_2}}{1 - r^2 e^{i2\varphi_2}} + \frac{rt^3 e^{i2(\varphi_2+\varphi_3)}}{1 - r^2 t^2 e^{i2(\varphi_2+\varphi_3)}}] \right| \tag{5.27}$$
$$\mathcal{A}_2 = \left| \frac{te^{i\varphi_2}}{1 - r^2 e^{i2\varphi_2}} - \frac{rt^2 e^{i(\varphi_2+2\varphi_3)}}{1 - r^2 e^{i2\varphi_3}} \right| \tag{5.28}$$
$$\mathcal{A}_2 = \left| \frac{t^2 e^{i(\varphi_2+\varphi_3)}}{1 - r^2 e^{i2\varphi_3}} \right| \tag{5.29}$$

Experimental validation Before exploring the model any further, we first test it against experimental data, for validation. Using the tracking method associated with the synthetic Schlieren technique described in Chapter 3, we measure average blade tip oscillations $\underline{X}$ for each row. In order to test the two array sizes, we run experiments for the following configurations :

- the array is composed of 2 rows ($N = 2$), and spacing l_2 between the rows is varied over range $[\frac{\lambda}{4}; \lambda]$
- the array is composed of 3 rows ($N = 3$), and spacing l_2 is fixed to $\frac{\lambda}{4}$ and spacing l_3 is varied over range $[\frac{\lambda}{4}; \lambda]$

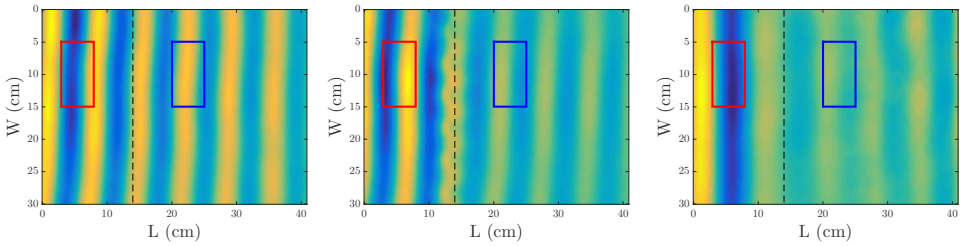

(A) Reference case (B) 1 row with $d = \lambda/2$ (C) 1 row with $d = \lambda/4$

FIGURE 5.5: Zones for the measurement of K_r and K_t coefficients on a single isolated row, based on the methods described in Chapter 3. Surface wave maps corresponding to the reference case without blades (A), a single row with constant spacing $d_1 = \lambda/2$ (B) and a single row with constant spacing $d_2 = \lambda/4$ (C).

Two lateral spacings d between blades are tested, chosen as $d_1 \sim \lambda/2$ and $d_2 \sim \lambda/4$. Reflection K_r and transmission K_t values are measured on a single isolated row for each spacing d, based on the methods described in Chapter 3, for which the equidistant zones of calculations are presented in Figure5.5 below. These coefficients are used for input values of local r and t in model, with approximately $\{r = 0.2; t = 0.7\}_{d_1}$ and $\{r = 0.3; t = 0.6\}_{d_2}$.

Using normalised average blade tip oscillations with those of the isolated row ($\tilde{X}_n = \underline{X}_n / \underline{X}_{single}$) (see Chapter 4), we can then compare these measured oscillation amplifications to calculated amplification factors $\mathcal{A}_n$ based on equations 5.11, 5.12, 5.19, 5.20, and 5.21 developed above. Results are presented for the larger spacing d_1 in Figure 5.6 below, for the array of 2 rows (a) and 3 rows (b).

Results for the second spacing d_2 are shown in Figure 5.7, for the array of 2 rows (a) and 3 rows (b). These were measured and averaged over two and three data sets, respectively. Model results show an overall good agreement with the experimental measurements of the two sets, within the error margins. The peaks and troughs of the blade oscillations are well represented by the model, although the strongest deviations remain noticeable for the lowest values of l and l_3.

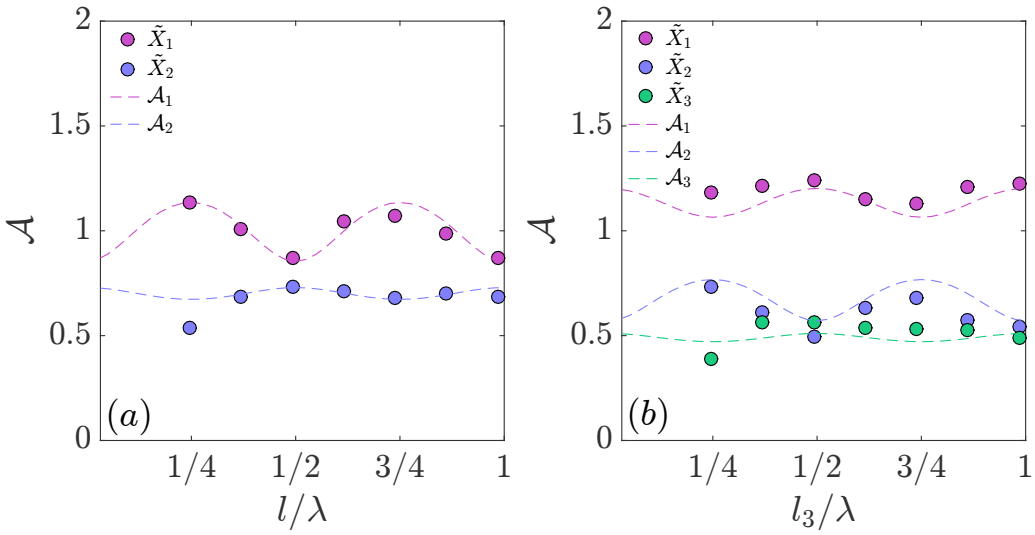

FIGURE 5.6: Normalised measured blade oscillations $\tilde{X}_n$ for rows 1 (purple circles), 2 (blue circles) and 3 (green circles) arrays composed of 2 rows (a) and 3 rows (b), for varying spacings l and l_3, respectively, within a range $[\frac{\lambda}{4};\lambda]$. Results are compared to calculated amplification factors $\mathcal{A}_n$. Results correspond to fixed lateral spacing $d = \lambda/2$.

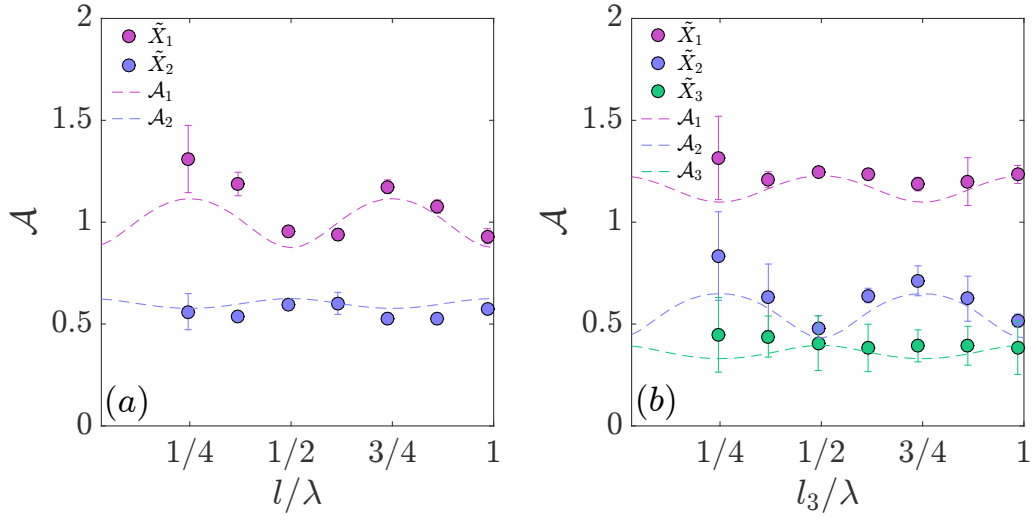

FIGURE 5.7: Normalised measured blade oscillations $\tilde{X}_n$ for rows 1 (circles markers), 2 (blue circles) and 3 (green circles) arrays composed of 2 rows (a) and 3 rows (b), for varying spacings l and l_3, respectively, within a range $[\frac{\lambda}{4};\lambda]$. Results are compared to calculated amplification factors $\mathcal{A}_n$. Results correspond to fixed lateral spacing $d = \lambda/4$.

5.1.2 Global analysis

With the test cases validated, we now wish to generalise these sets of equations, to a number N of rows, in order to perform a global analysis of the array interferences, based on local mechanisms. When considering multiple reflections within the array, the total number of reflected terms increases very rapidly with the number of rows N, leading to very complex formulations. For example, taking into account the first two terms only of all possible multiple reflections, row $n+1$ contributes 2 reflection terms, row $n+2$ contributes 4, row $n+3$ contributes 7 terms, and so on. Therefore, the number of added terms per row follows an arithmetic series with increasing common difference n, due to the increasing number of combinations of intermediate reflections. However, the coefficients r and t are both $\mathcal{O}(10^{-1})$, and so the terms of high order reflections reduce rapidly, and can be neglected.

Terms rising from multiple reflections between two non neighbouring rows, decrease by a factor of at least r^2t^2, corresponding to $\mathcal{O}(10^{-4})$, which leads to an infinite sum factor $\frac{1-(r^2t^2)^{N+1}}{1-r^2t^2} \approx 1$, where N here represents the total number of reflections. These terms therefore do not influence the first term of the sum and can be neglected. Multiple reflections are thus limited to the immediate neighbours only. For example, in a system consisting of 4 rows, the infinite reflections of waves reaching row 2 will be considered between row 2 and row 3 only, regardless of the source of emission, as shown in Figure 5.8 for the case of a 4-row array. The same holds for the transmission coefficient term.

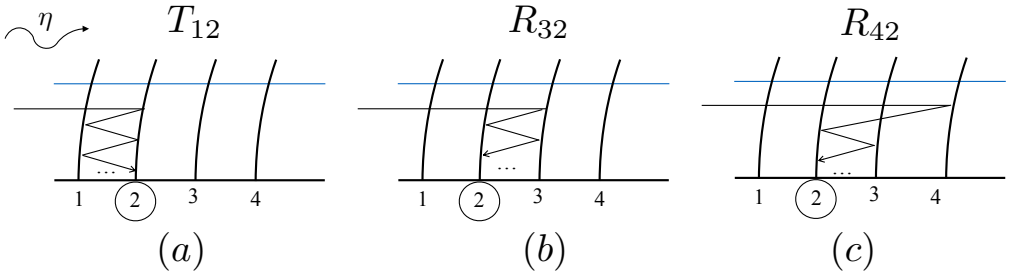

FIGURE 5.8: Example of the considered multliple reflections taken into account for the calculation of R_n and T_n applied to the case of row 2 in a 4-row array. Illustrations of the transmitted waves (a), reflected waves from row 3 (b) and reflected waves from row 4 (c).

Developing the expressions for the amplification factor calculation on row 2 gives the following:

$$T_{12} = \frac{te^{i[\varphi_1+\varphi_2]}}{1-r^2e^{i2\varphi_2}} \tag{5.30}$$

$$R_{32} = \frac{rt^2e^{i[\varphi_1+\varphi_2+2\varphi_3]}}{1-r^2e^{i2\varphi_3}} = \frac{rt^2e^{i[\varphi_1+\varphi_2]} \times t^0e^{i2\varphi_3}}{1-r^2e^{i2\varphi_3}} \tag{5.31}$$

$$R_{42} = \frac{rt^4e^{i[\varphi_1+\varphi_2+2(\varphi_3+\varphi_4)]}}{1-r^2e^{i2\varphi_3}} = \frac{rt^2e^{i[\varphi_1+\varphi_2]} \times t^2e^{i2[\varphi_3+\varphi_4]}}{1-r^2e^{i2\varphi_3}} \tag{5.32}$$

Each subsequent row (rows 3 and 4 in this case) will reflect waves that are themselves infinitely reflected locally to row 2, as represented in the denominator of both R_n terms (Eq. 5.31 and 5.32). A pattern is therefore identified in the total reflection term, with a second geometric series corresponding to the additional reflections

caused by subsequent rows. The generalised equations for any row n can then be written from the sums of these combined geometric series as follows:

$$R_n = \underbrace{\frac{rt^n e^{i[\sum_{m=1}^{n}\varphi_m]}}{1-r^2e^{i2\varphi_{(n+1)}}}}_{\text{immediate neighbours}} \underbrace{\sum_{k=0}^{N-n-1} t^{2k}e^{i2\sum_{m=n+1}^{k+n+1}\varphi_m}}_{\text{subsequent rows}} \qquad (5.33)$$

$$T_n = \frac{t^{(n-1)}e^{i\sum_{m=1}^{n}\varphi_m}}{1-r^2e^{i2\varphi_n}}$$

where $\varphi_n = \frac{l_n 2\pi}{\lambda}$ corresponds to the phase shift of incident transmitted waves η_{tn} at row n with respect to the incident wave η.
The global force amplification factor resulting from array wave interferences can therefore be predicted using equation 5.10 and provides an indication of the local excitation force applied onto each row of any N-sized array, and for any choice of φ_n. In the following sections, we derive expressions for global dissipation K_a, reflection K_r and transmission K_t coefficients, arising from this interference model.

Global Dissipation At the local scale of a single row, the energy associated to the incident wave is shared between a reflected part of ratio r^2, a transmitted part of ratio t^2, and a dissipated part of ratio $k_{diss} = 1-(r^2+t^2)$. The dissipated energy depends on the device oscillations and includes terms of both internal dissipation k_a due to the device's restoring force (elastic bending or Power Take-Off damping) and external dissipation k_d due to the added damping caused by the presence of the fluid (friction).
From the expressions derived in Chapters 2 for the total mechanical damping coefficient, we can easily show that K_a it is directly proportional to the blade tip oscillations X:

$$K_a = \frac{\mathcal{P}_a}{\mathcal{P}_w} = \frac{\Gamma_{int}(m+m_a)\dot{x}^2}{\frac{1}{2}\rho_w g a^2 \cdot v_g} \propto \dot{x}^2 \propto X^2 \qquad (5.34)$$

Therefore, the global absorption factor will also depend on the amplification factor as follows:

$$k_a(X^2) = 1-(r^2+t^2+k_d) \qquad (5.35)$$

$$K_a = \sum_{n=1}^{N} \mathcal{A}_n^2 k_a \qquad (5.36)$$

Using the amplification factor model, maximal potential energy dissipation is predicted using equation 5.36 above, based on the array layout.

In order to highlight the effect of the array on the global energy dissipation coefficient K_a, the results are compared to a theoretical reference coefficient $K_{a_{ref}}$, which we define as the sum of non-amplified individual dissipation coefficients, only taking into account cumulative reduced transmission throughout the array. This is expressed as:

$$K_{a_{ref}} = \sum_{n=0}^{N-1} t^{2n}k_a = k_a \cdot \frac{1-t^{2N}}{1-t^2} \qquad (5.37)$$

Note that the transmission coefficient is squared in order to remain in energy terms.

Global Reflection Following similar interference principles, we use the same method to predict the total global reflection coefficient of the array K_r. In this case, the sum of all reflected waves is considered at position x_1^+ in front of the first row. Taking only first-order reflections from subsequent rows, we have:

$$\eta_R = \eta_{r1} + \eta_{r2} + \eta_{r3} + ... + \eta_{rn} = \sum_{n=1}^{N} \eta_{rn} \tag{5.38}$$

Each row n reflects a wave η_{rn} with a phase shift $\varphi_n = \frac{l_n 2\pi}{\lambda}$ due to the distance l_n separating two neighbouring rows. If we first consider a simple case whereby the distance l_n between each row is the same constant l, then the sum of all reflected waves can be written as that of a power series (equation 5.41):

$$\eta_R = \Re\{rae^{ikx} + rt^2ae^{i(kx+2\varphi)} + rt^4ae^{i(kx+4\varphi)} + ... \tag{5.39}$$

$$... + rt^{2(n-1)}ae^{i(kx+2(n-1)\varphi)}\} \tag{5.40}$$

$$\eta_R = \Re\{ae^{i(kx)}\frac{r(1-(t^2e^{i(2\varphi)})^N)}{1-t^2e^{i(2\varphi)}}\} = \Re\{ae^{i(kx)} \cdot R_z\} \tag{5.41}$$

with $R_z = \frac{r(1-(t^2e^{i(2\varphi)})^N)}{1-t^2e^{i(2\varphi)}}$. The total reflection coefficient $K_r = |R_z|$ can therefore be calculated for any given phase shift φ. The results for the calculated global reflection K_r for varying array sizes ($N \in [2 : \infty]$) are provided in Figure 5.9 below. Measured reflection K_r and transmission K_t coefficients are used as input r and t parameters in the expression of R_z, taken from the experimental parametric study presented in Chapter 4 (c.f. Figure 4.19). These are approximately $t = 0.8$ and $r = 0.2$ for the rigid single row configuration.

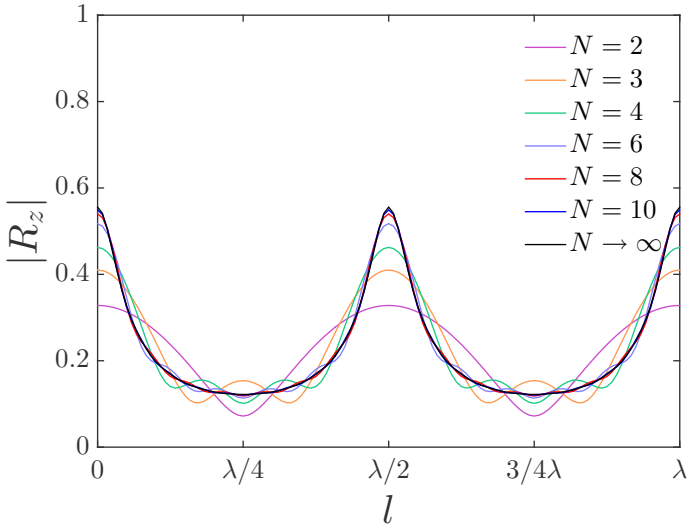

FIGURE 5.9: Calculated global reflection coefficient for array sizes, as a function of spacing l. Local r and t coefficients are taken as 0.2 and 0.8 respectively (see experimental study (Chapter 4).

The model demonstrates clear peaks Bragg scattering peaks at $l = n\lambda/2$, when the reflected waves are perfectly in phase with each other and with the incident

wave. These converge relatively quickly (from $N = 8$) to a maximal global reflection coefficient of 0.55. Note that in the case of an array composed of 4 rows, the calculated coefficient reaches 0.45, as that found experimentally (c.f. configuration l_{3rigid} in Figure 4.19, (f)). It can also be noted that the curve shape varies depending on array size, with troughs appearing at different values of l/λ. For example, when $N = 2$, the Bragg peaks are broad while the troughs are very localised at $l = \lambda/4$ and $l = 3\lambda/4$ (purple curve). Multiple troughs appear for $N \geq 3$, which reduce and converge onto the curve of $N \to \infty$ (black curve). It should be noted that while Bragg peaks of all array sizes fall at the same values of $l = n\lambda/2$, the curve minima do not, and are shifted by $\sim \lambda/6$ either side of $l = n\lambda/2 + \lambda/4$. The shape and intensity of this function depends of course on the values of local r and t, as shown in Figure 5.10 below, with $|R_z|$ for $r \in [0.1 - 0.5]$ (a) and for $t \in [0.5 - 0.9]$ (b). These plots demonstrate that the peak intensities depend more strongly on t while the response curve's shape and shift depend more strongly on r.

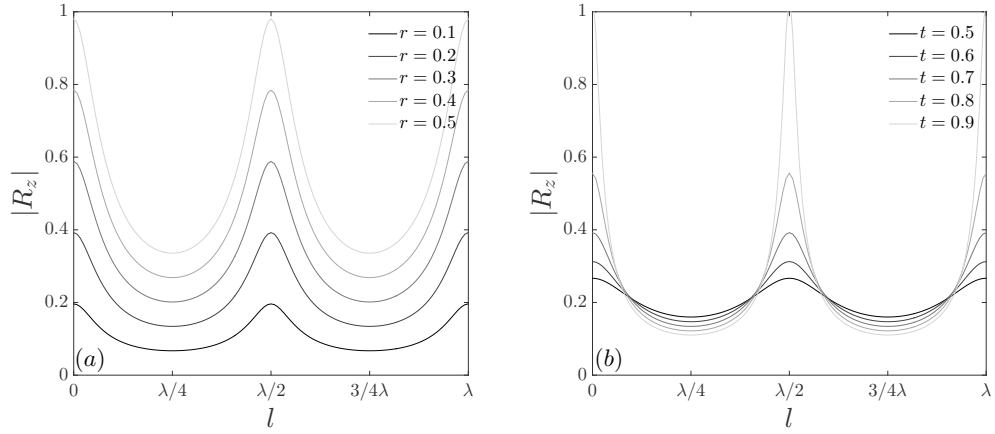

FIGURE 5.10: Calculated global reflection coefficient for an infinitely large array ($N \to \infty$), as a function of spacing l, for varying r (a) and varying t (b). The fixed values are $r = 0.2$ and $t = 0.8$.

If we now consider, as for the dissipation coefficient K_a, a theoretical case without array effects, the expression for global reflection becomes $K_{r_{ref}} = r\frac{1-t^{2N}}{1-t^2}$, which coincides with Bragg scattering ($\varphi = 0$).

Now considering independently varying values of l_n throughout the array, equations 5.33 and 5.41 lead to the following expression for the global reflection coefficient K_r of the entire array:

$$K_r = r \sum_{k=0}^{N-1} \frac{r^{2k} e^{i2\sum_{m=1}^{k+1} \varphi_m}}{1 - t^2 e^{i(2\varphi_{k+1})}} \tag{5.42}$$

Global Transmission Finally, following a similar reasoning, this interference model can also be used to predict the global transmission coefficient K_t. Without any array effects, the global transmission coefficient would simply be expressed as $K_{t_{ref}} = t^N$, where N is the total number of rows, and t is the local transmission coefficient of a single row. However, array layout affects wave interferences, leading to the following expression for the global transmission coefficient at position x_N^+ just behind the last row of the array:

$$K_t = \frac{t^N e^{i\sum_{m=1}^{N}\varphi_m}}{1 - r^2 e^{i2\varphi_N}} \tag{5.43}$$

where N is the total number of rows in the array.

Global energy balance - validation Based on local r and t coefficients, it is therefore possible to evaluate the total energy distribution in our system using global dissipation K_a (equation 5.36), reflection K_r (equation 5.42) and transmission K_t (equation 5.43) coefficients, for any given separating distances l_n.

Taking our test cases, we now test the model globally. Using the 2 and 3 row arrays tested with a lateral spacing $d \sim \lambda/2$, we measure global transmission, reflection and mechanical damping coefficients, using the methods described in Chapter 3. These are plotted in Figure 5.11 below. The experimental values (circles) are then compared with those calculated from the interference model (dotted lines). The top plots correspond to the 2-row array, while the 3-row resuts are shown in (c) and (d), and energy quantities are shown on the left plots, while amplification factors are represented on the right-hand side plots. Input coefficients for the model are taken as $r = 0.2$, $t = 0.7$ and $k_a = 0.1$, approximated from single row measurements.

Validation is also performed for the larger 4-row array tested in the parametric study described previously in Chapter 4, plotted in Figure 5.12 below. Deviations from the model are stronger in this case, in particular for the reflection peak. It should be reminded, however, that the experimental value here could be overestimated, since the value measured for the equivalent staggered case was lower ($\sim$ 0.45). Part of these deviations could therefore stem from larger experimental errors. Nonetheless, qualitative variations are well represented by the model.

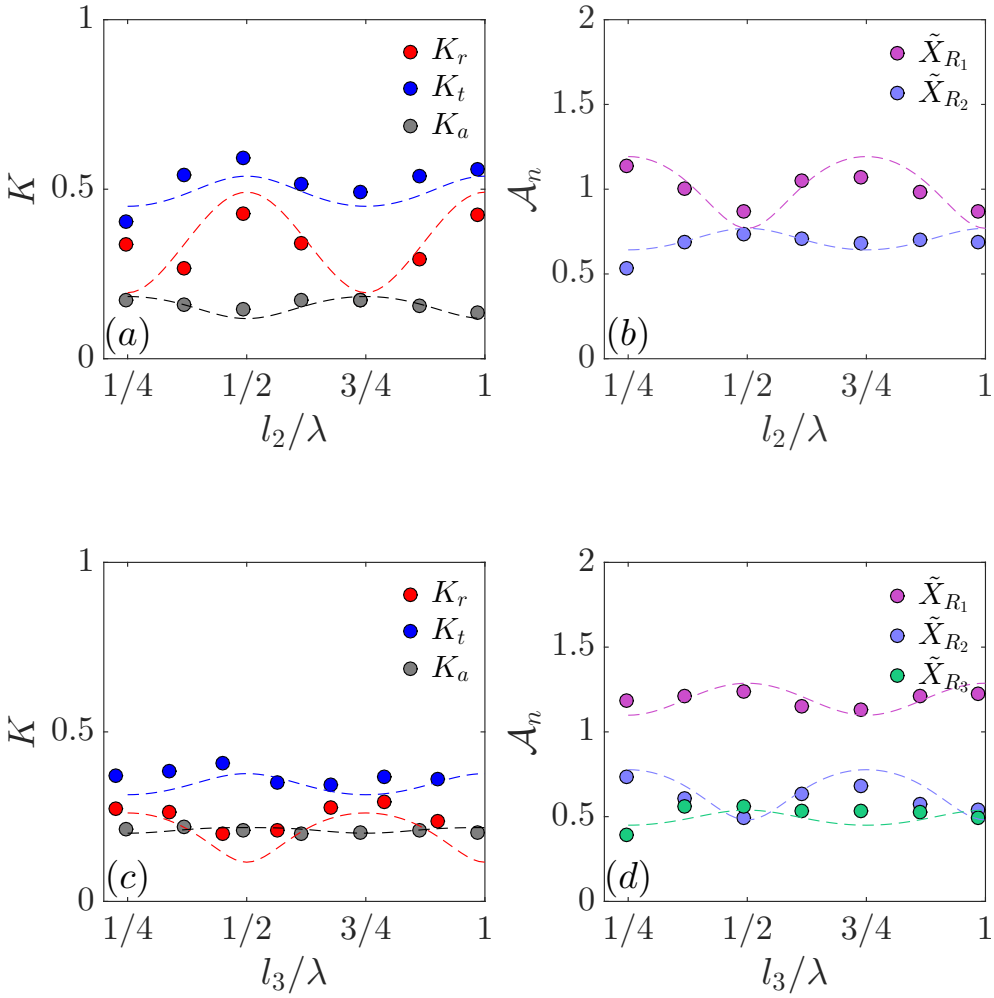

FIGURE 5.11: Measured (circles) versus calculated (dotted lines) values of reflection (red), transmission (dark blue) and total mechanical damping (grey) quantities for a 2-row array (a) and a 3-row array (c), as a function of increasing back row spacing. Normalised oscillations $\tilde{X}_n$ of rows 1 (purple), 2 (blue), 3 (green) are recalled in plots (b) and (d) for the corresponding arrays and compared to the calculated amplification factors $\mathcal{A}_n$. Lateral spacing $d \sim \lambda/2$ is fixed for all presented results.

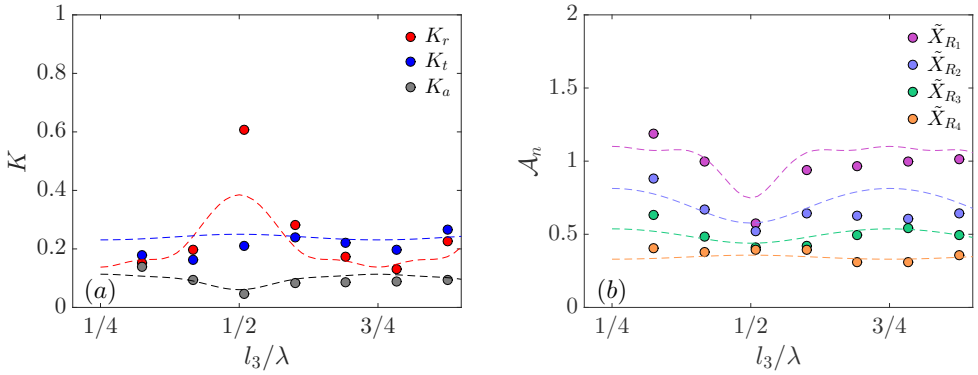

FIGURE 5.12: Measured (circles) versus calculated (dotted lines) values of reflection (red), transmission (dark blue) and total mechanical damping (grey) quantities for the full 4-row array (configuration $l_{flexible}$) tested in the parametric study presented in Chapter 4 (a). Normalised oscillations $\tilde{X}_n$ for rows 1 (purple), 2 (blue), 3 (green) and 4 (orange) plotted in (b) for the corresponding arrays and compared to the calculated amplification factors $\mathcal{A}_n$. Lateral spacing $d \sim \lambda/3$ is fixed for all presented results. Input parameters are estimated as $r = 0.5$, $t = 0.7$ and $k_a = 0.05$.

5.2 Optimisation

As explained at the beginning of the Chapter, the aim of this model is to describe our system for arrays of any size and of variable independent row spacings, so that both regular and irregular arrays can be tested. The goal then being to use this model in order to determine optimal configurations regarding both wave power absorption and minimal transmission.

Methods Given the infinite number of variables in our system, we look to solve our equations numerically for all φ_n of the array (step (1) in Figure 5.13), based on a discretised range of tested phase shifts φ varying between $\pi/2$ and π, with a phase step $\delta\varphi$ that is determined from a convergence test (see Figure 5.14). To do so, the calculation is based on a matrix Ψ_{ij} storing all φ_n permutations possible between rows, where indices i and j represent the permutation number and row number, respectively. For each row n, both T_n and R_n are calculated from equation 5.33 for all i combinations of φ_n defined in Ψ_{ij} (step (2) in Figure 5.13). Equation 5.10 can then be computed to obtain a resulting matrix $\mathcal{A}_{ij}$ storing all the amplification factors for each configuration i and row j (step (3) in Figure 5.13). The optimal configuration can then be identified by searching for combination i in $\mathcal{A}_{ij}$ that provides the maximum global amplification factor defined as $\sum_j \mathcal{A}_{ij}$ (step (4) in Figure 5.13). The corresponding optimal phase shift vector φ_{opt} extracted from Ψ_{ij} is then easily converted into an optimal spacing vector $l_{opt} = \frac{\lambda}{2\pi}\varphi_{opt}$ (step (5) in Figure 5.13).

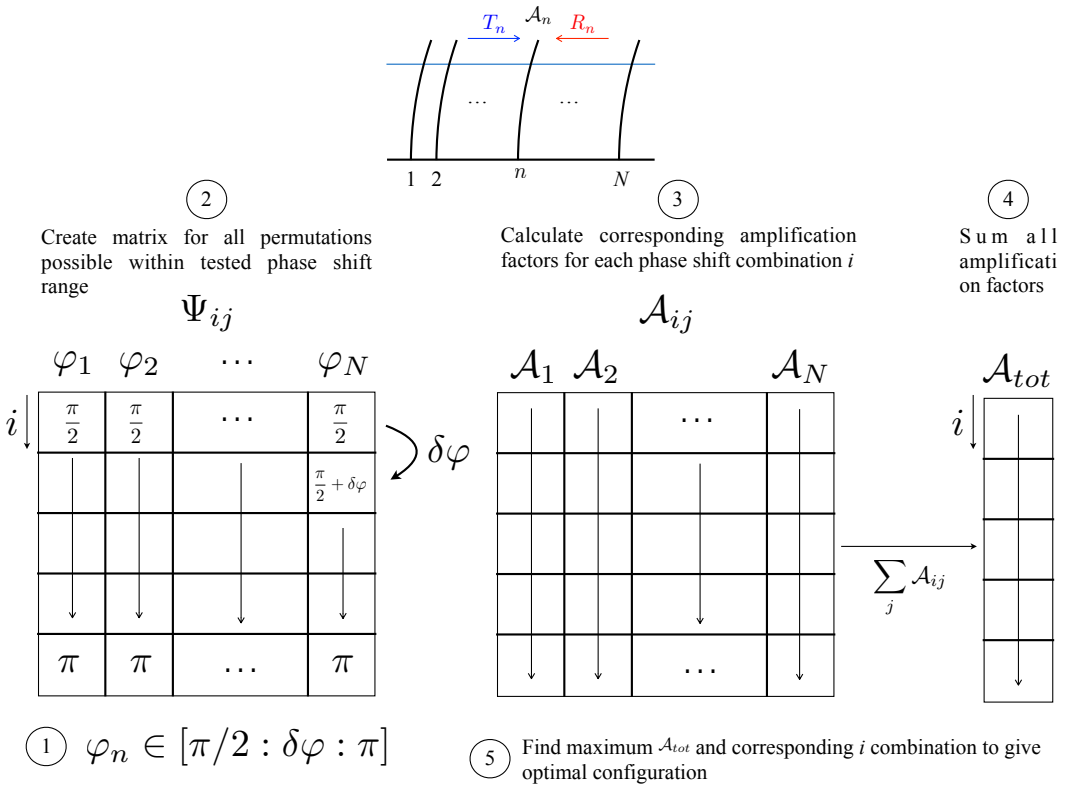

FIGURE 5.13: Optimisation method for any array composed of N rows. The method is composed of 5 steps: phase shift discretisation (1), phase matrix Ψ_{ij} preparation (2), amplification factor matrix $\mathcal{A}_{ij}$ calculation (3), total amplification vector $\mathcal{A}_{tot}$ (4), and finally optimal configuration identification (5).

Calculation time therefore depends on the size of the input matrix Ψ_{ij}, which itself varies exponentially with the number of rows in the array, and which also depends on the phase step $\delta\varphi$ chosen for the various values of φ_n tested. Given the symmetry found in the results for a 2-row array, the choices for φ_n can be varied between $\varphi_n \in [\pi/2; \pi]$, which corresponds to varying the spaces $l_n \in [\lambda/4; \lambda/2]$. A convergence test is then performed in order to determine the value of $\delta\varphi$. Figure 5.14 below presents the results for optimal spacings l_n and total amplitude factors $\mathcal{A}_{tot} = \sum \mathcal{A}_n$ for an array of 3 rows, as a function of phase shift step:

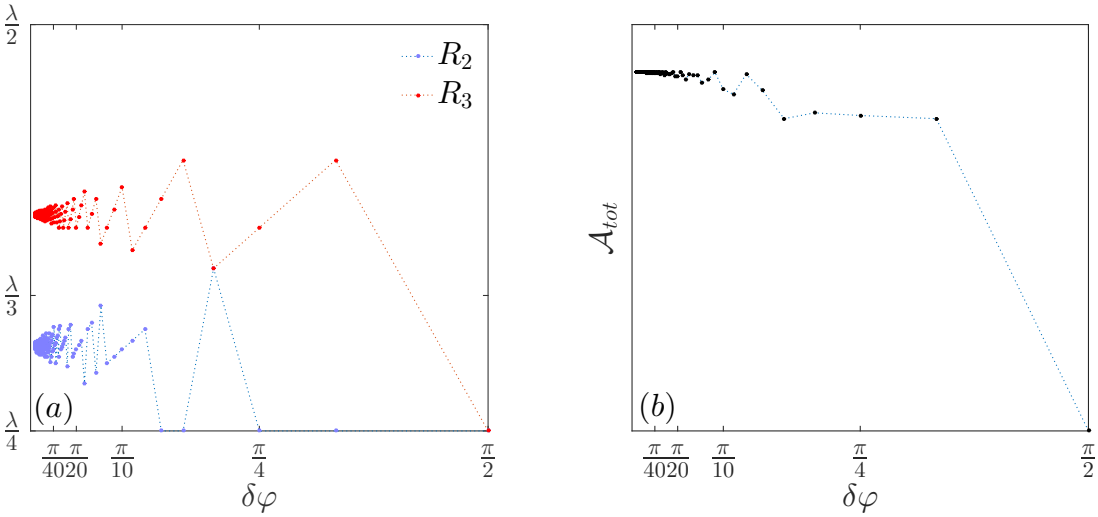

FIGURE 5.14: Convergence test. Optimal spacings (a) and sum of amplification factors for optimal configuration (b) as a function of phase shift step $\delta\varphi$.

The results show that the amplification factor values converge for $\delta\varphi < \frac{\pi}{10}$. However, the optimal spacing values are subject to 'jumps' for $\delta\varphi > \frac{\pi}{40}$. Step sizes are deemed sufficient for values $< \frac{\pi}{30}$, for which the error will be less than $\frac{1}{3}$%.

Regular arrays We now use the model described above to explore all possible array configurations, in order to evaluate their influence on blade oscillations and wave damping. We first compare two bounding cases for regular configuration patterns (i.e. arrays with constant spacing l between rows), which correspond to spacing ratios $l = \lambda/2$ and $l = \lambda/4$. Taking the same local coefficients as those measured experimentally ($r = 0.2$, $t = 0.7$, $k_a = 0.1$), amplification factors calculated from equation 5.10 are plotted in Figure 5.15 for each row as a function of the total number of rows in the array. The results are compared to a reference case without amplifications, i.e. assuming a series of single independent rows. These are represented by black asterisks and are calculated as t^{n-1} for each row n.

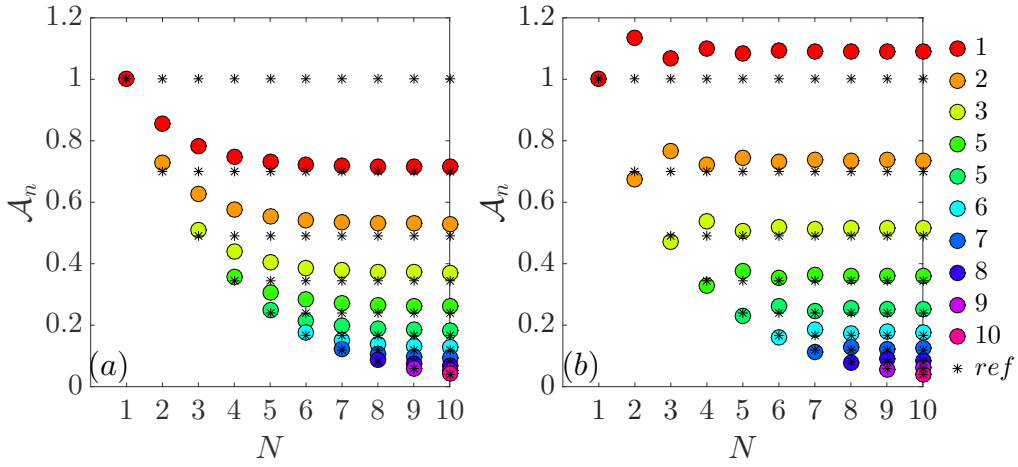

FIGURE 5.15: Predicted amplification factors $\mathcal{A}_n$ for each row n of the array as a function or array size (increasing number of rows N). Results for constant array spacing $l = \lambda/2$ (a) and constant array spacing $l = \lambda/4$ (b). Theoretical oscillation factors without amplifications (reference) are presented in black asterisks.

As expected, these results show the strong influence of the arrangement on front row oscillations, with a 30% decrease in values for $l = \lambda/2$ versus a 10% increase for $l = \lambda/4$ and these effects hold true throughout the array, with similar attenuated effects for each subsequent row.
The global reflection and transmission coefficients are also compared in Fig. 5.16, using equations 5.42 and 5.43. Here again, a reference case is plotted in black asterisks in order to identify the effect of array amplifications on K_t (note that results for K_r would match exactly those of $l = \lambda/2$, as described in the previous section).

As previously seen for amplification factors, a clear difference is noticed here again, especially regarding the reflection coefficients, with a maximum difference of around 25% reached for arrays of 10 rows. The transmission coefficients, on the other hand, fall on very similar curves, and do not deviate beyond 5% from the reference case (N=2). This suggests a competition between reflection and absorption, with a maximal gain in absorption when reflection is minimal, whereas transmission is not greatly affected and depends mainly on array size. Another noticeable difference concerns the change in variations for increasing array sizes. While K_r increases steadily with N for $l = \lambda/2$ before reaching a limit at N=5, it decreases very slightly and in oscillatory form for $l = \lambda/4$. A similar observation can in fact be made regarding amplification factors, with mirrored trends (recall Fig. 5.15). This oscillation is thought to come from a pairing effect of amplifications, with mimima observed for even arrays, and maxima for odd arrays.

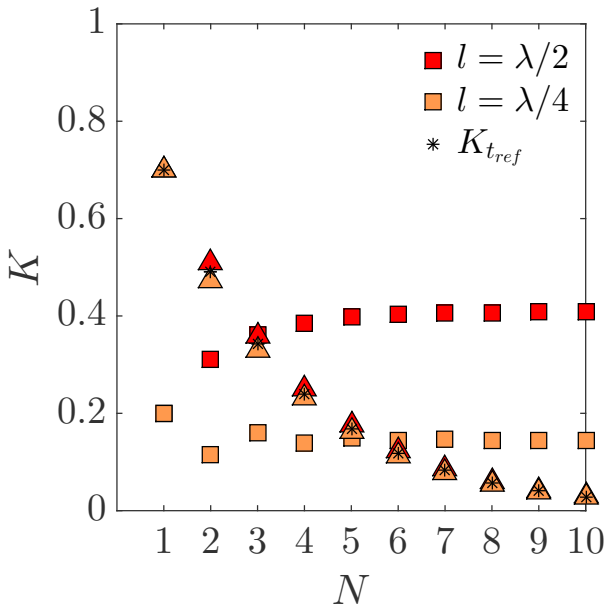

FIGURE 5.16: Predicted global reflection K_r (squares) and transmission K_t (triangles) coefficients as a function of array size (increasing number of rows N). Results for constant array spacings $l = \lambda/2$ and $l = \lambda/4$ are presented in red and orange, respectively. Results are compared to the reference case without amplification effects ($K_{t_{ref}}$).

Irregular arrays It is clear that convergence rates and variations of the K_r and K_t coefficients depend on the input parameters r and t, which are so far measured from experimental data. If these coefficients now varied, for example via a modification of the confinement ratio, or blade flexibility and shape, then these tendencies will be altered. Additionally, given that $\lambda/2$ is a multiple of $\lambda/4$, the benefits of $l = \lambda/4$ are diminished by the negative impact of $l = \lambda/2$ spacings on blade oscillations for arrays $N > 2$. This suggests that for larger arrays, configurations causing maximal blade oscillations could be irregular, i.e. when the spacing between rows is not constant. These optimal configurations are determined by scanning all possible combinations of l_n spacings and calculating their associated amplification factors $\mathcal{A}_n$. The optimal array is that providing the maximal global amplification factor $\mathcal{A}_{tot} = \Sigma\mathcal{A}_n$. In the following paragraphs, input parameters are varied assuming an energy balance of the form $r + t + k_a = 1$, where the local parameters each represent an energy coefficient. In this theoretical case, we assume no external dissipation k_d.

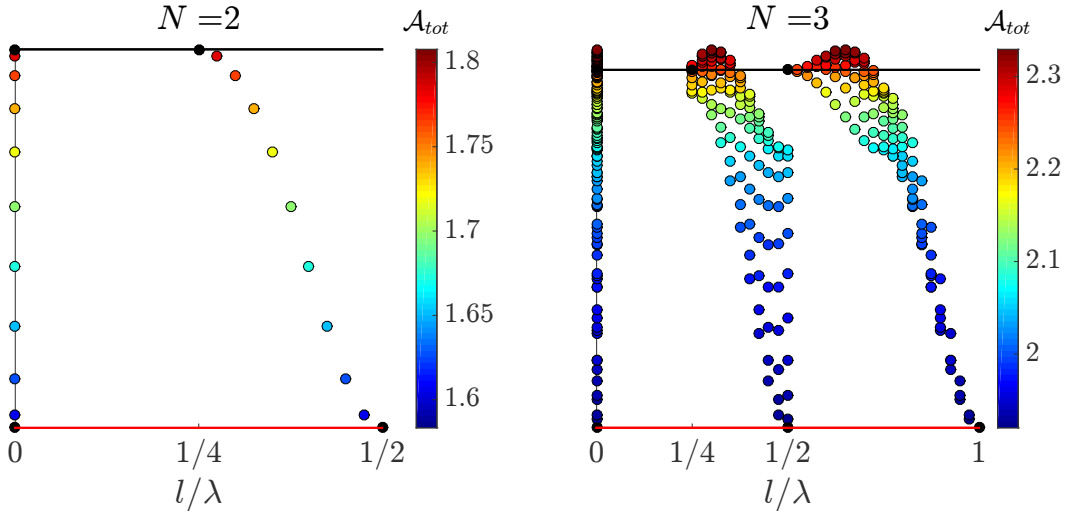

FIGURE 5.17: Representation of all scanned array configurations as a function of the global amplification factor $\mathcal{A}_{tot}$ for arrays composed of N=2 (left) and N=3 (right) rows. Local parameters are taken as those measured experimentally, i.e., r=0.2 and t=0.7. As a reference, regular arrays l=$\lambda/2$ and l=$\lambda/4$ are identified with red and black horizontal lines respectively.

Figure 5.17 first presents all scanned configurations for array sizes of 2 and 3 rows, ordered as a function of their calculated cumulative amplification factors $\mathcal{A}_{tot}$. The optimal configurations are therefore those at the top of the graphs and are compared to the two regular arrays $l = \lambda/4$ and $l = \lambda/2$ identified by means of black and red lines, respectively. Note that these results correspond to the fixed local parameters associated with the experimental data. As observed in the experimental results shown in Figure 5.6 (a), the optimal configuration for a 2-row array converges to the regular case $l = \lambda/4$, with an overall increase of about 12.5% compared to the configuration $l = \lambda/2$. For an array composed of 3 rows, however, the optimal case converges towards an array that is slightly offset from the regular case $l = \lambda/4$, with $l_2 = 0.3\lambda$ and $l_3 = 0.35\lambda$. This illustrates the compromise between the benefit of spacing $l = \lambda/4$ over the front row of two successive rows and the advantage of $l = \lambda/2$ for the back row. The resulting optimal configuration provides an increase of around 5% compared to the regular case $l = \lambda/4$.

Following the same procedure, resulting optimal configurations are presented in Fig. 5.18 for arrays ranging from 2 to 7 rows and for fixed local $k_a = 0.1$.

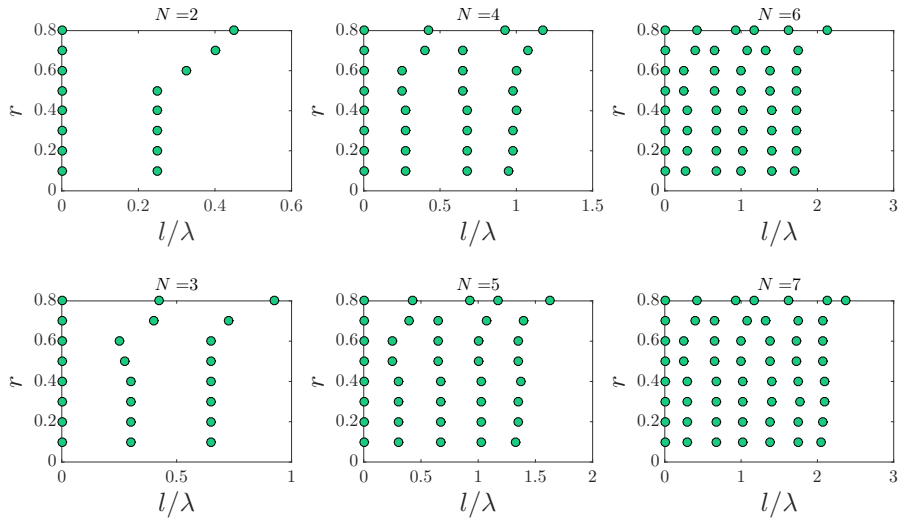

FIGURE 5.18: Optimal configurations as a function of $\{r; t\}$ values, for increasing array size between N=2 and N=7. Local damping coefficient k_a is fixed at 0.1.

In the case of even arrays, one can notice that optimal configurations vary between regular arrays of $l = \lambda/4$ for low values of r and $l = \lambda/2$ for larger values of r, with a transition through irregular patterns for the intermediate values of r.

This pattern shift is noticed starting at $r = 0.5$ for a $N = 2$ and can be explained through equation 5.33. Indeed, the case of a 2-row array, R_1 and T_2. Taking into account only first reflection terms, we notice that $R_1 \propto rt$ and $T_2 \propto t$. The variations of these two coefficients are plotted against r in Figure 5.19 below. These highlight the shift in R at $r = 0.5$. Beyond that point, values of R decrease. This suggests that the influence of the second row regarding the amplification factor for the first row will decrease. In other words, the total array forcing will be more and more influenced by the increase in $\mathcal{A}_2$ than by the decrease in $\mathcal{A}_1$.

Moreover, the total forcing acting on the second row only comes from waves traveling in the positive x-direction. Therefore, the internal reflections will act in the same direction as the transmitted wave, and will therefore amplify the overall coefficient T when these are in phase, i.e. at $l = \lambda/2$. This would explain the observed experimental variations of a 2 row array, whereby the front and back rows oscillation variations are mirrored: maxima are observed at $l = \lambda/4$ and $l = \lambda/2$.

On the other hand, optimal configurations for odd numbered arrays all seem to match irregular configurations. These variations are explained by the local nature of the amplification effects. Given that r and t are of $\mathcal{O}(10^{-2})$, interferences will only have an impact on neighbouring rows. This would explain why both even and odd arrays may transition through semi-regular configurations, composed of combined pairs of rows.

The benefit of the determined optimal configurations is further evaluated and the associated global damping coefficients are compared to those of the regular bounding cases, along with the reference case (black asterisks), as described in equation 5.37. Results are plotted in Fig. 5.20 for an array of 3 rows, for arbitrary variations of $k_a \in [0.1 - 0.4]$. These Figures clearly show the negative impact of regular arrays $l = \lambda/2$ as opposed to the benefit of both regular $l = \lambda/4$ and optimal arrays on

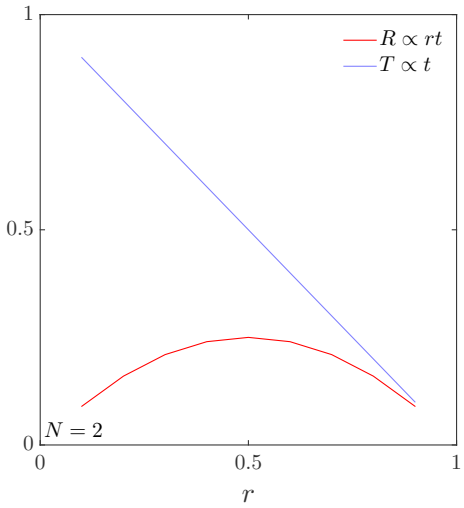

FIGURE 5.19: Variations of R and T coefficients as a function of r, for an array of 2 rows.

global wave dissipation, with deviations of up to $\pm 8\%$ ($k_a = 0.4$). However, the difference between optimal configurations and regular array $l = \lambda/4$ is negligible and visible only for specific cases. More globally, larger amplifications are found for lower values of r and k_a; the larger the amount of transmitted energy, the larger the impact of subsequent interferences.

In order to complete the analysis, the results are further studied in terms of performance and for various array sizes. Figure 5.21 presents the percentage increase in global dissipation coefficient K_a for optimal configurations compared to regular arrays $l = \lambda/2$ (left) and $l = \lambda/4$ (right), as well as the theoretical reference case (middle) (c.f. equation 5.37). The results are presented for increasing number of rows from N=2 to N=8 (top graphs) and for increasing reflection coefficient r (bottom graphs). Coefficient k_a is varied between 0.1 and 0.4.

Optimal configurations are seen to dissipate much more than regular arrays of $l = \lambda/2$ with an increase in K_a reaching up to 130% for an array of 8 rows (Figure 5.21 (a)). A large improvement is also noticeable compared to the reference case ($\approx$ 30%, c.f. Figure 5.21 (b)). In both cases, values increase steadily with array size. When compared to regular array $l = \lambda/4$, optimal configurations are shown to improve global dissipation for uneven arrays only, and the corresponding percentages decrease rapidly with values $\leq$ 1% beyond N=6. These observations suggest that optimal configurations generally tend towards the regular array of $l = \lambda/4$ with negligible improvements limited to a maximum of nearly 6%, reached for the specific case of N=3 (Figure 5.21 (c)).

Variations of K_a for increasing r show global parabolic tendencies for which the inflexion point is shifted towards lower values as k_a increases. These points correspond to the cases where $r \approx t$, i.e. when local reflection and transmission have the same impact. All maximum values are associated with local k_a coefficients equal to 0.1, i.e. in the case of maximal energy transmission towards neighbouring rows.

We now turn to the impact of the array on global reflection and transmission. Fig. 5.22 compares reflection and transmission coefficients of all three configurations, along with the reference K_{tref}, as a function of r and k_a. Once again, the results demonstrate the difference between the two regular arrays, with higher reflection and transmission when $l = \lambda/2$, in particular for values of $r \approx 0.2$ for which a

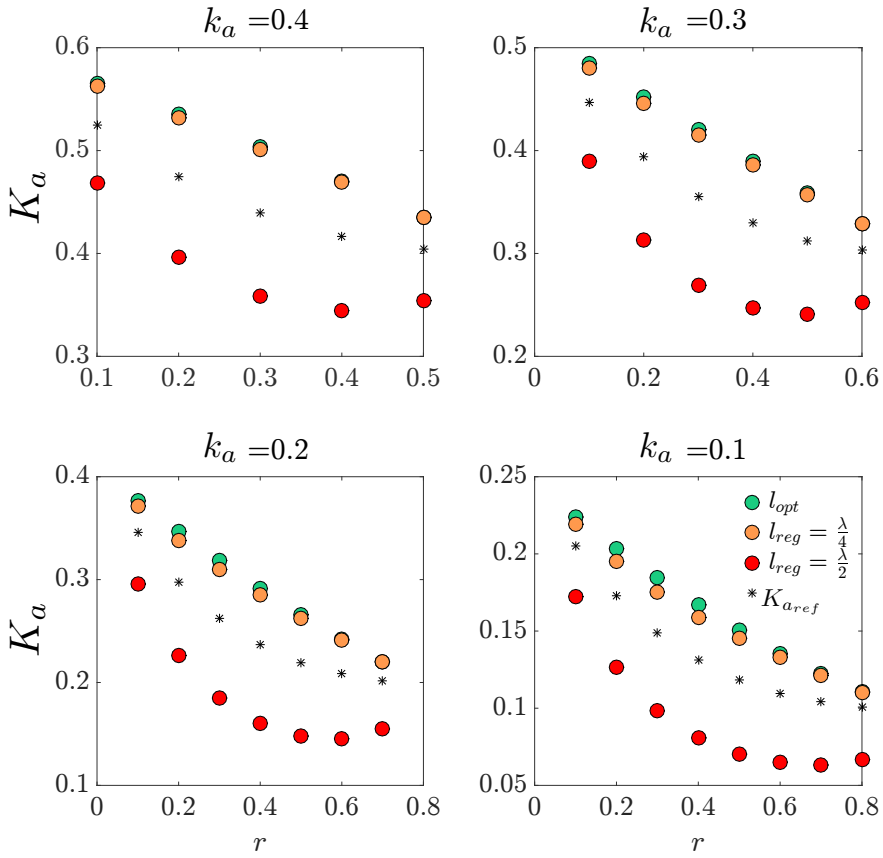

FIGURE 5.20: Variations of global dissipation coefficient K_a depending on local k_a and $\{r, t\}$ values for an array composed of 3 rows. Results for the optimal configuration and regular configurations are compared to the reference values without any array effects ($K_{a_{ref}}$). In this theoretical model, we assume no external dissipation k_d.

reduction of 15% can be reached. As noticed for blade oscillations, optimal configurations do not show large deviations with the results provided by regular arrays $l = \lambda/4$. The curves match perfectly in almost all cases, apart for reflections in low r and k_a regions. This is due to the fact that interferences play a larger role as more energy is transmitted through the successive rows. The difference does not exceed 5%. Finally, all results converge to the same values of K_r and K_t, when r coefficients are largest. This confirms the previous observations regarding optimal configurations for varying r values. It was found that optimal arrays indeed tended towards regular patterns of $l = \lambda/2$ for high values of r. In that case, the energy is shared between transmission and reflection, and dissipation becomes quasi-nil. It should be noted that similar results were also found for the larger arrays.

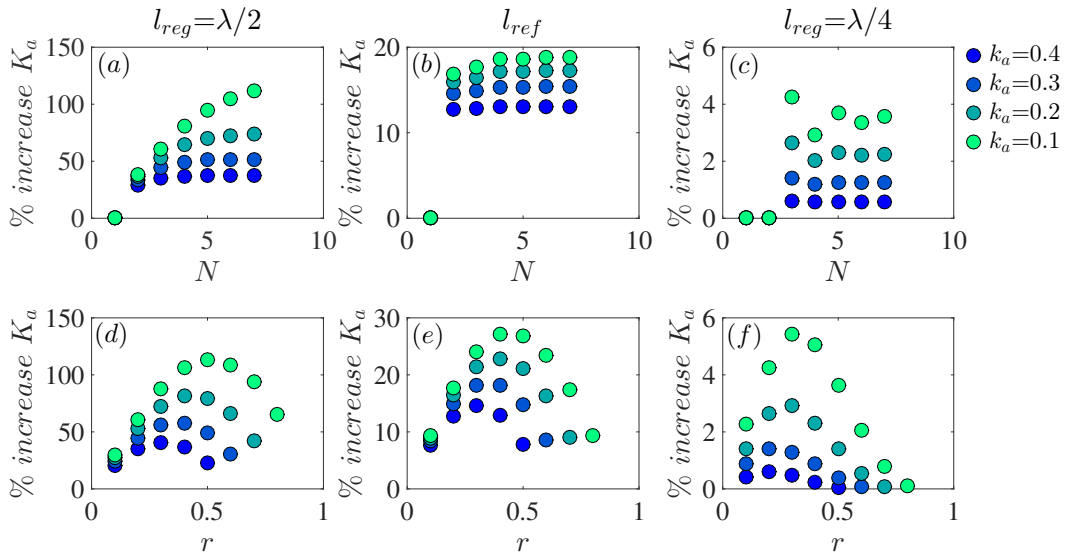

FIGURE 5.21: Increased performance of optimal arrays compared to regular and reference configurations as a function of number of rows N for fixed $r = 0.2$ (a)-(c) and for increasing local coefficient r with fixed number of rows $N = 3$ (d)-(f). Local k_a is varied between 0.1 and 0.4.

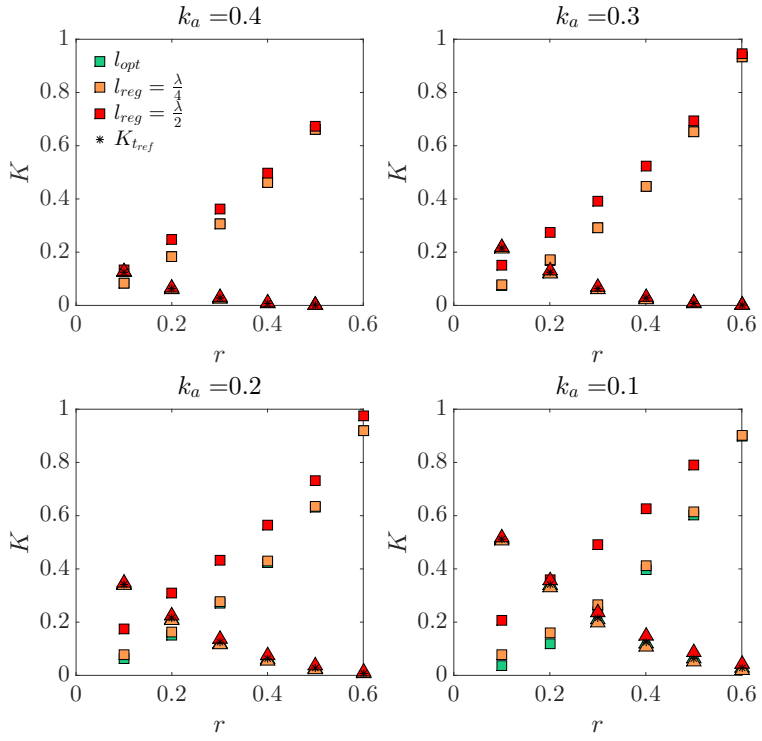

FIGURE 5.22: Variations of the global reflection K_r (squares) and transmission coefficients K_t (triangles) depending on local k_a and r, t values for an array composed of 3 rows. Reference transmission coefficients $K_{t_{ref}}$ are plotted in black for comparison.

5.3 Conclusion

Following previous observations made regarding the influence of array configurations on wave absorber oscillations, this chapter has presented a simple one- dimensional model able to predict the effects of wave interferences on array performance. Based on the known local reflection and transmission coefficients of an isolated row, this model was used to explore optimal array configurations regarding wave energy damping and absorption. Results have confirmed the previous experimental data by showing that in regular arrays, a separating distance $l = \lambda/2$ leads to a very large global reflection coefficient, and reduces blade oscillations, while the contrary is found for a separating distance $l = \lambda/4$. Optimal configurations regarding wave energy absorption were found to vary between these two regular configurations and irregular ones, depending on the number of rows and on the values of the input parameters $\{r, t, k_a\}$. However, these optimal configurations showed limited improvements over regular arrays of $l = \lambda/4$, with maximal differences appearing for global reflection and dissipation coefficients in arrays composed of 3 rows. This model has also shown a negligible impact of array interference on wave transmission, which would depend mainly on array size and on local parameters. This is seen to arise from a competition between reflection and damping, with large oscillations compensating for a low global reflection and vice versa. It should however be noted that the simple model may not be sufficient for the account of drag effects, which could potentially lead to larger variations of the transmission coefficients. In terms of WEC farm design, the results presented in this chapter suggest that array configurations can indeed help improve energy harvesting but will be limited in their impact on wave transmission. A more effective solution for the latter would be to seek means of reducing local transmission coefficients.

Chapter 6

Optimisation

In the previous chapter, we have developed and exploited a simple model describing array excitation forces resulting from multiple wave interferences. With this model, we were able to predict the variations of global energy absorption, as well as global reflection and transmission of waves, depending on the chosen distances separating the rows of flexible blades. The results highlighted the existing competition between global reflection and absorption coefficients, while the variations in global transmission were found to rely little on array pattern but rather on array size and on the local values of transmission coefficients. If we therefore search for an optimal hybrid system that could both transmit a minimal amount of waves, as well as absorb (or harvest) a maximum of their associated energy, then these would rely mostly on the search for maximum wave power absorption, i.e. maximal blade oscillation amplitudes X. The model's simplicity made it possible to determine optimal array configurations from both regular and irregular arrays of variable l_n spacings between neighbouring rows. From all the tested arrays, optimal irregular patterns were found to provide little improvement from the regular optimal configuration for which $l = \lambda/4$.

The findings of this chapter have served for a paper currently under preparation, in view of a submission to the *Journal of Fluid Mechanics* by the end of 2018.

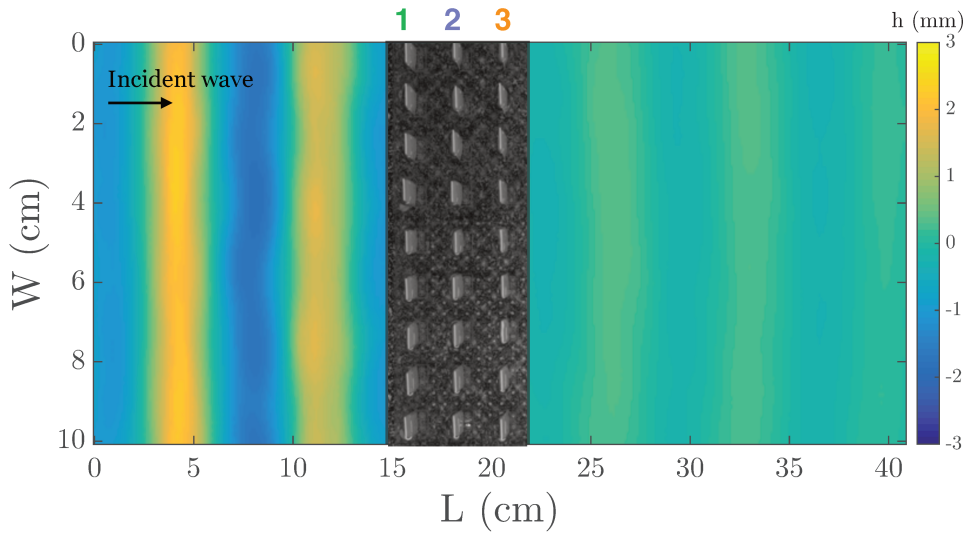

FIGURE 6.1: Illustration of a 3-row array. A typical raw image of the blade array with the dotted background is added onto its corresponding surface wave map treated by means of the Synthetic Schlieren method (c.f. Chapter 3).

6.1 Interferences in a 3-row array

These results are further investigated experimentally in this section. More specifically, we wish to understand why optimal configurations converge towards a regular pattern of spacing $l = \lambda/4$ while other optimal configurations are also found to produce similar global effects. This is studied using experiments performed in the small tank installation associated with the Synthetic Schlieren method, as described in Chapter 3.

A experimental study is performed, focused around a 3-row case sketched in Figure 6.2. This was chosen for the fact that the largest differences between optimal and regular configurations predicted from the interference model (Chapter 5) were found for this specific array size. An illustration of a typical configuration is recalled in Figure 6.1, with the superposition of a raw array image onto its corresponding treated surface wave maps. The presented image corresponds to spacings $d \sim \lambda/4$ and $l \sim \lambda/2$.

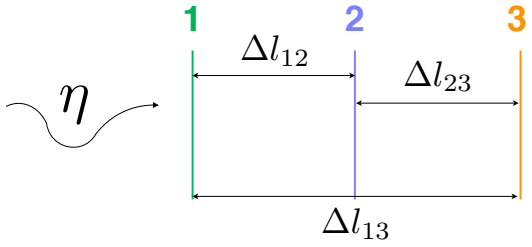

FIGURE 6.2: Sketch of the 3 row array, with separating distances Δl_{12}, Δl_{23} and Δl_{13} between all rows of the array.

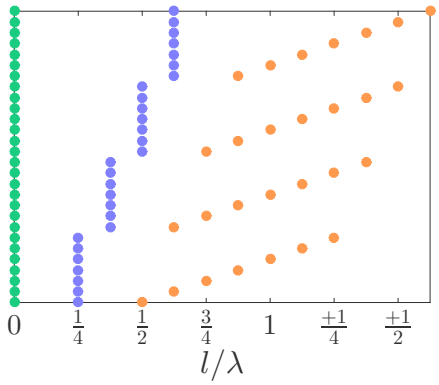

FIGURE 6.3: Visualisation of all tested configurations with the positions rows 1, 2 and 3 represented as, respectively, green, blue and orange dots.

Δl_{12}	Δl_{23}
$\lambda/4$	$[\lambda/4 - \lambda]$
$3\lambda/8$	$[\lambda/4 - \lambda]$
$\lambda/2$	$[\lambda/4 - \lambda]$
$5\lambda/8$	$[\lambda/4 - \lambda]$

TABLE 6.1: List of the varied separating distances between neighbouring rows.

With Δl_{ij} defined as the distance separating rows i and j, we perform our study by testing four possible spacings $\Delta l_{12} \in [\lambda/4 - 5\lambda/8]$ separating rows 1 and 2, combined with seven possible separating distances $\Delta l_{23} \in [\lambda/4 - \lambda]$ between rows 2 and 3. Spatial increments correspond to approximately $\lambda/8$. All spatial variations are summarised in Table 6.1 and represented graphically in Figure 6.3. These 28 configurations were tested for two lateral spacings $d_1 \sim \lambda/2$ and $d_2 \sim \lambda/4$ in order to

have two different values of local coefficients $[r, t]$. Typical images of the three arrangements are presented for the single row cases in Figure 6.4. The flexible blades here are made from Mylar sheets of thickness 350 μm, width 14 mm, length 9 cm, leading to a measured natural frequency in 8 cm deep water of ~ 5 Hz. Experiments were all run at that same imposed wave frequency, for which the measured wave length is approximately 6.5 cm.

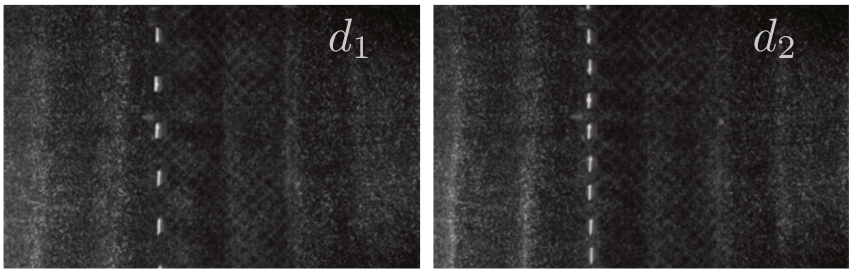

FIGURE 6.4: Typical images of the tested row configurations, with, from left to right, a single row of $d_1 \sim \lambda/2$ and a single row of $d_2 \sim \lambda/4$.

For each tested configuration, reflection K_r and transmission K_t coefficients are calculated and blade oscillations $X(t)$ are tracked using the methods described in Chapter 3. Two reference cases were further tested at the end of each series: a *Control* case without any blades in order to correct for the natural dissipation of waves in the evaluation of the transmission coefficients, as well as a case with a single row of blades, in order to measure both local values of r and t and a reference value for tip oscillations without interferences.
Since the ultimate goal of the system is to perform well in both wave attenuation (low transmission) and wave absorption (internal work of the material), the tested configurations are then compared regarding these two aspects.

6.2 Global analysis

We first perform a global analysis of the results obtained for all tested arrays, in search for optimal configurations regarding wave attenuation and wave absorption. In order to extract the best configurations in terms of wave attenuation, these are first sorted according to their reflection coefficients and as a function of their global transmission coefficient, represented in Figures 6.5. Each dot represents a row of the tested array, with the distance l/λ separating that same row from the first row (located at 0 for all cases), given by the horizontal axis grading. Depending on the array's value of K_r (a) or $\tilde{K}_t$ (b), the three dots that represent the 3-row array are sorted vertically, so that arrays with the largest coefficient values are placed at the top of the graphs. These orders are further illustrated by means of a colour gradient matching the range of coefficient values. In other words, three dots of identical colour and located at the same vertical position represent one configuration. The plotted results correspond to flexible cases with d_1.

In the case of reflection coefficients shown in Figure 6.5 (a), it is easy to notice that arrays with $\Delta l_{12} = \lambda/2$ are placed at the top of the plot, i.e. reflect the most, while the bottom half is shared between arrays with $\Delta l_{12} = \lambda/4$ followed by those with $\Delta l_{12} = \lambda/8$. This is expected, as it confirms that strong reflection is ruled by spacings $l = \lambda/2$ as we have seen in previous chapters. In fact, the most reflective array corresponds to configuration with constant $l = \lambda/2$, which we will refer to as l_{Bragg}, represented by the brown arrow in Figure 6.5 (a). On the other hand, the

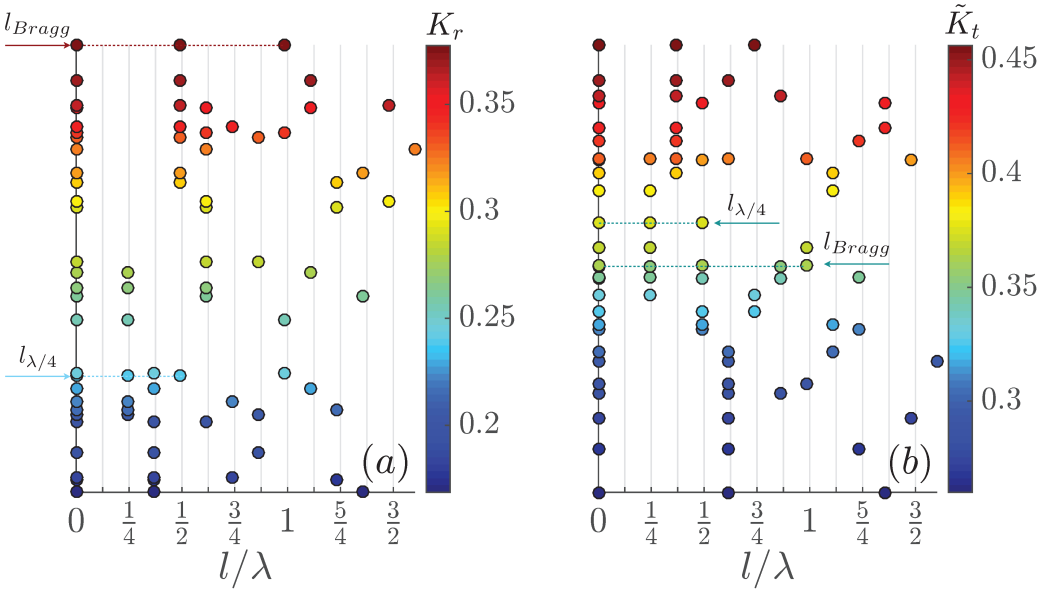

FIGURE 6.5: Graphical representation of all tested configurations, sorted as a function of increasing global reflection coefficient K_r (a) and global normalised transmission coefficient $\tilde{K}_t$ (b). Each configuration is represented by means of 3 circular markers of identical colour scaled to the associated global coefficient values. Vertical grid lines represent a spatial increment Δl of $\lambda/8$. Reference regular arrays $l_{\lambda/4}$ and l_{Bragg} are identified (arrows).

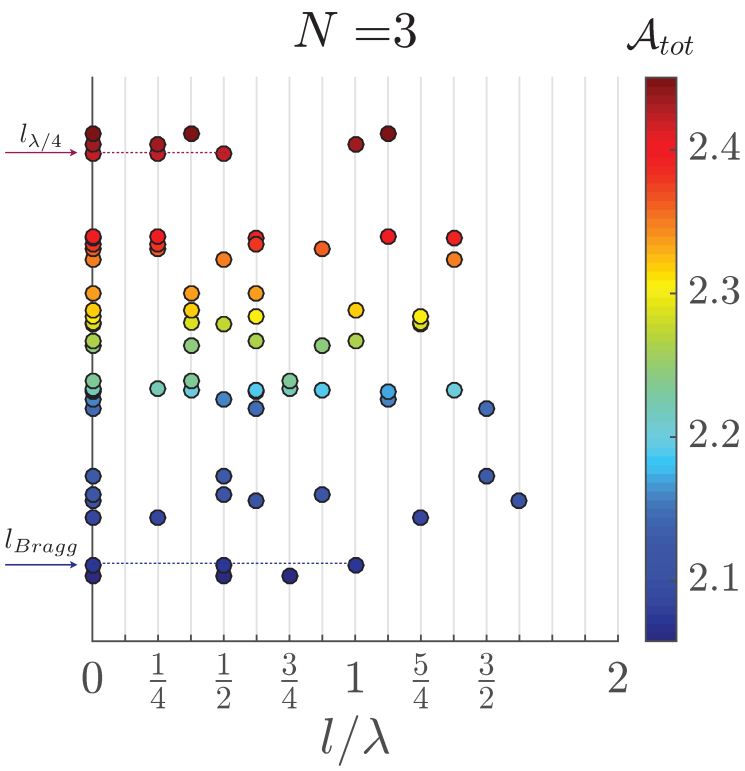

FIGURE 6.6: Graphical representation of all tested configurations, sorted as a function of increasing global amplification factor $\mathcal{A}_{tot}$. Each configuration is represented by means of 3 circular markers of identical colour scaled to the associated global coefficient values. Vertical grid lines represent a spatial increment of $\lambda/8$. Reference regular arrays $l_{\lambda/4}$ and l_{Bragg} are identified (arrows).

least reflective cases seen with $\Delta l_{12} = 3\lambda/8$ are not yet clear. For comparison, the regular configuration with constant $l = \lambda/4$ is also located with a blue arrow, near the bottom of the graph. This pattern will be referred to as $l_{\lambda/4}$.

Let us now consider the transmission plot (Figure 6.5 (b)). The arrays placed at the bottom of the plot, i.e. those transmitting the least amount of energy downstream correspond majoritarily to configurations for which $\Delta l_{12} = 5\lambda/8$ followed by those with $\Delta l_{12} = \lambda/4$ while those placed at the top of the plot have $\Delta l_{12} = 3/8\lambda$. Both reference patterns l_{Bragg} and $l_{\lambda/4}$ are located near the middle. This order does not mirror that seen previously for reflection (Figure 6.5 (a)) since transmission is also affected by the dissipation of waves caused by blade deflection. Transmission is a result of the competition between reflection and dissipation, therefore, blade oscillations must also be considered.

The same arrays are now sorted in terms of global blade oscillation amplification, which was shown to be proportional to energy dissipation (c.f. equation 5.36). Results are presented in Figure 6.6 below, with colours varying according to the measured coefficient $\mathcal{A}_{tot} = \sum_{n=1}^{N} \mathcal{A}_n$. As expected, we recognise our bounding reference cases with configuration l_{Bragg} located at the very bottom of the scatter plot (dark blue arrow) and regular case $l_{\lambda/4}$ placed third from the top (located with the brown arrow). The order in between remains to be understood.

6.3 Local analysis

Influence on the blade oscillations Let us now study these same results locally. In order to better understand the global results presented above, we investigate the influence of each separating distance Δl of the array on blade oscillations. Figure 6.7 below presents the normalised average blade oscillations of each row, as a function of separating distances Δl_{12} (a), Δl_{23} (b), and Δl_{13} (c) between rows. For a fixed separating distance Δl, the average results obtained from all tested configurations are presented by green, blue and orange markers for rows 1, 2 and 3, respectively and error bars are used to represent the standard deviation of all these results. As an example, consider the results for row 1 in green, located at $\lambda/2$ in Figure 6.7 (a). In this specific case, the marker represents the average value of all $\tilde{X}$ measurements taken for row 1, from all the configurations in which $\Delta l_{12} = \lambda/2$. The associated error bar therefore represents the deviation of the results found for all the different corresponding distances Δ_{23}. In other words, for that same marker, distance Δl_{12} is fixed while distance Δl_{23} is varied. With this representation, the influence of Δ_{12} on blade oscillations of row 1 is therefore evaluated by the fluctuations of the mean (circle marker) while the influence of Δ_{23} is represented through variations of the standard deviation.

Firstly, the results shown in Figures 6.7 (a-b) highlight the opposing influence of immediate neighbours. Indeed, when distance Δl_{12} is equal to half the wave length, row 1 oscillates with reduced amplitudes while those of row 2 are increased, and vice versa in the case of $\lambda/4$ (Figure 6.7 (a)). However, when it is distance Δl_{23} that is varied, these same responses are observed but shifted to rows 2 and 3 (Figure 6.7 (b)). The mechanism of these local impacts is summarised in the sketch of Figure 6.8 below, where positive contributions associated with constructive force interferences are illustrated in positive red sign while negative contributions associated with destructive force interferences are shown in negative blue signs. Two neighbouring rows oscillating in phase will have a negative impact on the front row oscillations and a positive contribution on the back row oscillations, while the opposite occurs

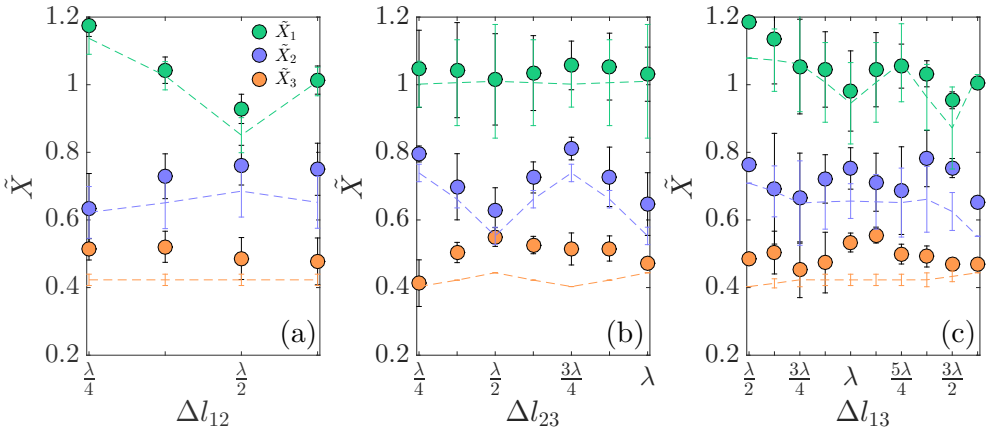

FIGURE 6.7: Normalised average oscillations of each row, as a function of separating distances between rows 1 and 2 (a), rows 2 and 3 (b) and rows 1 and 3 (c). Results associated with rows 1, 2 and 3 are presented respectively in green, blue and orange. Results are represented in averages (filled circles) and standard deviations (brackets) of all results obtained for the specific spatial shift Δl. Measured data is shown by circle markers while calculated values are plotted in dashed lines.

when oscillating out-of-phase. This mechanism confirms the results obtained previously in Chapter 5.

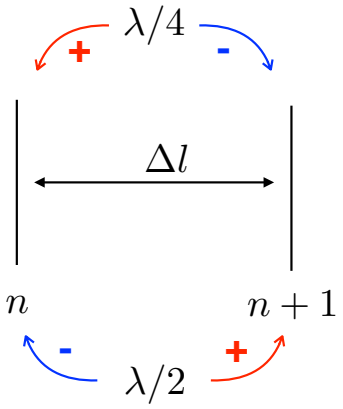

FIGURE 6.8: Sketch of the local effects due to interferences between neighbouring rows. For any row n, row $n+1$ placed directly behind will cause positive constructive force interference when their separating distance $\Delta l = \lambda/4$ and negative destructive force interference when $\Delta l = \lambda/2$. The contributions are mirrored for the back row $n+1$.

Furthermore, the results plotted in 6.7 also demonstrate that these influences remain essentially local. The value of Δl_{12} has a clear influence on the mean oscillations of rows 1 and 2, while little impact is observed on row 3 (Figure 6.7 (a)). On the other hand, the standard deviation of the results (represented by the brackets) is much smaller for results of $\tilde{X}_1$ than for $\tilde{X}_2$, which suggests that distance Δl_{23} has little impact on the oscillations of the front row. The response of row 1 is therefore dominated by the location of its immediate neighbour (row 2). The same results are seen when plotting results as a function of Δl_{23} (Figure 6.7 (b)), where row 1 is now almost un-impacted by the chosen distance, with average values remaining stable around 1, but demonstrates very large standard deviations, thereby confirming the

dominating influence of Δl_{12}. On the contrary, row 3 demonstrates some fluctuations but very limited variations in standard deviation. It is more strongly influenced by its distance from row 2 than from row 1. Row 2, however, shows large variations in both mean and standard deviation. Placed in the centre of the array, it is in fact an immediate neighbour to both rows 1 and 3 and is therefore impacted by both separating distances.

Finally, the results according to separating distance Δl_{13} plotted in Figure 6.7 (c) also suggest a local nature. Variations are much less obvious since this separating distance is the sum of Δl_{12} and Δl_{23}. Its influence therefore combines the effects stemming from both separating distances Δl_{12} and Δl_{23}, as seen from large variations in both averages as well as error bars for all three rows.

These experimental results therefore confirm the local nature of wave interferences on array excitation forces. The distance Δl separating two neighbouring rows that form a local pair have been shown to impact their oscillations, with minimal alterations observed on the rest of the array. However, these impacts are not equal between the neighbours and these contributions are found to have a larger influence on the front row of the pair. It is noted that the results obtained with the interference model are also plotted in Figure 6.7 and provide the same tendencies observed with the experimental data.

Contribution analysis In order to further understand these variations, we choose to quantify these local contributions, using equations 5.10 defined in the previous Chapter 5 and recalled below (equation 6.1).

$$\begin{aligned} R_n &= \frac{r t^n e^{i[\sum_{m=1}^{n} \varphi_m]}}{1 - r^2 e^{i2\varphi_{(n+1)}}} \sum_{k=0}^{N-n-1} t^{2k} e^{i2\sum_{m=n+1}^{n+k+1} \varphi_m} \\ T_n &= \frac{t^{(n-1)} e^{i\sum_{m=1}^{n} \varphi_m}}{1 - r^2 e^{i2\varphi_n}} \end{aligned} \tag{6.1}$$

The general expressions for R_n and T_n depend on local coefficients r and t, as well as on the phase shifts of interfering waves. We can therefore separate two types of contributions towards the resulting amplification factors: while the phase shifts of the interfering waves determine the nature of the amplification factors (positive or negative), the weight of these factors relies instead on local r and t coefficients, as identified in red and blue in equation 6.1. Taking our 3 row array, these weighing factors can be easily estimated for each row, as illustrated in the sketch given in Figure 6.9, in which reflecting contributions (related to R_n) are illustrated above the array, and transmission (related to T_n) at the bottom. The results corresponding to the case presented thus far (flexible array d_1) are underlined.

Local r and t were measured as 0.22 and 0.65, approximately, thus leading to a driving multiple reflection coefficient of $\frac{1}{1-r^2} \sim 1.05$. This means that the transmitted and reflected waves will be modified by 5% due to neighbouring multiple reflections. Applying this to our array, we therefore deduce that the choice of Δl_{12} will alter the reflected wave forcing for row 1 by 15%, but modify the transmitted wave force arriving onto row 2 by around 3% only. Recalling Figure 6.7 presented above, these percentages would correspond to the standard deviations. This contribution analysis confirms the results provided in Figure 5.15 in the previous Chapter, and demonstrates that row positions have a larger impact on the reflected component for wave forcing than on its transmitted part, i.e. $\mathcal{A}_n$ is more affected by its R_n component than by T_n. In our specific case, the benefit of row $n+1$ compared to that of

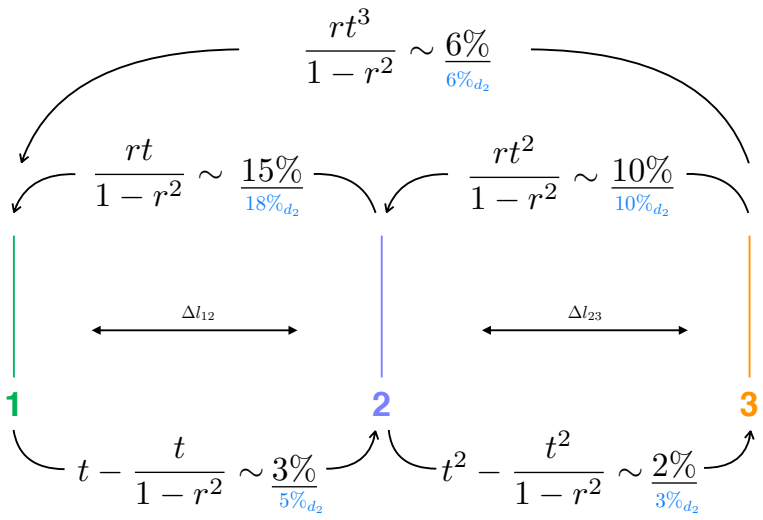

FIGURE 6.9: Sketch illustrating the contributions of each row within the array. The weight of each contribution is evaluated based on known r and t values, by means of equations 5.10 defined in the previous Chapter 5, for flexible d_1 (black underlined) and d_2 (blue) arrays. Results associated with reflection R_n and transmission T_n factors are illustrated above and below the sketched array, respectively.

row n is 5 times less. Given that the front rows are those that demonstrate largest oscillations since the waves are damped as they propagate through the array, their amplification factors will have the largest impact on the total array amplifications.

This is in fact observed when plotting global cumulative oscillation amplifications ($\Sigma\tilde{X}$) as a function of separating distances (c.f. Figure 6.10). This representation highlights the dominating effects of these interferences. Focusing on the distances separating immediate neighbours (a) and (b), global variations are seen to match those observed previously for front row 1 and middle row 2, when varying distances Δl_{12} and Δl_{23}, respectively. Recalling the 2-row item sketched in Figure 6.8, this would suggest that the contributions seen by the front row n overpowers those of row $n+1$ regardless of the presence of other additional rows. It is also noted that the results obtained with the interference model plotted in Figure 6.10 provide here again satisfying representations of the tendencies observed with the experimental data; the effects of Bragg scattering stand out clearly in the plots. However, calculated values are slightly lower than experimental data. This is thought to arise from tracking errors, evaluated at $\sim 6\%$ on the average. Taking as an example the normalised cumulative oscillations for Δl_{12} found to be around 2.3 experimentally compared to 2.15 with the model, the corresponding difference would indeed equal our error margin. This leads us to believe that the variations obtained from the interference model are valid.

Influence on the wave field Finally, the dominance of R_n over T_n seen found from the weighing factors calculated above (Figure 6.9) also holds true for global reflection K_r and transmission k_t coefficients. Figure 6.11 presents the measured K_r and $\tilde{K}_t$ coefficients, as a function of separating distances Δl_{12} (a), Δl_{23} (b), and Δl_{13} (c) between rows. Reflection and transmission coefficients are plotted in red and blue

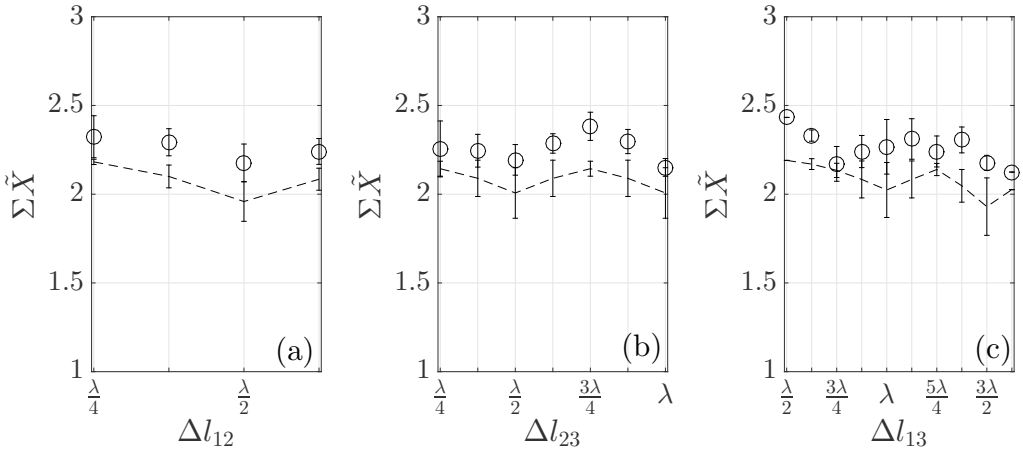

FIGURE 6.10: Normalised cumulative average oscillations in the array $\Sigma\tilde{X}$, as a function of separating distances between rows 1 and 2 (a), rows 2 and 3 (b) and rows 1 and 3 (c). Results are represented in averages (filled circles) and standard deviations (brackets) of all results obtained for the specific spatial shift Δl. Measured data is represented in circle markers while calculated values are plotted in dashed lines.

markers, respectively, along with their sum in grey. As before, error bars are used in order to represent the spread of the results obtained from all the tested configurations, for the specific studied spacing Δl. All cases demonstrate much stronger variations on the global reflection coefficients than on global transmission, which is coherent with the contribution analysis provided above.

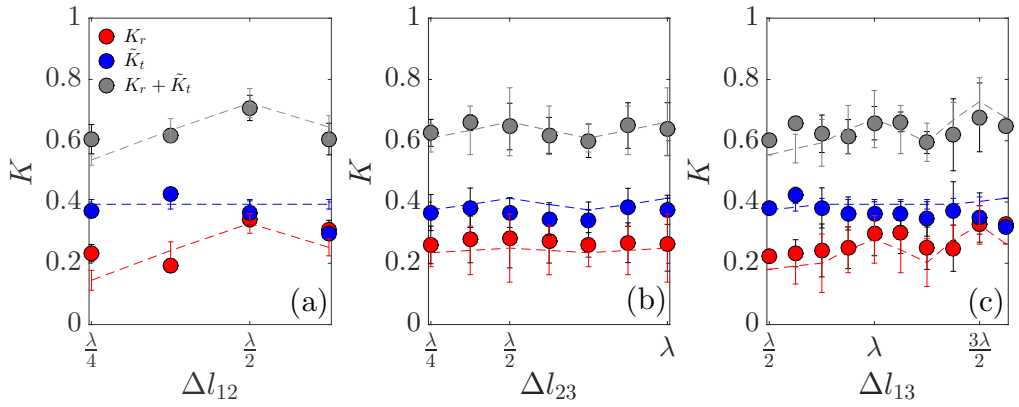

FIGURE 6.11: Global reflection K_r and transmission $\tilde{K}_t$ coefficients, as a function of separating distances between rows 1 and 2 (a), rows 2 and 3 (b) and rows 1 and 3 (c), for all tested configurations. Reflection and transmission coefficients are plotted in red and blue markers, respectively, along with their sum in grey. Results are represented in terms of averages (filled circles) and standard deviations (brackets) obtained for the specific spatial shift Δl. Measured data is plotted in circular markers while calculated values are represented with dashed lines.

The corresponding results obtained using the interference model are presented by means of dashed lines in the same Figure 6.11. Input parameters $r = 0.22$ and $t = 0.65$ are chosen here, which are close to those measured experimentally for a single row. The calculated variations agree well with those found with experiments, with reflection peaks found when immediate neighbours are separated by $\Delta l = n\lambda/2$. Transmission is hardly affected by the chosen distances Δl, thereby

leading to variations of the unabsorbed waves (grey markers) matching those of the reflection coefficients.

6.4 Optimal hybrid

We can now return to our original question, i.e. is there an optimal configuration regarding both wave attenuation and energy absorption? In order to evaluate the optimal array, in its dual application, we cross the solutions for minimum transmission and maximum oscillations. This is done by summing $\mathcal{A}_{tot}$ values and $(1 - \tilde{K}_t)$ values for each configuration, before sorting the results to find the configuration that provides a maximum total dissipation factor $\mathcal{K} = \mathcal{A}_{tot} + (1 - \tilde{K}_t)$, i.e. maximum wave attenuation and absorption.

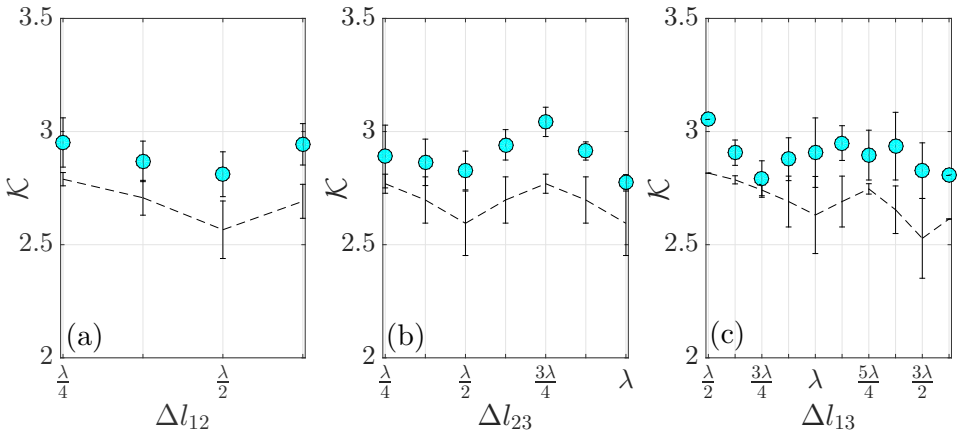

FIGURE 6.12: Measured $\mathcal{K}$ coefficients, as a function of separating distances between rows 1 and 2 (a), rows 2 and 3 (b) and rows 1 and 3 (c). Results are represented in averages (filled circles) and spread (brackets) of all results obtained for the specific spatial shift Δl, and compared with calculated results plotted in dashed lines.

Figure 6.12 plots these measured coefficients as a function of separating distances between rows 1 and 2 (a), 2 and 3 (b) and 1 and 3 (c). The observed variations are very close to those found previously regarding normalised oscillations $\Sigma\tilde{X}$, with minima found in the cases of Bragg scattering. Although these configurations might benefit attenuation, the previous results demonstrated that this benefit is counterbalanced by the reduction in blade oscillations and, thus, in global energy absorption. In fact, these plots confirm that in the case of flexible arrays, wave interferences have little effect on the global transmission coefficients, but, instead, affect the share between global reflection and absorption. It is therefore clear that optimal hybrid arrays rely mainly on maximal amplification factors.

The same results are presented via a scatter plot shown in Figure 6.13, in which all configurations are sorted according to coefficient $\mathcal{K}$ defined above. The bounding cases l_{Bragg} and $l_{\lambda/4}$ can be identified at the very bottom (dark blue) and third from the top (dark red), respectively. In this specific case, the difference between the optimal array and l_{Bragg} pattern is evaluated as approximately 14%. These results highlight the competition between reflection and absorption. It is therefore clear that an optimal hybrid array will in fact be that of minimum K_r.

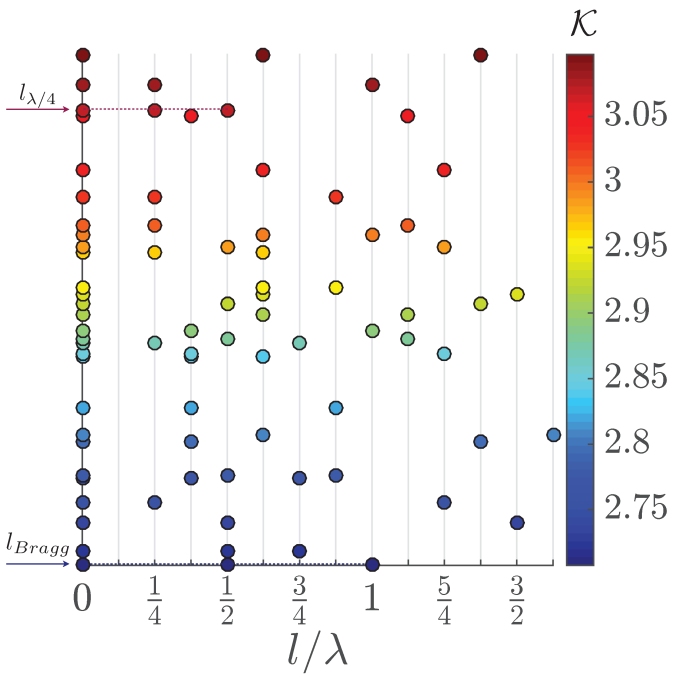

FIGURE 6.13: Measured optimal hybrid configurations. Graphical representation of all tested configurations, sorted as a function of increasing global dissipation factor $\mathcal{K}$ coefficient, representing maximal wave attenuation and absorption. Each configuration is represented by means of 3 circular markers of identical colour scaled to the associated global coefficient values. Vertical grid lines represent a spatial increment of $\lambda/8$. Reference regular arrays $l_{\lambda/4}$ and l_{Bragg} are identified (arrows).

6.5 Varying local parameters

Weighing factors It is clear that the results presented thus far rely strongly on the values of r and t and that the underlying local contributions will be altered as soon as these parameters are modified. This modification is first evaluated by comparing blade oscillations obtained for the flexiblearrays of d_2, i.e. for a lateral spacing d that is half that of configuration d_1.

Let us first compare results obtained for both flexible cases. Recall Figure 6.7 presenting the normalised average oscillations for each row, depending on separating distances Δl_{12} (a), Δl_{23} (b), and Δl_{13} (c) for flexible d_1 arrays. The same local analysis is performed on configurations d_2, i.e. for a lateral spacing d that is half that of configuration d_1, and plotted in Figure 6.14, using square markers. These are found to be very close to those presented for d_1, thereby validating the observed tendencies. Peaks and troughs of the measured variations are simply shifted in these new cases. This is understood by the fact that each row transmits a little less ($t \sim 0.55$) and reflects more ($r \sim 0.3$) leading to stronger interferences. Let us here again perform a contribution analysis. The same weighing factors described previously are estimated for the d_2 arrays and represented in blue in Figure 6.9. In this case, the contributions from row 3 are unchanged, while all other weighing factors are slightly higher than the previous d_1 case, which is coherent with the experimental observations. Variations are thus identical in nature (same phase shifts) but their intensity is altered by the new values of local r and t.

In order to further evaluate the variations of local parameters r and t as a function of confinement ratio, measurements of the local r and t coefficients were performed for the single row of flexible blades, for varying spacings $d \in [\lambda/8 - 5\lambda/4]$ (which

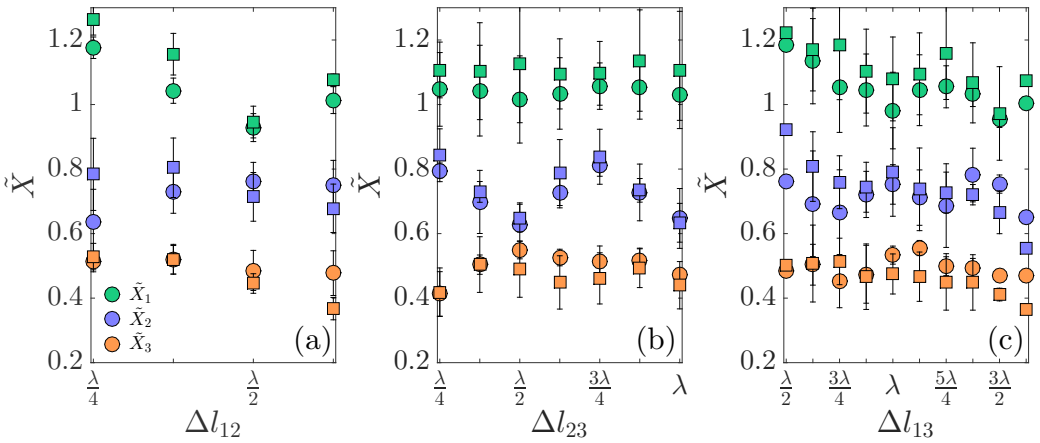

FIGURE 6.14: Measured normalised average oscillations of each row, as a function of separating distances between rows 1 and 2 (a), rows 2 and 3 (b) and rows 1 and 3 (c) for all tested configurations using flexible blades with lateral distances d_1 (circle markers) and d_2 (square markers). Values associated with rows 1, 2 and 3 are presented respectively in green, blue and orange. Results are represented in averages (filled markers) and standard deviation (brackets) of all results obtained for the specific spatial shift Δl.

include previous cases $d_1 = \lambda/2$ and $d_2 = \lambda/4$). The results are plotted in Figure 6.15.

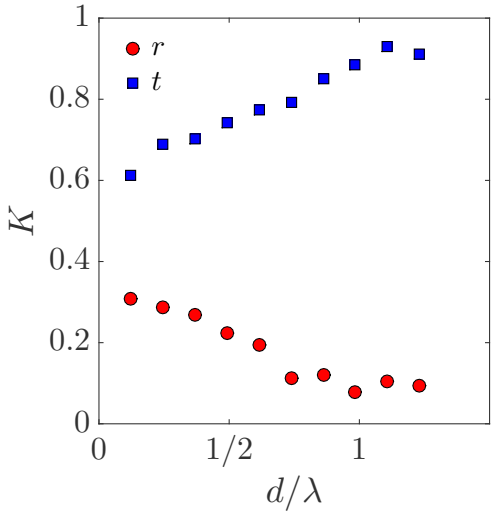

FIGURE 6.15: Measured reflection (red) and transmission (blue) coefficients for a single row of flexible blades, with varying lateral separating distance $d \in [\lambda/8 - 5\lambda/4]$.

The variations are measured to be approximately $r \in [0.1 - 0.3]$ and $t \in [0.6 - 0.95]$. With similar reflection coefficients found for rigid blades, it is reasonable to assume that $r \leq t$. Therefore, contributions through R_n will always exceed contributions through T_n, and, so optimal patterns will always converge towards those favouring front row amplifications.

Nature of interferences The competition between row contributions would therefore rely on these local coefficients. However, this still does not explain why optimal

configurations are not systematically $l = \lambda/4$. In fact, previous results demonstrated that optimal arrays deviate from regular patterns for odd-numbered arrays only, i.e. when $N = 3, 5, 7$ etc, (c.f. Figure 5.18 from Chapter 5). The reason for other possible patterns providing optimal amplifications lies in the phase shifts.

Recalling Figure 5.9 which represented the global reflection coefficient of varying array sizes of regular patterns, the same plot is provided for odd-numbered arrays in Figure 6.16. This representation gives a good indication of the effect of row spacings on interference. Unlike previously seen for even arrays, the plot demonstrates that the minima in global reflections are here shifted either side of local spacing $l = \lambda/4$, by $\sim \lambda/6$ in the case of $N = 3$ (represented by the orange arrows in Figure 6.16). Following the observation that oscillation amplitudes mirror global reflection, then these minima $|R_z|$ would lead to maximal oscillations. These are further multiplied and shifted as the total number of rows increases, and with decreasing magnitude as indicated by the orange (N=3), blue (N=5) and red (N=7) arrows. We can therefore see that this deviation converges rapidly (N>7) towards a minimum at $l_{\lambda/4}$ which corresponds to the case of infinitely large arrays (black curve). This explains the observations previously made regarding percentage increase in K_a between optimal configurations and regular patterns (c.f. Figure 5.21 in Chapter 5), where the values decreased rapidly for arrays larger than $N = 3$.

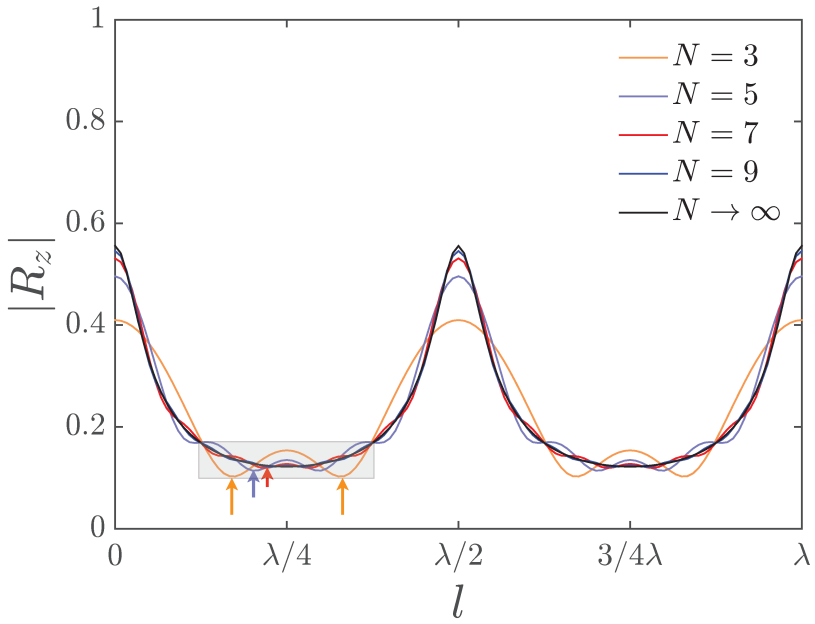

FIGURE 6.16: Calculated global reflection coefficient $|R_z|$ for odd-numbered arrays, as a function of spacing l and for increasing number of rows N.

These deviations, however, remain limited and do not exceed 3% from the reference curve (black). This is illustrated by the grey area in which all values of $|R_z|$ remain within the range $[0.10 - 0.16]$. This suggests that for this large bandwidth of low reflection, the corresponding impact on wave forcing will be very similar. Any choice of spacing l within that region will therefore provide similar amplification factors, which would explain why a wide range of configurations still provide similar results. Only the Bragg peak is very sharp and narrow and, thus, has a large impact on these factors leading to a strong reduction in array performance.

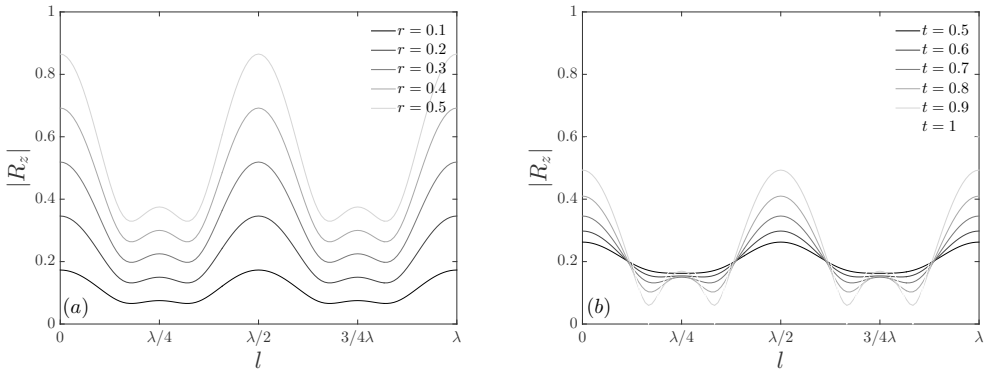

FIGURE 6.17: Calculated global reflection coefficient for an array composed of three rows ($N = 3$), as a function of spacing l, for varying r (a) and varying t (b). The fixed values are $r = 0.2$ and $t = 0.8$.

This global shape and size is once again strongly dependent on the values of r and t, as plotted in Figure 6.17, where the variations of $|R_z|$ are calculated for local values of $r \in [0.1 - 0.5]$ (a) and $t \in [0.5 - 1]$ (b). Notice how the variations are intensified by both r and t while these are also shifted upwards as r increases. In general, however, it can be concluded that these minima become more visible for the largest values of r and t, which correspond to the cases of largest energy transfer and associated interferences.

6.6 Conclusion

In this chapter, we have investigated the impact of wave interferences on array performances regarding both wave attenuation (low transmission) and power absorption (large blade oscillations). The study was undertaken by means of experiments performed with arrays composed of three rows, for which a large range of possible combinations of separating distances were tested. Global reflection and transmission coefficients were measured along with average blade oscillations for each row, from which amplification factors $\mathcal{A}_n$ could then be evaluated. The influence of interference on these three quantities was analysed both globally and locally and the results obtained were compared to model predictions. The study demonstrated that the array response mechanisms were in fact driven by local interference, with the strongest variations seen to depend on the phase shifts of immediate neighbours only. The full array can therefore be decomposed into pairs of rows, for which the associated spacing Δl affects the front and back row in an opposite manner. Therefore, since the front rows are those subject to the largest excitation forces (wave energy decreases as these travel through the array), then optimal configurations remain close to the regular pattern $l_{\lambda/4}$. The front row of each successive pair is then forced with maximal amplification.

As discussed in the previous paragraphs, however, these conclusions rely on the specific local coefficients of the single row case. One can therefore question whether such tendencies can be extrapolated for all arrays or if they in fact rely on the specific local parameters, such as r, t, as well as the total number of rows N. From typical measured values of r and t, it is reasonable to assume that the local reflection parameter r will not exceed 0.3. In this range of low values, optimal patterns will always converge to $l_{\lambda/4}$ for even numbered arrays. As t values decrease, i.e. absorption increases, interferences will reduce and amplifications of the performances will become less evident. Optimisation through collective array behaviour therefore proves to be most effective for the least individually efficient absorbers. Concerning odd-numbered arrays, optimal configurations deviating from this regular patterns are feasible, due to a shift in global reflection minima. However, their improved efficiency remains limited to the specific cases of small array sizes (3-rows) and larger values of r. When moving away from these specificities, the increase in wave forces will become negligible. In all cases, global wave reflection provides an indication of the opposing excitation force dynamics, and, so an indication of possible wave absorption. In other words, this quantity can be interpreted as the energy that is unavailable for absorption and, thus, Bragg scattering should be avoided.

Chapter 7

Conclusions and perspectives

7.1 Contributions

In this thesis, we have explored the interaction of arrays of flexible structures with surface gravity waves, and their effect on wave energy distribution. This investigation was performed primarily by means of experiments, complemented by the use of simplified physical models for the description. These interactions are complex and rely on many parameters relating to the characteristics of both the fluid and the solid. We chose to focus the study on the effect of geometrical arrangement on both the wave field and the array's response, while fixing the shape, size and material of the single model object, as well as its submergence ratio.

The experimental studies presented in Chapter 4 served to characterise our system by modifying its wave conditions and its spatial configuration, step by step. In the optimal conditions, i.e. when the blades were seen to oscillate with maximum deflection, the flexible arrays were found to attenuate waves by up to 40% more than their rigid equivalent, due to the energy dissipated through the motion of the blades. Only part of this additional dissipation is due to the internal mechanical work of the blade material. Regarding wave energy harvesting, it is this quantity that could be converted into electricity. In our system, this only accounted for a maximum of 10% of the total energy. The rest of the energy was shown to be lost to the fluid through an increased drag force between the oscillating blades and the moving fluid, due to a phase shift between the velocity of the solid structure and that of the fluid particles. This is true for inertia-dominating regimes. In these conditions, therefore, flexible structures will be more effective than their rigid equivalent in attenuating waves, by increasing external friction, regardless of the object's internal work. For a dual application therefore, optimal structures would be flexible structures tuned to the frequency of the incoming waves, with a high damping coefficient, and that are sized to match low KC numbers. These conditions would guarantee maximising the object's internal dissipation (potential harvesting energy) and external friction (increased wave attenuation).

Regarding the global wave field, these experiments also demonstrated that transmission depends essentially on wave frequency with respect to blade resonance, while reflection relies very much on geometrical spacing and object size. In parallel, the array's response was seen to vary according to both, with maximum deflection occurring at the blades' resonant frequency and external force amplitudes changing with wave interferences. Following these observations, we developed an interference model in Chapter 5, in order to describe and predict the array responses, based on known local reflection and transmission coefficients. The global performance of the array was shown to be dominated by local interferences associated with hydrodynamic inertial forces, i.e. with fluid particle accelerations. Given that

these follow opposite trajectories for opposite directions of propagations, their associated constructive and destructive interference are shifted by $\pi/2$ from wave amplitude interferences. Therefore, optimal configurations are found for regular spacings $l = n\frac{\lambda}{2} + \frac{\lambda}{4}$. This shift implies that amplifications resulting from such constructive effects cannot be accumulated for all rows, which provides a strong disadvantage regarding the performances of wave energy harvesters placed in arrays. This problem of array design was explored by testing additional irregular patterns by means of the model and experiments in Chapter 6. It was found that certain specific irregular patterns could indeed serve to amplify global excitation forces, although the benefit remained limited and many optimal cases converged towards a regular pattern of spacing $l = \lambda/4$. It was on the other hand clear that Bragg scattering is strongly detrimental regarding blade oscillations. Optimal configurations were seen to rely strongly on local values of reflection and transmission coefficients. The question remains as to how these values can be modified.

7.2 Perspectives

The conclusions of this thesis have provided a better understanding of the mechanisms involved between surface waves and an array of flexible structures. The key variables identified in our system are therefore the damping coefficient $\gamma_s = \Gamma_{int}/2m$ which determines how much energy will be damped through material work, the external drag coefficient C_D, which will determine how much energy will be dissipated and lost to the fluid, along with the damping coefficient γ_{rad} which also indicates how energy will be radiated in the far field, and which corresponds to another form of external damping. All of these will affect the driving parameters of the array's response, i.e. local reflection, transmission and dissipation coefficients. These variables rely on other factors that have not yet been studied, such as the role of flexibility, submergence ratio or shape. A preliminary study using cylinders instead

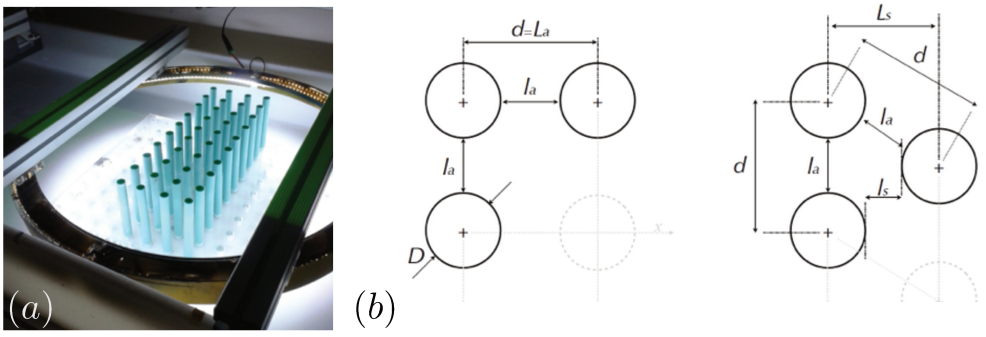

FIGURE 7.1: Photo of small-scale experiments run using flexible cylinders instead of blades (a). Sketch of associated aligned and staggered patterns (b).

of blades has shown that such a shape can indeed provide a means of absorbing wave energy more effectively (see Appendix C). For a similar measured Γ_{int}, the larger volume of material (and so the larger mass m) causes the damping coefficient γ_s to increase. Therefore, the internal damping is increased. Furthermore, the circular shape reduces form drag and, therefore, external frictional losses. Hence, the additional energy that is dissipated by the flexible array compared with rigid cylinders is in this case transferred to the beam more efficiently. The potential for energy

harvesting is increased. Furthermore, these circular beams would theoretically also be able to adapt to any angle of incident waves, since these are able to bend in all directions.

Regarding real applications for wave attenuation and energy harvesting, further work and explorations should also be undertaken in order to test the model against more realistic conditions. A preliminary study was undertaken at the Laboratory "Ondes et Milieux Complexes" (LOMC) in Le Havre in order to test our model at a larger scale (c.f. Figure 7.2 (a-b) and Appendix D)). This preliminary test showed the difficulty in up-scaling such a system; in which many parameters are involved. However, these first results are promising, with key tendencies and mechanisms being overall well represented in our model. Nonetheless, further work is necessary to confirm these. Studies at this scale would also enable an easier means of testing the system in other wave conditions, such as polychromatic waves and with larger amplitudes, as a better representation of realistic conditions. In this sense, the system could be tested in terms of its bandwidth for operation.

Finally, another clear step for this project would be the implementation of an actual means for extracting the energy that is stored in the mechanical bending of the objects. This was originally envisaged in the scope of the thesis by means of piezo-electric sheets, that would be attached onto our blades (or plates in the case of the larger scale). Discussions have in fact been undertaken with teams at the Hochchule Rhein Waal, GeorgiaTech, as well as the Jon Hopkins University regarding such projects. The latter has recently studied possibilities for optimising wave energy harvesting materials, by means of several tuning mechanisms for these materials (c.f. Figure 7.2 (c)). The aim would to be combine these methods together with array optimisation in order to obtain a multi-resonant system, for which both the bandwidth and the efficiency are increased.

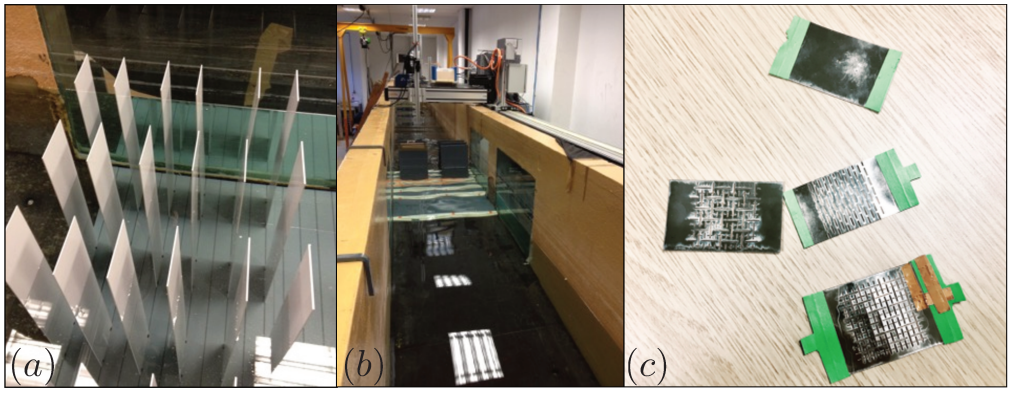

FIGURE 7.2: Photos of the up-scaled arrays used for the experiments run at the LOMC (a-b) and photos of typical tunable piezo-electric sheets developed by Jon Hopkins University (c).

Appendix A

Complementary details on experimental methods (Chapter 3)

A.1 Base effects

We wish to evaluate the effect of the chosen base board on the surface waves, in order to check the hypothesis of deep water waves. Measurements of the surface elevation η is taken for case with (red) and without (blue) the base, for a frequency of 4.5Hz as shown in figures A.1(a). These are measured for a single point of the treated wave map, averaged in the transverse $y-$direction, as indicated by the black area plotted in figure A.1(c). The associated FFT signals are provided in plot A.1(b).

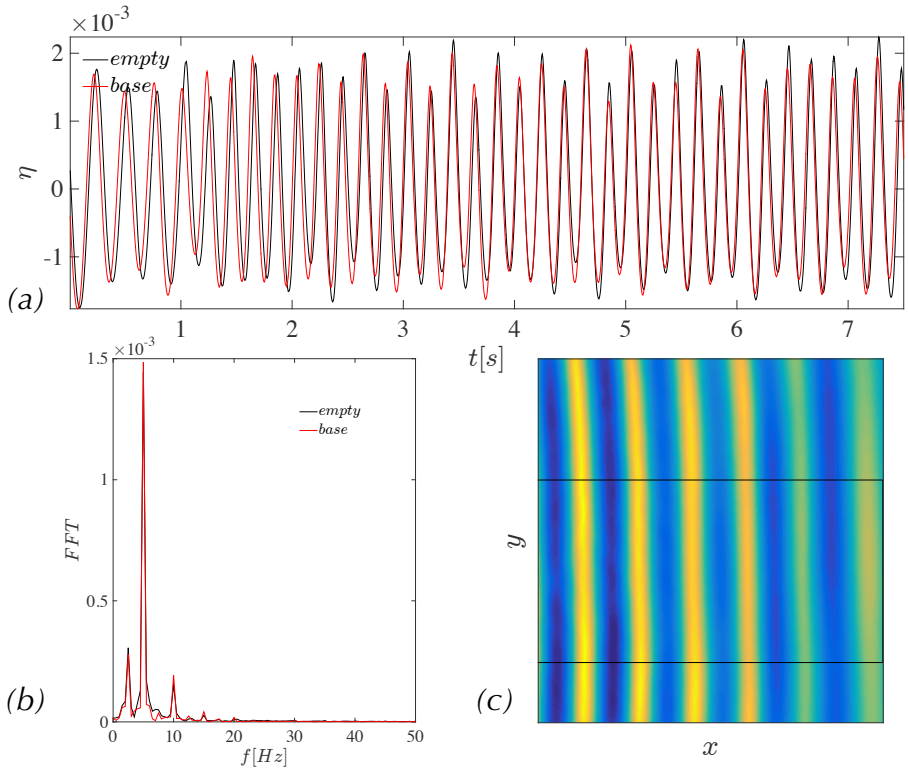

FIGURE A.1: Comparison between wave fields obtained with (red curves) and without (black curves) the lego base. Average signals over time during wave transient of the first 1500 images (a), FFT signals for time frame t∈[2-4]s, (b) and zone over which the transverse average is applied (c).

The results suggest that the presence of the base board can be neglected in our analysis.

A.2 Recording time frame

In order to avoid multiple tank reflections, the experiments are analysed for the first train of waves only, as described in chapter 3. The corresponding recording characteristics are summarised in table A.1.

$f[Hz]$	$v_g[m/s]$	$t_{begin}[s]$	$t_{end}[s]$	$\#T_{analysis}$	$margin[\%]$
2	0.35	5.42	12.66	7	53
2.5	0.32	6.02	14.04	8	58
3	0.28	6.86	16.02	10	63
3.5	0.24	7.82	18.26	11	68
4	0.21	8.84	20.65	13	71
4.5	0.21	9.74	22.73	15	74
5	0.18	10.67	24.92	16	76

TABLE A.1: Summary of recording characteristics for all tested frequencies for experiments run in the intermediate tank.

A.3 Convergence test for the selection of points x_a, x_b, and x_c

As explained in chapter 3, the selection of points x_a, x_b, and x_c for the measurement of reflection and transmission coefficients can provide erroneous results. In order to obtain more reliable and systematic measurements, these are instead selected randomly within the corresponding zones $Z1$ and $Z2$ i times. An example of the coefficient results is shown in figure A.2, for 100 iterations. One can once again notice sharp peaks and noisy results. The average values of these results are now

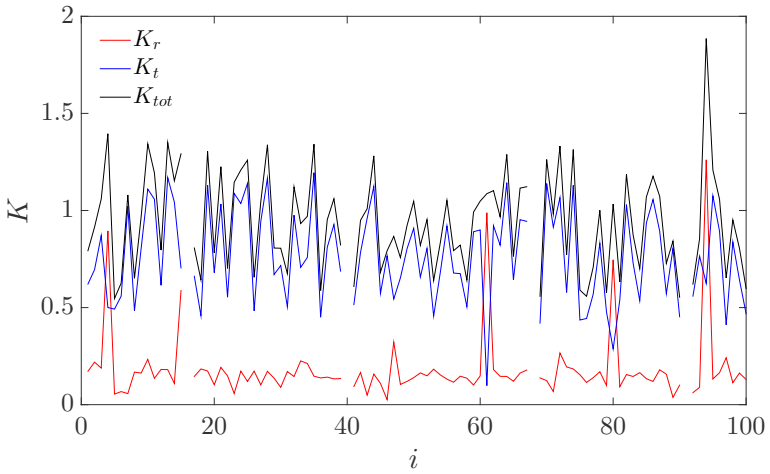

FIGURE A.2: Calculated K_r and K_t versus iteration number i for the randomly selected points $\{x_a; x_b; x_c\}$. The example is shown for a single row of rigid blades with $d = \lambda/2$.

taken so that $K = \bar{K}_i$ and the maximum number N of iterations is tested and presented in figure A.3, where K_r, K_t and the sum of the two are plotted in red, blue and black curves, respectively. From the results, a total number $N = 200$ was deemed sufficient to achieve convergence.

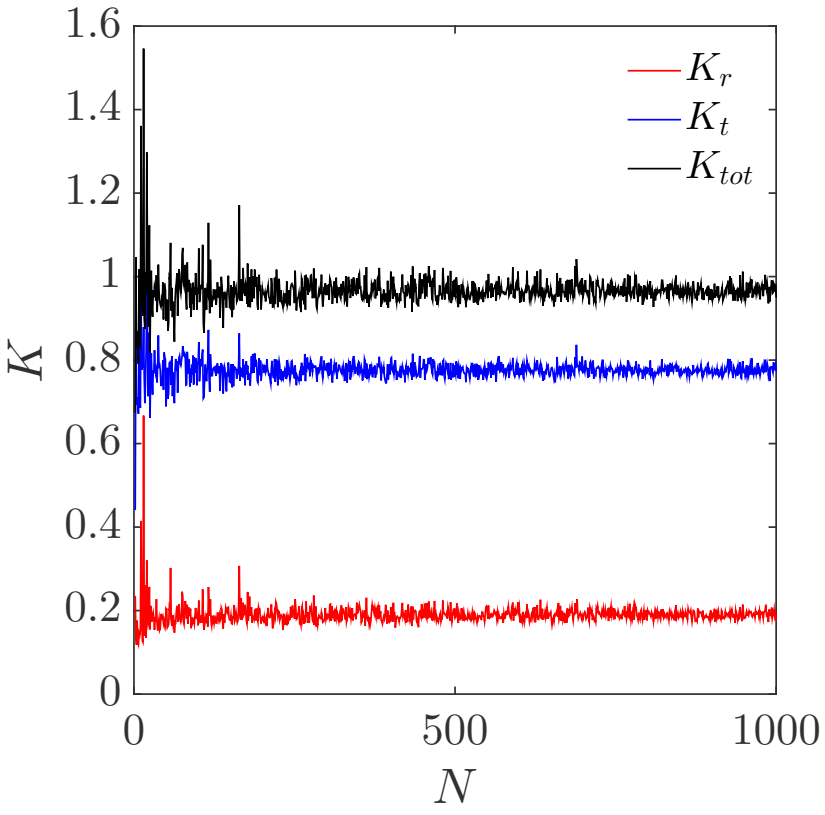

FIGURE A.3: Calculated K_r and K_t averaged over a total number N of iterations for the randomly selected points $\{x_a; x_b; x_c\}$. The example is shown for a single row of rigid blades with $d = \lambda/2$.

Appendix B

Relative velocity evaluation in oscillatory flow

We perform a study of the relative motion of water particles and blade tip oscillations in order to derive an expression for the relative velocity u_r used to estimate the drag force caused by the oscillating blade subject to surface waves in Chapter 4.

Relative motion measurements We compare the variations of the surface wave elevation η (amplitude a) and the blade tip oscillations x (amplitude X) as a function of time, as shown in the sketch provided in Figure B.1 (a). The spatio-temporal plot shown in Figure (c) corresponds to the red dashed line sketched in Figure B.1 (b). This plot shows that the amplitude a of the travelling wave does in fact reach the blade's resting location (represented by the dashed black line) when its deflection is maximum (X).

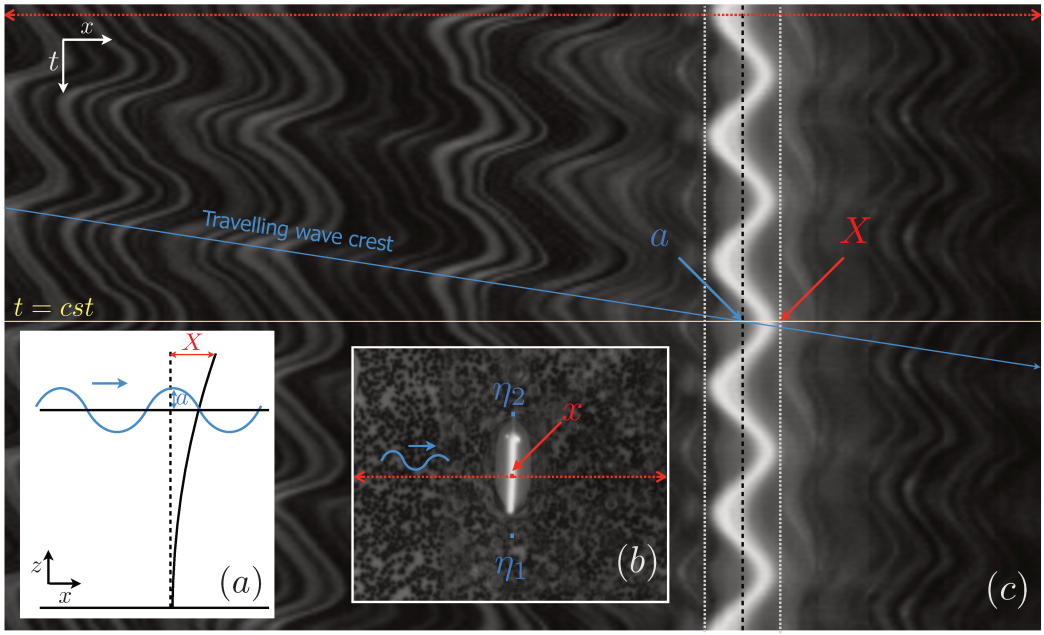

FIGURE B.1: Measurement of relative motion. Sketch of maximum blade tip amplitude X and wave amplitude a (a). Points of measurement (b) for blade tip motion $x(t)$ and two surface waves of similar location $\eta_1(t)$ and $\eta_2(t)$ for comparison in Figure B.2, along with the central line chosen for a spatio-temporal plot of (c).

However, this measurement method is not very precise and we chose to complete this by comparing the variations in times of η_1 and η_2 to the blade tip oscillations x

taken from the same video recording (c.f. Figure B.1 (b)). This is presented in figure B.2 (a).

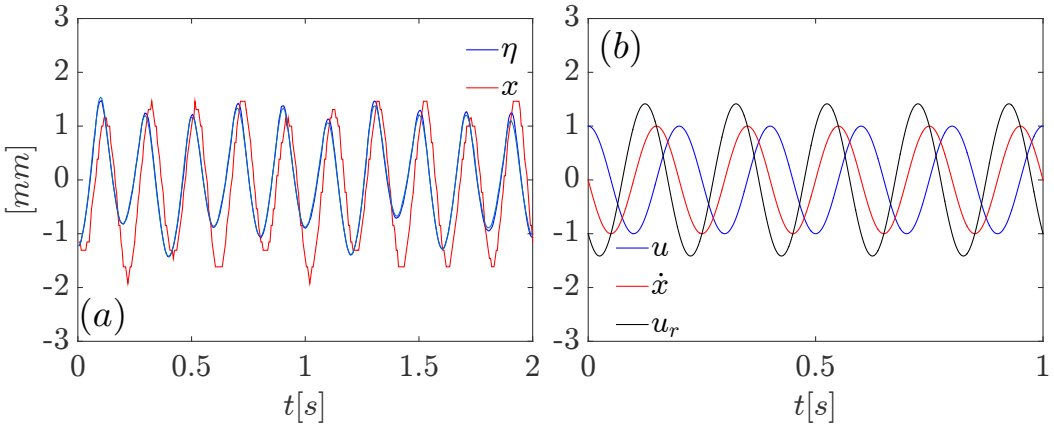

FIGURE B.2: Comparing wave and blade mechanics. Measured values of η_1 and η_2 (blue curves) along with measured blade tip oscillations x (red curve), as a function of time (a), based on the measurement points shown in Figure B.1 (b). Calculated variations of water particle velocity u (blue curve) and blade velocity $\dot{x}$ (red curve) as a function of time, for an equivalent velocity amplitude equal to 1 (b). The resulting relative velocity $u_r = \dot{x} - u$ is also plotted in black.

The results show a close match between the two quantities. Both measured wave elevations η fall on the same blue curve, while the tip oscillations are very slightly shifted forward (red curve). However, this slight shift is thought to come from a small measurement error due to the angled view of the blade in the camera frame.

Recalling the linear wave theory presented in Chapter 2, horizontal water particle velocities u vary in phase with the surface wave elevation η to give, in deep water conditions: $u(t) = \omega\eta(t) = \omega a\cos(\omega t)$. On the other hand, the blades will oscillate at their tip with a velocity $\dot{x}(t) = -\omega X\sin(\omega t)$, where ω is the wave frequency $2\pi f_0$. This suggests that in fact the two velocities are shifted by $\pi/2$. If we assume that the blade excursion has a similar amplitude as that describing the water particle motion, then we can estimate the resulting relative velocity amplitude and phase shifts through trigonometric working, as illustrated graphically in Figure B.2 (b).

Mathematical estimation of relative velocity magnitude Let $u(t) = \omega a\cos(\omega t)$ be the horizontal velocity of water particles at a single point of the water surface and $\dot{x}(t) = -\omega a\sin(\omega t)$ be the velocity of the blade section position $z = h$ located at the surface of the water. Both motions are assumed to have the same amplitude a and angular frequency ω.
Given the trigonometric identity:

$$A\sin\alpha - A\sin\beta = 2A\cos(\frac{\alpha+\beta}{2})\sin(\frac{\alpha-\beta}{2}) \tag{B.1}$$

we take $\alpha \to -\alpha$ and $\beta \to (\alpha + \pi/2)$ and show:

$$-A\sin(\alpha) - A\cos(\beta) = 2A\cos(\frac{-\alpha + \alpha + \pi/2}{2})\sin(\frac{-\alpha - \alpha - \pi/2}{2}) \tag{B.2}$$

$$= 2A\cos(\frac{\pi}{4})\sin(-\alpha - \frac{\pi}{4}) \tag{B.3}$$

$$= \sqrt{2}A\cos(\alpha + \frac{3\pi}{4}) \tag{B.4}$$

$$\tag{B.5}$$

In our specific case, $A = \omega a$ and $\alpha = \omega t$.
The relative velocity $u_r(t) = \dot{x}(t) - u(t)$ can then be expressed as:

$$u_r(t) = \sqrt{2}(\omega a)\cos(\omega t + \frac{3\pi}{4}) \tag{B.6}$$

$$\tag{B.7}$$

Therefore it is equivalent to the expression of $u(t)$ with an amplitude increased by a factor $\sqrt{2}$ and a phase shift of $\varphi = \frac{3\pi}{4}$. When estimating the drag forces, we therefore estimate the relative velocity amplitude u_r to be equivalent to $\sqrt{2} \cdot u$.

Appendix C

Preliminary study using cylindrical beams

In the experiments presented in this thesis, we have simplified our system into a single-dimensional problem in order to understand basic principles of wave-structure interaction of flexible arrays. This was done by using blades as a model for the flexible beams. However, natural flexible structures such as aquatic plants are not always blade-shaped and, for example, the main stem of individual kelp plants take the shape of circular beams. In order to study further wave-plant interactions, it would therefore be useful to also study model cylindrical beams. Additionally, in terms of wave energy extraction, limiting the harvester's motion to a single direction is not optimal since waves are in reality multi-directional. Circular beams would alleviate this restriction and allow for full 360° directional freedom. In theory, therefore, the beam could adapt to all directions of incoming waves.

Experimental methods This problem becomes quickly very complex given the infinite number of degrees of freedom involved. As a first preliminary step, we have investigated the role of spatial configuration and flexibility on wave attenuation for an array of circular beams subject to monochromatic and unidirectional waves, and tested 4 configurations, as follows:

- aligned flexible beams
- aligned rigid beams
- staggered flexible
- staggered rigid

It was thus possible to compare aligned configurations with staggered configurations, and flexible with rigid arrays for both configurations. For each case, arrays of rows $N \in [1-4]$ were tested, in which each row was composed of 10 beams.

Beam diameters were fixed at 14 mm and both aligned and staggered arrays consisted in regular spacing between neighbours. Distance d between centres was kept constant at 3.5 cm, which led to the various separating distances between rows sketched in Figure C.1 and summarised in Table C.1.

Experiments using flexible beams were conducted in two parts: first, surface wave maps were collected using the Fourier Transform Profilometry (FTP) method (Cobelli et al., 2009) —which has been successfully applied to obtain non-intrusive, high-resolution wave height maps in several fluid dynamics problems (e.g. Cobelli et al., 2011)— and second, blade movements were recorded using an LED light setting suitable for an accurate tracking of the beam-tip kinematics. FTP and tracking experiments were run back-to-back for each of the studied configurations, and both

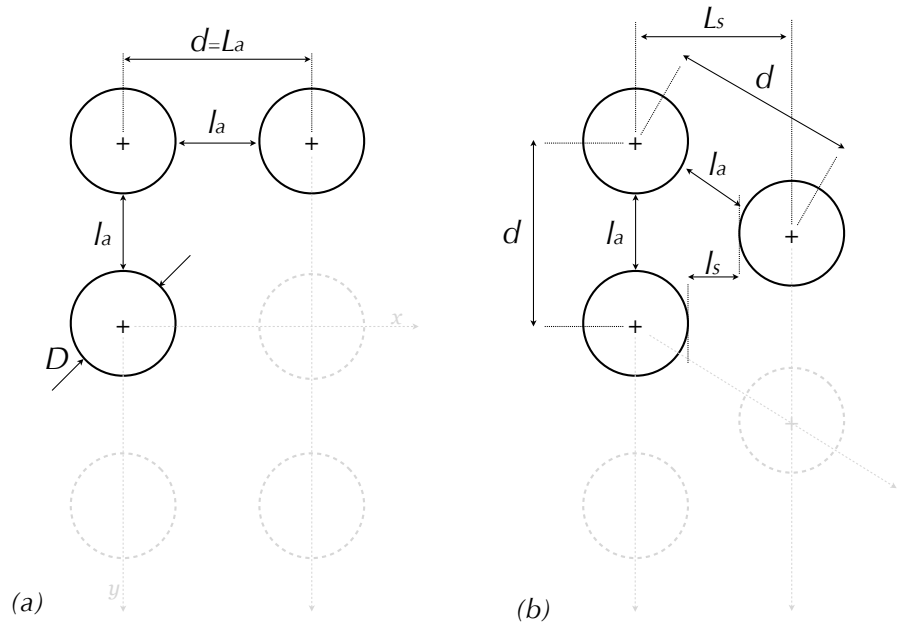

FIGURE C.1: Sketch of separating distances between beams in aligned (a) and staggered (b) configurations.

TABLE C.1: Separating distances between beams: aligned centre to centre L_a, aligned edge to edge l_a, staggered centre to centre L_s and staggered edge to edge l_s.

Configuration	$L[cm]$	*symbol*	L/λ	$l[cm]$	*symbol*	l/λ
Aligned	3.5	L_a	0.38	2.1	l_a	0.23
Staggered	3.03	L_s	0.33	1.6	l_s	0.17

with and without the blades (with only the plexiglas base remaining) to collect FTP data for the corresponding reference cases (*Control*). A partially submerged configuration was chosen in order to allow for maximal interaction between the incoming waves and the blades. With a water depth of 8 cm, the submergence ratio was $h_s/h = 1.38$. The average incident wave height H_0 was maintained at around 6 mm for all experiments. A Photron FASTCAM SA4 camera was used with an acquisition frequency of 60 fps, and each experiment was run using 300 reference images and 500 deformed images (which corresponds to 35 wave periods). The surface wave maps were then calculated using the FTP algorithm running on MATLAB®. The FTP method relies on a fringe pattern of controlled characteristics projected onto the free surface that is deformed by the surface perturbation produced by the wave field. In order to be able to project images onto the water surface, its light diffusivity is enhanced by the addition of a white (titanium-dioxide-based) liquid dye (see Cobelli et al., 2009). A digital video projector with a resolution of 1920×1280 pixels and 12-bit depth was used to project the fringe patterns.

The second part of the experiments was focused on the bending of the blades, which relies on the recording of the beam movements. Unlike seen in chapter 3 for the blades, a simple dimming of the lights was now insufficient given that the cylinders would reflect the light in all directions, thereby creating noisy images regarding contrast. Therefore, a dedicated lighting set-up was put in place, in which LEDs were placed in a circle surrounding the entire array. This provided very clean images for which an example is shown in Figure C.2 below.

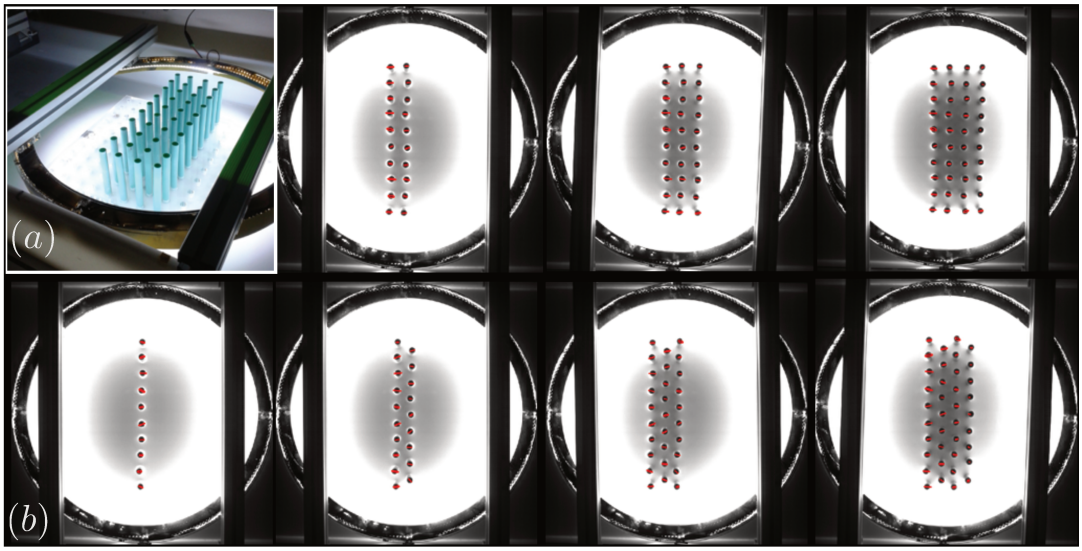

FIGURE C.2: (a) Experimental set-up for the tracking of the cylinder tips (in this case, the water is clear). (b) Example of a raw reference images (without waves) for increasing array sizes (left to right) and for both aligned (top) and staggered (bottom) configurations (b). Tip trajectories from the tracking method are plotted in red.

After each FTP record, 500 additional images were recorded without the projected pattern used for FTP, and with instead a specific lighting set-up. The top of each blade was painted black to contrast with the water made white by the mixed TiO_2 dye. The movement of each beam was quantified using a spatio-temporal stacking method as provided by the software package ImageJ©.

Results & discussion The results of reflection and transmission coefficients are presented in figure C.3. In the case of reflection (a), the curves vary depending on the test configuration, however, the general tendency is similar with a slow decrease as N is increased. Recalling Table C.1 above, separating distances do not exceed $\lambda/3$ and, in fact, edge to edge distances tend toward $\lambda/4$ or even $\lambda/6$ for the staggered case. This could explain the decrease in K_r as N increases, since the phase shifts between transmitted and reflected waves will cause destructive interferences, as opposed to a Bragg scattering configuration. Transmission, on the other hand, shows clearer tendencies, with the results for rigid arrays (black curves) separating from those obtained with the flexible arrays (green curves). All cases decrease rapidly with N and stabilise beyond $N = 3$. Since it is the case for both rigid and flexible arrays, this effect must be the result of wave scattering. Nonetheless, flexible arrays show an additional attenuation of waves of around 30% for the full arrays, compared to their rigid equivalent.

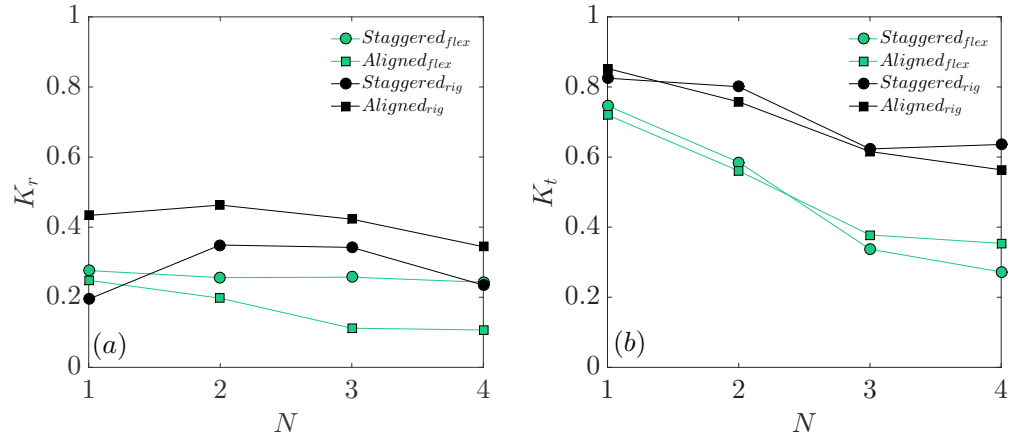

FIGURE C.3: Comparison of reflection (a) and transmission (b) coefficients for flexible (green) and rigid (black) configurations in both aligned (squares) and staggered (circles) configurations. Results are plotted against total number of rows N.

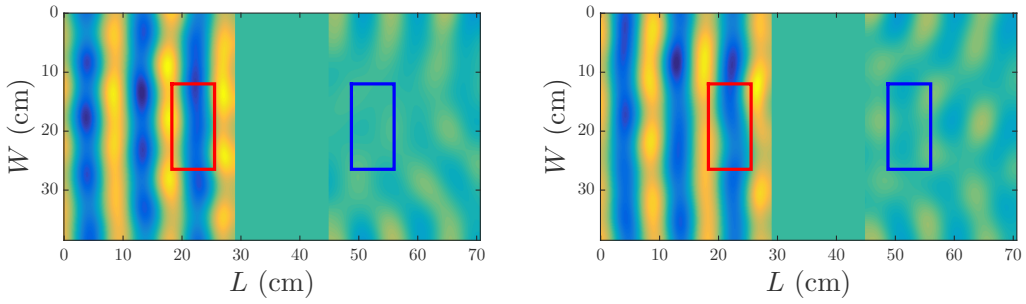

(A) Staggered (B) Aligned

FIGURE C.4: Flexible cases. Zones of calculation for K_r (red box) and $\tilde{K}_t$ (blue box) coefficients for an array of 4 rows.

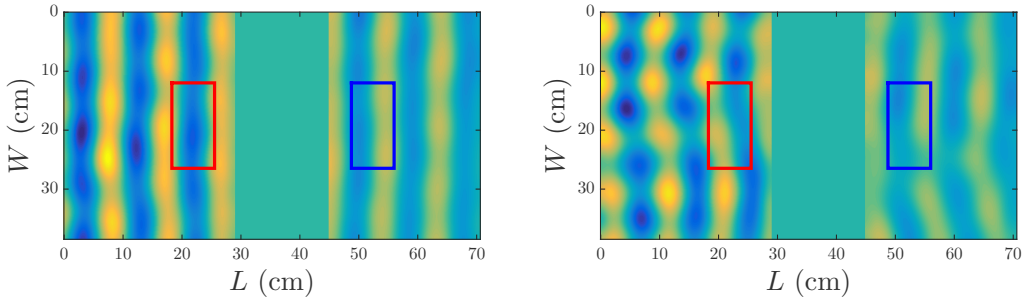

(A) Staggered (B) Aligned

FIGURE C.5: Rigid cases. Zones of calculation for K_r (red box) and $\tilde{K}_t$ (blue box) coefficients for an array of 4 rows.

Additionally, both aligned and staggered configurations transmit the same amount of energy. However, the surface wave map analysis show slight differences in the diffraction figures. While the staggered configuration demonstrates a full blurred triangular region downstream the beams, this is less clear in the aligned configuration, which presents lobs in the diffraction figure (see Figure C.4). This is made even more evident by the diffraction maps of the rigid cases presented Figure C.5. The analysis

used for the transmission and reflection coefficients does not represent these differences given that it relies on a transverse average of the waves. Further studies could look at using time and space Fourier transforms (from time-space $(t - x)$ domain to frequency-wave number $(\omega - k)$ domain).

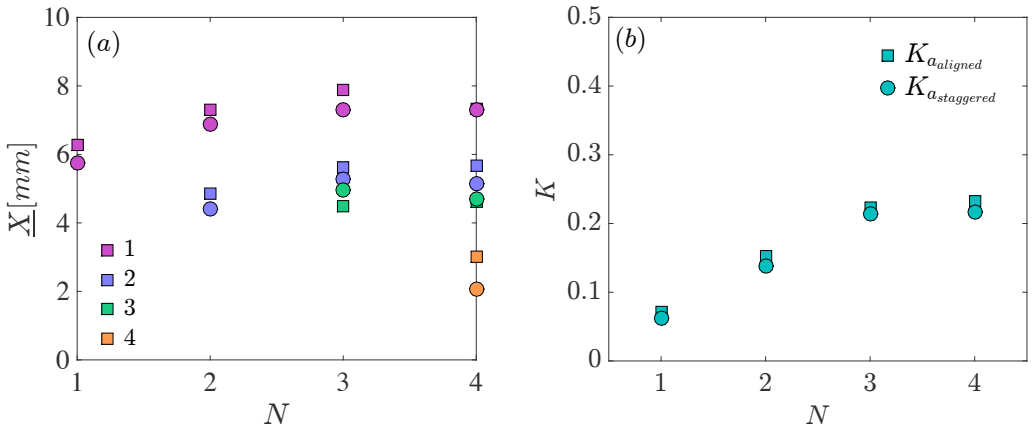

FIGURE C.6: Measured average blade tip oscillations for each row (a) and corresponding internal dissipated energy coefficient K_a (b) for both aligned (square markers) and staggered (circle markers) pattern, as a function of increasing number of rows. Comparison of average oscillations for aligned (squares) and staggered (circles) configurations, as a function of array size (number of rows). Oscillation amplitudes for rows 1, 2, 3, and 4 are plotted in purple, blue, green, and orange dots, respectively. Measurements correspond to the displacements taken in the x-direction only.

The results for measured average blade oscillations for each row are plotted in figure C.6 (a), for both aligned (square markers) and staggered (circle markers) arrays. As seen previously for the blade shaped objects (Chapter 4), both aligned and staggered patterns provide the same behaviour for blade oscillations. This is due to the single direction of the incident waves. It is also noticed that the oscillations of front rows increase as additional rows are placed in the arrays, until the fourth row is added (N=4). This effect mirrors that seen for transmission and is translated in the results obtained for the corresponding internal dissipation coefficients K_a plotted in Figure C.6 (b). These were calculated with an internal damping coefficient $\Gamma_{int} = 0.8s^{-1}$ measured from a free oscillation test in air. Both staggered and aligned configurations show an increasing amount of internal damping as the array size increases, for which the amount reaches just over 20%. This corresponds to about double that measured for the blade shaped beams (figure 4.23 in Chapter 4). With similar damping coefficients Γ, this is due to the larger volume of material which is subject to internal work. The rest of the energy is therefore lost to the fluid. This external frictional loss accounts for an additional 10% compared to the rigid arrays. Therefore, most of the added attenuation is transferred to the cylinders. In terms of energy harvesting potential, this shape is therefore more effective.

Conclusions & perspectives From this preliminary study, it is clear that using cylinder-shaped beams alters the interactions involved in our system. As before, the flexible arrays demonstrated a large benefit regarding wave attenuation with lower transmission values compared with the rigid cases. Unlike the blade shapes, the added attenuation is slightly less ($\sim$ 30% compared to $\sim$ 40% for the blades (c.f.

figure 4.19 from Chapter 4), but in this case the majority of the wave dissipation comes from internal damping. These shapes reduce resulting drag effects thereby maximising the energy harvesting potential. Further steps could be to test various angles of attack of the incident waves, in order to verify whether or not the response of the array remains the same, i.e. if this shape is indeed resilient to multi-directional waves.

Appendix D

Scaling-up

Following our experiments in the small wave canals, a natural step is then to test a similar system at a larger scale. This was undertaken in the Laboratory "Ondes et Milieux Complexes" (LOMC) in Le Havre, France, with the aim to scale our small laboratory model to an intermediate scale of the order $\mathcal{O}(\frac{1}{100})$ from realistic prototypes (based on a final width of device equal to $\mathcal{O}$(10m)). Furthermore, with this larger facility the produced waves are less subject to natural dissipation and canal reflections. These new experiments would therefore allow us to test the interference model developed in Chapter 5 on a more realistic system.

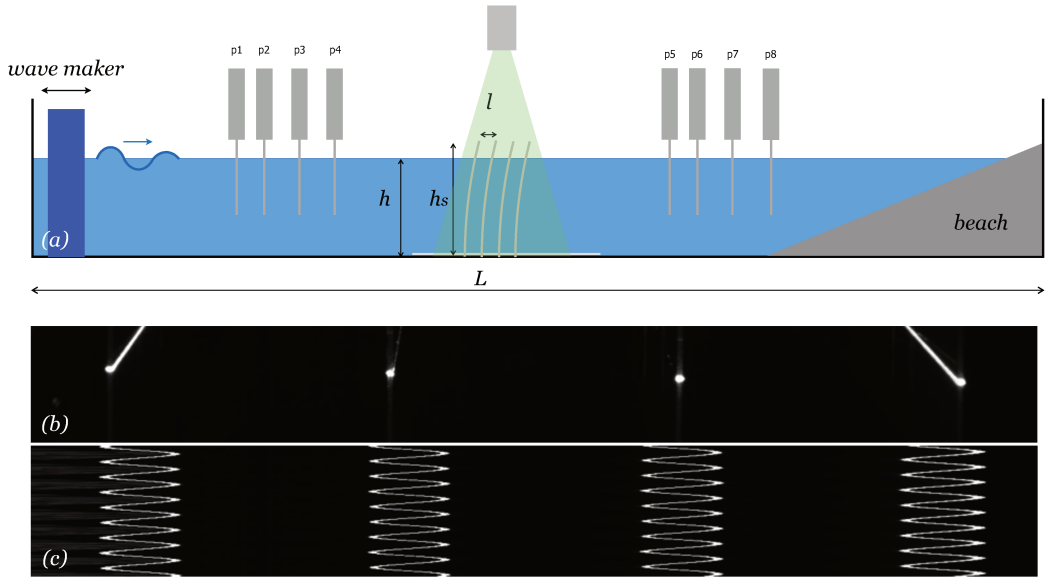

FIGURE D.1: Sketch of experimental set-up (a). Typical image of blade tips recorded using combined laser sheet and camera (b), and corresponding spatio-temporal plot (c).

D.1 Experimental set-up & Methods

Experiments in the LOMC were run in a long wave canal 34m$\times$0.9m$\times$1.2m, equipped with a linear wave maker (HR Wallingford) able to create regular monochromatic waves of imposed wave amplitude a and wave frequency f. Global measurements of surface waves are not feasible in large wave canals such as those provided by the LOMC laboratory, therefore wave gauges were used instead. This local measurement technique relies on direct voltage difference readings for each probe, which varies linearly with water depth (pressure differences). Careful calibration prior

to wave generation allows for precise and robust surface wave measurements. A sketch of the experimental set-up is provided in Figure D.1 (a).

The model array was upscaled using PVC sheets that were inserted into 10mm thick PVC base boards drilled to the bottom of the wave tank, in which slits had been manufactured at 5mm increments. The individual blades could therefore be placed at various distances in both the $x-$ and $y-$ directions. Photos of the experimental set-up are provided in Figure D.2. The tests were run with three types of blades: thin flexible blades 2mm thick, slightly rigidified (an additional bar of 4mm placed in their centre) *Type 1* D.2 (a), flexible blades strongly reinforced (with an additional bar of 15mm thick) *Type 2* D.2 (b), and large plates of thickness 6mm *Type 1* D.2 (c-d).

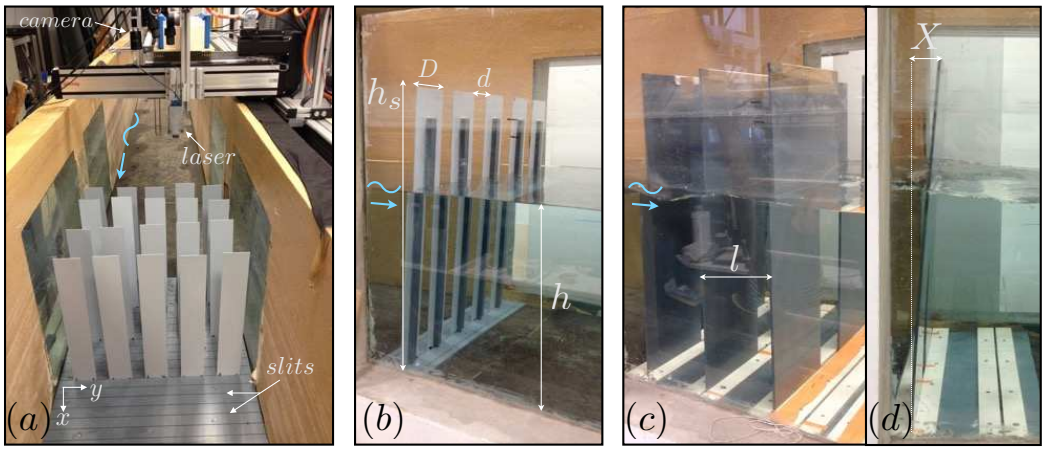

FIGURE D.2: Photos of the used experimental set-ups for the three model objects. Full array of thin flexible blades *Type 1* (a), one row of the reinforced blades *Type 2* (b), an array of the large plates *Type 3* (c) along with a view of their deflection (d).

Reflection and transmission of incoming waves was measured using 4 probes for which recordings were taken over 50 periods, with the same number of points taken per period. The sampling frequency was therefore adapted to the wave frequency of the wave maker. FFT analysis of the recorded signals were used for each probe before and after the array, in order to calculate the incident and reflected waves, and subsequent reflection and transmission coefficients. Examples of raw and FFT treated probe signals are given in Figure D.3. Reflection and transmission coefficients could then be deduced based on the theoretical expressions developed by (Mansard and Funke, 1980), a method that is commonly used for large scale surface wave measurements. The choice of probe positions was carefully chosen by avoiding distances equal to half the imposed wave length, as well as being multiples of each other. The validity of the calculation method is maintained with these conditions (Mansard and Funke, 1980).

In parallel, tracking of the beams was performed using a laser sheet placed above the array, so that its plane cut through a point belonging to the free tip of one blade for each row. The reflected laser points were then recorded by camera at 20fps, over a minimum of 20 periods for each wave frequency. The protocol was as follows: start the wave maker at the lowest frequency tested, wait 1.5 minutes for a steady state to be reached, start probe signal and camera recordings, stop wave maker, wait a few minutes for a calm water surface. Due to the size of the arrays, the recordings of each row were performed separately.

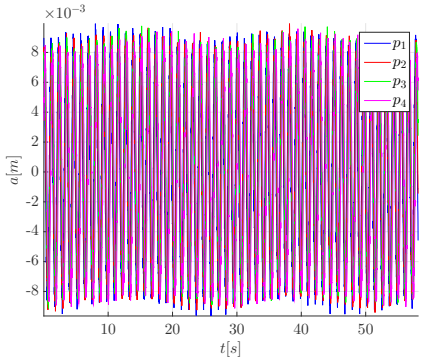

(A) Raw signal recorded by probes 1-4 (before array).

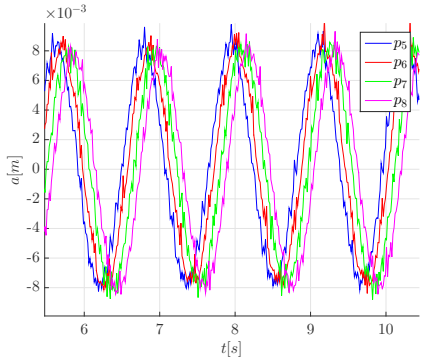

(B) Raw signal recorded by probes 5-8 (after array), zoomed in.

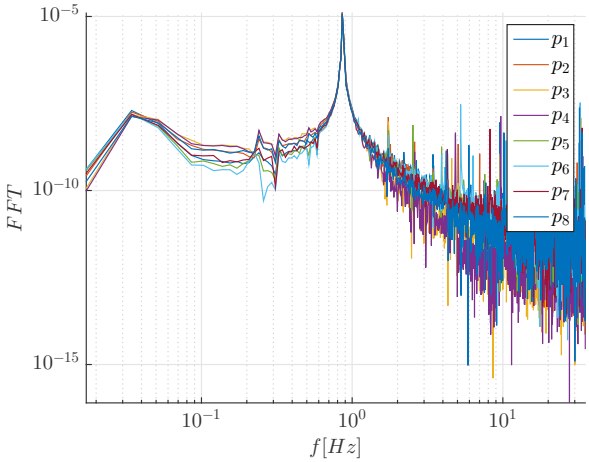

(C) FFT of all probe signals.

FIGURE D.3: Examples of probe data for configuration of 4 rows, at $f = 0.86Hz$, using blades *Type 1*, with spacing $d = 6cm$.

D.2 Tested configurations

The aim of this new set of experiments was to test our model array at a larger scale, in order to obtain more realistic wave conditions (reduced natural wave attenuation, limited reflection). Our model is based around inertia-dominating regimes, as

Model	scale	D [m]	f[Hz]	a[m]	λ[m]	h[m]
Small	1	14×10^{-3}	5	0.7×10^{-3}	7.16×10^{-3}	8×10^{-2}
Intermediate	7.5	10.5×10^{-2}	1.83	5.23×10^{-3}	0.47	0.6
Real	750	10.5	0.18	0.525	133	60

TABLE D.1: Characteristic values for small (PMMH), intermediate (LOMC) and real (sea) scale experiments, with object width D, wave frequency f, wave amplitude a, wave length λ and water depth h.

characterised by the dimensionless number $KC < 1$. Increasing the size of our initial model by a factor of 7.5 was deemed feasible, while maintaining dimensionless numbers $Fr = \frac{u_a}{\sqrt{gD}} = 0.059$ and $KC = \frac{u_a T}{D} = 0.314$ of the same order, where u_a is the wave particle velocity amplitude, D is the characteristic length of our obstacle (here, taken as the width of the blades), T the wave period. A summary of the key scale

Tested object	KC	R_n	f/f_0	$\mathcal{D}$	h/λ	h_s/h
Type 1	0.4	2×10^4	[5.7 - 12]	[0.05-0.22]	[0.3-1.27]	1.12
Type 2	0.4	2×10^4	1	0.04	0.18	1.5
Type 3	[0.3-0.6]	$[3\text{-}6]\times 10^4$	1	0.22	0.34	1.5
Small-scale blades	0.314	3×10^2	1	0.2	~ 1	1.2

TABLE D.2: Dimensionless parameters for each tested conditions

parameters are provided in Table D.1. However, KC alone is insufficient to maintain all the mechanical conditions of our fluid-structure interactions. Other dimensionless parameters that rule our array's response include the resonance ratio f/f_0, the diffraction number $\mathcal{D} = D/\lambda$, the water depth ratio h/λ and the submergence ratio h_s/h. As seen in the previous chapters, these will determine how the energy of the waves is distributed in our system. For this reason, several large-scale models were used in order to approach a good representation of our system at a larger scale. The relevant dimensionless numbers of the tested models in the intermediate scale are provided in Table D.2. For comparison, those of the small-scale model are also recalled.

These upscaled objects were tested in various array configurations. In the case of blades *Type 1*, arrays were tested for sizes $N = [1-4]$, with a fixed lateral spacing between blades $d = 6cm$ and fixed longitudinal spacing $l = 25cm$ between rows. The imposed waves were, however, varied between frequencies $f = [0.86 - 1.82]$ thereby varying the spatial parameter l/λ between $[\frac{1}{8} - \frac{1}{2}]$. These experimental conditions were undertaken far away from the resonant frequency of the blades, so that spatial configuration was the leading parameter.

In the other cases (blades *Type 2* and *Type 3*), experiments were run nearer the resonant frequency in order to obtain a stronger response from the blades. In these cases, therefore, the imposed wave frequencies were kept fixed. Instead, the spacing l separating rows was varied in order to test different values of l/λ.
Full array tests were run for regular arrays in both cases ($N = [1-4]$ and $N = 2$ for *Type 2*, $N = 3$ and $N = 2$ for *Type 3*). An additional optimal configuration l_{opt} of irregular spacing was tested with *Type 3* blades, as predicted by the interference model described in Chapter 5. These regular and irregular configurations are represented graphically in Figure D.4, for an array of 3 rows (case of *Type 3*).
A summary of all wave and blade characteristics for the different configurations are provided in tables D.3 and D.4, respectively.

In order to test the validity of our model, we compare experimental measurements of global reflection K_r, transmission K_t and normalised blade oscillations $\tilde{X}$ to those predicted by the interference model. Therefore, reference cases using a single row ('$N1$') were run for all cases in order to extract values of local r and t serving as input parameters in equations 5.42, 5.43 and 5.10 from Chapter 5. *Control* cases without any obstacle ('$N0$') were also run to serve as verification for natural dissipation and wave amplitudes.

Finally, in the experiments run with blades *Type 3*, an active absorption setting was used for the motor, so as to absorb reflected waves from the array, and avoid multiple reflections between the motor and the array. A gain factor setting of 2.8 was used for this.

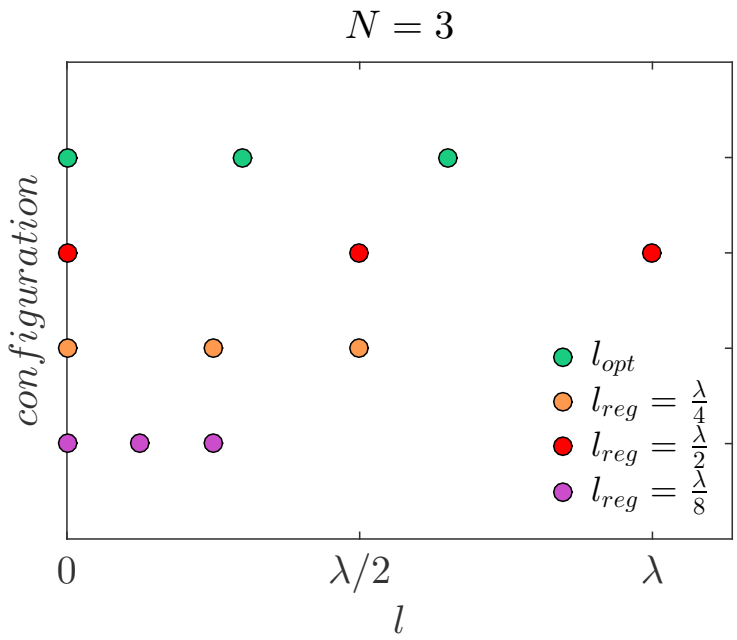

FIGURE D.4: Representation of tested configurations, using up-scaled system at the resonant frequency.

Model	$f[Hz]$	$a[cm]$	$\lambda[cm]$	$h[cm]$
Type 1	0.86	1	200	60
Type 1	1.013	1	150	60
Type 1	1.25	1	100	60
Type 1	1.49	1	75	60
Type 1	1.82	1	47	60
Type 2	0.71	1	250	45
Type3	1.07	1.5	1.32	45
Type3	1.07	2	1.32	45
Type3	1.07	3	1.32	45

TABLE D.3: Wave characteristics: Frequency f, amplitude a, wave length λ, and depth h of imposed waves.

Model	$h_s[cm]$	$D[cm]$	$b[mm]$	$d[cm]$	l/λ	N	B
Type 1	67.5	10.5	2(+4)	6	$[\frac{1}{8} - \frac{1}{2}]$	1-4	5
Type 2	67.5	10.5	2(+15)	6	$(\frac{1}{4}; \frac{1}{2})$	1-4	5
Type 2	67.5	10.5	2(+15)	6	$[\frac{1}{8} - \frac{1}{2}]$	2	5
Type 3	67.5	30	6	15	$(\frac{1}{8}; \frac{1}{4}; \frac{1}{2}; l_{opt})$	3	2
Type 3	67.5	30	6	15	$[\frac{1}{8} - \frac{1}{2}]$	2	2

TABLE D.4: Blade characteristics: Length h_s, width D, thickness b, transverse array spacing d, longitudinal array spacing l/λ scaled to the wave length λ, total number of rows N and number of blades B per row.

D.3 Results & Discussion

As presented above (Tables D.2 and D.4), the experiments run in this new scale cover many hydrodynamic and spatial parameters. We wish to study their effects on both the wave field (reflection and transmission) and the array response (oscillations).
First, the influence of imposed wave amplitude a (directly related to dimensionless number KC) is investigated from tests performed on a single row of blades *Type 3*. Experiments run on blades *Type 1* then serve to verify the importance of resonance and choice of parameter f/f_0 on the array's response. The influence of diffraction ratio $\mathcal{D}$ is also evaluated by comparing results obtained for 2-row arrays of blades *Type 2* and *Type 3*. Finally, optimal row spacings l are analysed from results obtained on full arrays of regular and irregular patterns. Blades *Type 2* and *Type 3* were used in these cases.

D.3.1 Influence of imposed wave amplitudes

We first wish to study the response of a single row of blades depending on the imposed wave amplitudes, which, in deep or intermediate water conditions, is directly related to the Keulegan-Carpenter by $KC \sim 2\pi a/D$. From experiments run with *Type 3* blades, results for a single row are provided in Figure D.5 below. Average oscillations $\bar{X}$ are shown in (a) for increasing imposed wave amplitude a, and demonstrates a linear relationship. Plot (b) presents the measured reflection K_r (red) and transmission K_t (blue) coefficients. It should be reminded here that the imposed waves match the resonant frequency of the blades.
K_r is found to decrease linearly from around 0.5 to 0.4 as wave amplitude a increases, while K_t remains stable around 0.6. The values presented here serve as the reference cases used for normalisation of the data presented for blades *Type 3* in the next sections.

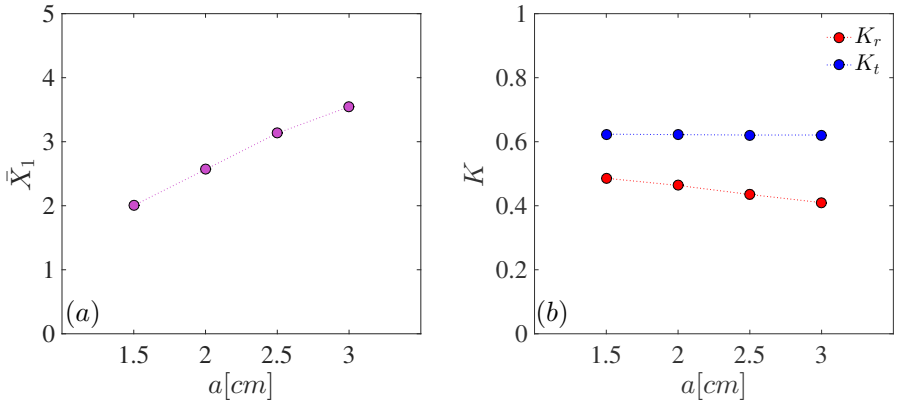

FIGURE D.5: Results for a single row of plates. Measured average oscillation amplitudes $\bar{X}$ for a single row of plates as a function of increasing imposed wave amplitude a (a). Measured reflection K_r (red) and transmission K_t (blue) coefficients for a single row (b).

D.3.2 Influence of f/f_0

Experimental results run with *Type 1* blades are plotted in Figure D.7. Measured reflection and transmission coefficients K_r, K_t for the 4 row array ($N = 4$), with spacing d =6 cm are plotted against calculated values using equations 5.42, 5.43 from

Chapter 5 (c.f. Figure D.6 (a)). Measured average oscillations $\bar{X}$ for all four rows of the array are normalised and plotted against corresponding calculated amplification factor $\mathcal{A}$, based on local values of r, and t, measured for cases of 1 row (c.f. Figure D.6 (b)). The associated total cumulative amplification is then presented in Figure D.6 (c). Amplification coefficients are calculated for discrete values only (represented by empty square markers) since local r and t are frequency dependent and each value of l/λ tested here corresponds to a different wave frequency.

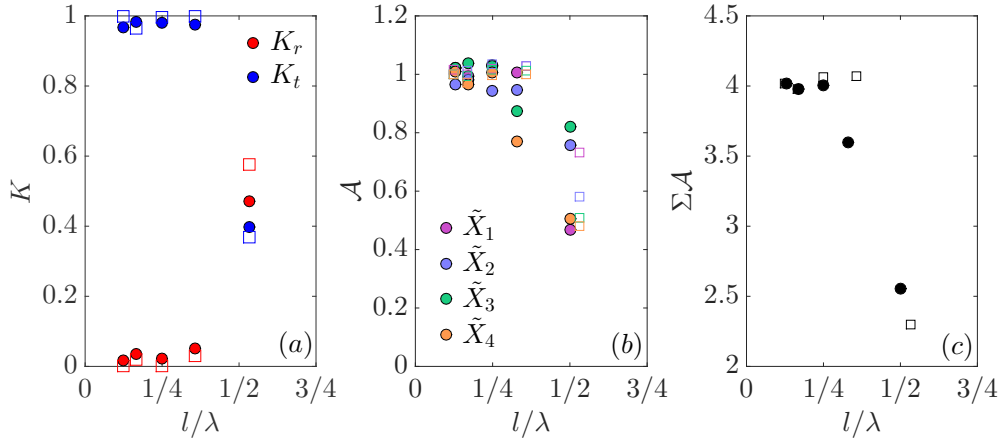

FIGURE D.6: Measured (filled dots) and predicted (squares) results for global reflection K_r and transmission K_t coefficients (a) and amplification factors (b).

The results show very little impact of the array on the wave transmission and reflection for most of the tested range of wave frequencies, apart from the case of spacing $l = \lambda/2$ (Figure D.6 (a)). The same behaviour is found for the oscillations that demonstrate a sharp decrease in values at the same point of $l = \lambda/2$ (Figure D.6 (b-c)). This corresponds to the Bragg scattering case, as expected. It should be noted here that as the incident wave lengths are modified, the spacing parameter d/λ is also modified. Distance $l = \lambda/2$ corresponds to the specific case of $f = 1.83Hz$ for which $d << \lambda$. This causes an increased local value of r, therefore causing a strong effect of the Bragg scattering.

The low effect for the other tested spacings is due to the fact that the resonant frequency of the blades in water is measured around $0.15Hz$, far below the tested range ([0.86Hz-1.32Hz]). Therefore, the conversion of the waves' energy into elastic bending energy is limited. Variations at blade resonance are discussed in the following sections. Finally, it is noted that the variations in results are overall well represented by the model, although the values do not match in the case of the point $l = \lambda/2$.

D.3.3 Influence of $\mathcal{D}$

Following results obtained with blades *Type 1*, we chose to work at the resonant frequency for all other cases. This led to the choice of blades *Type 2* and *Type 3*, for which we first describe the choices in size.

Due to the motor limits ($f_{min} \approx 0.3Hz$) and the desired spread of tested patterns, the original blades *Type 1* were therefore modified in order to increase their natural resonant frequency. This was done by increasing the thickness of the added block on its central line as well as by decreasing the water depth. Indeed, the resonant frequency in water $\omega_l \propto (\sqrt{b^3}; h_s^{-2})$, where b is the thickness of the blade, and h_s is

its length. Due to the density ratio of fluids, the loading of air is considered negligible compared with the loading of the submerged part. With an added thickness of 15mm placed 1cm above the clamping edge, and a water depth of 45cm, the natural resonant frequency of the blade was measured as $0.71Hz$. The dispersion relation gives a corresponding water wave length λ of 2.5m. In order to maintain the dimensionless number KC of the same order as our previous experiments, the wave amplitudes were kept equal to 1cm. The associated diffraction ratio of these blades was however limited and far from that of the small-scale models (0.04 vs. 0.2, respectively). Another set of blades was therefore determined, which correspond to *Type 3*.

In order to size these new blades, a compromise between the diffraction ratio, resonant frequency and wave length to canal width ratio had to be found. As discussed previously, a wavelength $\lambda/W > 1$ was required in order to avoid canal modes and strong lateral reflections, a diffraction ratio of 0.2 was sought to match that of the reduced model and to guarantee minimum wave scattering and interferences, and finally, a resonant frequency matching that of the imposed wave length was also needed so that blade responses were maximised. According to (Van Eysden and Sader, 2006), the resonant frequency of our submerged plate can be estimated from the following expression:

$$\omega_{fluid} = \frac{\omega_{vac}}{\sqrt{1 + \frac{\pi \rho_w D}{4 \rho b)}}} \tag{D.1}$$

where ρ_w is the water density, ρ is the density of the solid, D is the plate's width, b is its thickness, and ω_{vac} is the natural frequency of the plate in vacuum (c.f. equation 2.33 in Chapter 2). A play on plate geometry and wave conditions was undertaken using this equation along with the dispersion relation in order to determine the combined solution of plate and wave characteristics that satisfy the conditions mentioned above. A final condition was for the model plates to provide a reasonable representation of an infinite array, thereby requiring the edge spacing δ between the blades and the walls to equal half their lateral separation distance d, i.e. $\delta = d/2$. Any lateral reflections would then be ensured to cancel out through infinite reflections. Based on a PVC material, the resulting solution gave $f = 1.07Hz$, $h = 45cm$, for which $\lambda = 1.32m$, $D = 30cm$, and $t = 6mm$.

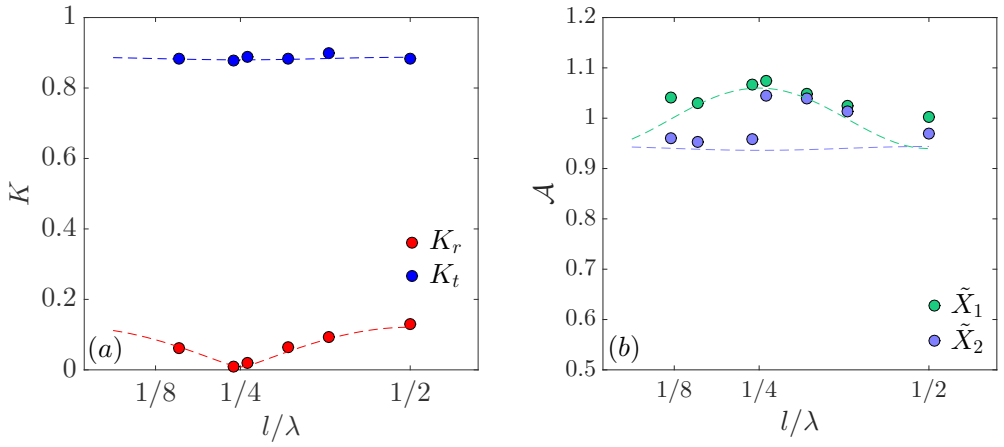

FIGURE D.7: Measured (filled dots) and predicted (dotted lines) results for global reflection K_r (red) and transmission K_t (blue) coefficients (a), as well as amplification factors for rows 1 (green) and 2 (blue) (b).

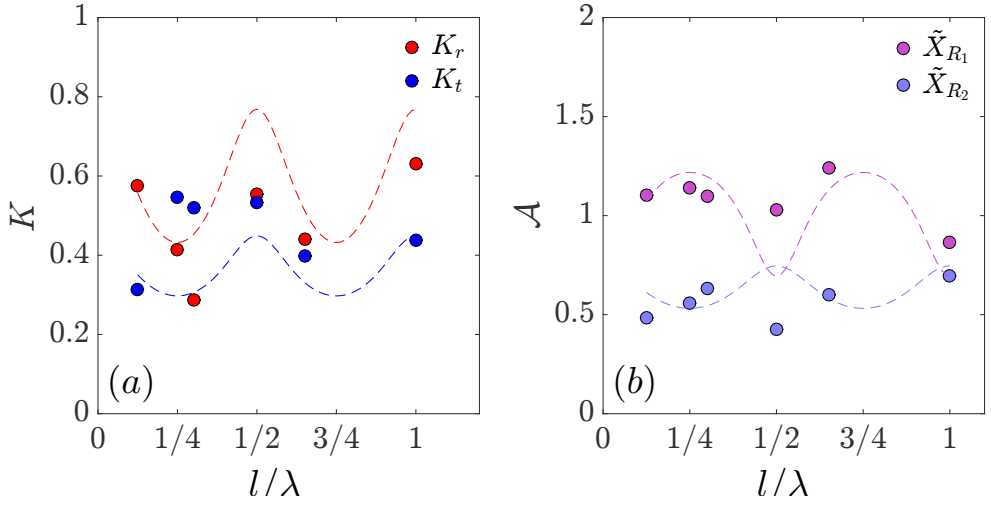

FIGURE D.8: Results of reflection (red) and transmission (blue) coefficients (a) and corresponding normalised average oscillations $\tilde{X}$ (b) for the case of a 2-row configuration, as a function of varying separating distance l/λ. Experimental data (circular markers) are compared to numerical predictions (dashed lines). Results in this case have been obtained with incident wave amplitudes of 3 cm.

We now evaluate the influence of $\mathcal{D}$ by comparing results obtained for a 2-row array composed of blades *Type 2* and *Type 3*, for which the diffraction ratios are equal to 0.04 and 0.22, respectively. Values of l are varied between $\lambda/8$ and $\lambda/2$. Results for blades *Type 2* are plotted in Figure D.7, where global reflection (red markers) and transmission (blue markers) are shown in (a) and normalised oscillation amplitudes for rows 1 (green) and 2 (blue) are shown in (b). Measured data are represented by filled markers and are compared with calculated values presented in empty square markers. While calculations fit well the reflection and transmission data, it is not the case for oscillating amplitudes. In fact, a jump is noted at $l = \lambda/4$, beyond which oscillations measured on both rows collapse onto the same curve. The results plotted correspond to a single set of data, therefore, this deviation could simply be caused by experimental errors. Another proposed hypothesis is that the reflected waves are too weak to travel farther than distance $l = \lambda/4$ and no longer affect the back rows via multiple interferences.

The same results are now plotted for blades *Type 3* in Figure D.8. Measured oscillation amplitudes normalised by the single row case are represented by circular markers for rows 1 (purple) and 2 (blue) and are compared to model results for calculations of amplification factors represented in dashed lines (a). Global reflection (red) and transmission (blue) coefficients are plotted in (b), also comparing measured data (circular markers) to predicted calculations (dashed lines).

D.3.4 Optimal configurations

We now wish to determine optimal spacing configurations, by comparing spacing parameter l between regular and irregular arrays.

Let us first consider the results obtained with blades *Type 2*, of low diffraction ratio. The results for the first tested pattern $l = \lambda/2$ are provided in Figure D.9. The predicted values of reflection K_r and transmission K_t coefficients fit well the experimental results as shown in Figure (a), with values of K_r increasing from 0.05 for a single row to 0.2 for the full array, and K_t decreasing linearly from 0.98 to 0.8 for the full array. In spite of some discrepancies, the oscillation tendencies are well

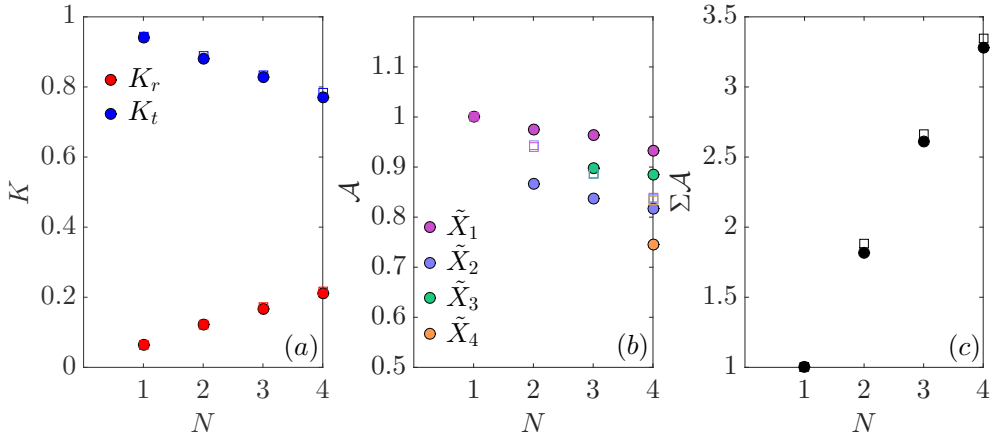

FIGURE D.9: Measured (filled dots) and predicted (lines) results for global reflection K_r (red) and transmission K_t (blue) coefficients as a function of total number of rows N (a). Associated amplification factors for rows 1 (purple), 2 (blue), 3 (green) and 4 (orange) (b), and corresponding total amplification factor $\mathcal{A}_{tot} = \sum \mathcal{A}$ of the array (c). Spacing ratio fixed as $l/\lambda = 1/2$.

represented by the model. It is clear from both calculations and experiments, that as the number of rows increases in a regular array of $l = cst = \lambda/2$, the oscillations of each row reduces. This fits the previous observations regarding Bragg reflections: transmitted and reflected waves lead to opposing wave forces, thereby reducing the resulting Froude-Krylov force acting on each row, and this effect is amplified as N increases. The opposing behaviour of the two coefficients is coherent with the observed linear decrease in oscillations for all rows in the array, thereby suggesting that for spacing $l/\lambda = 1/2$, wave interferences act in the same direction for all rows of the array.

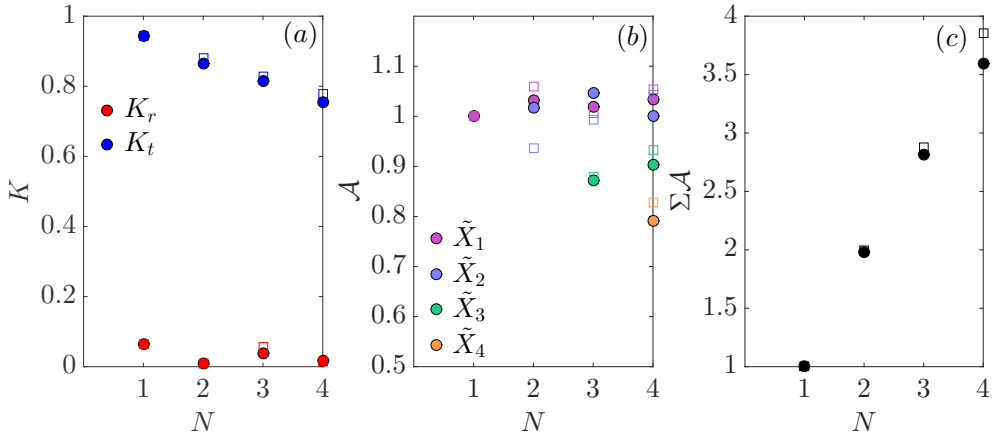

FIGURE D.10: Measured (filled dots) and predicted (lines) results for global reflection K_r (red) and transmission K_t (blue) coefficients as a function of total number of rows N(a). Associated amplification factors for rows 1 (purple), 2 (blue), 3 (green) and 4 (orange) (b), and corresponding total amplification factor $\mathcal{A}_{tot} = \sum \mathcal{A}$ of the array (c). Spacing ratio fixed as $l/\lambda = 1/4$.

The same results are plotted for arrays spaced with $l = \lambda/4$ in Figure D.10. While transmission (blue line) decreases linearly as for the previous case (Figure D.9 (a)), reflection, on the other hand, oscillates and reaches its minimum value when the

array is largest at $N = 4$. When adding the second row, waves interfere destructively while wave forces interfere constructively at the position of the front row. Adding the third row, on the other hand provides an additional reflection component, in phase with incident waves, thereby causing the increase of K_r. Resulting wave forces on row 1 are decreased by the associated destructive interference introduced by row 3. This general pattern continues as rows are added in the array. The benefit of arranging the blades in a regular pattern $l/\lambda = 4$ rather than $l/\lambda = 2$ is conserved in this scale-up version, with a slight increase of the global amplification faction $\mathcal{A}_{tot}$ ($\sim 9\%$).

Experiments were run comparing regular configurations to the optimal one as predicted by the model, for an array composed of 3 rows. Four configurations composed of 3 rows ($N = 3$) were tested at the resonant frequency of the plates (1.07Hz), with λ=1.32m according the dispersion relation. These correspond to three regular configurations with $l = \lambda/2$, $l = \lambda/4$ and $l = \lambda/8$, along with an optimal configuration, predicted using the 1D interference model described previously. This was estimated as $l_2 = 0.30\lambda$ and $l_3 = 0.65\lambda$ (recall Figure D.4 for a graphical representation of the tested configurations).

Results of reflection, transmission and normalised oscillation amplitudes are provided in Figure D.11 for all 3-row array cases. Error bars and shaded lines represent the spread of results obtained for the three tested amplitudes (c.f. Table D.3).

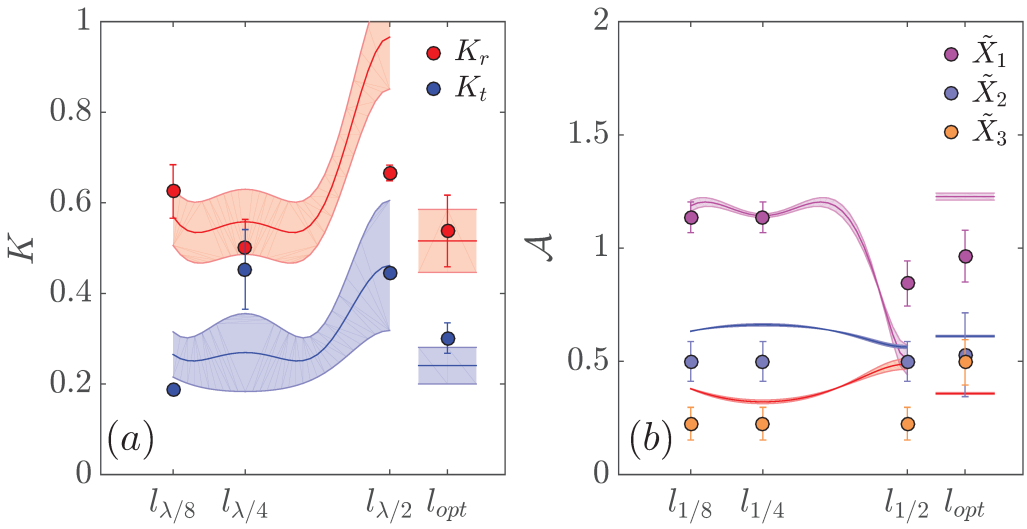

FIGURE D.11: Results of reflection (red) and transmission (blue) coefficients (a) and corresponding normalised average oscillations $\tilde{X}$ (b) for compared regular and optimal arrays composed of 3 rows. Experimental data (circular markers) are compared to numerical predictions (lines). Error bars and shaded lines correspond to the spread in results obtained for all three tested amplitudes a.

D.3.5 Experimental limitations

While results obtained with blades *Type 1* and *Type 2* were well represented by our interference mode, these were found to deviate for cases of *Type 3*, possibly due to experimental errors. Firstly, the experimental measurements of K_r and K_t were difficult. In fact, the probes used for transmission coefficients had to be placed much further away from the array edge than those measuring reflection. It is therefore possible that the local r and t values used are incorrect, which could explain why the calculated results do not match. Furthermore, the strong interferences caused by the array may have become too strong for the probe technique to remain accurate. Although an "absorption" feature was applied on the wave maker, in order to avoid multiple motor to array reflections, this may not have been sufficiently effective. In order to test this hypothesis, a second 'direct' measurement method was used based on amplitude ratios between the amplitudes measured from the wave signals of a tested configuration and those of a reference case without obstacles. Results are provided in Figure D.12.

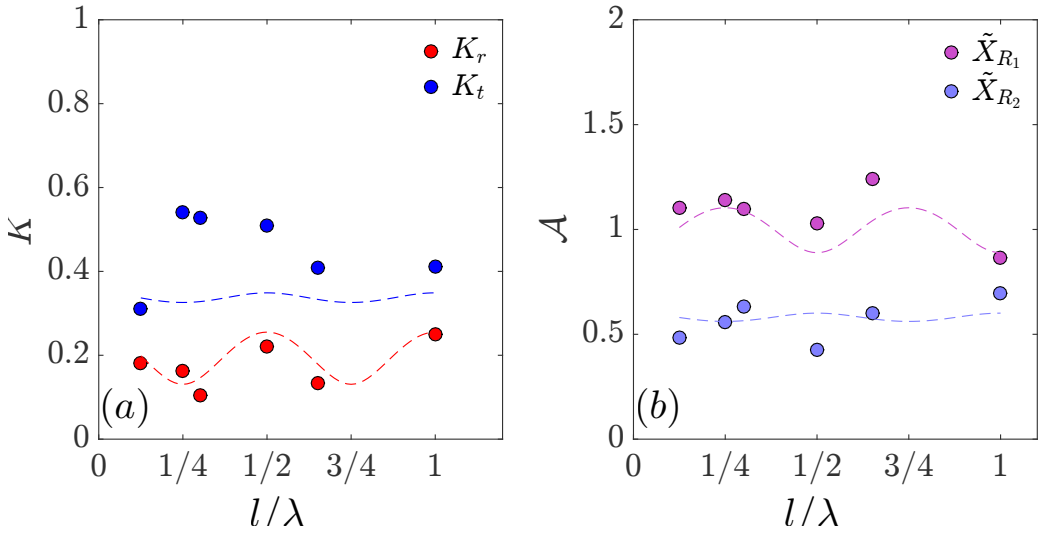

FIGURE D.12: Results of reflection (red) and transmission (blue) coefficients (a) and corresponding normalised average oscillations $\tilde{X}$ (b) for the case of a 2-row configuration, as a function of varying separating distance l/λ. Experimental data (circular markers) are compared to numerical predictions (dashed lines). Results in this case have been obtained with incident wave amplitudes of 3 cm. Values have been measured using a 'direct' method.

The results obtained are still very scattered. Another possible reason for experimental error is the larger weight of the plates, for which the anchoring mechanism was no longer sufficient. The plates were sometimes observed to be rocking or rolling in their slit rather than to be completely fixed. The clamping of the plate's base is a boundary condition to the deflection equation and, therefore, determines the entire response of the plate to the imposed forces. Additional bars were fixed on either side of the base slits in order to raise the length of the plate insertion, and were further tightened once the plates were in place. However, due to time restrictions, this could only be done at the very beginning of the campain and so very probably loosened over time. This is thought to be the main cause of the noisy measurements. This problem was not encountered for the much lighter 2mm thick and 10cm wide plates tested and presented in the previous experiments. Global tendencies are promising but additional experiments would be required to confirm (or refute) these

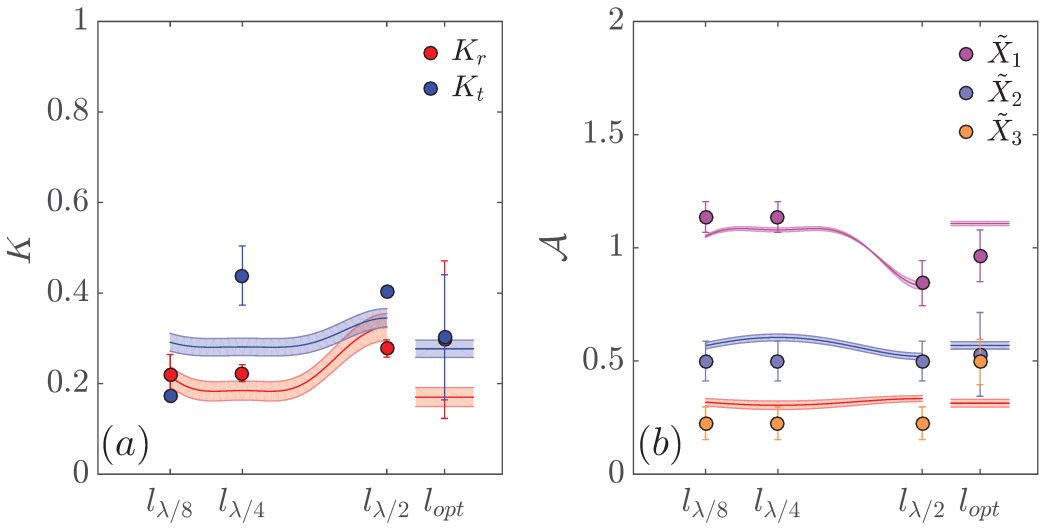

FIGURE D.13: Results of reflection (red) and transmission (blue) coefficients (a) and corresponding normalised average oscillations $\tilde{X}$ (b) for compared regular and optimal arrays composed of 3 rows. Experimental data (circular markers) are compared to numerical predictions (lines). Error bars and shaded lines correspond to the spread in results obtained for all three tested amplitudes a. Values have been measured using a 'direct' method.

tendencies and the validity of the model, so long as an appropriate clamping system is used.

D.3.6 Modal decomposition

Finally, the frequency decomposition of the wave signals demonstrated an additional effect of the array of the wave spectrum, with added peaks observed for sub-frequencies of the imposed waves. Figure D.14 below presents the FFT signals for the cases of maximal wave amplitudes (A=3cm). FFT signals show clear peaks appearing for the single row case (E), when compared to the reference case (F). While the latter presents a single clean peak of intensity at the fundamental mode (f_0=1.07Hz), multiple peaks at sub-frequencies $2f_0$, $3f_0$, and $4f_0$ appear in the case of one row. These peaks remain strong for all other cases of arrays with 3 rows. These observations are coherent with results previously obtained from small scale experiments. This could in fact explain the larger oscillations sometimes observed for cases where spacing $l \leq \lambda/4$. These could be due to interferences occurring at higher frequencies.

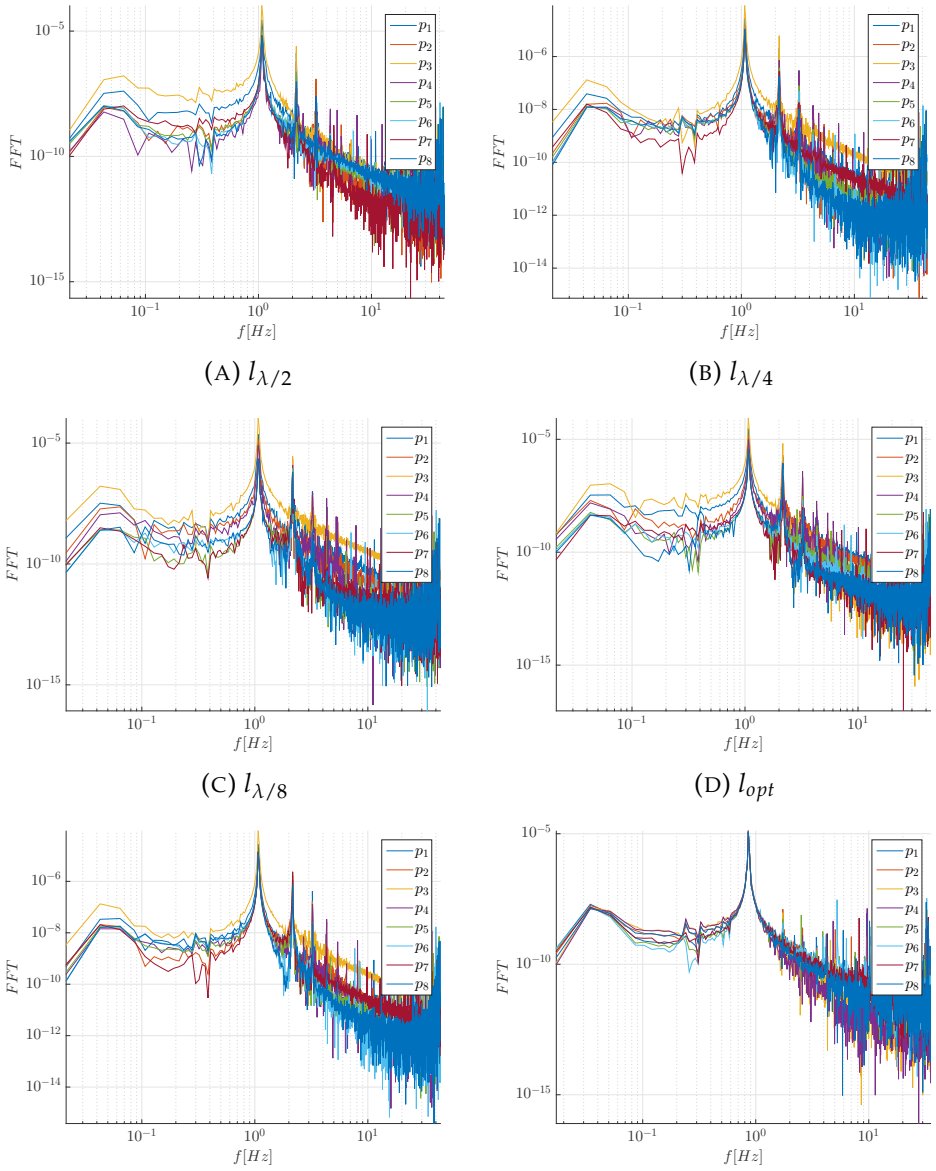

(A) $l_{\lambda/2}$ (B) $l_{\lambda/4}$

(C) $l_{\lambda/8}$ (D) l_{opt}

(E) N1 (F) N0

FIGURE D.14: FFT treated wave signals for regular configurations (A-C), optimal configuration (D), single row (E) and reference case (F).

D.4 Conclusion

In this chapter, we have presented the results obtained from larger scale experiments performed at the LOMC laboratory of the le Havre. The aim was to test previous results from the small-scale experiments at a different hydrodynamic scale, along with the interference model developed in Chapter 5.
Several difficulties were encountered when trying to increase the size of the model blades, since many parameters must be considered in the process, such as the KC number, the resonant frequency of the object, the wave conditions, or even the diffraction ratio. Three model blades were tested in order to investigate the role of these dimensionless parameters.
The results obtained from the first tests were satisfying and matched well with model predictions. The key tendencies and mechanisms therefore seem well represented. However, unlike these initial results, those obtained from more responsive model were quite scattered and difficult to interpret. The reason is thought to come from the additional experimental difficulties arising at this scale, including an appropriate clamping system for the full size model plates. Additional work would therefore be needed in order to conclude on the results.

Bibliography

Abanades, J, D Greaves, and G Iglesias (2015). "Coastal defence using wave farms: The role of farm-to-coast distance". In: *Renewable Energy* 75, pp. 572–582.

Anderson, M. E. and J. M. Smith (2014). "Wave attenuation by flexible, idealized salt marsh vegetation". In: *Coastal Eng.* 83, pp. 82–92.

Anderson, M. E., J. M. Smith, and S. K. McKay (2011). *Wave dissipation by vegetation*. Tech. rep. US Army Corps of Engineers.

Antonio, F de O (2010). "Wave energy utilization: A review of the technologies". In: *Renewable and sustainable energy reviews* 14.3, pp. 899–918.

Arnaud, Gwendoline et al. (2017). "Wave propagation through dense vertical cylinder arrays: Interference process and specific surface effects on damping". In: *Applied Ocean Research* 65, pp. 229–237.

Asano, T., H. Deguchi, and N. Kobayashi (1992). "Interaction between water waves and vegetation". In: *Coastal Engineering Conference*. Vol. 3. ASCE American Society Of Civil Engineers, pp. 2710–2710.

Augustin, L. N., J. L. Irish, and P. Lynett (2009). "Laboratory and numerical studies of wave damping by emergent and near-emergent wetland vegetation". In: *Coastal Eng.* 56.3, pp. 332–340.

Babarit, A (2013). "On the park effect in arrays of oscillating wave energy converters". In: *Renewable Energy* 58, pp. 68–78.

Babarit, Aurélien et al. (2009). "La récupération de l'énergie de la houle, partie 1: caractérisation de la ressource et bases de l'hydrodynamique". In: *revue 3EI*, pp–17.

Barsu, S. et al. (2016). "Drag measurements in laterally confined 2D canopies: Reconfiguration and sheltering effect". In: *Phys. Fluids* 28, p. 107101.

Borgarino, B, A Babarit, and P Ferrant (2012). "Impact of wave interactions effects on energy absorption in large arrays of wave energy converters". In: *Ocean Engineering* 41, pp. 79–88.

Buck, B. H. and C. M. Buchholz (2005). "Response of offshore cultivated Laminaria saccharina to hydrodynamic forcing in the North Sea". In: *Aquaculture* 250.3, pp. 674–691.

Chang, Che-Wei et al. (2017a). "Modeling transient long waves propagating through a heterogeneous coastal forest of arbitrary shape". In: *Coastal Engineering* 122, pp. 124–140.

— (2017b). "Periodic water waves through a heterogeneous coastal forest of arbitrary shape". In: *Coastal Engineering* 122, pp. 141–157.

Clément, Alain et al. (2002). "Wave energy in Europe: current status and perspectives". In: *Renewable and sustainable energy reviews* 6.5, pp. 405–431.

Cobelli, Pablo Javier et al. (2009). "Global measurement of water waves by Fourier transform profilometry". In: *Experiments in fluids* 46.6, p. 1037.

Cobelli, PJ et al. (2011). "Experimental study on water-wave trapped modes". In: *Journal of Fluid Mechanics* 666, pp. 445–476.

Couston, Louis-Alexandre, Mir Abbas Jalali, and Mohammad-Reza Alam (2016). "Sheltering the Shore via Nearshore Oblique Seabed Bars". In: *ASME 2016 35th International Conference on Ocean, Offshore and Arctic Engineering*. American Society of Mechanical Engineers, V007T06A041–V007T06A041.

Cummins, WE (1962). *The impulse response function and ship motions*. Tech. rep. David Taylor Model Basin Washington DC.

Dalrymple, R. A., J. T. Kirby, and P. A. Hwang (1984). "Wave diffraction due to areas of energy dissipation". In: *Journal of Waterway, Port, coastal, Ocean Eng.* 110, pp. 67–79.

Day, AH et al. (2015). "Hydrodynamic modelling of marine renewable energy devices: A state of the art review". In: *Ocean Engineering* 108, pp. 46–69.

De Chowdhury, S et al. (2015). "A review of hydrodynamic investigations into arrays of ocean wave energy converters". In: *arXiv preprint arXiv:1508.00866*.

De Langre, E. (2008a). "Effects of wind on plants". In: *Annu. Rev. Fluid Mech.* 40, pp. 141–168.

De Langre, Emmanuel (2008b). "Effects of wind on plants". In: *Annu. Rev. Fluid Mech.* 40, pp. 141–168.

Denny, M. and B. Gaylord (2002). "The mechanics of wave-swept algae". In: *J. Exp. Biol.* 205.10, pp. 1355–1362.

Dias, Frédéric et al. (2017). "Analytical and computational modelling for wave energy systems: the example of oscillating wave surge converters". In: *Acta Mechanica Sinica*, pp. 1–16.

Drew, Benjamin, Andrew R Plummer, and M Necip Sahinkaya (2009). *A review of wave energy converter technology*.

Dubi, A. and A. Torum (1994). "Wave damping by kelp vegetation". In: *Coastal Eng. Proc.* 1.24.

— (1996). "Wave energy dissipation in kelp vegetation". In: *Coastal Eng. Proc.* 1.25.

Duclos, G. and A. H. Clément (2004). "Wave propagation through arrays of unevenly spaced vertical piles". In: *Ocean Eng.* 31.13, pp. 1655–1668.

Elvin, Niell and Alper Erturk (2013). *Advances in energy harvesting methods*. Springer Science & Business Media.

Falnes, Johannes (2007). "A review of wave-energy extraction". In: *Marine structures* 20.4, pp. 185–201.

Feagin, R. A. et al. (2009). "Does vegetation prevent wave erosion of salt marsh edges?" In: *Proc. Natl. Acad. Sci.* 106, pp. 10109–10113.

FitzGerald, Duncan M et al. (2008). "Coastal impacts due to sea-level rise". In: *Annu. Rev. Earth Planet. Sci.* 36, pp. 601–647.

Garnaud, Xavier and Chiang C Mei (2009). "Bragg scattering and wave-power extraction by an array of small buoys". In: *Proceedings of the Royal Society of London A: Mathematical, Physical and Engineering Sciences*. The Royal Society, rspa20090458.

Godoy-Diana, R and B Thiria (2018). "On the diverse roles of fluid dynamic drag in animal swimming and flying". In: *Journal of The Royal Society Interface* 15.139, p. 20170715.

Göteman, Malin et al. (2015). "Optimizing wave energy parks with over 1000 interacting point-absorbers using an approximate analytical method". In: *International Journal of Marine Energy* 10, pp. 113–126.

Guazzelli, Elisabeth, Vincent Rey, and Max Belzons (1992). "Higher-order Bragg reflection of gravity surface waves by periodic beds". In: *Journal of Fluid Mechanics* 245, pp. 301–317.

Gunn, Kester and Clym Stock-Williams (2012). "Quantifying the global wave power resource". In: *Renewable Energy* 44, pp. 296–304.

Guo, Xiaoyu, Benlong Wang, and Chiang C Mei (2014). "Flow and solute transport through a periodic array of vertical cylinders in shallow water". In: *Journal of Fluid Mechanics* 756, pp. 903–934.

Henry, P.-Y., D. Myrhaug, and J. Aberle (2015). "Drag forces on aquatic plants in nonlinear random waves plus current". In: *Estuarine, Coastal and Shelf Sci.* 165, pp. 10–24.

Hu, Xinhua and CT Chan (2005). "Refraction of water waves by periodic cylinder arrays". In: *Physical review letters* 95.15, p. 154501.

Järvelä, J. et al. (2006). "Flow-vegetation-sediment interaction: Research challenges". In: *River Flow 2006*. Ed. by Ferreira et al. Vol. 2.

Jbaily, Abdulrahman and Ronald W Yeung (2015). "Piezoelectric devices for ocean energy: a brief survey". In: *Journal of Ocean Engineering and Marine Energy* 1.1, pp. 101–118.

Journée, Johan MJ and WW Massie (2001). *Offshore hydrodynamics*. Vol. 4. Delft The Netherlands, p. 38.

Kagemoto, H. and D. K. P. Yue (1986). "Interactions among multiple three-dimensional bodies in water waves: an exact algebraic method". In: *J. Fluid Mech.* 166, pp. 189–209.

Kaina, Nadege, Mathias Fink, and Geoffroy Lerosey (2013). "Composite media mixing Bragg and local resonances for highly attenuating and broad bandgaps". In: *Scientific reports* 3, p. 3240.

Kakuno, S. and P. L.-F. Liu (1993). "Scattering of water waves by vertical cylinders". In: *J. Waterway, Port, Coastal, and Ocean Eng.* 119.3, pp. 302–322.

Kamath, A. et al. (2015). "CFD Simulations to Determine Wave Forces on a Row of Cylinders". In: *Procedia Eng.* 116, pp. 623–630.

Koehl, M. A. R. (1984). "How do benthic organisms withstand moving water?" In: *Amer. Zool.* 24.1, pp. 57–70.

Koehl, M. A. R. and S. A. Wainwright (1977). "Mechanical adaptations of a giant kelp". In: *Limnology and Oceanography* 22.6, pp. 1067–1071.

Landau, E.M. Lifshitz (1970). *Theory of Elasticity*. Pergamon Press.

Le Méhauté, Bernard (1969). *An Introduction to Hydrodynamics and Water Waves Volume II: Water Wave Theories*.

Leclercq, T and E De Langre (2016). "Drag reduction by elastic reconfiguration of non-uniform beams in non-uniform flows". In: *Journal of Fluids and Structures* 60, pp. 114–129.

Leclercq, Tristan and Emmanuel de Langre (2018). "Reconfiguration of elastic blades in oscillatory flow". In: *Journal of Fluid Mechanics* 838, pp. 606–630.

Linton, C. M. and D. V. Evans (1990). "The interaction of waves with arrays of vertical circular cylinders". In: *J. Fluid Mech.* 215, pp. 549–569.

Liu, Philip L-F et al. (2015). "Periodic water waves through an aquatic forest". In: *Coastal Engineering* 96, pp. 100–117.

Løvås, S. M. and A. Tørum (2001). "Effect of the kelp Laminaria hyperborea upon sand dune erosion and water particle velocities". In: *Coastal Eng.* 44.1, pp. 37–63.

Luhar, M. and H. M. Nepf (2016). "Wave-induced dynamics of flexible blades". In: *J. Fluids Struct.* 61, pp. 20–41.

Manca, E. et al. (2012). "Wave energy and wave-induced flow reduction by full-scale model Posidonia oceanica seagrass". In: *Continental Shelf Res.* 50-51.C, pp. 100–116.

Mansard, Etienne PD and ER Funke (1980). "The measurement of incident and reflected spectra using a least squares method". In: *Coastal Engineering 1980*, pp. 154–172.

Martin, Paul A (2006). *Multiple scattering: interaction of time-harmonic waves with N obstacles*. 107. Cambridge University Press.

Massel, S. R., K. Furukawa, and R. M. Brinkman (1999). "Surface wave propagation in mangrove forests". In: *Fluid Dyn. Res.* 24.4, pp. 219–249.

Mei, Chiang C, I-Chi Chan, and Philip L-F Liu (2014). "Waves of intermediate length through an array of vertical cylinders". In: *Environmental Fluid Mechanics* 14.1, pp. 235–261.

Mei, Chiang C et al. (2011). "Long waves through emergent coastal vegetation". In: *Journal of Fluid Mechanics* 687, pp. 461–491.

Moisy, Frédéric, Marc Rabaud, and Kévin Salsac (2009). "A synthetic Schlieren method for the measurement of the topography of a liquid interface". In: *Experiments in Fluids* 46.6, p. 1021.

Möller, I. et al. (2014). "Wave attenuation over coastal salt marshes under storm surge conditions". In: *Nature Geoscience* 7.10, pp. 727–731.

Moretti, Giacomo, Marco Fontana, and Rocco Vertechy (2015). "Model-based design and optimization of a dielectric elastomer power take-off for oscillating wave surge energy converters". In: *Meccanica* 50.11, pp. 2797–2813.

Morison, JR, JW Johnson, SA Schaaf, et al. (1950). "The force exerted by surface waves on piles". In: *Journal of Petroleum Technology* 2.05, pp. 149–154.

Nepf, H. M. (2012). "Flow and transport in regions with aquatic vegetation". In: *Annu. Rev. Fluid Mech.* 44, pp. 123–142.

Nikora, V (2010). "Hydrodynamics of aquatic ecosystems: an interface between ecology, biomechanics and environmental fluid mechanics". In: *River Research and Applications* 26.4, pp. 367–384.

Pecher, Arthur and Jens Peter Kofoed (2017). *Handbook of ocean wave energy*. Springer.

Rangel-Buitrago, Nelson, Allan Williams, and Giorgio Anfuso (2017). "Hard protection structures as a principal coastal erosion management strategy along the Caribbean coast of Colombia. A chronicle of pitfalls". In: *Ocean & Coastal Management*.

Renzi, Emiliano and Frederic Dias (2012). "Resonant behaviour of an oscillating wave energy converter in a channel". In: *Journal of Fluid Mechanics* 701, pp. 482–510.

Renzi, Emiliano et al. (2014). "How does Oyster work? The simple interpretation of Oyster mathematics". In: *European Journal of Mechanics-B/Fluids* 47, pp. 124–131.

Sarkar, Dripta, Kenneth Doherty, and Frederic Dias (2016). "The modular concept of the Oscillating Wave Surge Converter". In: *Renewable Energy* 85, pp. 484–497.

Sarkar, Dripta, Emiliano Renzi, and Frederic Dias (2014). "Wave farm modelling of oscillating wave surge converters". In: *Proceedings of the Royal Society of London A: Mathematical, Physical and Engineering Sciences* 470.2167. ISSN: 1364-5021. DOI: 10.1098/rspa.2014.0118. eprint: http://rspa.royalsocietypublishing.org/content/470/2167/20140118.full.pdf. URL: http://rspa.royalsocietypublishing.org/content/470/2167/20140118.

Sarpkaya, Turgut (1976). *Vortex shedding and resistance in harmonic flow about smooth and rough circular cylinders at high Reynolds numbers*.

Smith, JMB and TP Bayliss-Smith (1998). "Kelp-plucking: coastal erosion facilitated by bull-kelp Durvillaea antarctica at subantarctic Macquarie Island". In: *Antarctic Science* 10.4, pp. 431–438.

Takeda, Mitsuo, Hideki Ina, and Seiji Kobayashi (1982). "Fourier-transform method of fringe-pattern analysis for computer-based topography and interferometry". In: *JosA* 72.1, pp. 156–160.

Van Eysden, Cornelis A and John E Sader (2006). "Resonant frequencies of a rectangular cantilever beam immersed in a fluid". In: *Journal of applied physics* 100.11, p. 114916.

Verbrugghe, Tim et al. (2017). "A Comparison Study of a Generic Coupling Methodology for Modeling Wake Effects of Wave Energy Converter Arrays". In: *Energies* 10.11, p. 1697.

Vogel, S. (1984). "Drag and flexibility in sessile organisms". In: *American Zoologist* 24.1, pp. 37–44.

— (1989). "Drag and reconfiguration of broad leaves in high winds". In: *J. Exp. Botany* 40.8, pp. 941–948.

Wei, Yanji et al. (2016). "Wave interaction with an oscillating wave surge converter. part ii: Slamming". In: *Ocean Engineering* 113, pp. 319–334.

Xie, XD, Q Wang, and N Wu (2014). "Potential of a piezoelectric energy harvester from sea waves". In: *Journal of Sound and Vibration* 333.5, pp. 1421–1429.

Yue, Dick (2005). *2.20 Marine Hydrodynamics (13.021)*. Massachussets Institute of Technology: MIT OpenCourseWare.

Zeller, R. B. et al. (2014). "Improved parameterization of seagrass blade dynamics and wave attenuation based on numerical and laboratory experiments". In: *Limnology and Oceanography* 59.1, pp. 251–266.

Bioinspiration & Biomimetics

PAPER

Surface wave energy absorption by a partially submerged bio-inspired canopy

RECEIVED
10 October 2017

REVISED
25 January 2018

ACCEPTED FOR PUBLICATION
12 February 2018

PUBLISHED
27 March 2018

C Nové-Josserand[1], F Castro Hebrero[2], L-M Petit[1], W M Megill[3], R Godoy-Diana[1] and B Thiria[1]

[1] Laboratoire de Physique et Mécanique des Milieux Hétérogènes (PMMH), CNRS UMR 7636, ESPCI Paris—PSL Research University, Sorbonne Universités—Université Pierre et Marie Curie—Paris 6, Université Paris Diderot—Paris 7, 10 rue Vauquelin, 75005 Paris, France

[2] Laboratorio de Fluidodinámica (LFD), Facultad de Ingeniería, Universidad de Buenos Aires (CONICET), Av. Paseo Colón 850, C1063ACV, Buenos Aires, Argentina

[3] Faculty of Technology and Bionics, Rhine Waal University of Applied Sciences, Kleve, Germany

E-mail: clotilde.nove-josserand@espci.fr

Keywords: wave damping, surface waves, wave-structure interactions, elasticity

Abstract

Aquatic plants are known to protect coastlines and riverbeds from erosion by damping waves and fluid flow. These flexible structures absorb the fluid-borne energy of an incoming fluid by deforming mechanically. In this paper we focus on the mechanisms involved in these fluid-elasticity interactions, as an efficient energy harvesting system, using an experimental canopy model in a wave tank. We study an array of partially-submerged flexible structures that are subjected to the action of a surface wave field, investigating in particular the role of spacing between the elements of the array on the ability of our system to absorb energy from the flow. The energy absorption potential of the canopy model is examined using global wave height measurements for the wave field and local measurements of the elastic energy based on the kinematics of each element of the canopy. We study different canopy arrays and show in particular that flexibility improves wave damping by around 40%, for which half is potentially harvestable.

1. Introduction

The energy in ocean waves is considerable and is especially evident when the water gets shallow near the shore. Coastal erosion is a major concern in many cases, and flooding prevention is a high priority for land use planners in vulnerable coastal regions. Studies of aquatic vegetation such as salt marshes or kelp have shown that natural flexible structures can withstand and dissipate the energy carried ashore by ocean waves (Koehl and Wainwright 1977, Koehl 1984, Dubi and Torum 1994, Denny and Gaylord 2002, Buck and Buchholz 2005). Denny and Gaylord (2002) reviewed the mechanics of wave-swept marine algae in order to understand how these plants can survive such forces, by looking at their size, shape and their interaction with the surrounding flow. While many aquatic organisms develop into small and tough objects, and tend to live in relative shelter on the sea floor, marine macroalgae (such as kelp) extend their long, flexible stipes to the surface of the water, where the wave energy is the highest and the hydrodynamic forces are the largest. Their ability to live in these rough conditions is in part thanks to their capacity to reconfigure (Vogel 1984, 1989). These plants can passively alter their shape in order to become more streamlined and reduce any drag forces imposed by the incoming flow, which suggests that the flexibility of the plant material plays a key role in their survivorship. A similar mechanism is evident in terrestrial vegetation subject to wind (see De Langre (2008), for a review).

The mechanisms involved in the reconfiguration of vegetation subject to fluid flow have been the focus of a number of recent studies (see e.g. Barsu *et al* 2016, Leclercq and de Langre (2016), Luhar and Nepf (2016)). This is especially interesting when looking at sediment transport (Järvelä *et al* 2006) and coastal erosion (Feagin *et al* 2009, Manca *et al* 2012). It has been observed that when flow passes through a vegetation field—which we refer to as canopy (Nepf 2012)—, the kinetic energy of the fluid is transferred to the plant through mechanical bending, which results in a damping of the flow. Experimental studies have investigated the interaction of flow over a bed of vegetation (Dubi and Torum 1996, Løvås and Tørum 2001, Anderson and Smith 2014, Möller *et al* 2014). In

particular, Augustin *et al* (2009) compared wave dissipation through emergent and near-emergent vegetation fields, and found the former to be more effective by 50%–200% per wavelength, due to the larger wave energy at the surface of the water. Nonetheless, both experimental data and field data provide varied results (Anderson *et al* 2011), and the role played by each parameter in these systems with strong fluid-structure interaction couplings is yet to be studied in more detail.

Several models have been developed for vegetation motion under wave-forcing in order to predict hydrodynamic forces and quantify wave energy dissipation (Asano *et al* 1992, Dubi and Torum 1994, Massel *et al* 1999, Henry *et al* 2015, Luhar and Nepf 2016), but these are limited as there is not yet a universally-accepted model for describing plant movement. Therefore, most studies base their results on fitted bulk drag coefficients (Luhar and Nepf 2016).

The most recent and complete model developed in Zeller *et al* (2014) is capable of simulating finite-amplitude deflections while accounting for drag and added mass. This model demonstrated that the drag generated by the vegetation motion depends strongly on the ratio of blade tip excursion to wave orbital excursion. More recently, Luhar and Nepf (2016) presented a simple, predictive framework to account for blade motion in wave energy dissipation models, based on experimental and numerical work. The results showed that for certain values of Cauchy number, which represents the ratio of the hydrodynamic forcing to the restoring force due to blade stiffness, the flexible blades exerted larger hydrodynamic forces than their rigid equivalent, possibly due to a vortex shedding that is yet missing in the simple model. Concerning hydrodynamic forces, the role of the canopy density is crucial because of the sheltering effect, as demonstrated recently in the experimental work of Barsu *et al* (2016). The spacing between elements in a model canopy will be the experimental parameter under scrutiny in the present paper. A number of works have addressed the problem of water wave diffraction by arrays of vertical structures (see e.g. Kagemoto and Yue (1986), Linton and Evans (1990)), leading to the evaluation of forces related to trapped modes within the rigid array (Kakuno and Liu 1993, Duclos and Clément 2004, Kamath *et al* 2015). Wave diffraction has also been considered as a result of a localised area of wave energy dissipation, a global perspective where the damping is a result of local energy losses due to a cluster of cylinders (Dalrymple *et al* 1984). Mei *et al* (2011, 2014) developed a semi-analytic theory for predicting wave propagation through patches of rigid emergent cylinders, which was later adapted to periodic arrays and circular forests (Guo *et al* 2014, Liu *et al* 2015) and extended to heterogenous forests (Chang *et al* 2017a, 2017b). The theory models turbulence with a constant eddy viscosity that is based on measured values of drag forces. These models, therefore, depend on experimental data and fitted factors.

Most studies focusing on wave energy dissipation by aquatic vegetation consider the context of protecting shorelines or understanding the hydrodynamics of the nearshore currents, rather than on how this dissipated energy could potentially be harvested. Regarding wave energy harvesting, works have been mostly directed at existing or developing technologies, such as the study by Sarkar *et al* (2014) on the Aquamarine Oyster device. This numerical work has looked at predicting the hydrodynamic behaviour of such devices when placed in a row or back to back. It aimed to study specifically the effects of spatial arrangements on the wave energy absorption efficiency. The principal observations conclude that as devices are placed further away from each other, these tend to behave as single units and therefore oscillate more, which benefits the amount of energy harvested. On the other hand, placing devices back to back was found to create destructive interferences causing each device to oscillate much less, leading to lower efficiency in the system. The present study aims to build on these predicted behaviours in order to improve our understanding of the interaction of wave-driven fluid motion and an array of flexible vegetation-inspired structures, with a focus on how the wave energy is distributed in such a system. Particular interest is given to the estimation of energy harvesting potential of the bending of our structures and their consequent de-energising effect on the wave-driven flow.

2. Methods

The experimental set-up consisted of an array of flexible slender blades subjected to a surface water wave field created in a small-scale laboratory wave canal 1.5 m wide and 4.3 m long, as represented in figure 1. A linear wave maker moving vertically was used to create controlled monochromatic waves and an angled polymer (PVC) sheet was placed at the end of the canal to act as a beach and minimise wall reflections.

The natural resonant frequency of the blades was measured equal to 4.5 Hz using a simple free oscillation test in water. Therefore, the imposed frequency of the wave maker was chosen to range from 2 Hz to 5 Hz. Dimensions of the water tank were chosen to fit capillary-gravity dispersion conditions, for a water depth of 8 cm. At the chosen frequency range, the conditions also match deep water conditions and, so, group velocity is assumed to equal half phase velocity. The imposed wave conditions are summarised in table 1 below.

The blades were made from Mylar® material of thickness 350 μm, density 1380 kg $\cdot$ m^{-3} and Young's Modulus (E) 5 GPa. Individual Mylar® blades were fixed to Lego® blocks, which were arranged on a Lego® base board. Each block-blade element could then be easily fixed and removed from the common base to

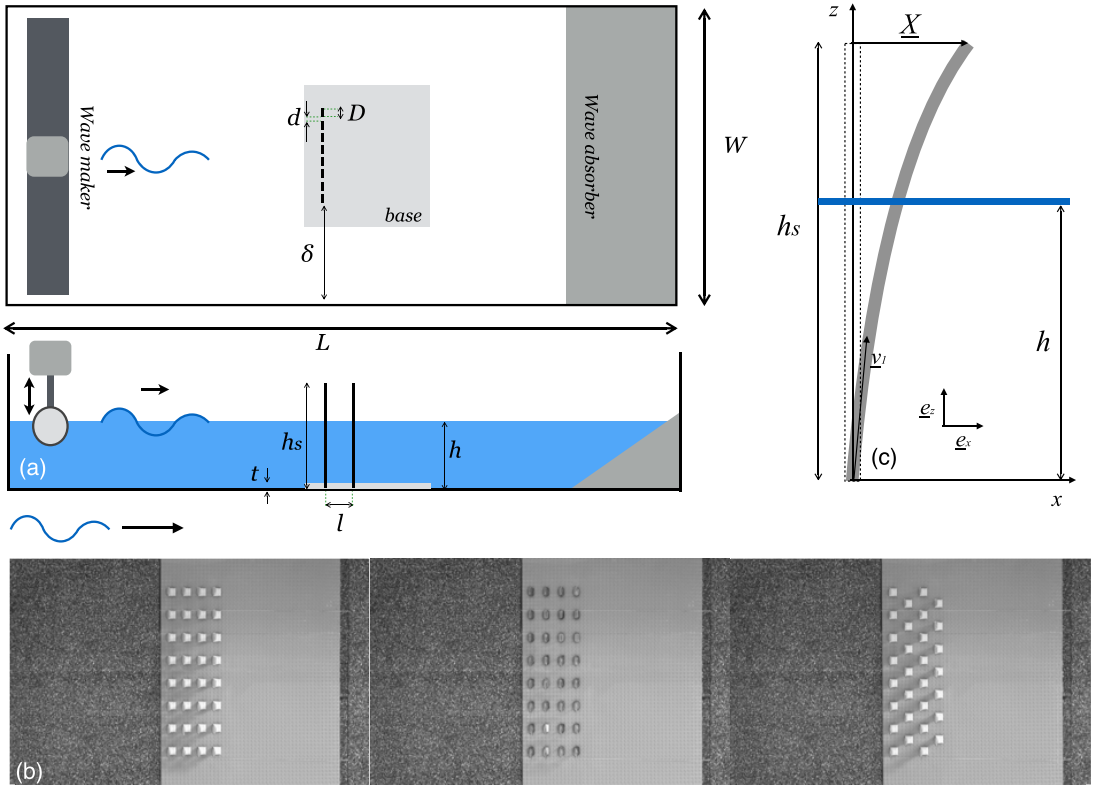

Figure 1. (a) Experimental set-up sketch. (b) Typical images from the experiment for configuration of R_4 flexible aligned (left), R_4 rigid aligned (middle), and R_4 flexible staggered (right). (c) Sketch of a cantilevered beam model.

create the desired blade arrangements. Blades were 14 mm wide and 12 cm long. Aspect ratio, defined as width over length, was $D/h_s = 0.12$ (see figure 1). To study the influence of blade spatial distribution on the wave energy distribution, three types of experiments were run:

1. varying the number $\mathcal{R}$ of rows, for fixed l and d,
2. varying the distance l, for fixed d and $\mathcal{R}$,
3. varying the distance d, for fixed l and $\mathcal{R}$.

Values of l and d were varied between $0.06 - 1.11\lambda$ and $0.03 - 0.92\lambda$, respectively. For each frequency, a reference case without blades (*Control*) was also run. A summary of the configurations is listed in table 1. To investigate the role of flexibility on wave energy damping, additional experiments were conducted using rigid blades of the same dimensions, cut from 2 mm thick plexiglas sheets. All configurations presented in table 1 were repeated with the rigid blades, along with an equivalent flexible staggered configuration for which the space l was kept identical. An example of all three case for configuration R_4 is presented in figure 1(b). All experiments were run using the same base board, 65.5 cm wide by 35 cm long. For both l and d configurations, the total number of blades was fixed to 32 (8 blades per row) in order to separate the influence of these two space parameters independently from the number of blades.

A partially submerged configuration was chosen in order to allow for maximal interaction between the incoming waves and the blades. With a water depth of 8 cm, the submergence ratio was $h_s/h = 1.38$. The average incident wave amplitude η varied between 0.7 and 3.5 mm, depending on the frequency of the wavemaker. Finally, the distance δ separating the edge of the array from the edge of the wave tank was chosen to be sufficiently large compared to the water wave lengths, in order to avoid strong lateral reflections and any subsequent diffraction within the array (see table 2).

In order to provide a realistic model of a potential wave energy converter (WEC) system, the dimensionless numbers of our reduced model in the laboratory must have the same order of magnitude as a planned prototype of oscillating blades in the sea. The Keulegan–Carpenter (KC) number quantifies the oscillatory forcing applied by waves on an obstacle and it is therefore commonly used to characterise WEC systems. It is defined as $\mathrm{KC} = \frac{UT}{D}$, with U being the wave particle horizontal velocity, T the wave period, and D the characteristic length of our object (its width in our case) (Keulegan 1958). This reduces to $\mathrm{KC} = 2\pi\frac{\eta}{D}$ in the case of sinusoidal waves and deep water conditions, thereby becoming the ratio between the wave amplitude and the obstacle width. Given the dimensions of our blades and the amplitudes of our waves, the values of KC produced in the laboratory range between [0.3–1.57] (see table 2). In real seas, wave amplitudes range between

Table 1. Configurations tested for varying number of rows, distance l in between rows, and distance d within rows.

Name	$\mathcal{R}$	l (cm)	d (cm)	l/λ	d/λ	δ/λ
1. Increasing number of rows						
R_1	1	3.2	3.4	[0.09–0.44]	[0.09–0.47]	[1.57–7.74]
R_2	2	↓	↓	↓	↓	↓
R_3	3					
R_4	4					
2. Increasing distance l						
l_1	4	2.4	3.4	[0.06–0.33]	[0.09–0.47]	[1.57–7.74]
l_2	↓	3.2	↓	[0.09–0.44]	↓	↓
l_3		4.0		[0.11–0.55]		
l_4		4.8		[0.13–0.67]		
l_5		5.6		[0.15–0.78]		
l_6		6.4		[0.18–0.89]		
l_7		7.2		[0.20–1.00]		
l_8		8.0		[0.22–1.11]		
3. Increasing distance d						
d_1	4	2.4	1.0	[0.06–0.33]	[0.03–0.14]	[1.87–9.20]
d_2	↓	↓	1.8	↓	[0.05–0.25]	[1.77–8.72]
d_3			2.6		[0.07–0.36]	[1.67–8.23]
d_4			3.4		[0.09–0.47]	[1.57–7.74]
d_5			4.2		[0.11–0.58]	[1.47–7.25]
d_6			5.0		[0.14–0.69]	[1.37–6.76]
d_7			5.8		[0.16–0.81]	[1.17–6.27]
d_8			6.6		[0.18–0.92]	[1.17–5.78]

Table 2. Experimental conditions: frequency f, amplitude η, wave lengths λ, with phase v_ϕ and group v_g velocities of imposed waves.

f (Hz)	η (mm)	λ (cm)	v_ϕ (m s^{-1})	v_g (m s^{-1})	KC
2	1.8	35.24	0.70	0.35	0.80
2.5	3.5	25.4	0.63	0.32	1.57
3	1.9	18.56	0.55	0.28	0.9
3.5	2.3	13.96	0.48	0.24	1.03
4	1.2	10.8	0.43	0.21	0.45
4.5	1	8.72	0.39	0.20	0.43
5	0.7	7.16	0.35	0.18	0.29

[1–5 m], which would impose a width of $\mathcal{O}(10–20)$ m for real scale blades, in order to maintain similar values of KC. Such sizes are coherent with the dimensions of existing WECs, such as Aquamarine's Oyster device which is 18 m wide (Sarkar *et al* 2014). Reynolds number defined as $\mathrm{Re} = \frac{\rho UD}{\mu}$ is used to compare inertial forces to friction forces. In the case of oscillatory flow, the characteristic velocity U is once again taken as the maximum amplitude of oscillation of the water particles (orbital velocity at the free surface), which, in sinusoidal waves can simplify to $u = \omega\eta$. From table 2, this gives values ranging from $\mathrm{Re} = [286 - 770]$.

In order to avoid canal reflections, each experiment was analysed over the period of the first travelling waves only. As shown in figure 2, the array is subject to both wave-maker and beach reflections, which both can distort the resulting behaviour of our system. Therefore, we chose to work in a restrictive time frame for which no reflections have yet reached the recording area of the camera. For each frequency tested, camera recordings were launched as the motor was started and these were taken over 500 images. For each test, a spatio-temporal plot was drawn using the software package ImageJ®, making it possible to determine the specific frame at which the first full wave has travelled through the array and reached the end of the recording area (x_1) (see figure 3). From the known wave characteristics and canal dimensions, one could then calculate the total number of frames over which the analysis could be done while remaining free of reflections.

With a starting distance d_{start} of 1.91 m and an ending distance d_{end} of 4.46 m, and with a fast camera acquisition frequency of 30 fps, it was calculated that the lowest frequency of 2 Hz allowed for a working window of 217 frames following the calculated t_{begin}. The analysis was performed over 100 images and began at the measured t_{begin}. These restrictions correspond to 7–16 wave periods and allowed for large error margins (see table 3 for details).

The surface wave maps were then calculated using the Schlieren method developed by Moisy *et al* (2009). This non-intrusive method relies on the analysis of refracted images of a known pattern, placed at the bottom of the canal bed. The apparent deformed images are then visualised and recorded through the transparent fluid using a fast camera placed above the water surface, and are compared to the reference image taken with a flat water surface. Each recorded image of size 1935×1216 pixels is then analysed using the PIVlab algorithm running on MATLAB® and based on stand-

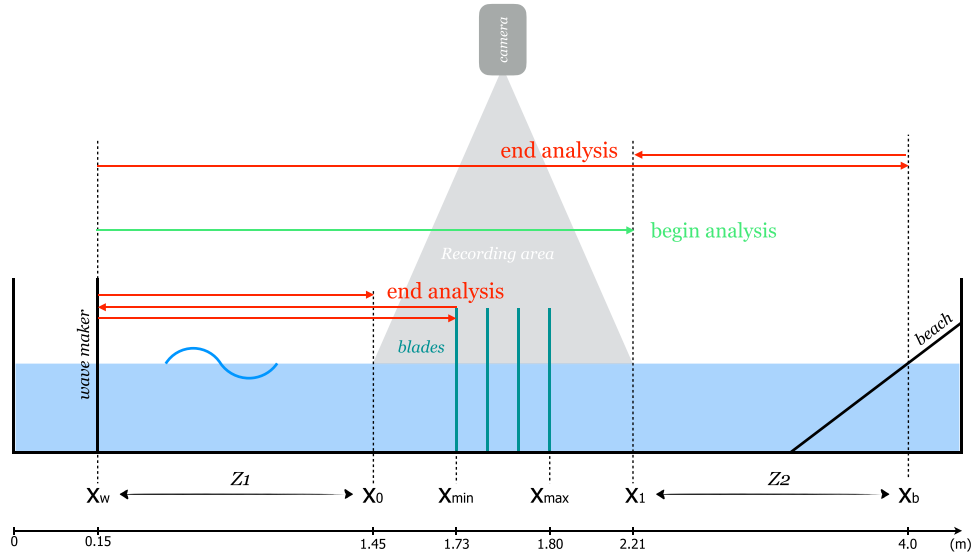

Figure 2. Sketch of analysis restrictions.

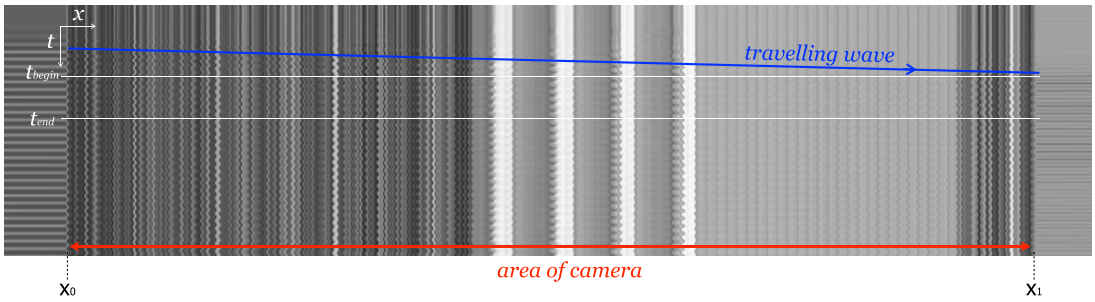

Figure 3. Illustration of the method for measuring t_{begin}, using a spatio-temporal plot of the travelling wave.

Table 3. Summary of recording characteristics for all tested frequencies.

f (Hz)	v_g (m s^{-1})	t_{begin} (s)	t_{end} (s)	$\#T_{analysis}$	Margin (%)
2	0.35	5.42	12.66	7	53
2.5	0.32	6.02	14.04	8	58
3	0.28	6.86	16.02	10	63
3.5	0.24	7.82	18.26	11	68
4	0.21	8.84	20.65	13	71
4.5	0.21	9.74	22.73	15	74
5	0.18	10.67	24.92	16	76

ard direct image correlation algorithms (DIC). Due to the correlation steps of analysis, the final treated images of the surface waves provide an image precision of 1.58 mm px^{-1}. An example of the treated images is given in figure 4.

The second part of the analysis was focused on the bending of the blades, which relies on the recording of the beam movements. The top of each blade was painted black to contrast with surroundings and the movement of each blade end was quantified using a spatio-temporal stacking method as provided by the software package ImageJ, (see figure 8). It was thus possible to track the movement of each blade using the same recorded images as those used for the surface wave maps, thereby ensuring that the data for both parts of the analysis sprung from identical experiments.

3. Results and discussion

Conservation of energy within our system imposes that the total energy of the incoming waves is shared between reflection, transmission and dissipation within the array. This energy analysis is performed in two parts: the first part focuses on the study of the surface wave maps (3.1) in order to determine reflection and transmission coefficients while the second part focuses on the mechanics of the blade array (3.2) in order to determine dissipation coefficients. Finally, both are combined in order to evaluate the energy distribution within our system.

3.1. Surface wave maps

For each configuration listed in table 1, the surface wave maps were studied before and after the blade array, as presented in figure 4(c). Although the Moisy correlation technique is designed to work with a

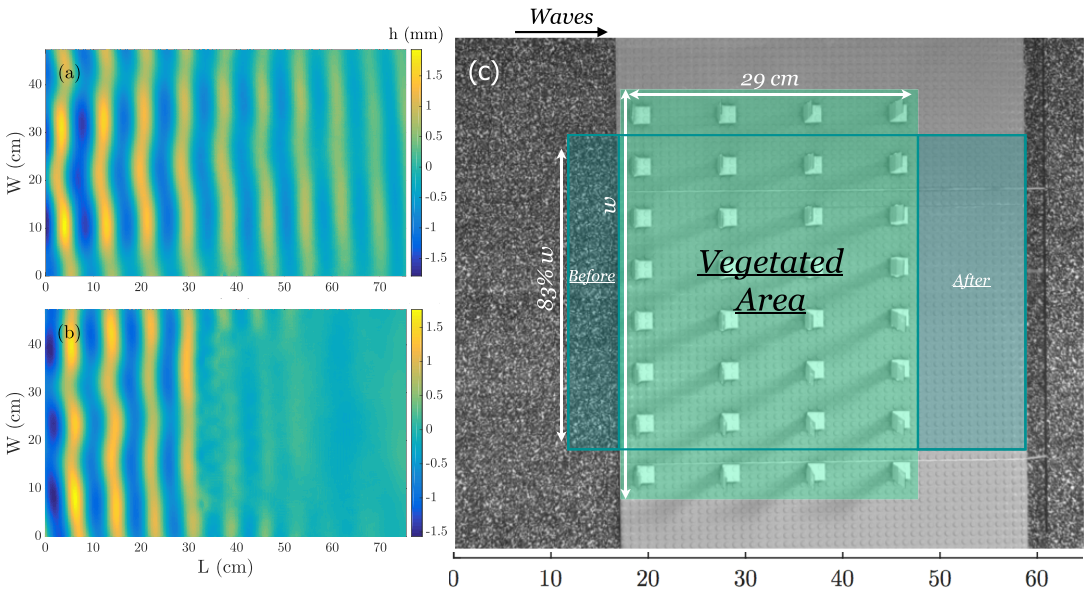

Figure 4. Typical surface wave maps obtained with the Schlieren method for *Control* (a) and configuration l_2 (b). Zones of analysis for transmission and reflection coefficients (c).

background pattern of random dots, we chose to work also in the area of our lego base, in order to extend the zone of analysis a little further. For the correlation function, the images of reference were taken before each one of the studied configurations, so that the dotted lego base blade also served as the element of comparison. Therefore, the wave maps were calculated before the array using the random pattern and after the array using the base. Although, the latter is less accurate, (the surface elevations obtained are 30% lower due, in part, to the lower light contrast), the ensuing method for calculating the transmission and reflection coefficients described below was carefully chosen in order to overcome these inaccuracies.

In the specific case of configuration *d*, the surface elevation maps had to be analysed over an adapted area in order to remain coherent throughout our study. Indeed, for larger *d* spacings, part of the vegetated area exceeded the camera view. Therefore, in order to maintain comparable results, the width *w* of the area of analysis was varied, depending on the configuration's *d* spacing. The visible ratio of camera field to vegetated field was calculated as 83% for the upper bound case (configuration d_8) and was applied to all other cases. These cropped surface maps served as the basis for wave energy analysis since wave energy density per unit area is related to local wave height η by $\mathcal{E}_w = \frac{1}{2}\rho g \eta^2$, where ρ is the density of the fluid.

In order to calculate transmission and reflection coefficients, the surface wave maps were analysed in their complex form using fast Fourier transform. We assume in our study that the imposed waves are linear, thereby allowing us to work with the 1st (fundamental) mode of the wave averaged over time:

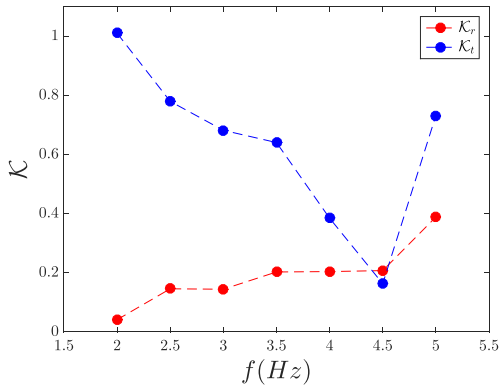

Figure 5. Variation of K_r and K_t coefficients for configuration l_2.

$$\eta_1(x,y) = \frac{2}{T}\int_0^T \eta(x,y,t)\cdot e^{i\omega t}dt. \quad (1)$$

Finally, these transformed surface wave maps are averaged transversally (in the *y*-direction).

From figure 2, we can define a zone *Z*1 located before the blades as $[0, x_{\min}]$ and a zone *Z*2 located after the blades as $[x_1, x_b]$. It is assumed that the waves in each zone have the form

$$\eta(x) = \begin{cases} ae^{-ikx} + K_r a e^{ikx} & \text{in } Z1 \\ K_t a e^{-ikx} & \text{in } Z2. \end{cases} \quad (2)$$

Taking x_a and $x_b \in Z1$, and $x_c \in Z2$, the reflection (K_r) and transmission (K_t) coefficients can then be defined as

$$K_r = \frac{e^{-ikx_b} - H_1 \cdot e^{ikx_a}}{H_1 \cdot e^{ikx_a} - e^{ikx_b}} \quad (3)$$

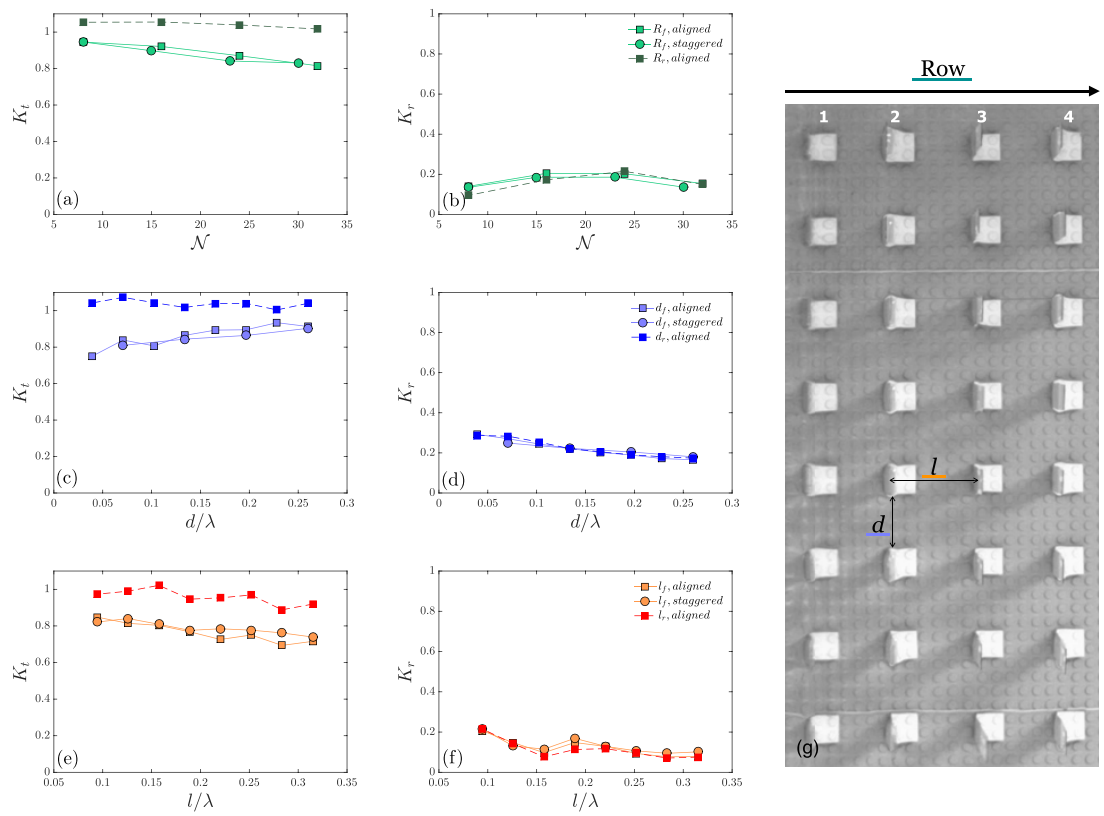

Figure 6. Proportion of power reflected K_r and transmitted K_t for an imposed frequency of 2.5 Hz, for varying parameters shown in figure (g). Configurations of increasing rows R are shown in figures (a) and (b), those of increasing spacing d are shown in figures (c) and (d), and those of increasing spacing l are shown in figures (e) and (f). Results are presented for flexible aligned (solid lines, squares), rigid aligned (dashed lines, squares), and flexible staggered (solid lines, circles) cases.

$$K_t = \frac{e^{-ikx_a} + K_r \cdot e^{ikx_a}}{H_2 \cdot e^{-ikx_c}} \tag{4}$$

where H_1 and H_2 are transfer functions defined as $\eta(x_b)/\eta(x_a)$ and $\eta(x_a)/\eta(x_c)$, respectively. All three points x_a, x_b, x_c were selected randomly and final coefficients were averaged over 200 iterations.

As explained previously, the canal width exceeds that of the array by a distance δ (see table 1). It is therefore worth noting that given the range of frequencies tested and the variable array widths, diffraction will be visible for cases where the total width of the array is of the order $\mathcal{O}(\lambda)$. It is the case, for example, for configuration d_1 at the resonant frequency 4.5 Hz. Nonetheless, these effects are limited, with a resulting error on the transmission coefficients of approximately 3%.

These coefficients are plotted in figure 5 over the entire range of tested frequencies for configuration l_2 (aligned, flexible case). The results show a decrease in transmission with a minimal value at 4.5 Hz, which corresponds to the natural resonant frequency of the blades measured in water. Therefore, the results for all configurations were chosen to be analysed at two bounding frequencies: 2.5 Hz (figure 6) and 4.5 Hz (figure 7). All configurations presented in table 1 are shown, and results are plotted as a function of the varied parameter: increasing number of blades $\mathcal{N}$, and increasing spacings d and l, both scaled to λ.

Results show that all configurations follow similar trends with a constant offset in the transmission coefficients between rigid (dashed lines) and flexible cases (solid lines). The value of this offset is measured around 0.2 for frequency 2.5 Hz and increases to reach values of up to 0.6 for frequency 4.5 Hz, thus showing that the flexible arrays can reduce wave damping by around 40% compared to rigid ones (see figure 7). This global observation highlights the role played by flexibility regarding wave energy transmission. It is found that as the imposed wave frequency tends towards the natural resonant frequency of the blades, these transmit less then their rigid equivalent, regardless of the spatial arrangement. This is expected since the oscillations of the blades are largest at their resonant frequency. Details on the mechanics of these oscillations will be presented in section 3.2 below. However, it is noticed that this distinction is not true regarding reflection. In fact, the curves for all three cases (rigid (dashed line), flexible aligned (squares, solid line) and flexible staggered (circles, solid line)) remain very close together, for both imposed frequencies (see figures 6 and 7), which suggests that flexibility has little influence on the reflection of waves. Furthermore, it is seen that the results of transmission and reflection coefficients are very similar between aligned and staggered configurations. In fact, most curves match exactly. This is unexpected given that in a staggered configuration, a larger number of blades are directly facing the incident

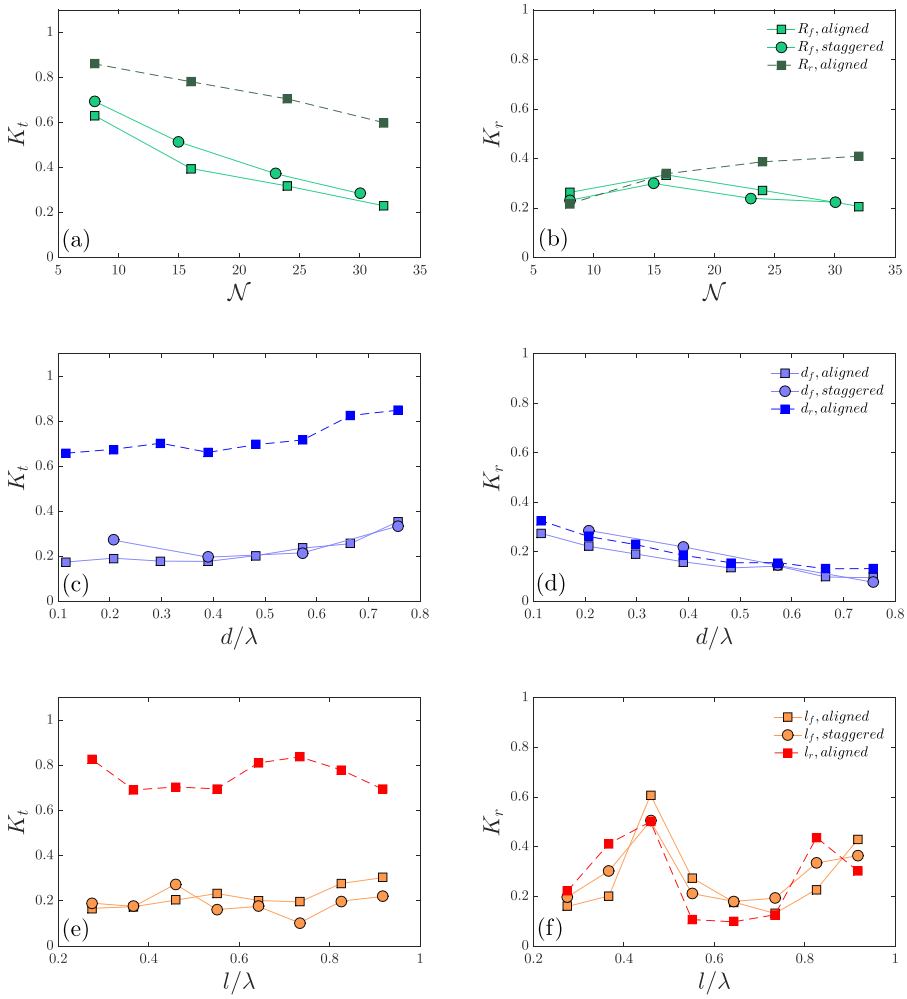

Figure 7. Proportion of power reflected K_r and transmitted K_t for an imposed frequency of 4.5 Hz, for varying parameters shown in figure 6(g). Configurations of increasing rows R are shown in figures (a) and (b), those of increasing spacing d are shown in figures (c) and (d), and those of increasing spacing l are shown in figures (e) and (f). Results are presented for flexible aligned (solid lines, squares), rigid aligned (dashed lines, squares), and flexible staggered (solid lines, circles) cases.

wave front. Yet, this result shows that the parameter l dominates the interference between rows, rather than the lateral offset of the neighbouring rows.

The results for frequency 2.5 Hz (see figure 6) show varying tendencies for each configuration. The transmission coefficient is seen to decrease as $\mathcal{N}$ increases (figure 6(a)), stabilising towards a minimal value of 0.8 beyond $\mathcal{N} = 24$ (configuration R_3). In parallel, a decrease in reflection is noticed at R_3 (figure 6(b)). This suggests that maximal efficiency regarding wave attenuation is reached with an array composed of 3 rows. In contrast, the transmission coefficient K_t for the flexible cases increases linearly with the spacing d (figure 6(c)), while the reflection coefficient K_r decreases (figure 6(d)). Both observations imply that as the array spreads out, i.e. d becomes larger, the waves interact less with the array leading to lower damping and reflection. Finally, transmission seems to remain more or less stable, regardless of the size of l (figure 6(e)), with values that fluctuate around 0.8 for the flexible cases. Similarly, reflection coefficients oscillate around 0.1 for all cases (figure 6(f)). Parameter d is therefore more influential than l at that frequency.

Figure 7 presents the same results for a wave frequency matching the natural frequency of the blades (4.5 Hz). As seen previously, increasing the number of rows leads to a decrease in transmission (figure 7(a)), reducing it by 10% for the rigid case and by 20% for the flexible cases. The collective behaviour of the flexible array would therefore benefit wave damping. An inflexion point at R_2 is noticed here again for K_r values of both flexible cases (figure 7(b)), also pointing towards an effect due to the interactions between blades. The mechanical behaviour of the array will be further discussed in the following section 3.2.

As before, increasing d increases transmission coefficients while the reflection coefficients decrease (figures 7(c) and (d)). It should however be noted that the increase in K_t is not quite linear and appears to sharpen starting from $d/\lambda = 0.5$ for both flexible cases. As a mirror, the reflection decreases sharply for lower values of d. This implies that this specific space size serves as a point of inflexion regarding the dominance of transmission versus reflection. In the case of a flexible aligned configuration, transmission overtakes reflection beyond spacing $d < \lambda/2$.

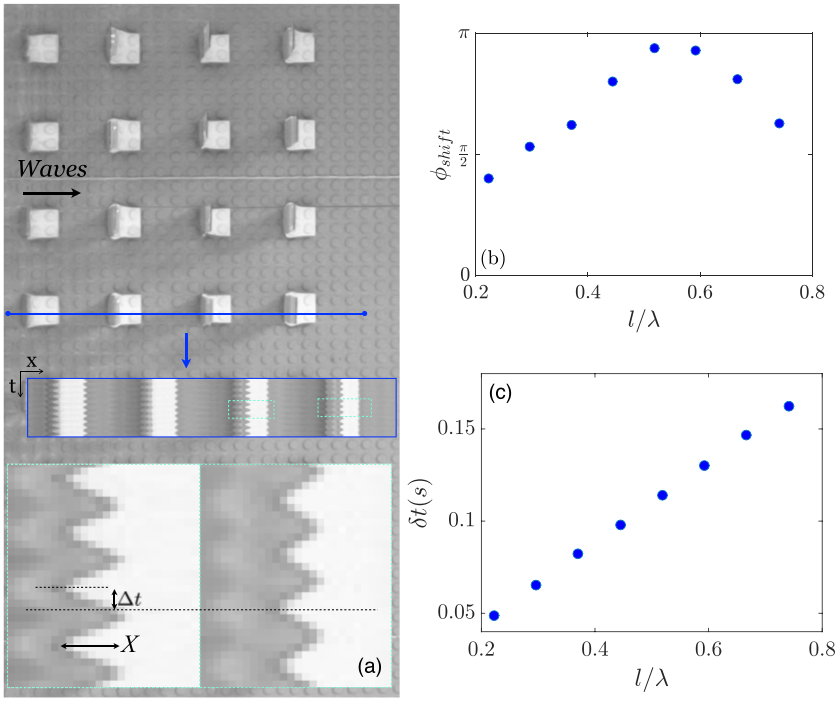

Figure 8. Tracking blade oscillations. Tracking set-up (a). Average phase shifts between rows as a function of the spacing l/λ (b). Time delay $\delta(t)$ between oscillation time shifts Δt and wave travel time t between two rows, as a function of the spacing l/λ (c). Example taken on configuration l at frequency 4 Hz.

Finally, increasing the size of l shows oscillatory variations in both transmission and reflection (figures 7(e) and (f)), with higher points near $l/\lambda = \{0.5; 1\}$ and lower K_t points near $l/\lambda = \{0.25; 0.75\}$, for flexible cases. The oscillations in K_t are mirrored in the case of rigid blades. This is due to the interference between incident and reflected waves within the array. Indeed, when a regular arrangement of obstacles such as ours in subject to incoming waves, crystallographic behaviours can be considered. Bragg's law states the condition for constructive or destructive interferences of incident waves as $2l \sin\theta = n\lambda$, with l being the spacing between two lattices and θ the incident angle of waves. When n is an integer, then the reflected waves are perfectly in phase with the incident wave, thereby building large amplitudes in the resulting waves. In our case, $\theta = \pi/2$, which simplifies the condition as $n = 2l/\lambda$. We therefore have $n = 1$ for $l/\lambda = 0.5$ and, similarly, $n = 2$ for $l/\lambda = 1$. This explains the large reflection coefficients obtained for these two points. In the case of rigid blades, these oscillations are mirrored in the transmission coefficient, due to the fact that this large reflected energy is not transmitted. While the same observation can be made for the flexible cases regarding reflection, this does not hold for transmission. In this case, although the resulting amplitudes are larger, the wave forcing is in fact lower leading to reduced blade oscillations (see figure 9).

3.2. Tracking

The second part of the experiment involved tracking the movement of the blades. A spatio-temporal stacking of each blade was performed, as shown in figure 8(a), to determine both the amplitude and the phase of their oscillations. The time shifts Δt of the blade oscillation peaks were directly measured and converted into phase shifts, with $\phi_{\text{shift}} = (\Delta t/T)2\pi$, where T is the oscillation period in seconds (see figure 8(b)). These oscillation time delays Δt were compared to the time taken for the wave to travel between blades $t = l/v_\phi$, where v_ϕ is the phase velocity of the wave, equal to $f\lambda$. Figure 8(c) shows this relationship is linear, which suggests that the phase shifts observed between rows depend directly on the time needed for the waves to travel between them.

The oscillation amplitudes X were also directly measured for each blade and the average $\bar{X}$ of each row is presented in figure 9, for all tests. In general, results show that for all cases, amplitudes $\bar{X}$ are largest in the first row, and decrease as we travel further into the array, due to both natural dissipation and to the interaction with each row.

Figures 9(a) and (b) show the variation of these amplitudes as a function of the number of rows for configurations R_{aligned} and $R_{\text{staggered}}$, respectively. In the case of an aligned configuration, the average amplitude of each row decreases when it remains constant for the staggered configuration, regardless of the number of rows present. This highlights the influence of the reflected waves within the array, depending on their longitudinal alignment. Indeed, it is suggested by Sarkar *et al* (2014) that for inline configurations, the presence of neighbouring oscillating structures in the x-direction (longitudinal direction) provides strong destructive interferences, leading to limited oscillating amplitudes. This is coherent with our observation.

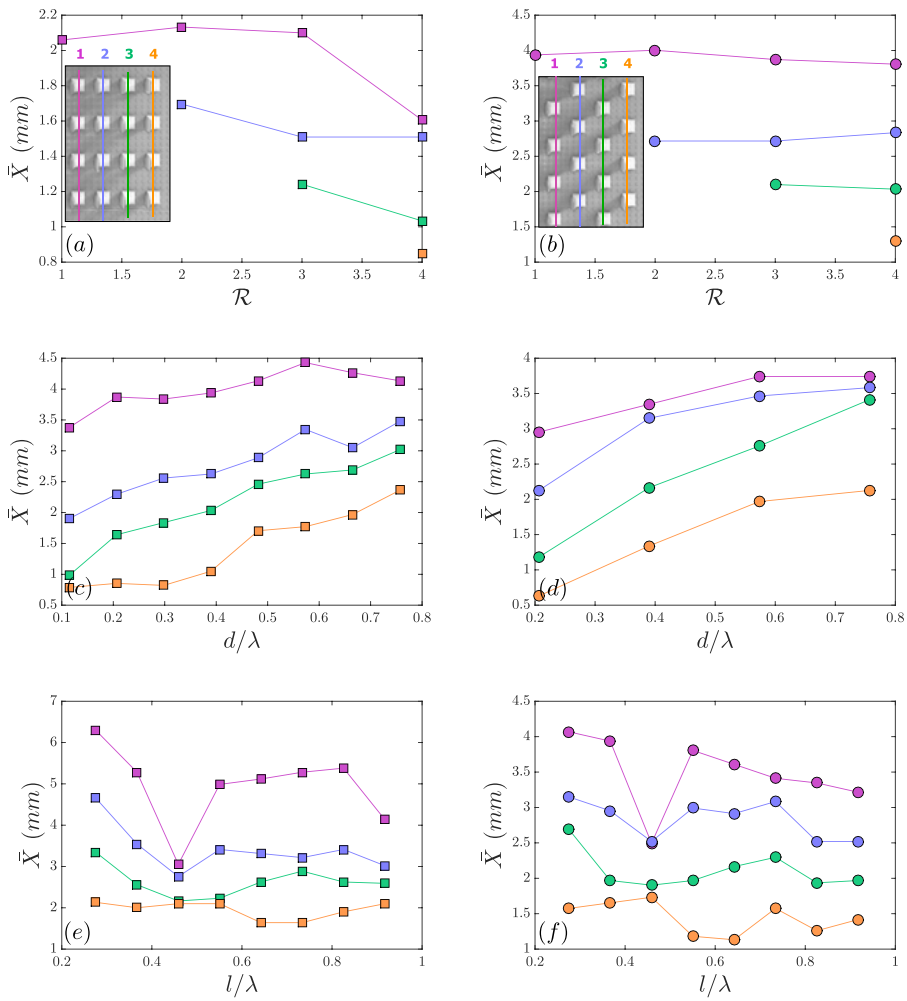

Figure 9. Comparison of average oscillating amplitude $\bar{X}$ for each row of blades between aligned (squares) and staggered (circles) cases. Results for configurations R_{aligned} (a) and $R_{\text{staggered}}$ (b), d_{aligned} (c) and $d_{\text{staggered}}$ (d), l_{aligned} (e) and $l_{\text{staggered}}$ (f).

The following two figures 9(c) and (d) plot the mean variations of amplitudes for each row belonging to configurations d_{aligned} and $d_{\text{staggered}}$, respectively. Both arrangements provide similar results, demonstrating that amplitudes increase with spacing d. Once again, Sarkar *et al* (2014) predict that as oscillating structures are spread out, these tend to behave like individual systems with larger movements. Yet, it should be noted that this increase is slowed down as d becomes larger, especially in the case of a staggered arrangement (figure 9(d)). This lower slope mirrors the steeper slope previously observed in the transmission coefficients (see figure 7(c)), found to occur for $d > \lambda/2$.

Finally, the amplitude variations for configurations l_{aligned} and $l_{\text{staggered}}$ are presented in figures 9(e) and (f), respectively. One can notice very similar behaviour between the two arrangements, with a narrow point of oscillation at $l = \lambda/2$. This confirms the observations made for both transmission and reflection coefficients in figures 7(e) and (f). As mentioned before, the corresponding spatial arrangement of the blades cause wave interferences within the array to be detrimental towards blade oscillations.

Tracking the movement of the blade tips was also used to determine the amount of energy absorbed through the movement of the flexible blades. Unlike their rigid equivalent, the Mylar blades are able to bend and oscillate as the wave fluid passes through each row of the array. This is caused by the movement of the surface particles, that oscillate with a velocity:

$$u(x,z,t) = \eta\omega \frac{\cosh k(h+z)}{\sinh kh} \cos(kx - \omega t). \quad (5)$$

For fixed t and x, we obtain the following expression describing the amplitude of the horizontal component of the velocity, function of z:

$$u_a(z) = \eta\omega \frac{\cosh k(h+z)}{\sinh kh}. \quad (6)$$

This water particle horizontal velocity component was calculated using equation (6) along the water column $h = 8$ cm for all wave frequencies tested.

The energy lost due to these oscillations is done through two mechanisms. Part of it is transferred into mechanical energy of bending (absorbed energy $\mathcal{E}_a$) and part of it is lost to the fluid due to the drag caused by the interaction between the blades and the surrounding fluid (dissipated energy $\mathcal{E}_d$).

We model our blades as simple cantilevered beams and assume linear theory to be valid given the small

oscillations observed (ranging from 2–8 mm in amplitude X). If we assume that each blade oscillates in its first mode of deformation, the local deflected shape v_1 for each beam section is given by (see e.g. Volterra and Zachmanoglou (1965)) (figure 1(c))

$$v_1(z) = \frac{1}{2}((\cos(k_1 z) - \cosh(k_1 z)) + \left(\frac{-\cos(k_1 h_s) - \cosh(k_1 h_s)}{\sin(k_1 h_s) - \sinh(k_1 z)}\right)(\sin(k_1 z) - \sinh(k_1 z))) \quad (7)$$

where h_s is the total length of the beam, k_1 is the first deformation mode coefficient. The local position of the beam section is described by the function $x(z,t) = \underline{v}_1(z) \cdot \underline{X}(t)$, given small deformations. Our blade becomes a damped oscillator for which the equation of movement is then

$$m\ddot{x} + kx = -\gamma\dot{x}. \quad (8)$$

This damping term must be further decomposed into an internal damping restoring force of the blade and the external drag damping force exerted by the external fluid. This second term is in fact nonlinear term related to the relative velocity of the blade, u_r. However, the experimental data matches a linear fit, which suggests that a linear term can be assumed in this case. The damping force of our blade becomes $\gamma_{\text{in}}\dot{x} + \gamma_{\text{ext}}u_r$. The relative velocity u_r of our blade is determined using the tracking data (amplitude X measured over a half period $T/2$) and the horizontal velocity of the fluid calculated from equation (5) above:

$$u_r(z) = u_a(z) - \dot{x}(z). \quad (9)$$

The mechanical power of the oscillating blade must equal the damped energy flux, so that

$$\mathcal{P} = (-\gamma_{\text{int}}\dot{x} \cdot \dot{x}) + (-\gamma_{\text{ext}}u_r \cdot u_r). \quad (10)$$

Given $\Gamma = \frac{\gamma}{2m}$ from equation (8), this power can thus be calculated from the damping coefficients Γ_{int} and Γ_{ext}, the blade velocity $\dot{x}$, the relative velocity u_r, the mass of the blade m and the added mass of displaced fluid m_a, as derived in

$$\mathcal{P} = 2[\Gamma_{\text{int}}(m + m_a)\dot{x}^2 + \Gamma_{\text{ext}}(m + m_a){u_r}^2] \quad (11)$$

with $\Gamma_{\text{int}} = 1.7\ \text{s}^{-1}$ and $\Gamma_{\text{tot}} = 6.4\ \text{s}^{-1}$, where $\Gamma_{\text{ext}} = \Gamma_{\text{tot}} - \Gamma_{\text{in}}$. These two values were measured from free oscillation tests by fitting an exponential curve of the form $A_0 e^{-\Gamma t} + c$ to the range of amplitudes observed in the experiments (8 mm–2 mm, see figure 9). These were obtained with 99% fitting precision using the least-squares method.

This power can be further separated between the internally absorbed power due to the work of the blade ($\mathcal{P}_a$), and the externally dissipated power due to the relative movement of the surrounding fluid ($\mathcal{P}_d$). The expressions are provided in

$$\mathcal{P}_a = 2\Gamma_{\text{int}}\left(\int_0^{h_s} \mu_s\left(\frac{\text{d}[v_1(z)X(t)]}{\text{d}t}\right)^2 \text{d}z + \int_0^{h} \mu_l\left(\frac{\text{d}[v_1(z)X(t)]}{\text{d}t}\right)^2 \text{d}z)\right) \quad (12)$$

$$\mathcal{P}_d = 2\Gamma_{\text{ext}}\left(\int_0^{h} \mu_s\left(u_a(z) - \frac{\text{d}[v_1(z)X(t)]}{\text{d}t}\right)^2 \text{d}z + \int_0^{h} \mu_l\left(u_a(z) - \frac{\text{d}[v_1(z)X(t)]}{\text{d}t}\right)^2 \text{d}z\right) = 2\Gamma_{\text{ext}}\left(\int_0^{h} (\mu_s + \mu_l)\left(u_a(z) - \frac{\text{d}[v_1(z)X(t)]}{\text{d}t}\right)^2 \text{d}z\right) \quad (13)$$

where μ_s and μ_l are the linear masses of the solid and of the displaced liquid, respectively.

The total incoming energy of the waves was calculated from the surface wave maps using the relationship $\mathcal{E}_w = \frac{1}{2}\rho g\eta^2$ defined previously. This provides the energy flux per unit area of the canal. Multiplying this energy by the wave group velocity v_g (which is equal to half the phase velocity v_ϕ in the deep water conditions of the present experiments) gives the wave energy flux per unit width:

$$\mathcal{P}_w = \mathcal{E}_w \cdot v_g. \quad (14)$$

In our case, we wish to compare the total available incident wave energy to the energy lost in our vegetated area. Therefore, the wave energy flux must be multiplied by the width of our area along with the number of waves within the area (ratio L/λ) in order to obtain the total wave energy flux entering our array

$$\mathcal{P}_{\text{tot}} = \mathcal{P}_w \cdot W = \frac{1}{2}\rho g\eta^2 v_g W\frac{L}{\lambda}. \quad (15)$$

Note that due the variability of η between experiments, average values were taken for each set of experiments (e.g. $l_{\text{staggered}}$), based on the previously calculated K_r coefficients, as follows: $\eta = \eta(x_{\min}) = \eta(x_0)/(1 + K_r)$ (see figure 2).

In parallel, the absorbed power of each individual blade is calculated using equation (12). The sum of individual $\mathcal{P}_a$ therefore provides the total power absorbed by our array as follows

$$\mathcal{P}_a = \sum_{i=1}^{\mathcal{N}} (\mathcal{P}_a)_i \quad (16)$$

where $\mathcal{N}$ is the total number of blades. The total dissipated power $\mathcal{P}_d$ was calculated in the same manner. It was then possible to estimate the proportion of the incoming power that was absorbed by the array using a coefficient $K_a = \mathcal{P}_a/\mathcal{P}_{\text{tot}}$, along with the proportion of the incoming power that was dissipated and lost to the fluid $K_d = \mathcal{P}_d/\mathcal{P}_{\text{tot}}$. The sum of these two values therefore quantifies the amount of power

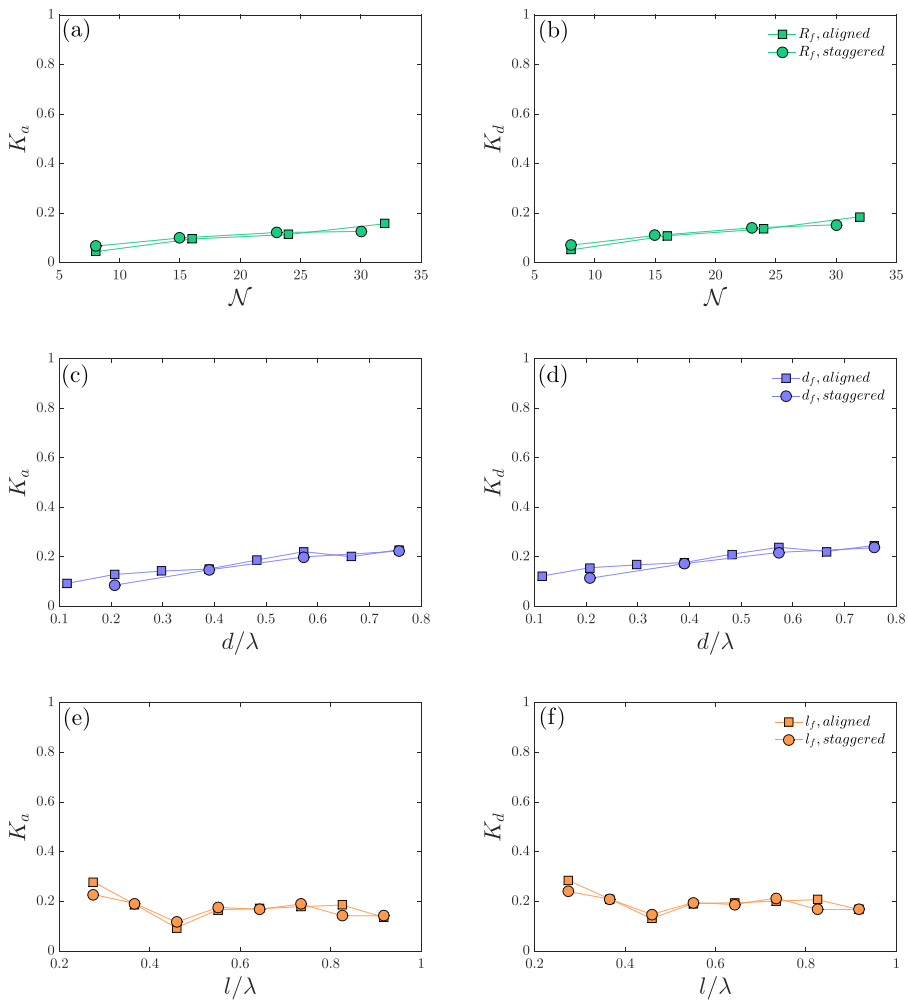

Figure 10. Proportion K_a of power absorbed by the blades through deflection (left) and proportion K_d of power dissipated by the surrounding fluid (right), as calculated from equations (12) and (13) using blade oscillation measurements given in figure 9. Results are presented for both aligned (squares) and staggered (circles) configurations R, d and l (from top to bottom), at frequency 4.5 Hz.

that is dissipated both internally and externally (K_m), due to the bending motion of the blades.

The results of these calculations are presented in figure 10 for all configurations at the excitation frequency of 4.5 Hz. The total amount of absorbed and dissipated power depends, of course, on the total number of blades present in the array and the results for configuration R in figures 10(a) and (b) show a maximal value of around 20% of absorbed power with an equivalent amount dissipated to the fluid. This amounts to a total loss of power within the array of around 40%, which corresponds to the difference in transmission between flexible and rigid cases (see figure 7). Similarly, increasing d also shows an increase in absorbed and dissipated power within the array, due to the increase in oscillation amplitudes seen in figures 9(b) and (c). Here again, the sum of K_a and K_d for configuration l_8 match the difference in transmission between the flexible array and its rigid equivalent as presented in figures 7(b) and (c), and this is overall the case for the other configurations of d. It is also noted that unlike wave damping, increasing d favours energy absorption. Finally, recalling figures 7(e) and (f), the transmission coefficients curves for configurations l and $l_{\text{staggered}}$ mirror the tendencies seen here for K_a and K_d (figures 10(e) and (f)). Once again, the troughs found at $l/\lambda = 0.5$ are caused by the lower amplitudes of oscillation of the blades due to wave interferences within the array. This lower amount of energy dissipation is therefore seen as a higher amount of transmission in figure 7.

4. Conclusion

This experimental study explored the role of flexibility and spatial distribution regarding wave dissipation and potential energy harvesting through a kelp-bed inspired array of partially submerged flexible beams. The spacing distances l between rows and d within rows were varied, along with the number of rows, and aligned and staggered arrangements were compared for each configuration. It was demonstrated that for both rigid and flexible blades, transmitted power reduces with the number of blades, increases with parameter d, and is globally independent of the spacing parameter l, i.e. maximal dissipation through the system is reached with large, dense arrays. Unexpectedly, reflection was not found to increase steadily. Instead, it was seen to

decrease slowly for arrays larger than two rows, as well as with large values of d, but it demonstrated strong fluctuations depending on parameter l/λ, which are caused by interferences internal to the array.

Wave energy damping was much improved when flexible beams were used, with a decrease in transmission of around 40%, compared to their rigid equivalent. This is consistent with previous field studies, which show flexible aquatic plants to play an essential role in erosion control. Moreover, it was demonstrated that the blades absorb an additional amount of energy through mechanical bending (around 20% of the total incoming energy), which represents in a sense the potential amount of energy that could be harvested into useful electricity. While this quantity remains limited compared to existing WEC devices, it relates to a minimalistic system, without any form of neither device nor array optimisation, and its value could certainly be improved by using more advanced systems. Furthermore, WEC arrays have not yet demonstrated strong effects on wave damping. The results presented in this paper demonstrate the potential for combining applications of an array of flexible oscillating blades to both wave damping and wave energy harvesting.

This study was focused on the influence of flexibility on wave energy distribution and was limited to simple cases: simple blade geometry and regular waves were used. Additional studies need to be undertaken with more complex systems to understand the influence of these fixed parameters on the energy harvesting capacity of a blade array. Further work is also needed to fully understand the energy distribution of the incoming waves. The wave energy has been shown here to be shared between transmission, reflection and mechanical damping, along with an additional loss representing up to 40% of the total initial energy in certain cases. The diffraction of waves within the array along with the drag imposed by the array are at least partly responsible for this loss and should be further investigated.

Acknowledgments

We acknowledge support from the Franco-Argentinian International Associated Laboratory in the Physics and Mechanics of Fluids (LIA PMF-FMF, CNRS France, CONICET Argentina) and from the BEC. AR program (Argentina). We are grateful to the *Manipulation d'Ondes de Surface* team at PMMH, in particular Eduardo Monsalve and Thomas Humbert, for allowing us to use their wave tanks and providing valuable help with the surface wave analysis, and Agnès Maurel for fruitful discussions.

ORCID iDs

C Nové-Josserand https://orcid.org/0000-0001-9316-6453
R Godoy-Diana https://orcid.org/0000-0001-9561-2699
B Thiria https://orcid.org/0000-0002-2449-1065

References

Anderson M E and Smith J M 2014 Wave attenuation by flexible, idealized salt marsh vegetation *Coast. Eng.* **83** 82–92
Anderson M E, Smith J M and McKay S K 2011 Wave dissipation by vegetation *Coastal and Hydraulics Engineering Technical Note ERDC/CHL CHETN-I-82* (U.S. Army Engineer Research and Development Center, Vicksburg, MS) (https://doi.org/10.21236/ad1003881)
Asano T, Deguchi H and Kobayashi N 1993 Interaction between water waves and vegetation *23rd Int. Conf. Coastal Engineering* pp 2709–23
Augustin L N, Irish J L and Lynett P 2009 Laboratory and numerical studies of wave damping by emergent and near-emergent wetland vegetation *Coast. Eng.* **56** 332–40
Barsu S, Doppler D, Jerome J J S, Rivière N and Lance M 2016 Drag measurements in laterally confined 2D canopies: reconfiguration and sheltering effect *Phys. Fluids* **28** 107101
Buck B H and Buchholz C M 2005 Response of offshore cultivated laminaria saccharina to hydrodynamic forcing in the north sea *Aquaculture* **250** 674–91
Chang C W, Liu P L F, Mei C C and Maza M 2017a Modeling transient long waves propagating through a heterogeneous coastal forest of arbitrary shape *Coast. Eng.* **122** 124–40
Chang C W, Liu P L F, Mei C C and Maza M 2017b Periodic water waves through a heterogeneous coastal forest of arbitrary shape *Coast. Eng.* **122** 141–57
Dalrymple R A, Kirby J T and Hwang P A 1984 Wave diffraction due to areas of energy dissipation *J. Waterway Port Coast. Ocean Eng.* **110** 67–79
De Langre E 2008 Effects of wind on plants *Annu. Rev. Fluid Mech.* **40** 141–68
Denny M and Gaylord B 2002 The mechanics of wave-swept algae *J. Exp. Biol.* **205** 1355–62
Dittrich A and Jarvela J 2005 Flow-vegetation-sediment interaction *Water Engineering Research* **6** 123–30
Dubi A and Tørum A 1995 Wave damping by kelp vegetation *Coast. Eng. 1994* pp 142–56
Dubi A and Torum A 1996 Wave energy dissipation in kelp vegetation *Coast. Eng. Proc.* 1 2626–39
Duclos G and Clément A H 2004 Wave propagation through arrays of unevenly spaced vertical piles *Ocean Eng.* **31** 1655–68
Feagin R A, Lozada-Bernard S M, Ravens T M, Möller I, Yeager K M and Bairs A H 2009 Does vegetation prevent wave erosion of salt marsh edges? *Proc. Natl Acad. Sci.* **106** 10109–13
Guo X, Wang B and Mei C C 2014 Flow and solute transport through a periodic array of vertical cylinders in shallow water *J. Fluid Mech.* **756** 903–34
Henry P, Myrhaug D and Aberle J 2015 Drag forces on aquatic plants in nonlinear random waves plus current *Estuarine Coast. Shelf Sci.* **165** 10–24
Kagemoto H and Yue D K P 1986 Interactions among multiple three-dimensional bodies in water waves: an exact algebraic method *J. Fluid Mech.* **166** 189–209
Kakuno S and Liu P L 1993 Scattering of water waves by vertical cylinders *J. Waterway Port Coast. Ocean Eng.* **119** 302–22
Kamath A, Bihs H, Chella M A and Arntsen Ø A 2015 CFD simulations to determine wave forces on a row of cylinders *Proc. Eng.* **116** 623–30
Keulegan G H and Carpenter L 1958 Forces on cylinders and plates in an oscillating fluid *J. Res. Natl Bur. Stand.* **60** 423
Koehl M A R 1984 How do benthic organisms withstand moving water? *Am. Zool.* **24** 57–70
Koehl M A R and Wainwright S A 1977 Mechanical adaptations of a giant kelp *Limnol. Oceanogr.* **22** 1067–71
Leclercq T and de Langre E 2016 Drag reduction by elastic reconfiguration of non-uniform beams in non-uniform flows *J. Fluids Struct.* **60** 114–29

Linton C M and Evans D V 1990 The interaction of waves with arrays of vertical circular cylinders *J. Fluid Mech.* **215** 549–69
Liu P L F, Chang C W, Mei C C, Lomonaco P, Martin F L and Maza M 2015 Periodic water waves through an aquatic forest *Coast. Eng.* **96** 100–17
Løvås S M and Tørum A 2001 Effect of the kelp laminaria hyperborea upon sand dune erosion and water particle velocities *Coast. Eng.* **44** 37–63
Luhar M and Nepf H M 2016 Wave-induced dynamics of flexible blades *J. Fluids Struct.* **61** 20–41
Manca E, Cáceres I, Alsina J M, Stratigaki V, Townend I and Amos C L 2012 Wave energy and wave-induced flow reduction by full-scale model Posidonia oceanica seagrass *Cont. Shelf Res.* **50–1** 100–16
Massel S R, Furukawa K and Brinkman R M 1999 Surface wave propagation in mangrove forests *Fluid Dyn. Res.* **24** 219–49
Mei C C, Chan I C and Liu P L F 2014 Waves of intermediate length through an array of vertical cylinders *Environ. Fluid Mech.* **14** 235–61
Mei C C, Chan I C, Liu P L F, Huang Z and Zhang W 2011 Long waves through emergent coastal vegetation *J. Fluid Mech.* **687** 461–91
Moisy F, Rabaud M and Salsac K 2009 A synthetic schlieren method for the measurement of the topography of a liquid interface *Exp. Fluids* **46** 1021
Möller I *et al* 2014 Wave attenuation over coastal salt marshes under storm surge conditions *Nat. Geosci.* **7** 727–31
Nepf H M 2012 Flow and transport in regions with aquatic vegetation *Annu. Rev. Fluid Mech.* **44** 123–42
Sarkar D, Renzi E and Dias F 2014 Wave farm modelling of oscillating wave surge converters *Proc. R. Soc.* A **470** 2167
Vogel S 1984 Drag and flexibility in sessile organisms *Am. Zool.* **24** 37–44
Vogel S 1989 Drag and reconfiguration of broad leaves in high winds *J. Exp. Bot.* **40** 941–8
Volterra E and Zachmanoglou E C 1965 Dynamics of vibrations *Dynamics of Vibrations* vol 1 (Columbus, OH: C.E. Merrill Books)
Zeller R B, Weitzman J S, Abbett M E, Zarama F J, Fringer O B and Koseff J R 2014 Improved parameterization of seagrass blade dynamics and wave attenuation based on numerical and laboratory experiments *Limnol. Oceanogr.* **59** 251–66

An interference model for an array of wave-energy-absorbing flexible structures

C. Nové-Josserand, R. Godoy-Diana, and B. Thiria
Laboratoire de Physique et Mécanique des Milieux Hétérogènes,
CNRS UMR 7636, ESPCI Paris, PSL Research University,
Sorbonne Universités, 7 Quai Saint Bernard, 75005 Paris, France.

Considerable work has been undertaken for the improvement of Wave Energy Converters (WEC) and array design. It has recently been suggested that by extracting wave energy, these farms could also serve to protect shorelines from wave damage. The present work focuses on the local effects of wave-structure interactions within an array of oscillating absorbers in order to optimise global effects, such as reflection, damping, and energy absorption. We use a model system of flexible blades, subject to monochromatic waves and develop a simplified one-dimensional model in order to predict optimal configurations, depending on various parameters, which include the number of blades, their spacing, and their flexibility. Optimal configurations are found to be close to regular patterns and the impact of array configurations is shown to remain limited regarding wave dissipation, mainly due to a competition between reflection and absorption.

PACS numbers: 88.60.nf,47.35.Bb

I. INTRODUCTION

Ocean waves present a large potential for renewable energy that could reach 2TW [1]. Yet, only a small portion is thus far harvested and mostly through early-stage prototypes [2]. Additionally, when this energy is not harvested, it is transmitted to the shoreline where it can cause coastal erosion. Absorbing the energy of waves through converters therefore presents a double advantage.

A large effort has been made in the last two decades regarding the development of wave energy converters (WEC), with many proposed designs (see [3–5] for reviews). These devices remain nonetheless limited in power output and efficiency and, thus, deployments in large arrays will be necessary. Each device can then be impacted by the presence of neighbours, due to wave interferences.

Many studies have explored the influence of array configurations on WEC performance and have highlighted the possible strong interferences between waves within the array [6–11]. In fact, one interesting phenomenon is observed when the devices are placed in regular patterns, separated by a distance equal to half the wavelength of the incoming wave. In this case, strong reflection is observed, similar to the Bragg resonance seen in wave scattering through crystal lattices [12]. This strong effect has been the source of extensive research in areas of solid-state physics and acoustics, with specific interest for the development of metamaterials that could absorb waves efficiently [13–17]. This research can also be extended to water waves [18] and could apply to WEC farm design. Indeed, these arrays could also serve to dampen waves and reduce coastal erosion since their aim is to extract the energy of waves over large surface areas [19–21]. In this sense, Bragg resonance could be very useful. Yet, while the associated array configuration could benefit wave damping, it is also found to reduce the device oscillations, thereby limiting power extraction. This was observed experimentally by [22] and numerically by [23]. The latter developed an analytical model describing the interaction of waves and an array of small wave energy converting buoys. Band gaps and array power absorption were predicted using the Froude-Krylov approximation to model the force on a WEC element and multiple scale analysis. The results demonstrated a clear reduction of the array's efficiency in case of Bragg resonance. Similarly, [24] studied the effect of lateral spacing of flap-type converters on the resulting capture factors. Results showed very clear peaks in performances. These observations highlight the difficulty in designing optimal wave farms, which will have to result from a trade-off between wave damping and energy harvesting.

The study of array optimisation has been undertaken by a number of numerical studies, based on various applied mathematical tools. A recent semi-analytical model has for example been developed by [25] in order to test configurations that minimise power fluctuations. However, most optimisation studies thus far have been limited to small arrays or to specific conditions, due to the costly and heavy numerical calculations used. It is therefore difficult to obtain general conclusions. In this paper, we develop a simple one-dimensional interference model in order to evaluate the benefit of optimal array configurations in terms of both wave energy absorption and damping. Following an experimental validation using a small-scale array of flexible blades, both regular and irregular arrays are considered and the influence of local coefficients on global performances are discussed.

II. METHODS

A. Theoretical model

Based on the small-scale experiments presented in [22], this paper studies the interaction between planar monochromatic waves and an infinite array of partially-

submerged slender flexible blades. The energy dissipated through the mechanical bending of these elastic structures is evaluated along with that associated to the reflected and transmitted waves, thus providing information on the global energy distribution within the system (see Fig. 1).

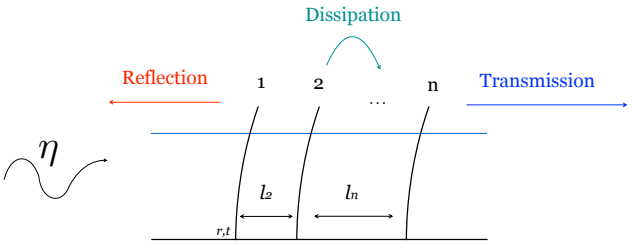

FIG. 1: Sketch of 1D model

1. Scaling

Each flexible blade within the array is subject to both inertial and viscous forces due to its interaction with water waves. This is expressed as:

$$\sum \underline{F}_{ext} = \underline{F}_{viscous} + \underline{F}_{inertia} = \underline{F}_{viscous} + \iint_S p\underline{n}dS \quad (1)$$

where p is the pressure due to the fluid acting on the wetted surface S in the normal $\underline{n}$ direction. Assuming potential flow, the pressure term is further expressed as:

$$p = \iint_S -\rho(\frac{\partial \Phi}{\partial t} + gz)\underline{n}dS \quad (2)$$

$$\Phi = \Phi_I + \Phi_D + \Phi_R \quad (3)$$

where Φ is the total wave potential such that fluid velocities can be written $\underline{u} = \nabla\Phi$, which includes an incident term Φ_I, a diffracted term Φ_D and a radiated term Φ_R. Total inertial forces are therefore shared between hydrodynamic forces in the undisturbed waves (Froude-Krylov force) and hydrodynamic forces due to the structure disturbing the waves (diffraction and radiation forces).
The importance of each force term can be evaluated using two dimensionless numbers: the Keulegan-Carpenter number $KC = \frac{uT}{D}$, which compares viscous terms to inertial terms, and the diffraction number $\mathcal{D} = \frac{D}{\lambda}$, which divides the size of the object by the wave length. Note that $u = |\underline{u}|$ is the orbital velocity of the fluid particles, T is the wave period, D is the characteristic size of the object, and λ is the wave length.
Flap-type wave energy converters can be described as line absorbers and rely on inertially driven forces. Therefore, they are generally associated with low KC numbers and tend to be wide objects in order to maximise their capture width and efficiency. Diffraction thus plays an important role in the array forces.

2. Interference model

Let η be the incident complex waveform with amplitude a, wave number k and angular frequency ω. As this wave travels through the array, it will interact with each row n of blades, which behave as obstacles transmitting part of the wave with a local coefficient t and reflecting another part with a local coefficient r (c.f. Fig. 1).

Considering a 1D-case, each row is then subject to the sum of forces induced by waves traveling in the two opposing directions. We take incident and transmitted (η_t) waves traveling in the positive x-direction and reflected waves (η_r) traveling in the negative x-direction. The associated horizontal wave particle motions are illustrated in Fig. 2 (a) and (b) below:

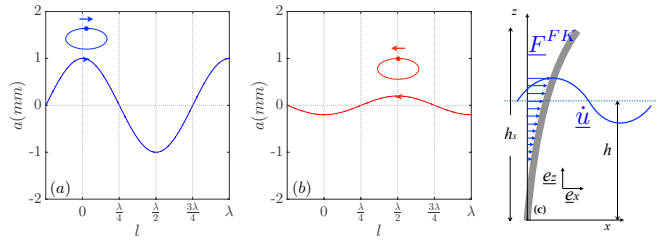

FIG. 2: Illustration of incident (or transmitted) (a) and reflected (b) waves with associated horizontal wave particle motion x. Sketch of the distributed Froude-Krylov wave force $\underline{F}^{FK}$ associated with the incident (or transmitted) wave on a partially submerged flexible blade (c).

Two waves traveling in opposite directions force water particles to move in opposite circular trajectories. Taking the transmitted wave $\eta_t = \Re\{tae^{i(kx-\omega t)}\}$ and reflected wave $\eta_r = \Re\{rae^{i(kx+\omega t)}\}$, the corresponding dynamic Froude-Krylov forces can be written as:

$$\underline{F}_t^{FK} = M\underline{\dot{u}}_t = F_t^{FK} \cdot \underline{e}_x \quad (4)$$

$$\underline{F}_r^{FK} = M\underline{\dot{u}}_r = F_r^{FK} \cdot (-\underline{e}_x) \quad (5)$$

where M is the mass of the displaced fluid, $\underline{\dot{u}}_t$ and $\underline{\dot{u}}_r$ are the orbital accelerations of the fluid particles, associated with transmitted and reflected waves, and $\underline{e}_x$ is taken to be the unit vector in the positive x-direction (c.f. Fig. 2 (c)). Given that for constant water depth, wave frequency and wave number, $\dot{u} = |\underline{\dot{u}}|$ is proportional to the wave amplitude a, the total force $\underline{F}_{tot}^{FK}$ acting on the front row becomes:

$$\underline{F}_{tot}^{FK} = \sum \underline{F}^{FK} = \underline{F}_t^{FK} + \underline{F}_r^{FK} = \mathcal{A}^{FK} \cdot \underline{F}_i^{FK} \quad (6)$$

where $\mathcal{A}^{FK}$ is an amplification factor of the incident dynamic Froude-Krylov force $\underline{F}_i^{FK}$, resulting from array interferences.

In the more general case, any row n of an array composed of N rows will be subject to the total wave force F_n^{FK} resulting from interfering transmitted (or incident) and reflected waves from the array:

$$\underline{F}_n^{FK} = \mathcal{A}_n^{FK} \cdot \underline{F}_i^{FK} \tag{7}$$

$$\mathcal{A}_n^{FK} = |T_n - R_n| \tag{8}$$

where the resulting R_n and T_n coefficients are obtained, as follows, from the sums of geometric series:

$$R_n = \underbrace{\frac{rt^n e^{i\sum_{m=1}^{n}\varphi_m}}{1 - r^2 e^{i2\varphi_{(n+1)}}}}_{\text{immediate neighbours}} \underbrace{\sum_{k=0}^{N-n-1} t^{2k} e^{i2\sum_{m=n+1}^{n+k+1}\varphi_m}}_{\text{subsequent rows}} \tag{9}$$

$$T_n = \frac{t^{(n-1)} e^{i\sum_{m=1}^{n}\varphi_m}}{1 - r^2 e^{i2\varphi_n}}$$

where $\varphi_n = \frac{l_n 2\pi}{\lambda}$ corresponds to the phase shift of incident transmitted waves η_{tn} at row n with respect to the incident wave η.

The global force amplification factor resulting from array wave interferences can therefore be predicted using equation 8 and provides an indication on the local excitation force applied onto each row. In the following sections, we derive expressions for global internal dissipation K_a, reflection $\mathcal{R}$ and transmission $\mathcal{T}$ coefficients, arising from this interference model.

3. Energy dissipation K_a

At the local scale of a single row, the energy associated to the incident wave is shared between a reflected part of ratio r^2, a transmitted part of ratio t^2, and a dissipated part of ratio $d = 1 - (r^2 + t^2)$. The dissipated energy depends on the device oscillations and includes terms of both internal dissipation (k_a) due to the device's restoring force (elastic bending or Power Take-Off damping) and external dissipation (k_d) due to the added friction losses caused by the presence of the fluid (drag).

The device is modeled as a cantilevered flexible beam (c.f. Fig. 3 (c)) bending on its first mode of deformation, for which the motion is described by that of a damped oscillator. Assuming small oscillations, linear beam theory applies, suggesting that the local position of the blade $x(z,t)$ is a function of the maximal blade tip deflection $\underline{X}(t)$ and is proportional to the total beam loading and the elastic restoring force:

$$x(z,t) = \underline{v}_1(z) \cdot \underline{X}(t) \tag{10}$$

$v_1(z)$ is the local deflected shape and is further expressed as follows:

$$v_1(z) = \frac{1}{2}\Bigg[\cos(k_1 z) - \cosh(k_1 z) + \left(\frac{\sin(k_1 h_s) - \sinh(k_1 h_s)}{\cos(k_1 h_s) - \cosh(k_1 z)}\right)(\sin(k_1 z) - \sinh(k_1 z))\Bigg] \tag{11}$$

where h_s is the total length of the blade, k_1 is the first root of the beam deflection equation. As described in [22], the power associated with internal and external dissipation can then be written as :

$$\mathcal{P} = 2[\Gamma_{int}(m + m_a)\dot{x}^2] + \frac{1}{2}\rho_w C_D A u_r^3 \tag{12}$$

$$u_r(z) = u_a(z) - \dot{x}(z) \tag{13}$$

$$u_a(z) = a\omega \cdot \frac{\cosh k(h+z)}{\cosh kh} \tag{14}$$

where Γ_{int} is the damping coefficient related to the internal work of the oscillator, m and m_a are respectively the mass of the beam and the added mass of the fluid displaced by the submerged part of the beam, C_D is an empirical drag coefficient taken equal to 2 for a plate shape, A is the projected surface subject to incoming flow, and u_r is the relative velocity between the blade and the fluid particles. For any given beam geometry and mechanical properties, and any imposed wave conditions, the dissipated power is therefore proportional to the oscillation amplitudes. Note that the oscillation amplitude depends itself on wave amplitude so that $\dot{x}$ varies together with X. The power of incoming waves per unit area is given by: $P_w = \frac{1}{2}\rho g a^2 \cdot v_g$, where v_g is the group velocity of the wave, and is related to phase velocity through $v_g = \frac{v_p}{2}(1 + \frac{2kh}{\sinh 2kh})$. The internal dissipation is given by the ratio of internal damping energy:

$$k_a = \frac{P}{P_w} = \frac{\Gamma_{int}(m + m_a)\dot{x}^2}{\frac{1}{2}\rho g a^2 \cdot v_g} \tag{15}$$

From equations 10 and 15, one can easily notice that $k_a \propto \dot{x}^2 \propto X^2$. Therefore, the global absorption factor will also depend on the amplification factor as follows:

$$k_a(X^2) = 1 - (r^2 + t^2 + k_d) \tag{16}$$

$$K_a = \sum_{n=1}^{N} \mathcal{A}_n^2 k_a \tag{17}$$

Using the amplification factor model, maximal potential energy dissipation is predicted using equation 17 above, based on the array layout.

In order to highlight the effect of array interferences on the global absorption coefficient K_a, the results are compared to a theoretical reference coefficient $K_{a_{ref}}$, which we define as the sum of non-amplified individual dissipation coefficients, only taking into account cumulative reduced transmission throughout the array. This is expressed as:

$$K_{a_{ref}} = \sum_{n=0}^{N-1} t^{2n} k_a = k_a \cdot \frac{1 - t^{2N}}{1 - t^2} \tag{18}$$

Note that the transmission coefficient is squared since the dissipation coefficient is a function of X^2 (c.f. equations 10 and 15).

4. Global reflection $\mathcal{R}$

Following similar interference principles, we use the same method to predict the total global reflection coefficient of the array $\mathcal{R}$. In this case, the sum of all reflected waves is considered at position x_1^+ in front of the first row. Taking only first-order reflections from subsequent rows, we have:

$$\eta_R = \eta_{r1} + \eta_{r2} + \eta_{r3} + ... + \eta_{rn} = \sum_{n=1}^{N} \eta_{rn} \tag{19}$$

Each row n reflects a wave η_{rn} with a phase shift $\varphi_n = \frac{l_n 2\pi}{\lambda}$ due to the distance l_n separating two neighbouring rows. If we first consider a simple case whereby the distance l_n between each row is the same constant l, then the sum of all reflected waves can be written as that of a power series (equation 20):

$$\eta_R = \Re\{ae^{i(kx)} \cdot R_z\} \tag{20}$$

with $R_z = \frac{r(1-(t^2e^{i(2\varphi)})^N)}{1-t^2e^{i(2\varphi)}}$. The total reflection coefficient $\mathcal{R} = |R_z|$ can therefore be calculated for any given phase shift φ. Note that the theoretical case without array effects gives $\mathcal{R}_{ref} = r\frac{1-t^{2N}}{1-t^2}$, which coincides with Bragg scattering ($\varphi = 0$).

Now considering independently varying values of l_n through the array, equations 9 and 20 lead to the following expression for the global reflection coefficient $\mathcal{R}$ of the entire array:

$$\mathcal{R} = r\sum_{k=0}^{N-1} t^{2k} e^{i2\sum_{m=1}^{k+1}\varphi_m} \tag{21}$$

5. Global transmission $\mathcal{T}$

Without any array effects, the global transmission coefficient would simply be expressed as $\mathcal{T}_{ref} = t^N$, where N is the total number of rows, and t is the local transmission coefficient of a single row. However, array layout affects wave interferences, which, based on a similar reasoning, leads to the following expression for the global transmission coefficient at postion x_N^+ just behind the last row fo the array:

$$\mathcal{T} = \frac{t^N e^{i\sum_{m=1}^{N}\varphi_m}}{1 - r^2 e^{i2\varphi_N}} \tag{22}$$

Based on local r and t coefficients, it therefore possible to evaluate the total energy distribution in our system using global dissipation K_d (equation 17), reflection $\mathcal{R}$ (equation 21) and transmission $\mathcal{T}$ (equation 22) coefficients, for any given separating distances l_n.

TABLE I: Wave characteristics: Frequency f, amplitude a, wave length λ of imposed waves, depth h of water.

[Hz]	**a[mm]**	**λ[cm]**	**h[cm]**
5	0.7	7.16	8

TABLE II: Blade characteristics: length h_s, width D, thickness e, Young's Modulus E, and density ρ of blades.

h_s[cm]	**D[cm]**	**e[μm]**	**E[GPa]**	**ρ[kg/m^3]**
9	1.4	350	5	1380

B. Experimental validation

In order to validate the model, small-scale experiments were run using an array of flexible slender blades subjected to a surface water wave field created in a wave canal 0.6 m wide and 1.8 m long. A flapping type wave maker was used to create controlled monochromatic waves and an angled polymer (PVC) sheet was placed at the end of the canal to act as a beach and minimise wall reflections. A sketch of the experimental set-up is presented in Fig. 3 (a). The blades were made from Mylar® material of thickness 350 μm, density 1380 kg.m^{-3} and Young's Modulus (E) 5 GPa. Individual Mylar® blades were fixed to Lego® blocks, which were arranged on a Lego® base board, thus allowing for easy configuration variations. Experiments were run at the natural resonant frequency of the blades, measured to be $f_0 = 5Hz$ in water. The blades were 9 cm long (h_s), fixed to a lego block of 1cm height and a base of 5mm thickness. The water depth was chosen to match deep water conditions, and was kept at 8cm, thus giving a submergence ratio of $h/h_s = 0.83$ (c.f. Fig. 3 (c)). The lateral spacing d between neighbouring blades was fixed at $\lambda/2$ (equal to 4 lego spaces, of 8mm each). Wave and blade characteristics are summarised in tables I and II, respectively.

In these conditions, the Keulegan-Carpenter number KC is of $\mathcal{O}(10^{-1})$, and the diffraction number D/λ is around 0.2, suggesting that inertia forces are dominating and array diffraction is not negligible. Our model therefore applies.

Two sets of experiments were run:

- The number of rows N was set to 2 and longitudinal spacing l_2 between rows 1 and 2 was varied over the range $[\frac{\lambda}{4}; \lambda]$.
- The number of rows N was set to 3 and longitudinal spacing l_3 between rows 2 and 3 was varied over the range $[\frac{\lambda}{4}; \lambda]$. Spacing l_2 between rows 1 and 2 was fixed equal to $\frac{\lambda}{4}$.

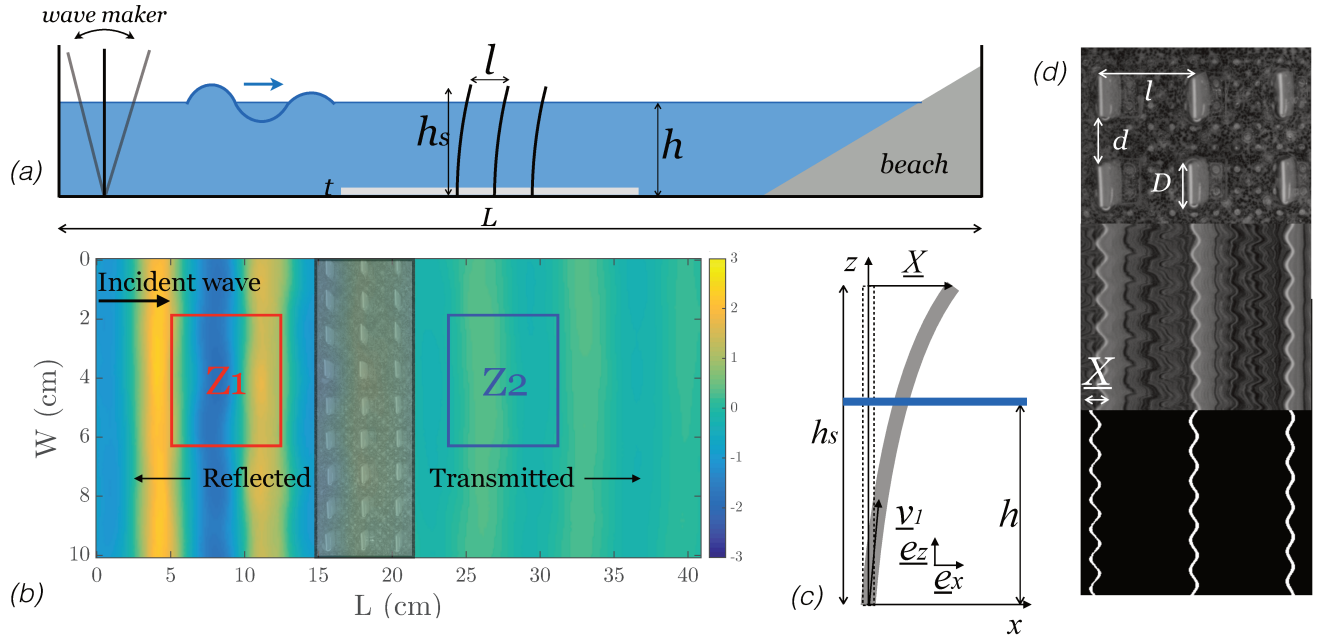

FIG. 3: (a) Sketch of the experimental set-up. (b) Example of a typical treated surface wave-map, before and after the blades, with selected zones of analysis $Z1$ (red) and $Z2$ (blue) for $\mathcal{R}$ and $\mathcal{T}$ measurements. (c) Sketch of the cantilever beam model. (d) Characteristic parameters of blades (top) and spatio-temporal plots (bottom) used for blade tip tracking analysis (please refer to [22] for detailed method description).

For each configuration, 400 images were recorded using a Phantom V9 camera at recording frequency of 200 fps, therefore covering 10 wave periods. In order to avoid strong lateral reflections and canal modes, recordings were launched when the first waves have traveled through the camera field. The surface wave maps were treated using the synthetic Schlieren method [26]. Transparent Lego base and blocks were used in order to benefit from this method over the entire image. Global reflection K_r and transmission K_t coefficients are then calculated from these treated surface wave maps, using two separate zones of analysis before ($Z1$) and after ($Z2$) the array (c.f. Fig. 3 (b)). It is assumed that the transverse average of the waves in each zone takes the form (equation 23):

$$\eta(x) = \begin{cases} ae^{-ikx} + \mathcal{R}ae^{ikx} & \text{in } Z1 \\ \mathcal{T}ae^{-ikx} & \text{in } Z2 \end{cases} \tag{23}$$

Taking x_a and $x_b \in Z1$, and $x_c \in Z2$, the reflection ($\mathcal{R}$) and transmission ($\mathcal{T}$) coefficients can then be defined as (equations 24 and 25):

$$\mathcal{R} = \frac{e^{-ikx_b} - H_1 \cdot e^{ikx_a}}{H_1 \cdot e^{ikx_a} - e^{ikx_b}} \tag{24}$$

$$\mathcal{T} = \frac{e^{-ikx_a} + \mathcal{R} \cdot e^{ikx_a}}{H_2 \cdot e^{-ikx_c}} \tag{25}$$

where H_1 and H_2 are transfer functions defined as $\eta(x_b)/\eta(x_a)$ and $\eta(x_a)/\eta(x_c)$, respectively. All three points x_a, x_b, x_c were selected randomly and final coefficients were averaged over 200 iterations.

Finally, the calculated transmission coefficient $\mathcal{T}$ of each configuration is normalised by that calculated for a reference case without blades $\mathcal{T}_0$ (giving $\tilde{\mathcal{T}}$), in order to separate array damping from natural wave dissipation. A reference case (without blades but with the base board) was therefore taken at the end of each set of experiments. These coefficients were calculated over the central area of the tank, where imposed waves are linear and monochromatic, thus justifying transverse averaging. The results obtained for a single row are: $\mathcal{R} \approx 0.3$ and $\tilde{\mathcal{T}} \approx 0.7$. These coefficients are those used for local r and t value inputs in the model. Note that due to the difficulties in avoiding beach and motor reflections, the measured reflection coefficient is not that representative of blade reflections only. Therefore, when calculating the global absorption K_a and transmission $\mathcal{T}$ coefficients, local r is replaced by that due to the presence of blades only, measured as $r_{blades} = r - r_{ref}$, where r_{ref} corresponds to the coefficient measured without blades (≈ 0.1). Results are presented in Fig. 4 (a) and (c) below.

The second part of the analysis was focused on the bending of the blades, which relies on the recording of the beam movements. The top of each blade was highlighted with white tape in order to contrast with the dark dotted pattern used for the Schlieren method. The movement of each blade end was quantified using a spatio-temporal stacking method as provided by the software package ImageJ, (see Fig. 3 (d)). We can therefore com-

pare normalised blade oscillations $\tilde{X}$ for each row, with normalised wave forcing $\tilde{F}^{FK}$ for each row. This is represented by the amplification factor $\mathcal{A}$ for both quantities. Results are presented in Fig. 4 (b) and (d) below. It should be noted that the experimental results are plotted against l/λ, where λ is found to vary between $[0.065 - 0.07]$. This may lead to a slight shift of the curves.

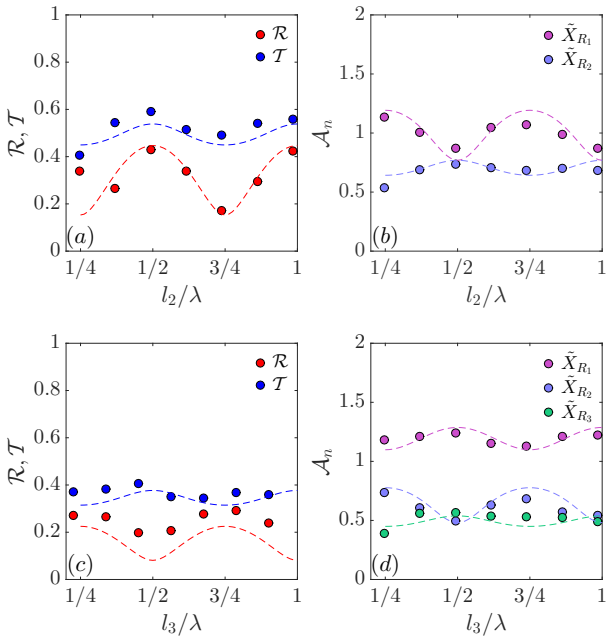

FIG. 4: Measured global reflection $\mathcal{R}$ and transmission $\mathcal{T}$ coefficients (dots) for an array composed of 2 (a) and 3 rows (c) compared with numerical values calculated from equations 21 and 22 (dotted lines). Normalised blade oscillations $\tilde{X}$ (dots) for each row R_n of an array composed of 2 (b) and 3 rows (d) rows compared with numerical values of $\mathcal{A}_n$ calculated from equation 8 (dotted lines). Spacings l_2 in the case of $N = 2$ and l_3 in the case of $N = 3$ are varied within $[\frac{\lambda}{4}; \lambda]$.

Results show good agreement between experimental data and model predictions, especially regarding blade oscillation amplification factors $\mathcal{A}$, with clear peaks and troughs at $l = \lambda/4$ and $l = \lambda/2$, as expected. Results regarding global reflection and transmission coefficients are slightly lower in the case of $N = 3$. This could be due to the experimental uncertainties for local r and t calculations. Qualitative variations are nonetheless coherent.

III. RESULTS & DISCUSSION

We now use the model described above to explore all possible array configurations, in order to evaluate their influence on blade oscillations and wave damping.

1. *Regular configurations*

We first compare two bounding cases for regular configuration patterns (i.e. arrays with constant spacing l between rows), which correspond to spacing ratios $l = \lambda/2$ and $l = \lambda/4$. Taking the same local coefficients as those measured experimentally ($r = 0.2$, $t = 0.7$, $d = 0.4$), amplification factors calculated from equation 8 are plotted in Fig. 5 for each row as a function of the total number of rows in the array. The results are compared to a reference case without amplifications, i.e. assuming a series of single independent rows. These are represented by black asterisks and are calculated as t^{n-1} for each row n.

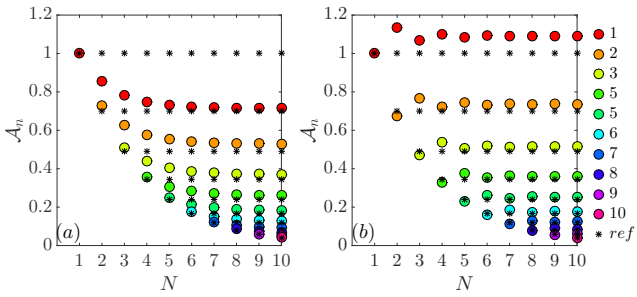

FIG. 5: Predicted amplification factors $\mathcal{A}_n$ for each row n of the array as a function or array size (increasing number of rows N). Results for constant array spacing $l = \lambda/2$ (a) and constant array spacing $l = \lambda/4$ (b). Theoretical oscillation factors without amplifications (reference) are presented in black asterisks.

As expected, these results show the strong influence of the arrangement on front row oscillations, with a 30% decrease in values for $l = \lambda/2$ versus a 10% increase for $l = \lambda/4$ and these effects hold true throughout the array, with similar attenuated effects for each subsequent row.

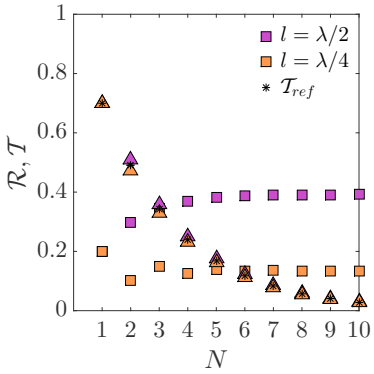

FIG. 6: Predicted global reflection $\mathcal{R}$ (squares) and transmission $\mathcal{T}$ (triangles) coefficients as a function of array size (increasing number of rows N). Results for constant array spacings $l = \lambda/2$ and $l = \lambda/4$ are presented in red and orange, respectively. Results are compared to the reference case without amplification effects ($\mathcal{T}_{ref}$).

The global reflection and transmission coefficients are also compared in Fig. 6, using equations 21 and 22. Here again, a reference case is plotted in black asterisks in order to identify the effect of array amplifications on $\mathcal{T}$ (note that results for $\mathcal{T}$ would match exactly those of $l = \lambda/2$, as described in section II A 4). As previously seen for amplification factors, a clear difference is noticed, especially regarding the reflection coefficients, with a maximum difference of around 25% reached for arrays of 10 rows. The transmission coefficients, on the other hand, fall on very similar curves, and do not deviate beyond 15% from the reference case (N=5). This suggests a competition between reflection and absorption, with a maximal gain in absorption when reflection is minimal, whereas transmission is little affected and depends mainly on array size. Another noticeable difference concerns the change in variations for increasing array sizes. While $\mathcal{R}$ increases steadily with N for $l = \lambda/2$ before reaching a limit at N=5, it decreases very slightly and in oscillatory form for $l = \lambda/4$. A similar observation can in fact be made regarding amplification factors, with mirrored trends (recall Fig. 5). This oscillation is thought to come from a pairing effect of amplifications, with mimima observed for even arrays, and maxima for odd arrays.

2. *Optimal configuration*

It is clear that variations of $\mathcal{A}_n$, $\mathcal{R}$ and $\mathcal{T}$ coefficients depend on the input parameters r and t, which are so far measured from experimental data. If these coefficients now become changeable, for example via a modification of the confinement ratio, or blade flexibility and shape, then these tendencies will be altered. Additionally, given that $\lambda/2 = 2 \times \lambda/4$ the benefits of $l = \lambda/4$ are diminished by the negative impact of $l = \lambda/2$ spacings on blade oscillations for arrays $N > 2$. This suggests that for larger arrays, configurations causing maximal oscillation amplifications may be irregular, whereby the spacing between rows is no longer constant. These optimal configurations are determined by scanning all possible combinations of l_n spacings and calculating their associated amplification factors $\mathcal{A}_n$. The optimal array is that providing the maximal global amplification factor $\mathcal{A}_{tot} = \Sigma\mathcal{A}_n$. Resulting configurations are presented in Fig. 7 for arrays ranging from 2 to 7 rows and for varying local r coefficients with a fixed local dissipation coefficient $d = 0.4$ (taken from experimental data). In our experimental case, internal dissipation k_a accounts for approximately 1/3 of the total dissipation d. In the following sections, we therefore choose to arbitrarily vary our local coefficients based on the local energy balance condition: $r^2 + t^2 + d = 1$, with $k_a = d/3$.

As expected, optimal configurations deviate from regular arrays for all sizes of $N > 2$. While the observed patterns are not yet understood, the reason for these variations are thought to stem from the local nature of the amplification effects. Given that r and t are of $\mathcal{O}(10^{-1})$,

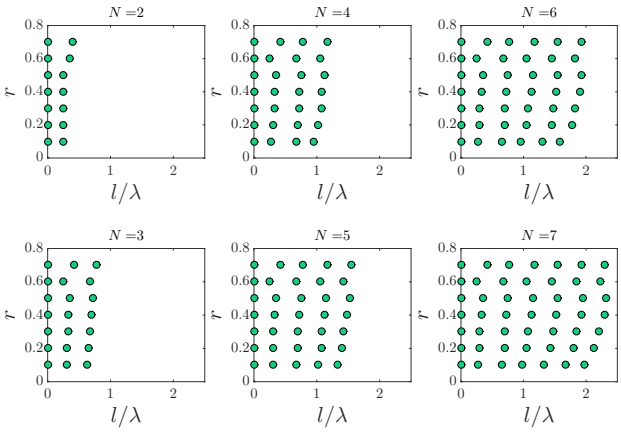

FIG. 7: Optimal configurations as a function of $\{r; t\}$ values, for increasing array size between N=2 and N=7. The local dissipation value d is fixed at 0.4.

interferences will only have an impact on neighbouring rows. This would explain why both even and odd arrays may transition through semi-regular configurations, composed of combined pairs of rows.

The benefit of the determined optimal configurations is further evaluated and the associated global dissipation coefficients are compared to those of the regular bounding cases, along with the reference case (black asterisks), as described in equation 18. Results are plotted in Fig. 8 for an array of 3 rows, for varying local dissipation coefficient $d \in [0.1 - 0.8]$. These figures clearly show the negative impact of regular arrays $l = \lambda/2$ as opposed to the benefit of both regular $l = \lambda/4$ and optimal arrays on global wave absorption, with deviations of up to $\pm 50\%$ ($d = 0.2$). However, the difference between the optimal configurations and the regular array $l = \lambda/4$ reduces as dissipation increases, and becomes negligible when $d = 0.8$. More globally, larger amplifications are found for lower values d and when $r \times t$ is at its maximum; the larger the amount of transmitted energy, the larger the impact of subsequent interferences.

Fig. 9 compares reflection and transmission coefficients of all three configurations, along with the reference $\mathcal{T}_{ref}$, as a function of r and d. Once again, the results demonstrate a clear difference between the two regular arrays, with overall higher reflection and transmission when $l = \lambda/2$, in particular for lowest values of d, for which a reduction of 60% can be reached. As noticed for blade oscillations, deviations between results obtained for optimal configurations compared with regular arrays $l = \lambda/4$ depend strongly on the values of d. The curves match almost perfectly in the low range of d, while in the larger range, reflection values for optimal configurations strongly deviate from the regular $l = \lambda/4$ case. This is due to the fact that interferences play a larger role as more energy is transmitted through the successive rows. The differences calculated reach up to 50% (when $d = 0.2$ and $r = 0.4$). Furthermore, these deviations vary with

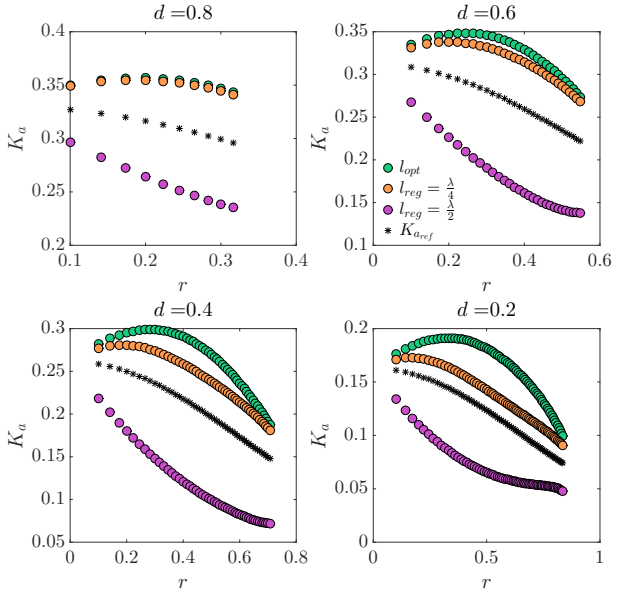

FIG. 8: Variations of global dissipation coefficient K_a depending on local d and $\{r, t\}$ values for an array composed of 3 rows. Results for the optimal configuration and regular configurations are compared to the reference values without any array effects ($K_{a_{ref}}$).

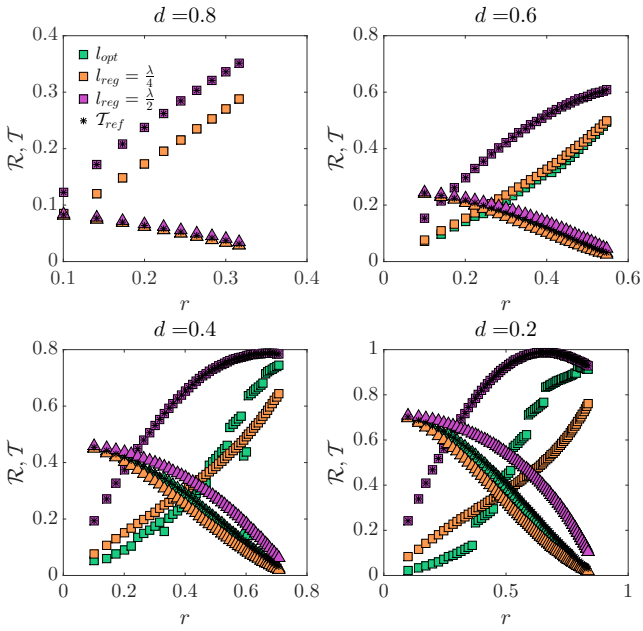

FIG. 9: Variations of global reflection $\mathcal{R}$ (squares) and transmission coefficients $\mathcal{T}$ (triangles) depending on local d and r, t values for an array composed of 3 rows. Reference transmission coefficients $\mathcal{T}_{ref}$ are plotted in black for comparison.

an inflexion point located around $r = 0.5$ beyond which optimal configurations provide larger reflections. This corresponds to the point at which optimal configurations demonstrate a shift in pattern (c.f. Fig. 7). Finally, all results converge towards similar values of $\mathcal{R}$ and $\mathcal{T}$, when r coefficients are largest. In that case, the energy transferred is quasi-nil and the effect of subsequent rows becomes negligible so that the performance of all three configurations relies mostly on the performance of the front row only. It should be noted that similar results were also found for the larger arrays.

IV. CONCLUSION

Following previous observations made regarding the influence of array configurations on wave absorber oscillations, this study has presented a simple one-dimensional model able to predict the effects of wave interferences on array performance. Based on known local reflection and transmission coefficients of an isolated row, this model was used to explore optimal array configurations regarding wave energy damping and absorption. Results have confirmed the previous experimental data by showing that in regular arrays, a separating distance $l = \lambda/2$ leads to a very large global reflection coefficient, but reduces blade oscillations, while the contrary is found for a separating distance $l = \lambda/4$. Optimal configurations regarding wave energy absorption were found to converge towards varying irregular patterns, depending on the number of rows and on the values of the input parameters $\{r, t, d\}$. However, these optimal configurations showed limited improvements over regular arrays of $l = \lambda/4$, with maximal differences appearing for low dissipation values. This model has also shown a negligible impact of array interference on wave transmission, which would depend mainly on array size and on local parameters. This is seen to arise from a competition between reflection and damping, with large oscillations compensating for a low global reflection and vice versa. It should however be noted that the simple model may not be sufficient for the account of drag effects, which could potentially lead to larger variations of the transmission coefficients. In terms of WEC farm design, the results presented in this paper suggest that array configurations can indeed help improve energy harvesting but will be limited in their impact on wave transmission. A more effective solution for the latter would be to seek means of reducing local transmission coefficients.

Acknowledgments

We acknowledge support from INSIS-CNRS PEPS et Réseaux “Ingénierie verte” 2018 program through the project “Bio-inspired wave-energy absorbers”. We are also grateful to the *Manipulation d’Ondes de Surface* team at PMMH for their valuable help and support.

[1] Benjamin Drew, Andrew R Plummer, and M Necip Sahinkaya. A review of wave energy converter technology, 2009.

[2] Alain Clément, Pat McCullen, António Falcão, Antonio Fiorentino, Fred Gardner, Karin Hammarlund, George Lemonis, Tony Lewis, Kim Nielsen, Simona Petroncini, et al. Wave energy in europe: current status and perspectives. *Renewable and sustainable energy reviews*, 6(5):405–431, 2002.

[3] Johannes Falnes. *Ocean waves and oscillating systems: linear interactions including wave-energy extraction*. Cambridge university press, 2002.

[4] S De Chowdhury, J-R Nader, A Madrigal Sanchez, A Fleming, B Winship, S Illesinghe, A Toffoli, A Babanin, I Penesis, and R Manasseh. A review of hydrodynamic investigations into arrays of ocean wave energy converters. *arXiv preprint arXiv:1508.00866*, 2015.

[5] AH Day, Aurélien Babarit, A Fontaine, Y-P He, M Kraskowski, M Murai, Irene Penesis, F Salvatore, and H-K Shin. Hydrodynamic modelling of marine renewable energy devices: A state of the art review. *Ocean Engineering*, 108:46–69, 2015.

[6] Frédéric Dias, Emiliano Renzi, Sarah Gallagher, Dripta Sarkar, Yanji Wei, Thomas Abadie, Cathal Cummins, and Ashkan Rafiee. Analytical and computational modelling for wave energy systems: the example of oscillating wave surge converters. *Acta Mechanica Sinica*, pages 1–16, 2017.

[7] Aurélien Babarit. On the park effect in arrays of oscillating wave energy converters. *Renewable Energy*, 58:68–78, 2013.

[8] B Borgarino, A Babarit, and P Ferrant. Impact of wave interactions effects on energy absorption in large arrays of wave energy converters. *Ocean Engineering*, 41:79–88, 2012.

[9] Dripta Sarkar, Emiliano Renzi, and Frederic Dias. Wave farm modelling of oscillating wave surge converters. In *Proc. R. Soc. A*, volume 470, page 20140118. The Royal Society, 2014.

[10] Dripta Sarkar, Kenneth Doherty, and Frederic Dias. The modular concept of the oscillating wave surge converter. *Renewable Energy*, 85:484–497, 2016.

[11] Yanji Wei, Thomas Abadie, Alan Henry, and Frederic Dias. Wave interaction with an oscillating wave surge converter. part ii: Slamming. *Ocean Engineering*, 113:319–334, 2016.

[12] Gwendoline Arnaud, Vincent Rey, Julien Touboul, Damien Sous, Bernard Molin, and Fabrice Gouaud. Wave propagation through dense vertical cylinder arrays: Interference process and specific surface effects on damping. *Applied Ocean Research*, 65:229–237, 2017.

[13] Nadege Kaina, Mathias Fink, and Geoffroy Lerosey. Composite media mixing bragg and local resonances for highly attenuating and broad bandgaps. *Scientific reports*, 3:3240, 2013.

[14] Andrea Colombi, Philippe Roux, Sebastien Guenneau, Philippe Gueguen, and Richard V Craster. Forests as a natural seismic metamaterial: Rayleigh wave bandgaps induced by local resonances. *Scientific reports*, 6:19238, 2016.

[15] Stéphane Brûlé, EH Javelaud, Stefan Enoch, and Sébastien Guenneau. Experiments on seismic metamaterials: molding surface waves. *Physical review letters*, 112(13):133901, 2014.

[16] Marco Miniaci, Anastasiia Krushynska, Federico Bosia, and Nicola M Pugno. Large scale mechanical metamaterials as seismic shields. *New Journal of Physics*, 18(8):083041, 2016.

[17] Bhisham Sharma and Chin-Teh Sun. Local resonance and bragg bandgaps in sandwich beams containing periodically inserted resonators. *Journal of Sound and Vibration*, 364:133–146, 2016.

[18] Xinhua Hu and CT Chan. Refraction of water waves by periodic cylinder arrays. *Physical review letters*, 95(15):154501, 2005.

[19] J Abanades, D Greaves, and G Iglesias. Coastal defence using wave farms: The role of farm-to-coast distance. *Renewable Energy*, 75:572–582, 2015.

[20] Elisabeth Guazzelli, Vincent Rey, and Max Belzons. Higher-order bragg reflection of gravity surface waves by periodic beds. *Journal of Fluid Mechanics*, 245:301–317, 1992.

[21] Louis-Alexandre Couston, Mir Abbas Jalali, and Mohammad-Reza Alam. Sheltering the shore via nearshore oblique seabed bars. In *ASME 2016 35th International Conference on Ocean, Offshore and Arctic Engineering*, pages V007T06A041–V007T06A041. American Society of Mechanical Engineers, 2016.

[22] C Nové-Josserand, F Castro Hebrero, LM Petit, WM Megill, R Godoy-Diana, and B Thiria. Surface wave energy absorption by a partially submerged bio-inspired canopy. *Bioinspiration & biomimetics*, 13(3):036006, 2018.

[23] Xavier Garnaud and Chiang C Mei. Bragg scattering and wave-power extraction by an array of small buoys. In *Proceedings of the Royal Society of London A: Mathematical, Physical and Engineering Sciences*, page rspa20090458. The Royal Society, 2009.

[24] Emiliano Renzi and Frederic Dias. Relations for a periodic array of flap-type wave energy converters. *Applied Ocean Research*, 39:31–39, 2013.

[25] Malin Göteman, Jens Engström, Mikael Eriksson, and Jan Isberg. Optimizing wave energy parks with over 1000 interacting point-absorbers using an approximate analytical method. *International Journal of Marine Energy*, 10:113–126, 2015.

[26] Frédéric Moisy, Marc Rabaud, and Kévin Salsac. A synthetic schlieren method for the measurement of the topography of a liquid interface. *Experiments in Fluids*, 46(6):1021, 2009.